

5-2017

Understanding the Bonding Process of Ultrasonic Additive Manufacturing

Qing Mao

Clemson University, QINGM@CLEMSON.EDU

Follow this and additional works at: https://tigerprints.clemson.edu/all_dissertations

Recommended Citation

Mao, Qing, "Understanding the Bonding Process of Ultrasonic Additive Manufacturing" (2017). *All Dissertations*. 1926.
https://tigerprints.clemson.edu/all_dissertations/1926

This Dissertation is brought to you for free and open access by the Dissertations at TigerPrints. It has been accepted for inclusion in All Dissertations by an authorized administrator of TigerPrints. For more information, please contact kokeefe@clemson.edu.

UNDERSTANDING THE BONDING PROCESS OF
ULTRASONIC ADDITIVE MANUFACTURING

A Dissertation
Presented to
the Graduate School of
Clemson University

In Partial Fulfillment
of the Requirements for the Degree
Doctor of Philosophy
Mechanical Engineering

by
Qing Mao
May 2016

Accepted by:
Dr. Georges Fadel, Committee Chair
Dr. Nicole Coutris
Dr. Mohammed Daqaq
Dr. James Gibert
Dr. Henry Rack
Dr. Gang Li

Abstract

Ultrasonic additive manufacturing (UAM) is an additive manufacturing technology that combines an additive process of joining thin metal foils layer by layer using ultrasound and a subtractive process of CNC contour milling. UAM can join similar or dissimilar materials and allows for embedded objects such as fibers and electronics. Despite these advantages, the UAM process exhibits a critical bonding failure issue as the height of the built feature approaches its width. Based on previous studies, we believe that the loss of bonding is due to complex dynamic interactions between the high frequency excitations of the sonotrode and the built feature. While the previous investigations have qualitatively explained the cause of the height to width ratio problem by showing the change of dynamic states as new layers of foils are deposited, they do not explain how the change of dynamics affects bond formation. Specifically, a UAM model is needed to be able to predict the bond quality, i.e. bond or debond, as the dynamics of the substrate state change.

In order to establish the model, a comprehensive understanding of the welding process and bonding mechanisms is required. Due to the complexity of the bonding process, the model is first decomposed into several sub-models based on the different factors that affect the process. The key factors that govern the bonding process: material plasticity, heat transfer, friction, and dynamics need to be characterized. An experiment setup is designed to investigate and characterize the effects of ultrasound on aluminum 6061-O, 6061-T6,

1100-O, and Copper 11000-O. A plasticity model is proposed by modifying the Johnson-Cook plasticity model to introduce strain-rate hardening and acoustic softening effects. A lumped parameter model consisting of mass-spring network is proposed to replace the finite element dynamic model for reducing computational cost. An asperity layer model based on sinusoidal shape solid asperities is proposed to associate the plastic deformation of the material to the linear weld density of the bonding at the interface. Other sub-models (thermal and friction models) are defined based on studies in the literature. The sub-models are implemented in the commercial software ABAQUS by using user subroutines and are integrated into one UAM model. The model is validated by comparing its prediction with experimental results in the literature. The proposed model can thus be used to understand the effects of dynamics on the stress state close to the bond interface, understand the energy flow within the UAM system, and evaluate the effects of different process parameters on the bond quality for process optimization.

Dedication

To my parents who love and support me unconditionally.

Acknowledgments

I would like to thank my advisor Dr. Georges Fadel for providing me with the opportunity to work on this amazing project with a group of brilliant people. Your enlightenment and guidance will continue to benefit me in my career. Special thanks to Dr. Nicole Coutris for your advising without which I would never be able to finish my work. Thanks to Dr. James Gibert and Dr. Mohammed Daqaq for all the instructions and suggestions that help my research take off. I am also grateful to Dr. Henry Rack for enlightening me with your outstanding expertise. Thanks to my committee member Dr. Gang Li for the valuable suggestions on my research. Thanks to Dr. Cecil Huey for your valuable input to my experimental setup design. I would also like to thank Michael Justice and Jamie Cole for all the technical support.

I would like to recognize my office mates with whom I've shared my laughter and tears in the past five years. Special thanks to Wenshan Wang, Ivan Mata, Jingyuan Yan, Anthony Garland, and Nafiseh Masoudi for being by my side in good and hard days for research and for life in Clemson. Thanks to all CEDAR faculties and students for the presentation feedbacks and social fun time.

I would also like to thank my friends from Clemson who have loved, supported, and helped me in every way. Your love and kindness are appreciated and will always be remembered.

Table of Contents

Abstract	ii
Dedication	iv
Acknowledgments.....	v
Table of Contents	vi
List of Tables	xii
List of Figures	xiv
1 Introduction	1
1.1 Overview of Ultrasonic Additive Manufacturing	1
1.2 Motivation	7
1.3 Dissertation Outline.....	7
2 Literature Review	11
2.1 Bonding Principles of UAM	12
2.1.1 Overview of the Bonding Process	12
2.1.2 Bond Mechanisms.....	13
2.2 Influential Elements for Plastic Deformation.....	15

2.2.1	Effect of Ultrasonic Energy	16
2.2.2	Effect of High Strain Rate Deformation	24
2.2.3	Effects of Temperature	27
2.2.4	Effects of Friction	29
2.2.5	Effects of Dynamics.....	30
2.2.6	Summary	32
2.3	Modeling Methods for UAM	32
2.3.1	Inverse Modeling	32
2.3.2	Decomposition and Integration of Models	33
2.4	Existing UAM Models	34
2.4.1	Plasticity Model	34
2.4.2	Thermal Model	36
2.4.3	Friction Model	37
2.4.4	Dynamic Model	38
2.5	Bond Quality Evaluation.....	40
2.5.1	Lap-shear Test.....	40
2.5.2	Peel Test.....	41
2.5.3	Three-point Bending Test	42
2.5.4	Push-Pin and Finite Element Method	43

2.5.5	Linear Weld Density	44
2.5.6	Process Optimization	45
2.5.7	Relating Plastic Deformation to Bond Quality	46
2.6	Hypotheses and Research Questions.....	47
2.6.1	Summary of Gaps in Literature	47
2.6.2	Primary Hypotheses.....	49
2.6.3	Secondary Hypotheses.....	49
2.6.4	Research Questions.....	50
3	Experimental Investigation of Acoustic Softening.....	52
3.1	Design of Experimental Setup.....	53
3.1.1	Review of Existing Setups.....	53
3.1.2	Proposed Design of Setup.....	59
3.1.3	Special Considerations in Designing the Setup	61
3.2	Experimental Details	63
3.2.1	Preparation of Materials.....	63
3.2.2	Specimens	65
3.2.3	Testing Procedure	66
3.3	Observations and Discussions.....	69
3.3.1	Experimental Observations.....	69

3.3.2	Comparison of Acoustic Softening Among Different Materials	89
3.4	Analytical Model of Acoustic Softening.....	94
4	A Plasticity Model for UAM	98
4.1	Strain Rate Hardening	101
4.2	Acoustic Softening	107
4.3	Thermal Softening.....	109
4.4	Summary	113
5	A Thermal and a Friction Model for UAM.....	116
5.1	Thermal Model in UAM	116
5.2	Friction Model in UAM	120
6	The Assembly of Submodels for the UAM Model	124
6.1	Integration of Sub-models.....	124
6.1.1	Plasticity Model Integration.....	125
6.1.2	Thermo-mechanical Model Integration	131
6.1.3	Friction Model Integration.....	133
6.1.4	Summary	134
6.2	The Setup of UAM Model in ABAQUS.....	135
6.3	Bond Quality Evaluation using Asperity Layer Model.....	139
6.3.1	Introduction.....	139

6.3.2	Model Setup.....	141
6.3.3	Preliminary Test.....	142
6.4	Results.....	145
6.4.1	Validation of UAM Model	145
6.4.2	The Effect of Height-to-width Ratio on Stresses.....	149
6.4.3	Energy Flow in UAM	159
6.4.4	Associating the UAM Predictions to Bond Quality	166
6.5	Summary	172
7	Concluding Remarks.....	174
7.1	Research Question 1.....	175
7.2	Research Question 2.....	176
7.3	Research Question 3.....	177
7.4	Research Question 4.....	177
7.5	Research Question 5.....	178
7.6	Contributions.....	178
7.7	Future Work	179
	Appendices.....	181
	Appendix A The User Defined Material Subroutine (VUMAT)	181
	Appendix B A Dynamics Model for UAM.....	188

Introduction	189
2-D Mass-spring Models	191
3-D Mass-spring Models	194
Model Validation.....	197
Summary.....	211
Bibliography	213

List of Tables

Table 3.1 Chemical compositions of Aluminum 6061-T6, Aluminum 1100-O, and Copper 11000-O.....	64
Table 3.2 Summary of operation parameters of testing.....	68
Table 3.3 Comparison of effects of ultrasound applied in elastic and plastic deformation regions	71
Table 3.4 The repeated tests of effects of ultrasound applied in elastic and plastic deformation regions.....	72
Table 3.5 The summary of the calculated stress reduction.....	76
Table 3.6 The comparison of microstructure of four different aluminum....	86
Table 3.7 The value of model constant d for different materials.....	93
Table 4.1 JC model constants for Aluminum 6061 –T6 and -O	97
Table 4.2 JC model parameter values for aluminum 6061-T6 and -O	102
Table 4.3 The acoustic softening constants for aluminum 6061-T6 and -O	106
Table 4.4 The values of thermal exponent for Aluminum 6061-T6 and -O.	110
Table 4.5 Constants for the modified Johnson-Cook model.....	111
Table 5.1 Constants for thermal model.....	115
Table 5.2 Model constants for friction model.....	119
Table 6.1 The operating parameters used for UAM simulation.....	132

Table 6.2 The material properties assigned to the asperity model.....	134
Table 6.3 Model constants of the modified JC model for Aluminum 1100 .	139
Table 6.4 The prediction of width deformation by UAM model	142
Table B.1 The material properties of aluminum alloys.....	177
Table B.2 Comparison of the mode shapes for the first five modes in 2-D case	180
Table B.3 Modal frequency predictions with different mesh resolutions in 2-D	181
Table B.4 Comparison of the mode shapes for the first five modes in 3-D case	185
Table B.5 Modal frequency predictions with different mesh resolutions in 3-D	186

List of Figures

Figure 1.1 Additive step of UAM.....	2
Figure 1.2 Subtractive step of UAM.....	2
Figure 1.3 Material combinations for UAM.....	4
Figure 1.4 The height to width ratio problem of UAM.	5
Figure 2.1 Acoustic softening and residual hardening reproduced from Langenecker	19
Figure 2.2 Softening effect induced by ultrasound (left) and the softening effect induced by heating (right); the “zero stress” is reached at ultrasonic intensity of 50 watt/cm ² (left).	19
Figure 2.3 Ion-induced SE image (a) and EBSD orientation map (b) of a cross- sectional foil cut from an indent made by 0.05 kg load without vibrating the sample. Ion-induced SE image (c) and EBSD orientation map (d) of a foil cut from an indent by 0.05 kg load made with 2 lm vibration. Many tiny subgrains with clear boundaries and sharp contrast can be seen	21
Figure 2.4 The strain rate sensitivity diagram of aluminum 6061-T6 reproduced from	27
Figure 2.5 The stick/slip motions at different height-to-width ratios	32
Figure 2.6 The failure mode of foils in lap-shear tests.....	41

Figure 2.7 Peel test specimen preparation and peeling test apparatus	42
Figure 2.8 Test configuration for the three-point bending test	43
Figure 2.9 General process window for aluminum 6061 – T0 based on peel test and linear weld density	45
Figure 3.1 Blaha and Langenecker’s first setup (left) and second setup (right)	54
Figure 3.2 Daud’s setup.....	56
Figure 3.3 Siu’s setup (left) and Yao’s setup (right).....	57
Figure 3.4 Dutta’s setup.	58
Figure 3.5 Experimentation setup: the CAD model (left) and the actual setup (right)	60
Figure 3.6 Frame Design: the CAD model (left) and the actual frame (right).	61
Figure 3.7 The propagation of the ultrasonic waves into specimen and into frame	63
Figure 3.8 Specimen design: specimen dimension (top) and actual specimen (unit: inch) made of Aluminum 6061-T6 (bottom) (Mao, Gibert, and Fadel 2014)..	65
Figure 3.9 Specimen design: specimen dimension (a) and actual specimens (unit: inch) made of Aluminum 6061-O (b), Aluminum 1100-O (c), and Copper C11000-O (d).	66
Figure 3.10 Load profiles: MTS tensile test machine (left), Branson ultrasonic welder (right).....	68

Figure 3.11 Schematics of history of stresses applied to specimens	68
Figure 3.12 Stress strain relations with ultrasonic vibrations: ultrasonic vibration in elastic deformation region (top), and ultrasonic vibration in plastic deformation region (bottom).....	70
Figure 3.13 The engineering stress-strain relations at different levels of ultrasound (US) (top). The zoom-in of the stress-strain relations to show the details of the softening phenomena (bottom).....	74
Figure 3.14 The work hardening rate with true stress-strain curve for Aluminum 6061-T6, overview (top) and enlarged view (bottom).....	75
Figure 3.15 The stress reduction versus ultrasonic energy input relation.....	76
Figure 3.16 The effect of ultrasound on stress-strain curves of aluminum 6061-O: overview (top), details of softening (bottom).....	79
Figure 3.17 The stress reduction versus ultrasonic energy input relation.....	79
Figure 3.18 The effect of different irradiation time intervals on the softening and residual behavior of material	80
Figure 3.19 The work hardening strain rate with true stress-strain for aluminum 6061-O.....	81
Figure 3.20 The effect of ultrasound on stress-strain curves of aluminum 1100-O: overview (top), details of softening (bottom).....	82
Figure 3.21 The stress reduction versus ultrasonic energy input relation.....	83
Figure 3.22 The effect of ultrasound on stress-strain curves of Copper 11000-O: overview (top), details of softening (bottom).....	84

Figure 3.23 The stress reduction versus ultrasonic energy input relation.....	85
Figure 3.24 The stress-intensity curves of all materials under study.....	85
Figure 3.25 Comparison of stress-intensity curves between aluminum single crystals and aluminum 1100-O	88
Figure 3.26 Comparison of stress-intensity curves between Aluminum 6061-T6 and Aluminum 6061-O.....	90
Figure 3.27 Comparison of stress-intensity curves between Aluminum 1100-O and Aluminum 6061-O	91
Figure 4.1 The comparison of experimental data and model prediction for Aluminum 6061 -T6 (left) and -O (right).	97
Figure 4.2 The strain rate sensitivity diagram reproduced from Yadav and Chichili.....	101
Figure 4.3 The strain rate sensitivity comparison between model prediction and experimental data for aluminum 6061-T6 and aluminum	103
Figure 4.4 The effect of strain rate hardening in Aluminum 6061-T6 (top) and -O (bottom)	104
Figure 4.5 The acoustic softening for Aluminum 6061-T6 (top) and -O (bottom).....	107
Figure 4.6 The temperature dependencies of Aluminum 6061-O and T6 ...	109
Figure 4.7 The comparison between model prediction and experimental data for thermal softening in ALuminum 6061 -6 (top) and -O (bottom).....	110

Figure 5.1 The variation of friction coefficient as a function of temperature reproduced from.	117
Figure 5.2 The variation of friction coefficient with respect to the normal pressure reproduced from.....	117
Figure 6.1 The couplings between sub-models.....	128
Figure 6.2 UAM model overview (left), and the plastic deformation layers between the top foil and built feature (right, the sonotrode is removed for clarity)	130
Figure 6.3 the amplitude and wavelength of 2-D sinusoidal shape (left) and the 3-D sinusoidal shape (right)	135
Figure 6.4 3-D top foil and sinusoidal asperity layer with $w/A=8$ (left) and $w/A=20$ (left).	136
Figure 6.5 Steady state stress and strain response of asperity layer subjected to 30 MPa pressure.	137
Figure 6.6 Displacement of the rigid plane subjected to 30 MPa pressure .	138
Figure 6.7 Effective contact ratio subjected to 30 MPa pressure	138
Figure 6.8 The contact length between top foil and sonotrode	141
Figure 6.9 The strain history of element on the edge of the top foil.....	141
Figure 6.10 he comparison of width deformation between model prediction and experimental data. Experimental data is reproduced from work of Kelly et al	142

Figure 7.1 The unit cell without diagonal springs fails in shear test (left) the unit cell with diagonal springs (right).	172
Figure 7.2 Arbitrary displacement of a discrete mass in a square unit cell	173
Figure 7.3 Elementary spring configurations for 3-D cubic unit cell.....	174
Figure 7.4 Modal frequency predictions from 20x20 and 60x60 finite element model in 2-D.....	180
Figure 7.5 Convergence of the mass-spring model (top) and the finite element model (bottom) in 2-D.....	183
Figure 7.6 Relative errors (comparing to 60x60 finite element model) of frequency prediction of 20x20 mass-spring model	183
Figure 7.7 Convergence of the mass-spring model (top) and the finite element model (bottom).	187
Figure 7.8 Modal frequency predictions from 3x3x6 mass-spring model and 30x30x60 finite element model in 3-D	188
Figure 7.9 Relative errors of frequency prediction of 20x20 mass-spring model	188
Figure 7.10 The effect of Poisson's ratio on the transient response of the built feature.	190

Chapter 1

1 Introduction

1.1 Overview of Ultrasonic Additive Manufacturing

The ultrasonic additive manufacturing (UAM) is a solid-state free form fabrication process that combines ultrasonic welding and CNC contour milling. The technology was invented and patented by Dawn White, and was commercialized by Solidica Inc. Now the technology is owned by Fabrisonic Inc. The fabrication process consists of an additive step (Figure 1.1) and a subtractive step (Figure 1.2). It begins with the placement of a thin metal foil (typically 100 - 150 μm thick) on a sacrificial base plate that is bolted on a moderately heated (150 $^{\circ}\text{C}$) anvil. The foil is compressed onto the base plate or on previous layers under moderate compressive load (50 – 1600 N) by a rolling ultrasonic horn, which vibrates at a frequency of 20 kHz in a direction transverse to its rolling direction. The vibration amplitude ranges between 5 and 40 μm . The vibrating horn grabs the foil because of its textured surface, and as they vibrate together, the surface oxides at the foil-to-foil interface are displaced or eliminated through friction, the surface asperities are leveled off (Kong, Soar, and Dickens 2003; Ram, Yang, et al. 2007), the foils are compressed, and atomic

bonding is initiated by allowing metal-to-metal contact. When the bonding of a layer is completed, the next layer is welded to the previously deposited layer using the same procedure. Typically, four layers of deposited metal foils are defined as one level in UAM. When one level is finished, the subtractive step is started. A CNC milling head is used to shape the deposited layers to the required sliced contour. The additive-subtractive process is repeated until the desired dimensions of the feature are reached.

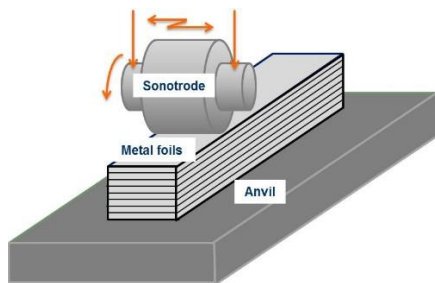


Figure 1.1 Additive step of UAM

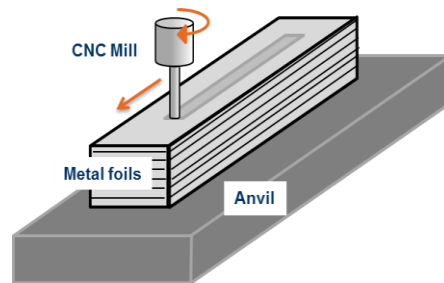


Figure 1.2 Subtractive step of UAM

In the additive step, the mechanism for bonding deposited foils originates from the ultrasonic metal welding (UMW). The UMW was invented over 60 years ago and has been under study ever since. It is a solid-state joining process in which metals are joined due to the introducing of ultrasonic vibrations and moderate compression. The joining process has been studied by many researchers but the exact mechanism is still not completely understood (de Vries 2004). However, the most widely accepted theory is that by applying a moderate compression normal to the foil-to-foil interface and a high frequency differential motion parallel to the foil-to-foil interface, the asperities on the surfaces of the foils are

progressively sheared and plastically deformed, dispersing oxides and contaminants to allow for an increasingly close contact of pure metals (de Vries 2004). The contact of pure metals then leads to the formation of bonds which are then plastically deformed by the differential motion and generate heat. The heat generated further promotes the diffusion, recrystallization, mechanical interlock, or possibly localized melting of materials at the foil-to-foil interface, resulting in true metallic bonds.

The UAM allows for joining of a wide variety of metallic foils. The most commonly used foils are made of aluminum (ex. Aluminum 3003, 6061, and 1100) because of their extensive applicability. Other materials such as copper, nickel, and titanium can also be joined depending on the application. In theory, all of the metallic materials that can be joined through UMW are compatible with UAM. A list of the material combinations is shown in **Figure 1.3**. By joining different materials, the UAM process allows for the production of metal matrix composites, functionally graded materials, fiber/sensor embedded metal structures, etc. (Fabrisonic 2016).

The UAM has several advantages when compared to other metal additive manufacturing processes such as selective laser sintering (SLS), direct energy deposition (DED), and electron beam melting (EBM). Most of the metal printing processes operate at a temperature close to or above the melting temperature of the metals, which negatively impacts the original mechanical properties obtained from heat treatment, leaves thermal residual stresses, and generates porous structures with limited ductility and low surface finish (J. Gibert 2009). In contrast, the overall temperature at which the UAM operates is claimed to be less than half of the melting point of the metals (White 2003). The joining process keeps

the mechanical properties of the stock materials and leaves little thermal residual stresses. The hybrid fabrication process of UAM allows for grinding steps to be added in between additive steps for better control over the surface finish. Additionally, UAM is capable of fabricating parts with large dimensions. The work space of UAM can be as large as 6 ft. in length, 6 ft. in width, and 3ft. in height (Fabrisonic 2016).

	Al	Be	Cu	Ge	Au	Fe	Mg	Mo	Ni	Pd	Pt	Si	Ag	Ta	Sn	Ti	W	Zr
Al Alloys	●	●	●	●	●	●	●	●	●	●	●	●	●	●	●	●	●	●
Be Alloys	●	●			●											●		
Cu Alloys	●		●		●	●	●	●	●	●	●		●	●		●	●	●
Ge				●							●							
Au	●	●						●	●	●	●	●	●			●	●	●
Fe Alloys					●			●	●	●	●		●	●		●	●	●
Mg Alloys						●							●			●		
Mo Alloys							●	●			●			●		●	●	●
Ni Alloys									●	●	●			●		●	●	
Pd										●				●				
Pt Alloys											●	●		●		●	●	
Si													●	●				
Ag Alloys													●	●				●
Ta Alloys														●		●	●	
Sn															●			
Ti Alloys																●	●	
W Alloys																	●	
Zr Alloys																		●

Figure 1.3 Material combinations for UAM (KE Johnson 2008)

Despite the advantages of being able to operate at relatively lower temperature (150 °C), to yield higher surface finish, and to produce larger dimension structures than other metal additive manufacturing techniques, UAM has not established itself as an attractive

manufacturing alternative because of a critical operational issue known as “height to width ratio problem” (Robinson, Zhang, and Ram 2006). Specifically, as the height of the built feature approaches its width, bonding failure occurs between the foil and the feature and additional layers cannot be bonded. The issue is observed to be independent of the length of the feature. In aluminum 3003, the bond failure is observed as the height to width ratio of the feature falls in the range of 0.7 to 1.2. As the aspect ratio of the feature exceeds the critical range, however, the bond can be re-initiated (J. M. Gibert, Austin, and Fadel 2010) (**Figure 1.4**).

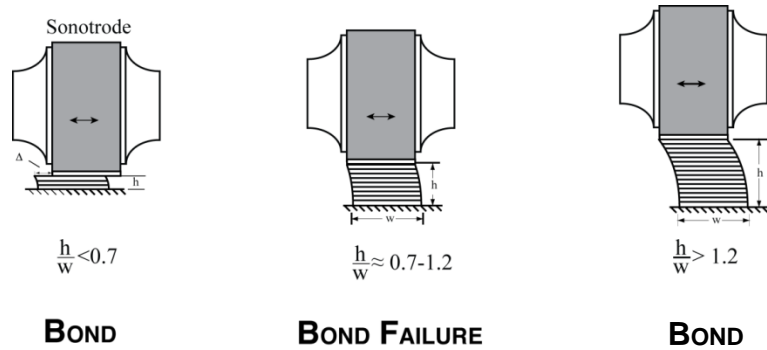


Figure 1.4 The height to width ratio problem of UAM (J. M. Gibert, Austin, and Fadel 2010).

The causes of bond failure at the critical aspect ratio has been studied by several researchers. Robinson et al. claim that the bond degradation is due to a decrease in the static lateral stiffness of the structure (Robinson, Zhang, and Ram 2006). They explain that, as the height of the feature increases, the static stiffness of the structure decreases, resulting in a deflection that decreases the magnitude of differential motion between the foil and the built feature. This differential motion is critical in removing the oxide layer and initiating

bonding. Later, Zhang et al. investigated the stresses and strains distribution within the built feature and identify the superposition of ultrasonic waves within the built feature as responsible for the decreasing differential motion (Cunbo Zhang, Zhu, and Li 2006).

Gibert et al. observe that as the height of the built feature exceeds a certain value, bonding can be re-initiated (J. M. Gibert, Austin, and Fadel 2010). Based on the observation, they state that if static stiffness alone is responsible for this bonding failure, then one would expect that bonding can never be re-initiated as long as the stiffness of the feature is reduced. By investigating the dynamic response and vibration modes of the built feature experimentally and analytically, they demonstrate that resonance of the built feature is excited as the height to width ratio falls in the range of 0.7-1.2 and that the resonance significantly reduces the differential motion between the foil and the substrate. The reduction of differential motion leads to either pure stick or aperiodic stick-slip motions, resulting in insufficient plastic deformation for removing surface oxides and initiating bonding (J. M. Gibert, Fadel, and Daqaq 2013). Further, Gibert et al. show that by increasing the kinetic friction coefficient at the bond interface or the compression load, the aperiodic stick-slip is reduced and the bond quality is improved. The bond degradation can also be avoided by adding a support structure next to the built feature. The natural frequency of the built feature is shifted and the resonance is avoided (Swank 2010).

Researchers such as Zhang et al. and Gibert et al. qualitatively show that the bond degradation is due to the decrease of differential motion which is caused by changes in the

dynamic state of the built feature. However they do not further quantify that decrease, explain the change of material behavior in response to the change of dynamics, nor relate the built feature dynamics to bond quality.

1.2 Motivation

This research goes beyond the macroscopic dynamics perspective and focuses on the understanding of the mechanisms of the bonding process under dynamic conditions. While the previous investigations have qualitatively explained the cause of the height to width ratio problem by showing the change in the dynamics of the system as new layers of foils are deposited, they do not explain how the change of dynamics affects bond formation. Consequently, a better understanding of the UAM process is needed to capture the material behavior as bonding occurs and predict the resulting bond quality, i.e. bond or debond, as the dynamics of the built feature changes. In order to establish the model, a comprehensive understanding of the bonding process and bonding mechanisms is required. The key factors that govern the bonding process need to be identified experimentally and characterized. A model is developed and then used to predict the material behavior and to assess bond quality. In summary, the UAM model serves as a key link that connects the macroscopic dynamics of the built feature and the material behavior which determines bond quality at the interface. This dissertation presents the development of such a model and its use to predict bond formation and quality.

1.3 Dissertation Outline

The dissertation is organized as follows.

Chapter 2 starts with reviewing the literature related to the bond process and bond mechanisms of UAM in order to identify the most critical factor that governs the bond formation. Section 2.2 explores the literature in search of all the influential elements. Once the critical factor and its influential elements are identified, the third section 2.3 presents a review of the modeling techniques that are available in the literature to model the critical factor(s) and account for all its influential elements. The fourth section 2.4 reviews the existing models of UAM to identify the gaps in the literature. The last section 2.5 summarizes the identified gaps and proposes the research questions with the associated hypotheses.

Chapter 3 presents an experimental investigation of acoustic softening. The chapter starts with a review of the existing experimental setups and then proposes a design of the setup. The test procedures are described. The observations of acoustic softening in four different materials are presented and discussed. Finally, a macroscopic model is proposed to characterize the acoustic softening in a plasticity framework.

Chapter 4 presents a plasticity model for UAM. The first section 4.1 discusses the hardening in case of a high strain rate deformation process of UAM, develops an analytical model for characterizing the effect, and incorporate the model into the plasticity framework. The second section 4.2 introduces the acoustic softening model developed in section 3.4 into the plasticity model. Section 4.3 discusses thermal softening of the specific materials used in this study and presents the model constants that are identified based on thermal

softening data in the literature. In section 4.4, the final plasticity model is presented with the associated model constants.

Chapter 5 presents the thermal and friction models developed for UAM. The chapter first describes the thermal model and the associated boundary conditions. The model constants are determined based on studies from the literature. Then the friction model is presented starting with a short review about the influential factors that should be accounted for in modeling the friction coefficient. Then the friction model is developed and taken into account the most influential factors.

Chapter 6 describes how the dynamic, thermal, plasticity, and friction models are combined for developing a thermo-mechanical, finite element UAM model. Specifically, the integration of the sub-models are shown in section 6.1. The integrated model is then implemented in a commercial finite element software as explained in section 6.2. Section 6.3 presents an asperity model that associates the prediction from the UAM model to the linear weld density of the bond. In section 6.4, the predictions from the UAM model are first validated by comparing to experimental results in the literature and then used to study the effects of dynamics on the stresses necessary for bonding. Furthermore, different energies dissipations are determined to understand the energy flow within the process. Last, The UAM model is run at different combinations of weld parameters and the resulting bond qualities (the linear weld densities) are evaluated for identifying an optimum process window.

Chapter 7 summarizes the work by addressing the list of research questions presented in chapter 2. Then, the contributions from this work are presented to show its impact

on the understanding of the fundamental principles of UAM as well as the application of UAM technique. Last, the future work is discussed to show how this research could be possibly expanded to have a broader impact.

Appendix B presents a lumped parameter model consisting of mass-spring networks for characterizing the dynamics of the built feature. The related work which is mostly found in the field of computer graphics are reviewed and the mechanics principles behind the lumped model are explained. The 2-D and 3-D lumped models are then presented. The performance of the model is then evaluated by comparing its prediction and computational cost to those of a finite element dynamic model. Finally, details are presented regarding how the lumped model can be interfaced with the finite element model of UAM for predicting the transient dynamics of the built feature.

Chapter 2

2 Literature Review

This chapter provides background literature necessary to start the research. Specifically, Section 2.1 presents the literature that studies the bonding process and bonding mechanisms of UAM. From the literature, the most critical factor that governs the bond formation is identified for characterization. In section 2.2, all the possible influential elements that could affect the critical factor are identified. Knowing the critical factor and its influential elements, Section 2.3 reviews the modeling techniques that are available in the literature for modeling the critical factor. Section 2.4 reviews the existing modeling work of UAM for identifying the gaps in the literature. Section 2.5 presents the results of studies related to bond quality evaluation. Based on the literature, a set of criteria can be extracted to deduce from the modeling prediction of bond quality. Section 2.6 summarizes the identified gaps and proposes the research questions with the associated hypotheses.

2.1 Bonding Principles of UAM

This section aims to identify the most critical factor that governs the bond formation by reviewing the literature related to UAM bonding principles. Due to the fact that UAM shares with UMW the same bonding mechanism, the literature cited comes from both processes. The sections starts with a general overview of the bond formation process without specifying the underlying mechanisms. Then the different bonding mechanisms are presented followed by a summary discussion.

2.1.1 Overview of the Bonding Process

There exist three stages in the UAM bonding process. It is a point on which researchers agree. It was originally proposed by Wodara and later generalized by de Vries (de Vries 2004; Wodara 1986). In the first stage, the surfaces to be welded are drawn together by normal compression from the sonotrode. At microscale, the asperity tips are brought into contact and plastically deformed by the combined effect of normal stresses generated from normal compression and interfacial shear stresses generated from interfacial vibration. Simultaneously cracks are generated in the brittle surface oxides due to the difference in hardness between the hard oxides and the pure metals. The metal becomes even softer and plastic regions are formed as the ultrasonic energy and the plastic and frictional heat are dissipated into the material, thus facilitating the breakup of surface oxides. In the second stage, the metal-to-metal contact area increases and the interfacial voids are closed by the plastic flow as the weld cycle proceeds. Meanwhile, the broken oxides are carried by the metallic flow and are dispersed to the edge of the weld zone. In the third

stage, a strong bond is formed across the interface where surface oxides are removed and close metallic contacts are maintained. The already formed bonds are maintained by the plastic deformation that accommodates the interfacial vibration. The three stages of bond process take place within very short time intervals and are therefore hard to separate. For the modeling purpose, an underlying assumption can be deduced from the generalized three stages: the plastic deformation promotes bonds formation by dispersing surface oxides and contaminants, increasing contact areas of pure metal, and maintaining the already formed bonds (Ram, Yang, et al. 2007; de Vries 2004).

2.1.2 Bond Mechanisms

The bonding mechanism of UAM has been studied for decades, yet no uniform conclusion has been achieved. Metallurgical adhesion is supported by many researchers as the bonding mechanism (Kong, Soar, and Dickens 2003; Lee 2013; Ram, Yang, et al. 2007; de Vries 2004). The theory states that layers of atoms move across the bond interface and form “adhesive” bonds due to van der Waals forces under intimate metal-metal contact (Czichos 1972). The intimate contact requires surface asperities and adjacent bulk material to undergo elasto-plastic deformation for removing surface oxides and generating metallic flows that fill the valleys between asperities (Kong, Soar, and Dickens 2003; Ram, Yang, et al. 2007). Diffusion across the weld interface is supported by some researchers based on the observed evidences of high strain rate plastic deformation. The high strain rate is believed to enhance diffusion significantly by increasing vacancy concentrations within materials (Cheng and Li 2007; Gunduz et al. 2005). Moreover, the high vacancy concentration

resulted from high strain rate is supposed to lower the melting temperature of the material significantly, thus allowing localized melting to occur (Gunduz et al. 2005). Recrystallization is also proposed as a cause of bonding (Kenik and Jahn 2003; D. E. Schick et al. 2010). The grains are observed to become finer in aluminum and copper after the UAM process, indicating the occurrence of recrystallization. It is believed that severe plastic deformation and temperature rise due to the continuous input of ultrasonic energy provide the necessary conditions for recrystallization. Mechanical interlocking is reported by a few researchers who studied the bonding of dissimilar materials as one material being soft and the other hard (K. Johnson et al. 2011; Joshi 1971; Ram, Yang, et al. 2007). Severe plastic deformation is observed in the soft material.

In summary, plastic deformation is identified as the key factor that governs the bonding process. Specifically, it plays a vital role in all stages of bond formation: 1) at the beginning of the bonding process, plastic deformation is observed in a thin layer of pure metal (~20 μm thick) beneath the surface oxides. The metallic flow helps break up brittle oxides and disperse broken fragments. 2) When oxides are removed and pure metals are in contact, the plastic deformation of asperities increases metal-to-metal contact areas and the metallic flow closes the voids, resulting in a more complete, intimate contact of foils and higher quality bonding. 3) When bonds are partially formed, a layer of metal (20-60 μm thick) underneath the bonded locations are believed to undergo plastic deformation to accommodate the differential motion and to protect the bonds from breaking up (de Vries 2004). Moreover, while the exact bond mechanism is still subjected to argument among researchers, plastic deformation is shown to enhance bonding regardless of the theories in

use: metallic adhesion, diffusion, recrystallization, mechanical interlock, and localized melting. As a result, it can be concluded that plastic deformation serves as a critical factor in promoting bond formation regardless of its causes.

2.2 Influential Elements for Plastic Deformation

The section aims to identify all the elements that influence the plastic deformation of materials at the bond interface. From the energy point of view, the sonotrode, top foil, built feature, and substrate form a system which is subjected to three external energy input: work due to ultrasonic vibration and compression, and thermal energy due to external heating. While the external heating has only one effect on plastic deformation: the thermal softening effect, vibration and compression could affect plastic deformation in multiple aspects. Specifically, the ultrasonic vibration on one hand directly delivers ultrasonic energy into the metals, on the other hand generates frictional forces together with compression. According to Kong, the ultrasonic energy has two types of effects on material plasticity: 1) a volumetric effect referred to as “acoustic softening” that occurs in the bulk materials and 2) a surface effect referred to as thermal softening caused by friction that occurs only close to the bonding interface (Kong, Soar, and Dickens 2003). Eaves et al. observe that the thermal energy reduces plastic stresses by 45% while the ultrasonic energy reduces it by 75% (Eaves et al. 1975). The frictional forces have two effects: 1) the high strain rate which causes hardening in the bulk materials, 2) the forced vibration of the built feature which causes stick-slip motion at the bond interface that affects the bonding. The deformation strain rate is believed to reach up to 10^3 s^{-1} due to the high frequency oscillation

of the sonotrode (Gunduz et al. 2005). It has been observed that the high strain rate (above $10^3 s^{-1} \sim 10^5 s^{-1}$) deformation leads to an abrupt increase in flow stresses for a variety of metals with face-center-cubic (f.c.c.) structures (Lesuer, Kay, and LeBlanc 2001). Gibert et al. showed that bonding is affected by the stick-slip interfacial motion which is governed by the dynamics of the built feature (J. M. Gibert, Fadel, and Daqaq 2013). When the built feature undergoes resonance, the interfacial motion becomes pure slip and the bond degrades. In summary, the plastic deformation is affected by the ultrasonic energy, high strain rate deformation, temperature, friction, and dynamics of the built feature which need to be accounted in the modeling work. The detailed review of each of these factors is shown as follows.

2.2.1 Effect of Ultrasonic Energy

It is widely believed that ultrasonic energy has a significant effect on metal plasticity. This effect, known as “acoustic softening”, is first documented by Blaha and Langenecker (Blaha and Langenecker 1955). It results in a significant reduction of static yield stress in tensile tests when applying longitudinal ultrasonic waves to various metals. The physics that governs acoustic softening is still not well understood and its effects are still not fully characterized. Since ultrasonic energy serves as the major energy input in the UAM process, the acoustic softening effect needs to be well understood.

2.2.1.1 Experimental observations of acoustic softening

In 1955, Blaha and Langenecker reported a significant decrease of stress in tensile test of zinc single crystal induced by an ultrasonic field (Langenecker 1963). Later, they also observed acoustic softening on aluminum single crystal, steel, iron, cadmium, beryllium, tungsten, and titanium (Langenecker 1966). The softening effect takes place as soon as the ultrasound passes through the material. The stress reductions are observed in both elastic and plastic regions and are “proportional” to the applied ultrasonic intensities (Langenecker 1963). When the intensity of ultrasound exceeds a certain critical value (typically depends on the material), a “zero stress” is reached in both the elastic and plastic regions of the stress strain curve. When the intensity of ultrasound remains below a certain critical value, no residual effects are observed on stress strain relations after the ultrasound stops (shown on curve a'b in **Figure 2.1**). When the intensity of ultrasound exceeds the critical value, however, residual hardening is observed and permanent changes in the microstructure of metals are observed (shown on curve b' and curve c' in **Figure 2.1**). Moreover, the softening effects are shown to be strongly similar to thermal effects (**Figure 2.2**). However, Blaha and Langenecker calculated that the required ultrasonic energy is 10^7 times less than the required thermal energy to reach a similar stress reduction on the stress strain curve (Langenecker 1966). Based on the observations, Langenecker concluded that the ultrasonic energy is preferably absorbed at dislocations, which are the regions responsible for plastic deformation of materials.

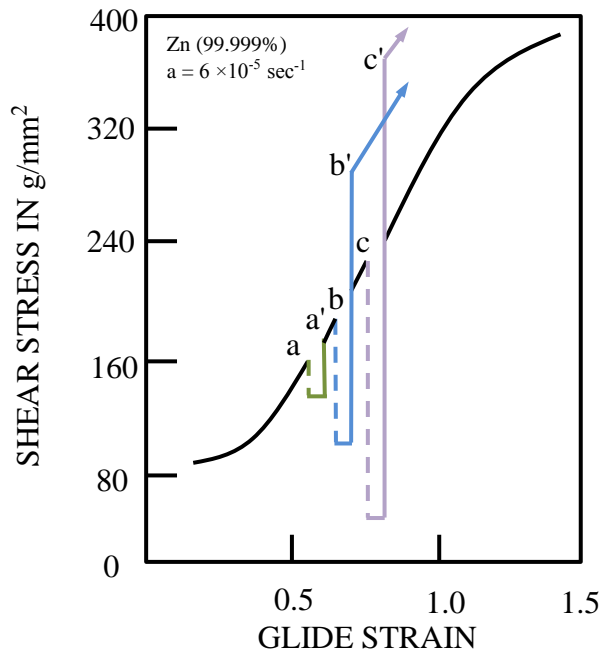


Figure 2.1 Acoustic softening and residual hardening reproduced from Langenecker (Langenecker 1966)

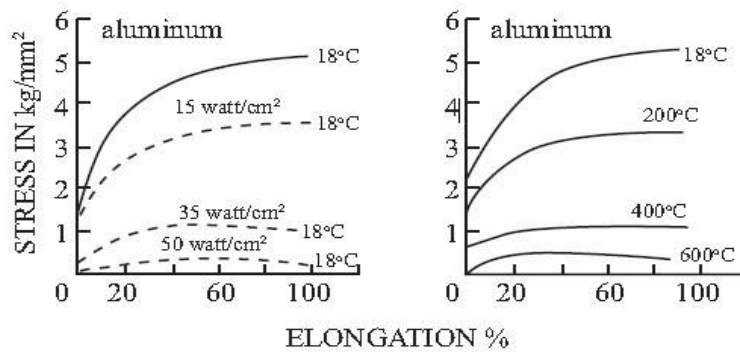


Figure 2.2 Softening effect induced by ultrasound (left) and the softening effect induced by heating (right); the “zero stress” is reached at ultrasonic intensity of 50 watt/cm² (left). (Langenecker 1966)

Though Langenecker’s observations are largely recognized and cited by many researchers, different observations also exist. Nevill and several other researchers conducted experiments similar to Langenecker’s and reported that rather than being a function of ultrasonic intensities, the stress reduction is a linear function of vibration amplitude (Biddell

and Sansome 1974; Nevill and Brotzen 1957; Pohlman and Lehfeldt 1966; Winsper and Sansome 1969). Some researchers reported that ultrasound does not change the Young's modulus of metals (Biddell and Sansome 1974; Pohlman and Lehfeldt 1966). Other researchers documented a “residual softening” effect as opposed to the “residual hardening” effect observed by Langenecker (D. R. Culp and Gencsoy 1973; Huang et al. 2009; Lum et al. 2009).

In recent studies, Siu (Siu, Ngan, and Jones 2011) investigated the deformation of microstructure of polycrystalline aluminum with and without ultrasonic irradiation using scanning electron microscope (SEM), ion-induced secondary electron (SE) imaging and electron backscattered diffraction (EBSD). They observed a significant increase of sub-grain formations in the microstructure after ultrasonic irradiation and further predicted the reduction of dislocation density (**Figure 2.3**). Different from Siu's observation, Dutta investigated the microstructure of DC 04 steel after ultrasonic irradiation utilizing SEM, EBSD and X-ray diffraction (XRD) and observed a reduction in sub-grain formation (Dutta et al. 2013). They further point out that the contradiction between their observations with those of Siu's could be due to the difference in the microstructures of the materials.

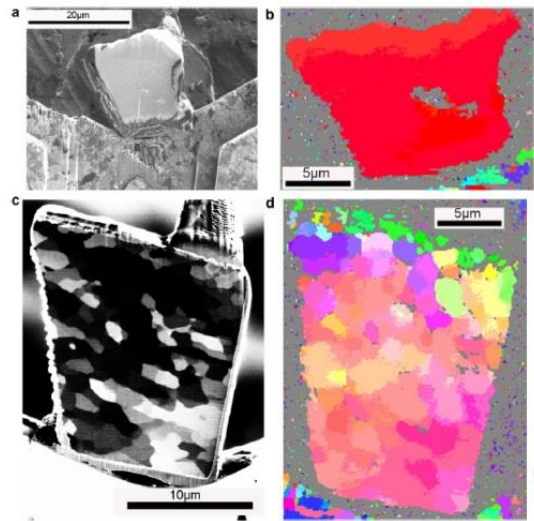


Figure 2.3 Ion-induced SE image (a) and EBSD orientation map (b) of a cross-sectional foil cut from an indent made by 0.05 kg load without vibrating the sample. Ion-induced SE image (c) and EBSD orientation map (d) of a foil cut from an indent by 0.05 kg load made with 2 Hz vibration. Many tiny subgrains with clear boundaries and sharp contrast can be seen (Siu, Ngan, and Jones 2011)

From the reviewed literature, it is clear that ultrasonic energy has a significant influence on material plasticity (Blaha and Langenecker 1955; Langenecker 1963, 1966). Yet the specific behavior of materials under ultrasound is still elusive due to the many contradicting observations of experiments conducted with various materials from different researchers. As a result, it is not possible to characterize the effects of acoustic softening based on the existing literature to define an appropriate model. Experimentations are necessary to characterize acoustic softening before starting modeling.

2.2.1.2 Models of acoustic softening

The existing acoustic softening models are reviewed in order to introduce acoustic softening in the modeling of UAM bonding. Notice that all these analytical models rely largely on the researchers' experimental observations and assumptions about the physical mechanisms governing acoustic softening. Different assumptions may result in distinctive

analytical models. As a result, these assumptions are summarized before reviewing the analytical models.

1) **Stress superposition** assumes that the observed stress reduction on a stress strain curve is due to a simple superposition of quasi-static tensile stresses and alternating acoustic stresses induced by ultrasound (Nevill and Brotzen 1957). It is assumed that the stress superposition does not change the microscopic structure of materials.

2) **Dislocation activation** assumes that in metals the ultrasonic energy is preferably absorbed at dislocations whose motions and interactions with obstacles are responsible for plastic deformations (Blaha and Langenecker 1955). The absorbed energy increases the potential energy of dislocation lines by means of internal friction, allowing dislocations to move and overcome obstacles at much lower stresses than those required at room temperature.

3) **Dislocation annihilation (in polycrystalline aluminum)** assumes that the superposition of ultrasound-induced stresses and quasi-static tensile stresses facilitates dipole annihilation of screw dislocations in polycrystalline material (Siu, Ngan, and Jones 2011). The annihilation leads to a reduction of the dislocations density, which is responsible for intrinsic flow resistance, i.e., the stress necessary to deform polycrystalline materials. The superimposed oscillatory stress periodically slows down the motion of dislocations which allows them to have greater chances to cross slip and annihilate, leading to a reduction in dislocations.

4) **Contraction of extended dislocations**, based on Gilman's theory, assumes that the extended dislocations moving at high speed tend to contract into unit dislocations and

cross-glide without the aid of thermal activation (Gilman et al. 2015; Amir Siddiq and El Sayed 2011). The ultrasonic energy causes the speed of dislocations to increase such that the extended dislocations become movable without aid of thermal activation energy.

Based on abovementioned explanations of mechanisms, various models are reviewed and evaluated highlighting their benefits and limitations. These models are proposed based on one or multiple assumptions.

Winsper and Sansome assumed the mechanism of acoustic softening to be the stress superposition, i.e., the stress reduction on stress strain curve equals the acoustic stress induced by ultrasound (Winsper and Sansome 1971). This acoustic stress can be written as:

$$\sigma = \frac{\omega X E}{c} \quad (2.1)$$

σ is stress reduction, ω the radius frequency, X the vibration amplitude, E the Young's modulus, and c the wave speed defined in terms of the Young's modulus and the density by $c = \sqrt{\frac{E}{\rho}}$. This equation was obtained by Timoshenko for modeling the stress wave in a vibrating rod (Timoshenko 1970). In contrast, Kirchner et al. studied the actual internal stresses inside a sample subjecting to ultrasonic irradiation and found them to be extremely difficult to quantify since they are not homogeneously distributed (Kirchner et al. 1985). Additionally, the stress superposition theory indicates that the stress reduction should be direction dependent. The reduction reaches its maximum when the directions of ultrasound and tensile stresses are parallel, and reach its minimum when these directions are perpendicular. However, no such dependency is observed in the literature (Krausz and Krausz

1996; Yao, Kim, Wang, et al. 2012). In summary, the prediction from stress superposition theory is not sufficient to account for the observed stress reduction.

Rusinko proposed an analytical model to characterize the effects of ultrasound based on Rusynko's synthetic theory of irreversible deformation (Rusinko 2011; Rusynko 2001). The synthetic theory, based on Langenecker's observations, utilizes the same set of constitutive equations to characterize both acoustic softening and residual hardening (Langenecker 1966). Rusinko assumes that the combined effects of static loading and ultrasonic oscillation decrease the dislocation density by activating the blocked dislocations whereas the ultrasonic oscillation alone increases the dislocation density by generating more dislocations which become entangled with each other. However, the model prediction lacks support of experiments. Additionally, the synthetic theory which the model relies on applies to only small strains of plastic hardening materials, thus limiting the application of the model.

Yao et al. modeled acoustic softening based on the Kocks' thermal activation model which assumes that the flow stress at constant strain rate is significantly affected by temperature (Kocks 1987; Yao, Kim, Wang, et al. 2012). The original thermal activation model is in described by the Arrhenius equation (Frost and Ashby 1982)

$$\dot{\gamma}_p = \dot{\gamma}_0 \exp\left(\frac{\Delta G}{kT}\right) \quad (2.2)$$

where (Frost and Ashby 1982; Kocks 1987)

$$\Delta G = \Delta F \left[1 - \left(\frac{\tau}{\tau_0}\right)^p\right]^q \quad (2.3)$$

where $\dot{\gamma}_p$ is the shear plastic strain rate; $\dot{\gamma}_0$ the pre-exponential factor; k the Boltzman constant; T the Kelvin temperature; ΔG the Gibbs free-energy of activation for dislocation to

overcome an obstacle; ΔF the activation energy; $\hat{\tau}$ the “mechanical threshold”: the yield strength at absolute zero temperature; p and q are obstacle distribution parameters set as $p = q = 1$ based on work by Frost and Ashby (Frost and Ashby 1982).

The stress reduction is characterized in terms of the ultrasonic energy and the mechanical threshold is defined using a power law. Notice that although the authors claim that the acoustic softening model is derived from the theory of thermal activation of dislocations proposed by Langenecker (Blaha and Langenecker 1955), the model is essentially phenomenological based on experimental observations:

$$\Delta\lambda = \beta \left(\frac{E}{\hat{\tau}}\right)^m \quad (2.4)$$

where $\Delta\lambda$ is the static stress reduction; E is the applied ultrasonic energy intensity; β and m are constants determined by curve fitting. The characterization of acoustic softening using the power law is simple and effective. However, the assumed mechanism of thermal activation is debatable. Additionally, the sound wave frequency in the study is 9.6 kHz, which is far below the ultrasound threshold (20 kHz).

2.2.2 Effect of High Strain Rate Deformation

Due to the high frequency oscillation of the sonotrode, the material close to the sonotrode undergoes plastic deformation at a high strain rate. The evidences of the high strain rate deformation in the UAM bonding process have been shown by Gunduz et al. who calculated the diffusivity and the effective vacancy concentration within metals and found the strain rate to be up to 10^3 /s (Gunduz et al. 2005). Several other researchers

reported the maximum plastic shear strain in UAM to be $10^4 - 10^5/s$ (Sriraman et al. 2011; Sriraman, Babu, and Short 2010; Yang, Janaki Ram, and Stucker 2009). The high strain rate is claimed to cause adiabatic heating and a significant increases in local temperature (Sriraman et al. 2011). This increase leads to the thermal softening of the material and therefore the decrease of flow stress.

In addition to thermal softening, the high strain rate is also observed to cause a dramatic increase of dependence of dynamic flow stress on the instantaneous strain rate as the strain rate exceeds certain threshold (typically around $10^3 /s$) (Lesuer, Kay, and LeBlanc 2001; Sakino 2006). Luseur et al. showed that this abrupt change of strain rate sensitivity of the flow stress is due to the change of deformation mechanism (Lesuer, Kay, and LeBlanc 2001). At low strain rate, the deformation is governed by the cutting or bypassing of obstacles by the dislocations. As the strain rate exceeds the threshold, the deformation starts to be controlled by phonon drag forces and the flow stress necessary to deform the material increases abruptly (**Figure 2.4**).

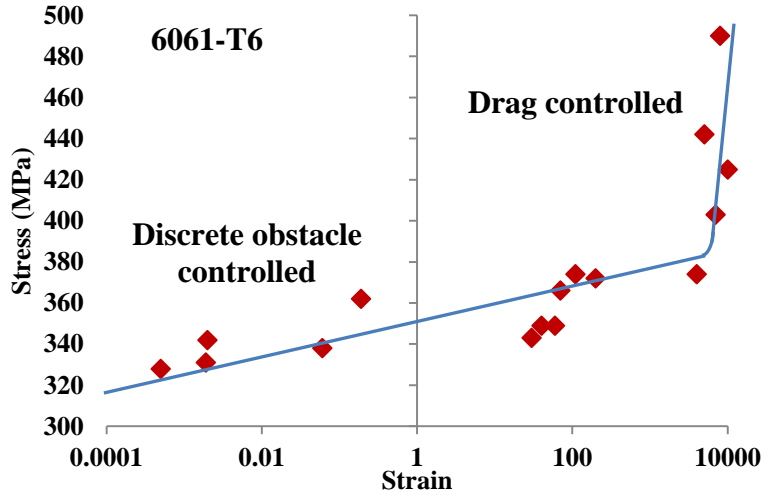


Figure 2.4 The strain rate sensitivity diagram of aluminum 6061-T6 reproduced from (Lesuer, Kay, and LeBlanc 2001)

Based on their observations, Lesuer et al. proposed a model which, based on the change of the mechanism, characterizes the strain rate dependencies with different equations. At low strain rate (below 10^3 /s), a relation in form of Arrhenius equation is introduced based on the work of Frost and Ashby (Frost and Ashby 1982):

$$\dot{\epsilon}_1 = \dot{\epsilon}_0 \exp\left[\frac{Q}{kT} \left(1 - \frac{\sigma}{\tau}\right)\right] \quad (2.5)$$

Where $\dot{\epsilon}_1$ represents the strain rate at which cutting and bypassing of obstacles by the dislocation is dominant, $\dot{\epsilon}_0$ is a reference strain rate which is determined by the attempt frequency (the number of attempts made to thermally activate the dislocation) and the strain achieved with each successful attempt. The value of $\dot{\epsilon}_0$ varies between 10^5 s^{-1} and 10^{10} s^{-1} . Q is the activation energy, k is Boltzmann's constant, σ is the flow stress, τ is the strength of obstacles at 0 K, and T is temperature in Kelvin. At high strain rate (beyond 10^4 /s), the relation is a power law equation:

$$\dot{\varepsilon}_2 = C_1 \sigma^{C_2} \quad (2.6)$$

where $\dot{\varepsilon}_2$ represents the strain rate at which the phonon drag force on dislocation is dominant, C_1 and C_2 are constants whose values are obtained through curve fitting. At the intermediate strain rate (between $10^3 /s$ and $10^4 /s$), the strain rate sensitivity is controlled by both low and high strain rates:

$$\dot{\varepsilon}_{eff} = \frac{\dot{\varepsilon}_1 \dot{\varepsilon}_2}{\dot{\varepsilon}_1 + \dot{\varepsilon}_2} \quad (2.7)$$

Similar models can also be found in the works by Manes et al and Sakino (Manes et al. 2011; Sakino 2006).

2.2.3 Effects of Temperature

The temperature affects the plastic deformation by means of thermal softening, i.e. the reduction of the flow stress of the materials when heated. Thermal softening has been thoroughly studied as one of the most common material behaviors and therefore will not be reviewed. The temperature changes in UAM, instead, is reviewed in order to understand its influences on plastic deformation.

The temperature during the UAM process has been measured by embedding thermocouples (Cheng and Li 2007; D. Schick et al. 2011; Sriraman et al. 2011). Sriraman et al. observed that the measured peak temperatures close to the bond interface increase with the increase in shear strength of the material and the ultrasonic vibration amplitude, which indicates that the rise in interfacial temperature is directly related to the heat dissipation due to plastic deformation. Moreover, since the plastic strain rate is so high and the de-

forming process is very rapid, there is no sufficient time to conduct heat away. Consequently, the heating process is considered “adiabatic”. The authors further point out that the temperature increase could be used as an indicator of bond quality: the higher the temperature, the more sufficient the plastic deformation and the higher the bond quality. Cheng and Li found in ultrasonic spot welding that heating is due to both friction and plastic deformation. The heat flux due to friction is high but unstable whereas the heat flux due to plastic deformation is low but stable (Cheng and Li 2007). Schick et al. showed that 30% of the ultrasonic energy that propagates across all layers is converted into heat which increases temperature at all interfacial layers. The top layer absorbed 10% of the ultrasound-induced heat whereas 90% are absorbed by the built feature (D. Schick et al. 2011). In addition, they found that the actual thermal diffusivity is much lower than the theoretical value of the bulk materials, suggesting that the voids and defects at the bond interfaces significantly increase the thermal contact resistance across the layers

Based on this thermal study, it is concluded that interfacial friction and plastic deformation are the two major heat sources responsible for temperature increase in the thermal process of UAM. The generated heat is mostly conducted through the built feature and the convection can be neglected. The thermal conductivity is anisotropic within the built feature due to the voids and oxides at the bonded interfaces. It also affects the temperature distribution.

2.2.4 Effects of Friction

Friction affects bonding in three aspects: 1) breaking and removing surface oxides, 2) driving elasto-plastic deformation of surface asperities to form close contact, and 3) dissipating heat from friction work and softening materials close to bond interface. This study focuses on the material behaviors after the removal of surface oxides.

Based on the role of friction in UAM bonding process, a number of influential factors are identified: material combination, initial surface roughness, normal load, slip rate, and temperature. The bonding of the same materials is governed by the metallurgical adhesion process. The initial surface roughness is found to have a strong influence on the static friction coefficient but not on the kinetic friction coefficient (Espinosa, Patanella, and Fischer 2000). The kinetic friction coefficient is controlled by the plastic deformation of asperities and the associated contact area (Moore 2013; Pei et al. 2005). The increase of normal load is shown to reduce the friction coefficient due to the nonlinear increases of contact area (Kragelski 1965). The slip rate shows no direct influence on the friction coefficient according to the experimental studies by Zhang et al. (Cunbo Zhang, Zhu, and Li 2006). However, the normal load and slip rate contribute to dissipation which affects the local temperature. The temperature is shown to have the most significant influence on the friction coefficient (Kragelski 1965). As the temperature increases, the friction coefficient first increases due to the increasing viscous plastic stress and then decreases due to the thermal softening of the deformed asperities.

In conclusion, the most influential factors for the friction coefficient are the normal load and the temperature. The two factors are considered when developing the friction model.

2.2.5 Effects of Dynamics

The dynamics of the UAM system has a profound influence on the plastic deformation at bond interface by affecting the differential motion between the top foil and the built feature. As additional layers are deposited, the dynamic response of the built feature changes and the differential motion changes accordingly. The change in the differential motion induces the so called “stick-slip friction” at the top foil-built feature interface. Specifically, when the differential motion is large enough, due to the slip between the top foil and built feature, kinematic friction is dominant; when the differential motion is small enough, the top foil and the built feature stick to each other and static friction is dominant. In between large and small differential motions, stick and slip alternate resulting in a complex variation of the friction coefficient at the interface. This variation of friction coefficient further affects the plastic deformation at the interface.

Robinson et al. studied a bond degradation as the height of the built feature approaches its width, i.e. the height-to-width ratio approaches unity (Robinson, Zhang, and Ram 2006). Zhang and Li associated the bond failure to the change in dynamic response resulting from the superposition of the traveling ultrasonic waves as additional layers are added (Cunbo Zhang and Li 2006). Gibert et al. found that the loss of bonding can be reinitiated beyond the critical aspect ratio of one (J. M. Gibert, Austin, and Fadel 2010).

By measuring the dynamic response of the built feature using a laser vibrometer, they also found that the built feature is excited to resonate at the critical aspect ratio, which leads to stick-slip or pure stick between the top foil and the built feature (**Figure 2.5**). They further show that stick-slip is aperiodic due to the complex dynamic interaction (J. M. Gibert, Fadel, and Daqaq 2013). As the aspect ratio is far from the critical value, however, the response becomes steady and periodic. The undesired stick-slip or pure stick can be reduced by increasing either the normal load or the kinematic friction coefficient. Pal and Stucker also account for the stick-slip effect in studying the inhomogeneous deformation at the bond interface (Pal and Stucker 2012). It is shown that a severe plastic deformation takes place within a depth of 20 μm from the interface and is profoundly affected by stick-slip at the bond interface.

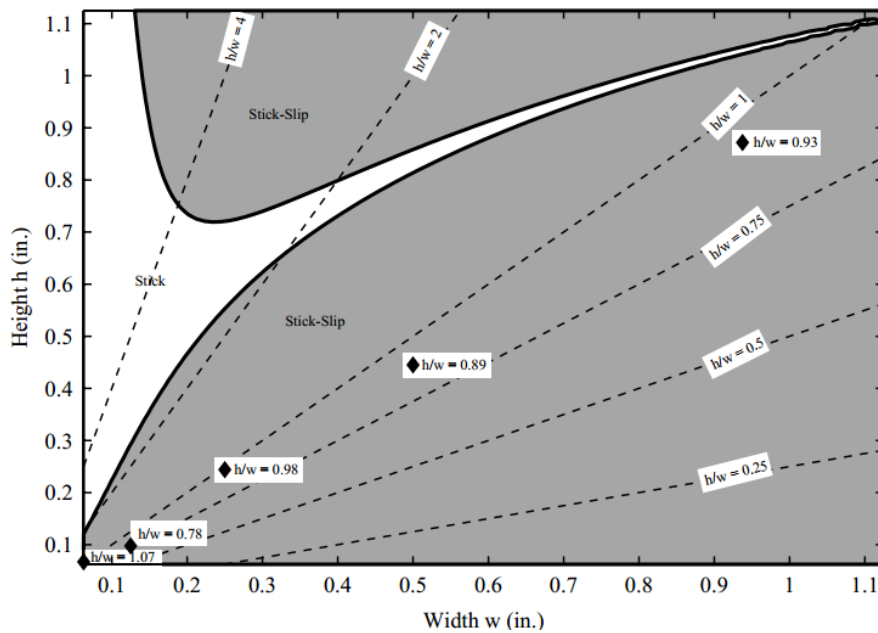


Figure 2.5 Stick/slip at different height-to-width ratios (J. M. Gibert, Austin, and Fadel 2010)

2.2.6 Summary

In summary, the bonding process is affected by acoustic softening due to ultrasound, thermal softening due to temperature increases, strain rate hardening due to high strain rate deformation, friction, and stick-slip due to the dynamics of the built feature. All of these factors require investigations and characterizations. The modeling approaches for characterizing these factors are discussed in the next section.

2.3 Modeling Methods for UAM

In this section, the general methodology used for modeling the UAM bonding process is detailed. Plastic deformation has been identified as the major modeling objective as explained above. The major difficulties involved in the modeling of plastic deformation are: 1) plastic deformation is closely coupled with a number of factors such as temperature and friction, which makes direct modeling difficult, and 2) the values of model parameters are difficult to identify in a coupled model. By reviewing the literature, a viable path is identified to overcome these difficulties.

2.3.1 Inverse Modeling

Some of the earliest analytical models of ultrasonic bonding are proposed by Mayer and Schwize (Mayer and Schwize 2003), who characterize the bond growth in the ultrasonic ball bonding process using a modeling method known as “inverse modeling”. They

use the measurements of observable parameters to calculate the values of the model parameters of interest. Notice that in the inverse modeling process, the number of observable parameters does not necessarily equal the number of model parameters. There are three possible cases: 1) if the number of observable parameters is greater than the number of model parameters, then the problem is over constrained and there could be no solution. 2) If the number of observable parameters is less than the number of model parameters, then there is more than one set of values for the model parameters and optimization needs to be introduced to determine the optimal set of values. 3) If the number of observable parameters equals the number of model parameters, the model could yield a unique set of solution. The inverse modeling is used by many researchers (G Kelly 2012; GS Kelly and Advani 2013; A. Siddiq and Ghassemieh 2008a; Amir Siddiq and El Sayed 2011; Amir Siddiq and Sayed 2012; Amir Siddiq and Schmauder 2006) to establish analytical models and study certain specific parameters.

2.3.2 Decomposition and Integration of Models

Siddiq and Ghassamieh proposed a finite element thermo-mechanical model to characterize the UAM process (A. Siddiq and Ghassemieh 2008a). The process involves multiple factors: plasticity, heat transfer, and friction. Each of the factors is coupled with the others. In order to model the bonding process, they first start a decomposition based on the factors and established several analytical sub-models: plasticity model, thermal model, and friction model. The analytical models are then integrated into a unified model and solved using finite element method. By using explicit integration schemes, all the sub-

models are solved simultaneously and the couplings are accounted for at each time increment. Inverse modeling method is used to identify the values of model parameters in the integrated model. This work provides an approach to comprehensive modeling of ultrasonic welding process. Later the method is applied in multiple works (G Kelly 2012; A. Siddiq and Ghassemieh 2008a; Amir Siddiq and El Sayed 2012; Amir Siddiq and Schmauder 2006).

To summarize, the general modeling methodology for the UAM is to decompose the problem into sub-problems, model each sub-problem separately, and considering the coupling effects integrate the sub-models into a unified comprehensive model. The inverse modeling method is used to identify the value of the model parameters for each sub-model.

2.4 Existing UAM Models

A limited number of models are found related to the UAM bonding process in literature (J. Gibert 2009; G Kelly 2012; A. Siddiq and Ghassemieh 2008a; Amir Siddiq and Schmauder 2006; de Vries 2004; C Zhang and Li 2008). Each of the model considers some of the influential elements discussed in section 2.2 but none of the models accounts for all the factors. In order to clarify this point, these models are compared and evaluated in terms of each of the sub-models. Gaps are identified through comparisons. The sub-models presented below are: plasticity model, thermal model, friction model, and dynamic model.

2.4.1 Plasticity Model

The material plasticity in UAM has been studied by many researchers. Siddiq and Ghassemieh utilized the cyclic plasticity model of Lemaitre and Chaboche to model plastic deformation of aluminum 6061 (Brogiato, Campana, and Cortese 2008; A. Siddiq and Ghassemieh 2008b). By modifying its isotropic and kinematic hardening rules, the cyclic plasticity framework is able to account for “acoustic softening”: a unique effect of ultrasound under which the flow stress on a stress-strain curve of metals is reduced considerably (Blaha and Langenecker 1955). However, the proposed model relies on the experimental data of a different material and under a different test condition. For instance, the cyclic data are collected from aluminum 6060 loaded at a strain rate of 10^{-3} s^{-1} which is much lower than the strain rate in UAM (10^4 s^{-1} - 10^5 s^{-1}) (Hopperstad, Langseth, and Remseth 1995). The acoustic softening data are collected from aluminum single crystals rather than aluminum 6061 (Langenecker 1966). Kelly et al. proposed a power law function to capture the plastic deformation (GS Kelly and Advani 2013). The acoustic softening effect is characterized as a constant factor added to the power law function. Due to the lack of acoustic softening data, the factor is calibrated such that the prediction of the foil deformation from the plasticity model matches the experimental measurements. Siddiq and El Sayed modified the crystal plasticity model of Hill and Rice (Hill and Rice 1972) in order to account for the acoustic and thermal softening of aluminum single crystal (Amir Siddiq and Schmauder 2006). The model is then extended to polycrystalline aluminum based on EBSD studies of aluminum 6061-O (Zhu et al. 2009). The model provides insights to the mechanism of acoustic softening but is very complicated. A large set of model parameters needs to be identified based on a small set of experimental data. Pal and Stucker established a

dislocation-based constitutive model within the finite element crystal plasticity framework and studied the inhomogeneous plastic deformation at the bond interface (Pal and Stucker 2012). The model sheds light to the deformation mechanisms under UAM condition but requires further experimental validation.

In summary, the existing plasticity models of UAM suffer from the following two issues. First, the acoustic softening effect lacks experimental studies to support the modeling. The models are built on either qualitative experimental observations or experimental data of a different material. Second, the plasticity models are either too simple to fully account for all the influential factors in UAM or too complicated and thus require a large set of experimental data to realistically reflect the material behavior. In order to address these issues, experimental studies and characterizations are necessary for the materials specific to the UAM. The plasticity model should account for all the influential factors and be sufficiently calibrated by experimental data of the material considered.

2.4.2 Thermal Model

The thermal model characterizes the heat transfer between the sonotrode, top foil, built feature, and ambient environment. De Vries proposed that in UAM process heat is generated from two sources: the interfacial friction and plastic deformation (de Vries 2004). A 2-D finite element thermal model is established accordingly. The model considers only heat conduction and neglect convection. The thermal model is not coupled with the mechanical model. Zhang and Li established a 3-D finite element thermo-mechanical model assuming that the frictional heat is the only heat source due to limitations of the software (C Zhang and Li 2008). They also neglected the lamination-induced anisotropy

of the thermal conductivity of the built feature. Koellhoffer et al. established a 2-D lumped parameter thermal model for UAM assuming that the temperatures are spatially invariant within foils due to the high conductivity of the bulk material (Koellhoffer et al. 2011). Kelly et al. established a 2-D thermo-mechanical model that accounts for heat generation from both friction and plastic deformation (G. S. Kelly, Advani, and Gillespie 2012). The thermal properties of the laminated built feature are approximated using those of the bulk material.

2.4.3 Friction Model

The friction model characterizes the interaction between the top foil and the built feature. The existing models are either oversimplified or has redundant dependencies on different variables. A constant friction coefficient has been extensively used for simplicity and a value of 0.4 is taken in most of the studies (J. M. Gibert, Austin, and Fadel 2010; de Vries 2004; Chunbo Zhang, Zhu, and Li 2006). Zhang and Li modeled the friction coefficient as a function of temperature based on experimental studies of sliding of aluminum sheets (Chunbo Zhang and Li 2007). Siddiq and Ghassemieh further studied the dependency of the friction coefficient on the contact pressure and the number of weld cycles in addition to temperature (A. Siddiq and Ghassemieh 2008a). However, the dependency of friction on the weld cycles and the temperature may be coupled. Kelly et al. modeled the friction coefficient as a function of amplitude, compression, frictional heat, and vibration

frequency (G. S. Kelly, Advani, and Gillespie 2012). Again, the dependencies on the amplitude, frequency, and frictional heat may be coupled, thus making it difficult to derive an explicit form of the relation.

2.4.4 Dynamic Model

The studies of UAM dynamics is motivated by solving the height-to-width problem which is first documented by Robinson et al. Zhang and Li developed a 2-D finite element model to study the behavior of contact frictional stresses and interfacial displacement as the height to width ratio of the build feature increases from 0.25 to 2.0 (Cunbo Zhang, Zhu, and Li 2006). The model introduces a sonotrode, a foil being welded to the built feature and a substrate made of deposited foils. The substrate is assumed to remain elastic and the friction coefficient at the mating interface is assumed constant. By running transient dynamics analysis on the 2-D model, they observed a decrease in contact frictional stress and interfacial displacement at the mating interface as the height-to-width ratio of the substrate approaches a critical value. They associated the observations to complicated interference or superposition of traveling vibrational waves in the substrate. However, the illustration of wave superposition is vague. There is no quantitative study that shows how the bond process is affected by the change of dynamics of the UAM.

Later, Zhang et al. introduced material plasticity and the stick/slip friction conditions to the finite element model (C Zhang and Li 2008). To validate the prediction of the finite element model, they built a 2-D analytical model of the substrate to compare the predictions of strains. However, both models are macroscopic dynamic models in which

the bonding process is not accounted. Some of the crucial factors such as the acoustic softening are not considered. Other factors such as plasticity and friction are implemented but are not explained in terms of how they affect the macroscopic dynamics of the UAM.

Gibert et al. proposed that resonance of the built feature at the critical height to width ratio is responsible for the bond failure (J. Gibert 2009). By using the Rayleigh-Ritz method, they showed that an increase in height to width ratio causes several natural frequencies of the substrate to approach the 20 kHz excitation frequency of the sonotrode. They also developed a 3-D finite element model and a 2-D lumped parameter model to show a substantial decrease of differential motions due to resonance as the height to width ratio approaches critical values. In these models, the change in differential motion leads to pure slip, stick-slip and pure stick motions which further leads to changes in friction. However, the dynamic model does not consider material plasticity, heat transfer, or variation of friction coefficient.

It is apparent that there exists a gap between the study of the dynamics and the thermo-mechanical bonding process. Research in UAM dynamics concentrates on the dynamics of the built feature without considering the thermal mechanical aspects of the bonding process. Research on the bonding process concentrates on material plasticity, heat transfer, and friction without considering the change in dynamics as the height of the substrate increases. For a comprehensive UAM model, both dynamics and bonding process have to be considered simultaneously.

In summary, the UAM bonding process is a complicated welding process that involves elastic and plastic deformation of the materials, contact and friction at bond interface, heat transfer, and dynamic interaction between different components of the welding system. All the influential factors should be considered and properly modeled. Some of the unique effects of ultrasound, such as acoustic softening and extremely high strain rate require further understanding and characterization.

2.5 Bond Quality Evaluation

This section reviews the studies related to bond quality evaluation in UAM. Based on the literature, a set of criteria can be extracted to connect the modeling prediction to bond quality.

2.5.1 Lap-shear Test

Lap-shear tests are first performed by Kong et al. in order to test the shear strength of the bonds (Kong, Soar, and Dickens 2004). The specimens are prepared by welding two overlapped foils. The overlapped distance is controlled to be approximately 10 mm. The specimens are then installed in a tensile test machine for lap-shear tests. The test procedure follows the standard BS EN 1465:1995 where possible.

The lap-shear tests, however, proves to be unsuccessful because the thickness of the foil is too small (Kong, Soar, and Dickens 2004). All specimens under testing broke within the base metal adjacent to the weld, including specimens within which visibly poor

welds were produced. The foils are too thin to provide the moment necessary to initiate shear at the bond region. As a result, the specimens break in tensile rather than shearing mode (**Figure 2.6**).

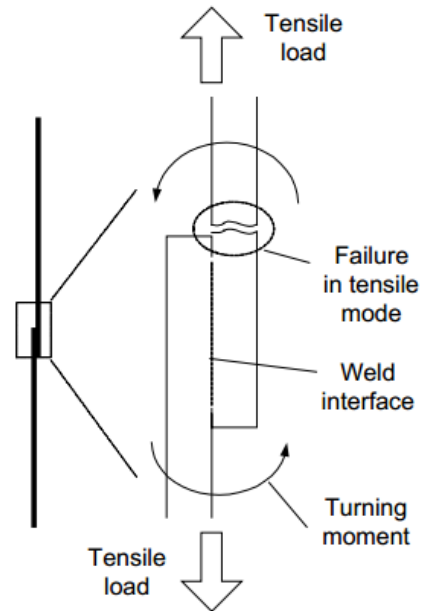


Figure 2.6 The failure mode of foils in lap-shear tests (Kong, Soar, and Dickens 2004)

2.5.2 Peel Test

Kong applied a peel test, which is normally associated with adhesive bonding and is based on the maximum load a specimen can withstand, to evaluate the bond quality of aluminum 6061 in the UAM process (Kong, Soar, and Dickens 2003). The peel test specimens are prepared by first welding a layer of foils to a supporting plate and then welding a second layer to the first, as is shown in steps 1 and 2 in **Figure 2.7**. The supporting plate is used to prevent specimen from bending during the peel test. The specimen is installed on

a peeling apparatus and the peeling apparatus is attached to a tensile test machine (step3, **Figure 2.7**). By recording the tensile load applied during the peel test, the bond quality is evaluated in terms of the required tensile load and the observed failure modes: “clear break”, “teeth formation” and “peel off”. Specifically, the “clear break” indicates a good bond with little or no tearing and a high resistance to peeling (>70 N). The “teeth formation” represents a less favorable bond with tearing propagating from the contact points and a relatively low peeling loads (45 – 70 N). The “peel-off” indicates that the second layer of foils peels completely away from the first layer with no tearing observed and a low resistance to peeling (<45 N). By applying peel tests to specimens made under various combinations of the operating parameters (amplitude, compression load, and weld speed), it was observed that the peel load increases as compression load increases and weld speed decreases.

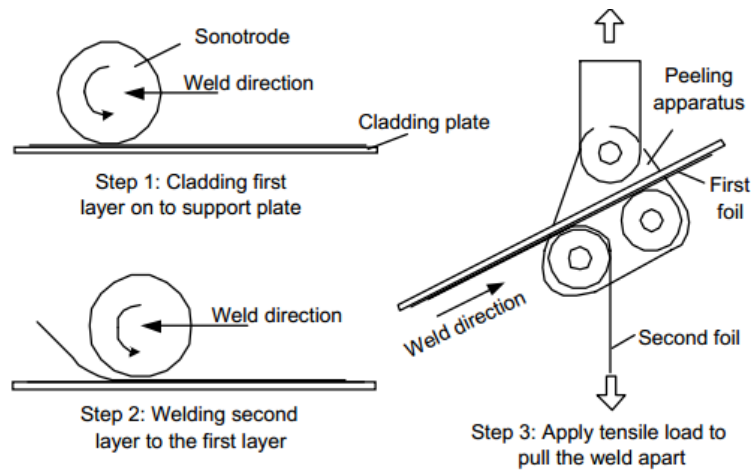


Figure 2.7 Peel test specimen preparation and peeling test apparatus (Kong, Soar, and Dickens 2004)

2.5.3 Three-point Bending Test

In addition to lap-shear and peel tests, other testing methods are introduced to evaluate the strength of UAM-built specimens. Leagon utilized three-point bending to measure the inter-laminar shear strength along the build feature (Leagon 2007) (). It was found that the interlaminar shear strength is around 55% of the ultimate shear strength of the wrought material. The tensile strength of laterally-oriented specimens is around 78% of the ultimate tensile strength of the wrought material.

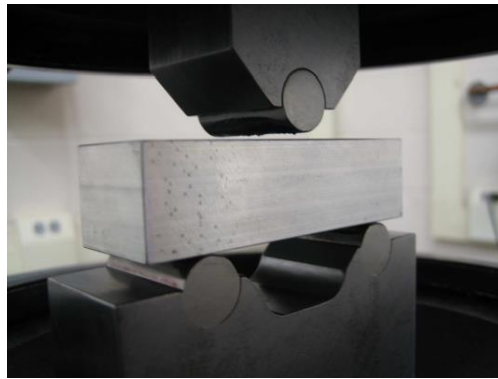


Figure 2.8 Test configuration for the three-point bending test (Leagon 2007)

2.5.4 Push-Pin and Finite Element Method

Zhang and Li proposed a push-pin experiment coupled with a finite element (PPFE) method to evaluate the bond strength (C. (Sam) Zhang, Deceuster, and Li 2009). To prepare the specimen, a built block feature is made using ultrasonic consolidation. A hole is machined from the bottom of the baseplate while the depth of the hole depends on the depth of interface of which the bond strength is to be measured. A push-pin experiment is performed such that a uniform load is applied with a given strain rate on the specimen by a push rod until the specimen fails while the force-displacement history is recorded. The

method follows three steps: 1) conduct push-pin experiment and record the force and displacement data, 2) develop a layer-structured FE model with the same dimensions to simulate the push-pin experiment; 3) try different settings of material properties (Young's modulus and yield strength) until the curves of force versus displacement calculated from the FE model match those from the experiment, 4) pick the maximum stress normal to bonded areas from the FE model as the bond strength. The limitation of the method is that the identified values of material properties are not unique since there are two model parameters that need to be identified (Young's modulus and yield strength) whereas there is only one observable parameter (the displacement load data).

2.5.5 Linear Weld Density

In addition to the lap-shear and peel test, Kong also introduced the concept of "linear weld density (LWD)" for evaluating the bond quality (Kong, Soar, and Dickens 2004). The LWD is defined as the percentage of real contact area over the apparent weld area.

$$LWD = \frac{A_{real}}{A_{apparent}} \times 100\% \quad (2.8)$$

The LWD is measured from micrographs of the bond interface of specimens. The specimens are made by welding two layers of foils to the base plate and cut from the beginning, center, and end of the bond interface. These cut specimens are mounted, polished, and etched with Keller's solution. The LWD is observed at the cut interface using an x200 optical microscope. By varying the operating parameters, the LWD is observed to increase linearly as amplitude increases. However, the bond strength does not increase at this point possibly because the excessive vibration weakens the already formed bonds.

2.5.6 Process Optimization

Based on the reviewed bond quality evaluation methods, the UAM process can be optimized in order to achieve the optimum bond quality. Kong conducted peel tests and measured linear weld density on specimens made under various combinations of operating parameter values (Kong, Soar, and Dickens 2005). As a result, they identified a general process window for aluminum 6061 in the UAM process (**Figure 2.9**). The window is defined based on the peel load greater than 69 N and the linear weld density of $45\% \pm 5\%$. From a design perspective, the optimum process window is identified through a design of experiment (DOE). The identification process requires multiple experiments which are energy, material and labor consumptive. Moreover, the result is material specific. If a different material is to be used, the entire process has to be repeated.

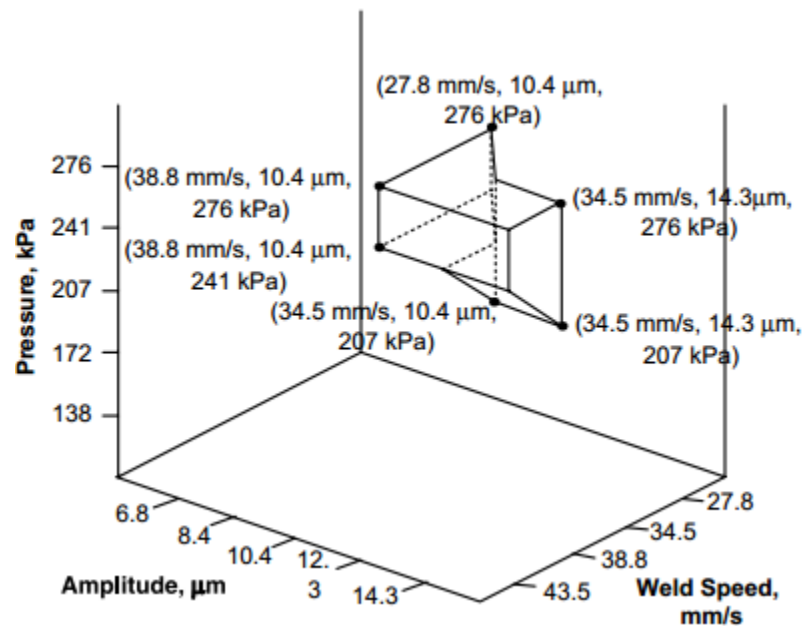


Figure 2.9 General process window for aluminum 6061 – T0 based on peel test and linear weld density (Kong, Soar, and Dickens 2004)

In summary, different methods of bond quality evaluation are reviewed in this section. All existing evaluations are post-weld evaluation and are destructive to the bonds. The proposed UAM model which predicts *plastic stress, strain, displacement, temperature, contact stress and contact area* between the built feature and the foil, is potentially capable of predicting bond quality provided that a solid relation can be established between the bond quality and the plastic deformation of the foils.

2.5.7 Relating Plastic Deformation to Bond Quality

The initial surface roughness, even though has little influence on kinematic friction during bonding, is shown to influence the ultimate bond quality. Due to the relatively low stiffness and high stress concentration, the initial asperities undergo plastic deformation rapidly at the beginning of bonding and provide materials necessary to form the bonds. Johnson shows in electron micrographs of multiple bond interfaces that severe plastic deformation takes place in the surface layer of material with a depth of approximately 20-60 μm from the mean plane of the asperities (K. E. Johnson 2008). This plastic deformation layer, according to Johnson, is the primary driver of the solid state bond quality. Furthermore, multiple experimental studies reveal that a rougher initial surface leads to stronger bonds (Friel et al. 2010; Kulakov and Rack 2010; Truog 2012; Wolcott, Hehr, and Dapino 2014). Others found the roughened initial surface being the source of bond defects (Ram, Robinson, et al. 2007). Li and Soar point out that the roughened surface has a significant

influence on bond quality because, on one hand, it facilitates the transfer of ultrasonic energy to the built feature and, on the other hand leads to voids that do not get filled by plastically deformed materials when the consolidation amplitude is not sufficiently high (Li and Soar 2009). Troug found that a rougher foil surface improves bond quality using high power UAM (9 kW) (Truog 2012). Wolcott et al. theorize about the asperities and deduce that larger asperities introduce more plastic deformation and larger friction force which drives dynamic recrystallization, resulting in higher bond strength (Wolcott, Hehr, and Dapino 2014). *As a result, the deformation of asperities serves as a good indicator of bond quality. If a model of asperity layer can be established, it can then be directly used to predict bond quality based on the degree of deformation of the layer.*

2.6 Hypotheses and Research Questions

2.6.1 Summary of Gaps in Literature

In this chapter, the literature associated with UAM bond process is reviewed. Gaps are summarized below:

1. *The acoustic softening effect has not been fully investigated and characterized.* The existing literature reports diverging observations of acoustic softening in metals, making it difficult to characterize for a specific metal without conducting experiments. Most of the existing analytical models of acoustic softening reviewed lack support of experimental data. Moreover, to the best knowledge of the author, few acoustic softening data are found

in the literature for metals that are extensively used in UAM, such as Aluminum 6061, 1100, or Copper 11000.

2. There exists a gap between the modeling work of dynamics and bonding process. It can be seen from the literature that the dynamics models do not consider the bonding process, whereas some models that focus on the bonding process, although they include the dynamic equations, do not take into account the change in dynamics due to the change of the built feature geometry. In order to have a comprehensive understanding of the UAM process, both the macroscopic dynamics and the local bonding process at the interface need to be taken into account.

3. None of the existing models have considered all of the influential factors discussed in this work. These factors include acoustic and thermal softening, strain rate hardening, temperature, friction, and dynamics.

4. None of the reviewed models has associated their model prediction to bond quality.

5. None of the existing models have been used to identify the optimum process parameters for UAM. In the literature, process optimization has been conducted through design of experiment (DOE), i.e. setting up a series of experiments in which operating parameters (vibration amplitude, compression, weld speed, and temperature) are varied to search for the set of parameters that yield the optimum bond quality. However, it has never been investigated using UAM models to the knowledge of the author. If the DOE is replaced by running UAM models, the number of tests can be increased, leading to smaller increments of design variables and a larger design space.

6. *None of the existing models have been used to understand the energy flow.* Many researchers have investigated the energy flow in the UAM process. The energy flows are difficult to be quantified experimentally but are relatively easy to compute in numerical models. By varying the energy input and observing the change in kinematics, strain energy, heat dissipation, etc, the model could help gain insights into understanding energy flow within the UAM process.

2.6.2 Primary Hypotheses

Primary hypothesis: the dynamics of UAM system affect the plastic deformation of materials at the bond interface and vice versa. The change in dynamics leads to a change in differential motion and therefore a change in the degree of plastic deformation. The plastic deformation is also believed to affect the dynamics in return. In the elasto-dynamic model where the stiffness of the components is modeled as the stiffness of an elastic spring, the plasticity can be qualitatively modeled by introducing nonlinear dampers that alter the dynamics of the system.

2.6.3 Secondary Hypotheses

Secondary hypothesis 1: in order for bonding to take place there is a minimum amount of plastic deformation needed. The degree of plastic deformation is positively correlated to bond quality, i.e., the higher the plastic deformation, the better the bond quality. The hypothesis supports the soundness of considering plastic deformation as a linkage to

connect macroscopic dynamics and the bond quality localized at the bond interface. The degree of plastic deformation depends on a series of factors including acoustic and thermal softening, strain rate hardening, heat transfer, and stick-slip friction. These factors further depend on the type of material, geometry of the built feature, and the operating parameters: amplitude, compression, weld speed, and heating temperature of the substrate.

Secondary hypothesis 2: the bond quality can be characterized by the degree of plastic deformation of the asperities on the sonotrode-textured surface of the built feature.

With this hypothesis the degree of plastic deformation can be further characterized in terms of contact stresses, contact area, and separation distance between the bonding interfaces.

2.6.4 Research Questions

Based on the hypotheses, five research questions are proposed:

1. How can the acoustic softening effect be taken into account in the modeling of the UAM process?
 - How can one design an experiment to quantify the acoustic softening effect?
 - How to analytically model acoustic softening?
2. Which analytical models should be integrated to better characterize the UAM process?
 - How to establish a plasticity model that incorporates acoustic and thermal softening?
 - How to account for all the factors associated with heat transfer and friction in UAM?
 - How to account for the variation of dynamic conditions in a UAM model?

- How can the UAM model be validated?
3. What are the criteria and how can they be used to evaluate the performance of the UAM model?
 4. How can one evaluate the performance of the proposed UAM model in terms of optimization of process parameters?
 5. How can one quantify the energy flow in the UAM process?

We are hoping that, by answering these questions, a comprehensive thermo-mechanical UAM model can be established to have a better understanding of the solid state bonding process.

Chapter 3

3 Experimental Investigation of Acoustic Softening

Blaha and Langenecker are the first to document the phenomenon known as “acoustic softening”: a significant reduction of static stress in tensile tests when applying longitudinal ultrasonic waves to various metals. Since then different researchers have endeavored to investigate the phenomenon. Different experimental setups have been designed to test the effects of ultrasound on various materials, leading to diverging observations and alternative theories of the softening process. In order to clarify the acoustic softening in the UAM bonding process, we have conducted experimental investigations on two types of metals that are extensively used in UAM: aluminum alloys and copper alloys. Specifically, the aluminum alloys include Aluminum 6061-T6 and -O, and Aluminum 1100-O. The copper alloy is Copper C11000-O. This chapter first details the design of the setup, the execution of the test, and observations, and then proceeds to discuss the results by comparing the softening in different materials. Finally, an analytical model is developed to characterize the acoustic softening in different materials.

3.1 Design of Experimental Setup

3.1.1 Review of Existing Setups

The difference in the designs of the experiments could potentially lead to differences in observations, causing differing interpretations of the results and the formation of competing theories. Therefore, in this section, we review the different experimental setups in order to identify an optimum design that measures acoustic softening with minimum noise factors.

In 1955, Blaha and Langenecker reported a significant decrease of static stress, in stress strain relations of zinc single crystal subject to an ultrasonic field (Blaha and Langenecker 1955). In their experiment, the researchers place a standard tensile specimen in a liquid CCl_4 bath (**Figure 3.1**, left). While being tensioned, the specimen is subjected to ultrasonic oscillations generated from the liquid bath. Based on the experiment, the authors concluded qualitatively that a reduction of required tensile stress occurs when the ultrasounds start and disappears when the ultrasounds cease. Later the researchers simplified the experiment by removing the liquid bath and applying the ultrasound directly to the specimen (Langenecker 1963). A filament tensile test machine is combined with an ultrasonic transducer to provide tensile loading and ultrasonic vibration respectively (**Figure 3.1**, right). The ASTM standard circular tensile test specimens made of aluminum single crystals, beryllium single crystals, low-carbon steel, stainless steel, and tungsten are tested with the setup.

The experimental setup proposed by Blaha and Langenecker was later adopted by many researchers for its effectiveness in measuring the effect of ultrasound on the tensile

stress strain relation of metal specimen (Baker and Carpenter 1965; Daud, Lucas, and Huang 2006; Mignogna and Green J. 1979; Nevill and Brotzen 1957; Pohlman and Lehfeltdt 1966; Winsper and Sansome 1969). The setups used by Mignogna and Green, Daud and Huang are very similar to Blaha and Langenecker's setup and will not be discussed in details (Daud, Lucas, and Huang 2006; Mignogna and Green J. 1979). Nevill and Brontzen, Baker and Carpenter, Pohlman and Lehfeltdt, Winsper and Sansome made small modifications on the design of the specimens (Baker and Carpenter 1965; Nevill and Brotzen 1957; Pohlman and Lehfeltdt 1966; Winsper and Sansome 1969). Instead of using standard tensile circular specimens, they used long thin metal wires with the longitudinal length tuned to one half or multiple halves of the wave length of the ultrasound. Note that one issue with using the long thin wire is that the effect of the ultrasound could be significantly reduced as the wave is attenuated by propagation.

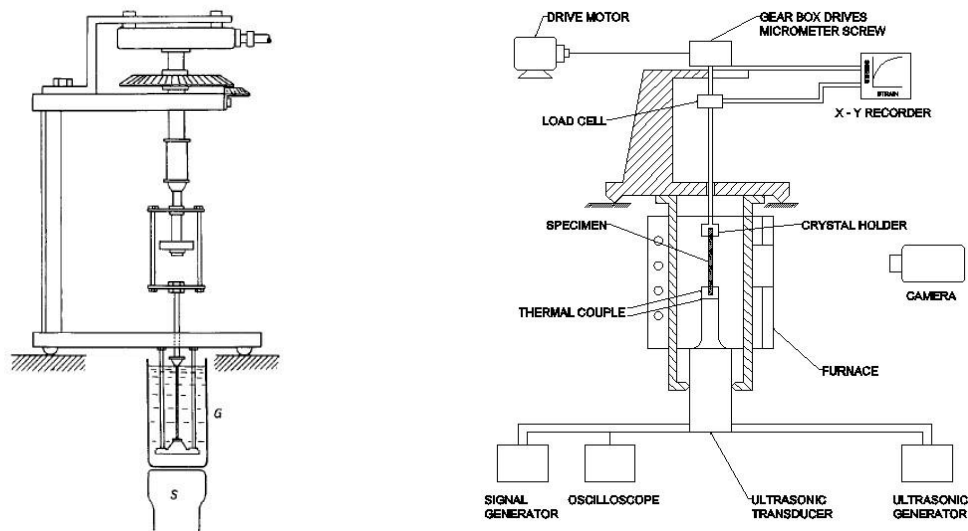


Figure 3.1 Blaha and Langenecker's first setup (left) and second setup (right), reproduced from (Blaha and Langenecker 1959b; Langenecker 1963).

In addition to investigating tensile tests for application in extrusion type metal processes, researchers investigated compression type tests for possible application of ultrasound in compression type processes, such as upset forging and wire bonding (D. Culp and Gencsoy 1973; Daud, Lucas, and Huang 2006; Huang et al. 2009; Hung, Tsai, and Hung 2007). In their experimental setups, the specimen is fixed at one end and subjected to both compressional loading and ultrasonic vibration at the other end (**Figure 3.2**). The shapes of the specimens include short cylinders (D. Culp and Gencsoy 1973; Daud, Lucas, and Huang 2006), rings (Hung, Tsai, and Hung 2007) and ball shapes (Daud, Lucas, and Huang 2006), depending on the specific industrial application. The material softening in compressional stress strain relations shows qualitatively similar behavior to the material softening in tensile stress strain relations. However, the compressional tests introduce contact friction as specimens deform, which must be considered when quantifying material softening induced by ultrasound. Hung et al. investigated the frictional effect of superimposing ultrasonic vibration during upsetting (Hung, Tsai, and Hung 2007). They demonstrated that the frictional condition at the horn-specimen interface has a noticeable influence on the static compressional force. They concluded that the effect of friction requires it to be decoupled from the effect of ultrasound in compressional tests.

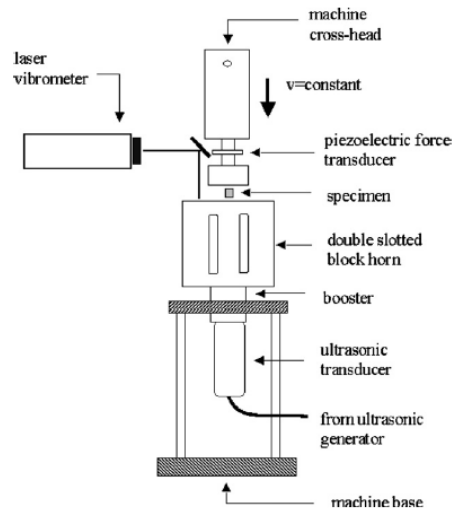


Figure 3.2 Daud's setup (Daud, Lucas, and Huang 2006).

Some researchers modified the compression tests by replacing longitudinal vibration with transversal vibration of the ultrasonic horn on the specimen (Siu, Ngan, and Jones 2011; Yao, Kim, Wang, et al. 2012). Siu et al., for instance, use a hardness tester equipped with a Vicker's indenter tip and an ultrasonic transducer to perform such an experiment (Siu, Ngan, and Jones 2011). A polycrystalline aluminum square slab (10 x 10 x 1.5 mm) is glued onto the tip of an ultrasonic horn and is subjected to compression. The horn vibrates transversally while the Vicker's indenter presses down against the slab along a longitudinal direction (**Figure 3.3**, left). The microstructures of the indents are then analyzed using transmission electron microscopy (TEM) and crystal orientation mapping by electron backscattered diffraction (EBSD). Yao et al. describe a similar setup, using short cylindrical specimens that are compressed by an acoustic horn vibrating in the transverse mode (**Figure 3.3**, right) (Yao, Kim, Wang, et al. 2012). The material softening is measured in form of stress reduction in the stress strain relations. By substituting longitudinal vibration

with transversal vibration in compression tests, significant frictional heat is introduced at the horn-specimen interface. The interfacial friction causes thermal softening of the specimen which is not easily separated from acoustic softening. In Siu's work, no discussion is found describing the effect of frictional-heating on sub-grain formation which they have observed at the indentation site (Siu and Ngan 2013; Siu, Ngan, and Jones 2011). Similarly, Yao et al. do not consider the effect of frictional-heat on material softening, although they report a temperature rise by 10 °C within specimen during acoustic softening (Yao, Kim, Faidley, et al. 2012).

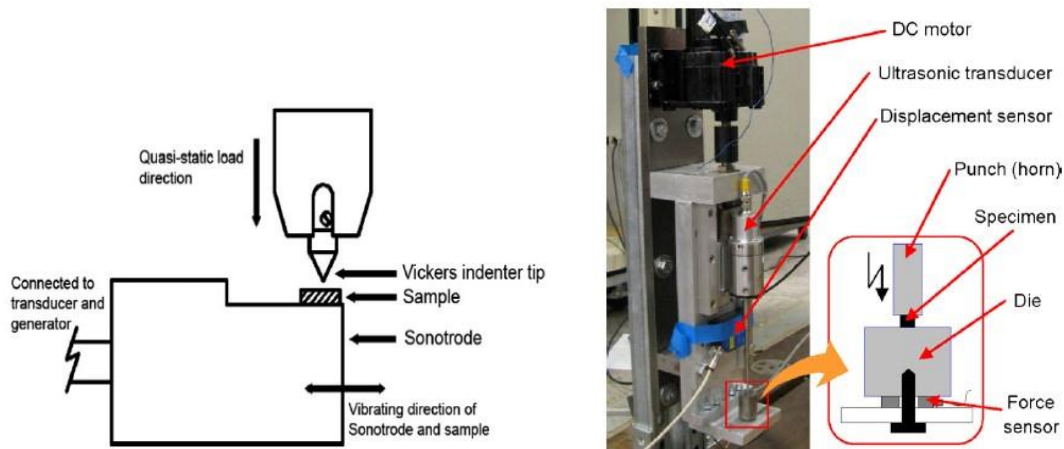


Figure 3.3 Siu's setup (left) and Yao's setup (right).

Dutta et al. present another variation of setup for tensile tests. They designed the experimental apparatus so that longitudinal ultrasonic vibration is applied in a direction perpendicular to the axis of the specimen (**Figure 3.4**) (Dutta et al. 2013). They used ASTM standard tensile specimens made from steel sheets. The contact force between horn and specimen is carefully controlled to prevent excessive bending of specimens. The material softening is identified as the static stress decreases on the stress strain curves. In this setup, both contact friction and interfacial friction are avoided. However, the stress caused by

bending requires decoupling from the stresses caused by tensile loading, when evaluating the tensile stress reduction induced by ultrasound.

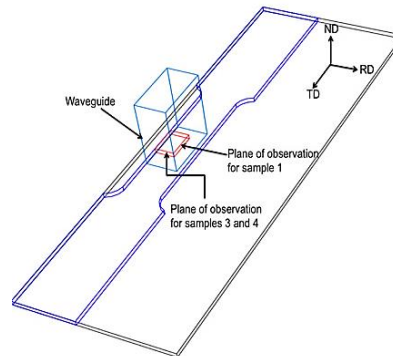


Figure 3.4 Dutta's setup (Dutta et al. 2013).

In summary, it is evident that the various experimental setups are combinations of tensile or compressional tests and longitudinal or transversal ultrasonic vibration. Furthermore the following conclusions can be drawn:

1. In general, compressional tests introduce more friction than tensile tests.
2. Transversal ultrasonic vibration introduces more friction than longitudinal ultrasonic vibration.

Blaha and Langenecker, together with other researchers who used similar setups, effectively minimize the effect of friction by using an apparatus that utilizes tension with longitudinal ultrasonic vibration. Based on this observation, we describe our experimental setup.

3.1.2 Proposed Design of Setup

Figure 3.5 shows our design of experimental setup. It follows the design of Blaha and Langenecker, and consists of an MTS hydraulic tensile test machine with an Instron controller (Instron 8800, software version 8.4, build 244), a Branson 2000 ultrasonic plastic welder and a rigid frame made of steel plates of 1” thickness. The MTS tensile test machine provides static tensile load from the bottom end of the specimen in the vertical direction, stretching or compressing the material to its failure. The loading profile is recorded by an MTS load cell (2000 lbs) that connects the MTS actuator and the specimen while the deformation history is recorded by an Instron 2630 extensometer (gauge length: 1 inch, travel: 0.5 inches). The Branson ultrasonic welder delivers ultrasonic energy to the upper end of specimen. The welder consists of an ultrasonic transducer that converts electric energy into ultrasonic vibration, a booster that amplifies ultrasonic vibration and an ultrasonic horn that further magnifies and delivers ultrasonic vibration onto the specimen. The vibration frequency is fixed by the transducer at 20 kHz whereas the vibration amplitude is mainly determined by the profile of ultrasonic horn and the amount of energy delivered. In our current setup, a circular high gain horn made of aluminum heat-treated aluminum alloy is used and the maximum vibration amplitude is 24 microns based on measurement from a laser vibrometer. Due to the fact that the ultrasonic welder is designed to take compressional load rather than tensile load, the ultrasonic horn cannot be directly connected to the specimen that is tensioned by the MTS machine. Therefore, a steel frame had to be built to provide a fixing position for the specimen to take the tensile load off the welder. The specimen is installed such that it oscillates with the ultrasonic horn at its upper end, fixed to the

frame at a point just below the oscillating end, and is stretched at the bottom end (**Figure 3.6**). In addition, a Polytech laser vibrometer measures the vibration amplitude of specimen. A FLIR thermal camera and Omega DP490 thermo-couples are used to observe the temperature of the specimen surface close to the deformation region.

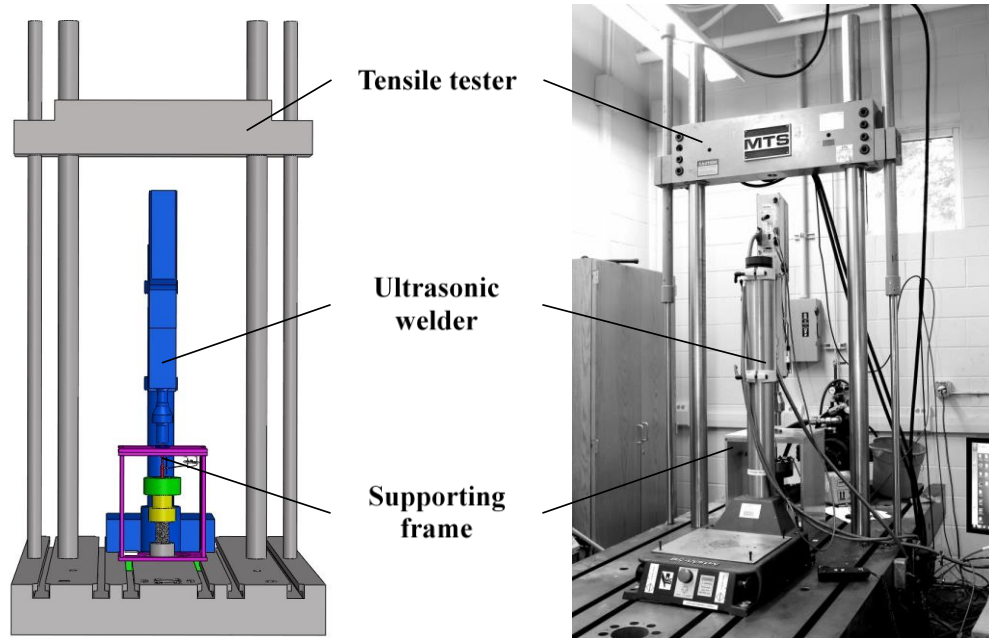


Figure 3.5 Experimentation setup: the CAD model (left) and the actual setup (right)

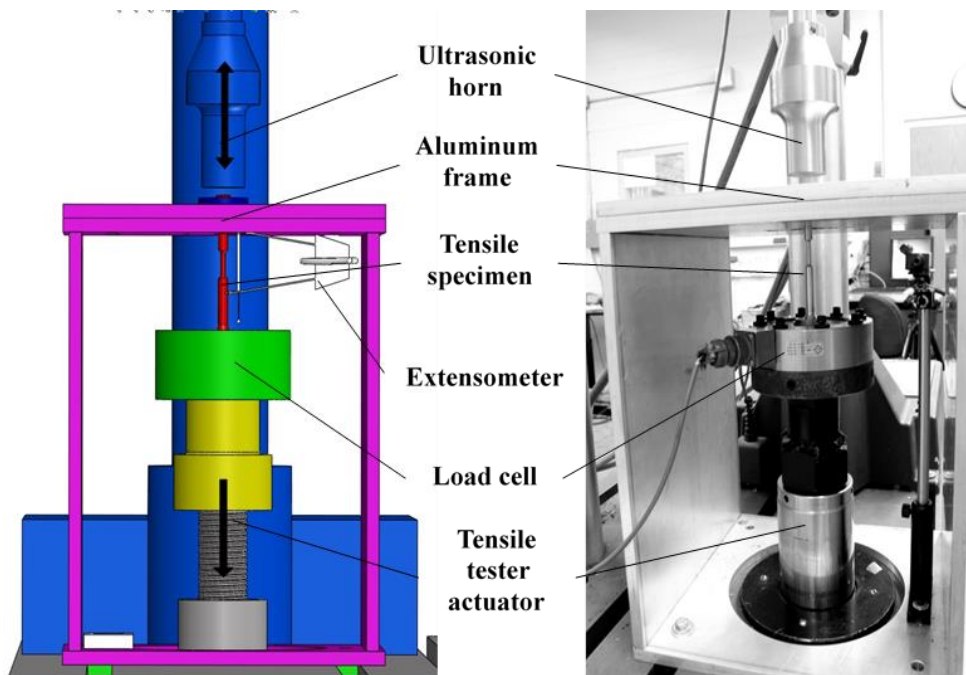


Figure 3.6 Frame Design: the CAD model (left) and the actual frame (right).

3.1.3 Special Considerations in Designing the Setup

Special considerations are taken in designing the setup to ensure that the loss of ultrasonic energy is minimized. Specifically, due to the fact that the specimen is fixed to the frame at a location below the ultrasonic vibration interface, a portion of the ultrasonic energy will propagate through the frame instead of the specimen, causing ultrasonic energy losses and reduction of acoustic softening effects (**Figure 3.7**). In order to minimize the energy losses, three steps are taken while building the frame: 1) the frame is designed such that it is much stiffer than the specimens under testing. The frame is built using hot rolled steels which are much harder than the aluminum and copper alloys used for specimens. The steel plates are of 1" thickness and are bolted together to build in a box structure in

order to achieve high stiffness. 2) A dynamic analysis is performed on the 1:1 size CAD model using ABAQUS 6.10 to ensure that the ultrasonic horn does not excite any resonances in the frame. Modal analysis is carried out to examine the first five modal frequencies of the frame to make sure that they are far away from the operating frequency which is 20 kHz. We also performed a dynamic transient analysis by imposing 20 kHz vibration to the frame model. The dynamic response, stress distribution, and deformation are examined to ensure minimal deflection at the application point to the specimen, and that stress is well below the yield stress. 3) Dry lubricants are applied to all the contact interfaces where ultrasonic waves propagate from one solid medium to another. Dry lubricants are applied to the horn-specimen and the specimen-frame interfaces to minimize vibration-induced friction. The friction on one hand dissipates ultrasonic energy by means of frictional work, on the other hand introduces noises to the measuring of acoustic softening. The dry lubricants applied include extreme fine graphite and Molly EP. The extreme fine graphite can minimize metal-to-metal contact and wear of sliding surfaces. The Molly EP has the extreme pressure (EP) additives that can react with steel surfaces under pressure to form a surface film and to prevent metal-to-metal contact or welding.

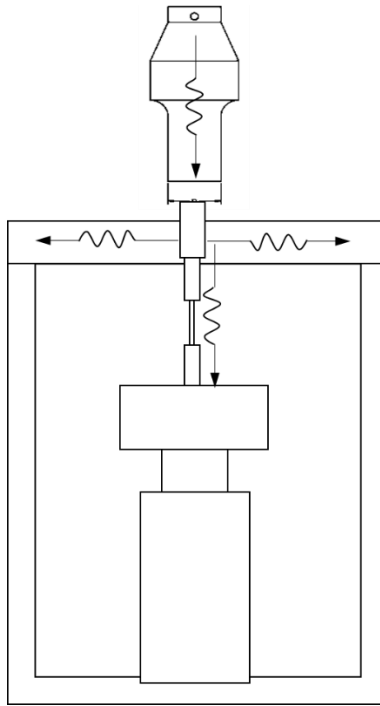


Figure 3.7 The propagation of the ultrasonic waves into specimen and into frame

3.2 Experimental Details

This section documents details of the experiments including the preparation of materials, design of specimen, experimental procedures, and some special considerations in executing the experiment.

3.2.1 Preparation of Materials

The materials under study are Aluminum 6061-T6, Aluminum 6061-O, Aluminum 1100-O, and Copper C11000-O due to their extensive application in UAM and availability. The Aluminum 6061-T6 and Aluminum 1100-O are used as received, whereas the Aluminum 6061-O and Copper 11000-O are obtained through heat treatment. Specifically, the

annealing of Copper 11000 involves heating the material to 370 °C for 1 hour and cooling it down in an oven. The annealing process of Aluminum 6061 includes heating the material to 417 °C for 2.5 hours and then cooling it down from oven to room temperature. The Aluminum 6061-O is obtained by annealing Aluminum 6061-T6 to –O temper. Therefore the composition of Aluminum 6061-T6 and –O are the *same*. The chemical composition of Aluminum 6061-T6, Aluminum 1100-O, and Copper 11000 are shown in **Table 3.1**.

Table 3.1 Chemical compositions of Aluminum 6061-T6, Aluminum 1100-O, and Copper 11000-O (“McMaster Carr” 2015)

Aluminum 6061-T6		Aluminum 1100-O		Copper 11000	
Al	95.1-98.2%	Al	97.85-99.4%	Copper	99.9%
Mg	0.8-1.2%	Si + Fe	0.55-1.0%	Pb	0-0.005%
Si	0.4-0.8%	Cu	0.05-0.2%	Bi	0-0.005%
Cr	0.4-0.8%	Mn	0-0.05%	O	0-0.04%
Fe	0-0.7%	Mg	0-0.05%		
Cu	0.05-0.4%	Zn	0-0.1%		
Mn	0-0.15%	Ti	0-0.6%		
Ni	0-0.05%	Other	0-0.15%		
Zn	0-0.25%				
Ti	0-0.15%				
Zr	0-0.25%				
Other	0.15%				

3.2.2 Specimens

The design of specimens, where possible, follows the ASTM standard E8-04. However, due to the limited capacity (2000 lbs) of the load cell and high yield strength of the test material, the gauge diameter for specimens made of aluminum 6061-T6 is constrained to 3/16 inch and the specimen profile deviates from the standard profile. The profile dimensions and the actual specimen are shown in **Figure 3.8**. The rest of the specimens that are made of Aluminum 6061-O, Aluminum 1100-O, and Copper C11000-O conform to the standard profile and have a gauge diameter of 1/4 inch. The profile dimensions and the actual specimens are shown in **Figure 3.9**.

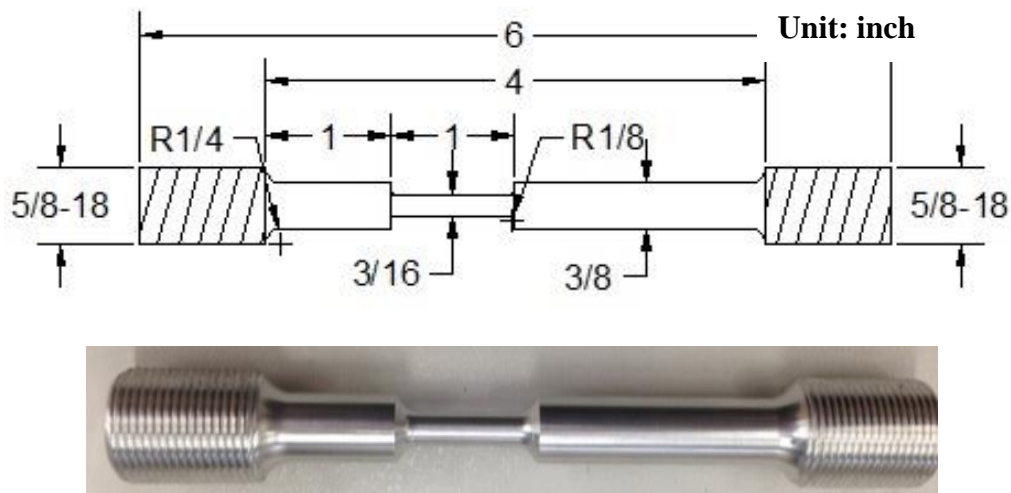
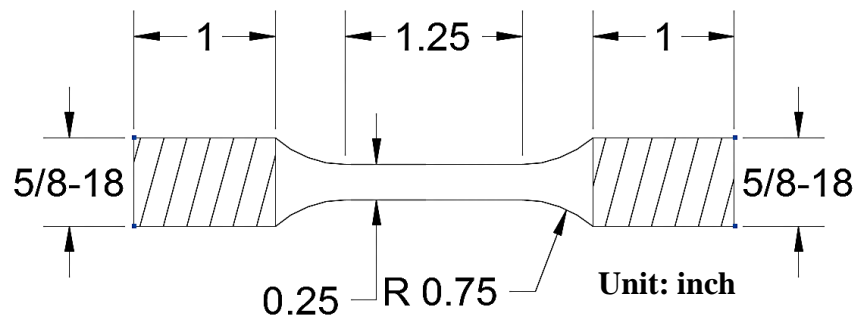
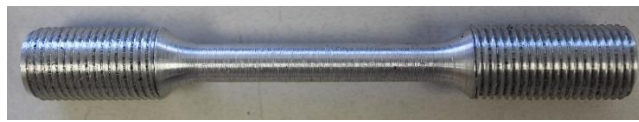


Figure 3.8 Specimen design: specimen dimension (top) and actual specimen (unit: inch) made of Aluminum 6061-T6 (bottom) (Mao, Gibert, and Fadel 2014).



(a)



(b)



(c)



(d)

Figure 3.9 Specimen design: specimen dimension (a) and actual specimens (unit: inch) made of Aluminum 6061-O (b), Aluminum 1100-O (c), and Copper C11000-O (d).

3.2.3 Testing Procedure

The tests starts with a standard quasi-static tensile test operated in displacement-controlled mode. The specimen is subjected to quasi-static tensile load at a constant loading

speed of 0.1 mm/s until it fails. Meanwhile, the ultrasonic welder is started after the specimen begins to yield. As the welder starts, the ultrasonic horn is brought into contact with the upper end of the specimen at a constant speed and is compressed on top of the specimen with a moderate force of around 150 lbs. The compressive preload is critical for the propagation of ultrasonic waves within the specimen. Some may argue that this compressive preload would affect the measuring of tensile stress from the load cell. Based on our observation, however, the compressive force barely changes the measured stress since it is counteracted by the clamping force exerted by the frame. As soon as the compressive force reaches the set value, the ultrasound starts and the longitudinal ultrasonic waves propagate through the specimen that is being tensioned. The ultrasonic irradiation lasts for 10 seconds for Aluminum 6061-T6 and 20 seconds for the other three materials before it stops. The compression is then removed and the ultrasonic horn is brought up. The amount of ultrasonic energy applied during the irradiation is recorded by the welder controller and can be retrieved when the test completes.

The testing procedure is summarized in **Figure 3.10**. **Figure 3.10 (left)** shows the load profile from the MTS tensile test machine and **Figure 3.10 (right)** from the Branson ultrasonic welder. The MTS machine is run in displacement-controlled mode and the displacement s follows a ramp curve with its slope being fixed to 0.1 mm/s. The Branson welder is run in amplitude-control mode and the displacement A follows a sinusoidal curve with its frequency fixed at 20 kHz and its amplitude to the set percentage. **Figure 3.11** shows a schematic of the stress history in response to the loads. At the beginning, a tensile

stress is established in response to the quasi-static loading of the tensile tester. The ultrasound is started after yielding, introducing an oscillating stress in addition to tensile stress. The oscillation interval is t_u and the oscillating stress amplitude is far smaller than the magnitude of the tensile stress. However, the resulted reduction in tensile stress is significant. By comparing the load-induced stresses and the actual softened stress curves in section 3.3.1, it is shown that acoustic softening is not a result of simple superposition between tensile and ultrasonic stresses. Finally, the operating parameters used in the testing are summarized in **Table 3.2**.

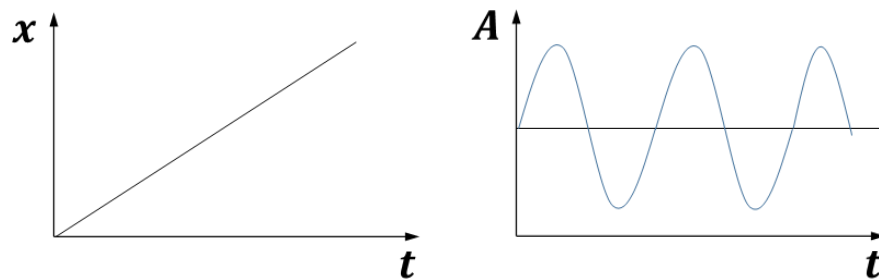


Figure 3.10 Load profiles: MTS tensile test machine (left), Branson ultrasonic welder (right).

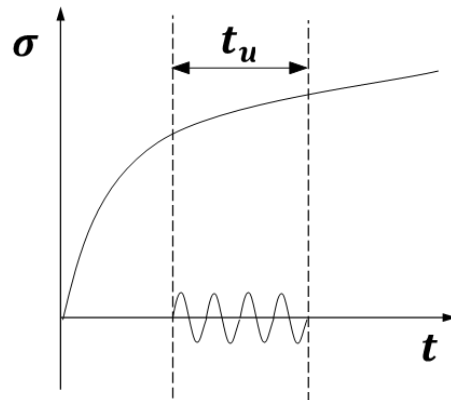


Figure 3.11 A schematic of history of stresses induced by external loading

Table 3.2 Summary of operation parameters of testing

Amplitude	Frequency	Preload	Load Speed	Ultrasound-on Time
0-24 μm	20 kHz	140–160 lbs	0.1 mm/s	20 s (10s for Al6061-T6)

3.3 Observations and Discussions

This section presents the observations from each material tested and then compares the observations between these materials. The differences in acoustic softening are interpreted based on the materials' similarities and differences in the microstructure. Finally a macroscopic analytical model characterizing acoustic softening effect is proposed based on these observations.

3.3.1 Experimental Observations

The observations are presented for Aluminum 1100-O, Aluminum 6061-O, Aluminum 6061-T6, and Copper 11000-O. The Aluminum 1100-O is tested as received while the Aluminum 6061-O and Copper 11000-O are annealed. The details of the heat treatment as well as the chemical composition of each of the materials are presented in section 3.2.1.

3.3.1.1 Aluminum 1100-O

A total of 7 tests are carried out successfully and the results of 5 tests are shown in **Figure 3.12**. The stress-strain curves are obtained with ultrasound being set to 5 different

levels: 0 J (quasi-static loading), 9053 J, 10041 J, 10869 J, and 11394 J. The energy levels are normalized by the maximum energy to show their relative magnitude. The strains used in the plot are estimated based on the displacement of the tensile tester actuator rather than being measured by the extensometer due to some technical issues. The details of the softening process can be seen from the enlarged view of the plot. When the ultrasound starts, the stress drops drastically to a minimum point and then increases slightly before stabilizing at a low stress level. The curve shows strain hardening during the application of ultrasound. In Aluminum 1100-O, strain hardening is induced by the multiplication and interactions of dislocations. Interestingly, when the energy level is high enough, the curves become ragged which suggests that the ultrasound has certain effects on the moving of dislocations. As the ultrasound stops, the stress increases radically but still stays below the tensile stress without ultrasonic irradiation. This effect is known as “residual softening”. As the tensile load continues, the stress continues to increase due to strain hardening. However, depending on the level of the ultrasonic energy applied, the residual softening effect could remain in effect till the end of loading (i.e., the fracture of the specimen) or gradually die down before loading is completed.

Figure 3.13 shows the work hardening rate of true stress-true strain curve for Aluminum 1100-O. The work hardening rate is defined as the derivative of true stress with respect to true strain: $\theta = \frac{d\sigma}{d\varepsilon}$. The solid line shows the work hardening rate when being subjected to an ultrasonic energy input of 11349 J and the dashed line shows the one without ultrasound. The two curves highly overlap before and after the application of ultrasound but diverge in between. The softened curve shows two large spikes which correspond to

the abrupt change in stress at the start and the end of the ultrasonic irradiation. The magnitudes of the spikes indicate how radical the stress varies in response to the ultrasound. The small fluctuation during the irradiation indicates the influence of ultrasound on the interactions of dislocations.

Figure 3.14 shows the reductions of stresses with respect to different levels of ultrasonic energy. The stress reduction increases as the energy level escalates and a linear relation can be drawn between the two.

Finally, the observations from the Aluminum 1100-O are summarized as:

1. An instantaneous change in stresses is observed in response to the application of ultrasound.
2. The ultrasound reduces the stress necessary to deform material in the plastic deformation region.
3. The stress reduction is linearly proportional to the ultrasonic energy consumed.
4. A residual softening effect is observed when ultrasound stops.
5. The ultrasound is found to have an influence on the interactions between dislocations.

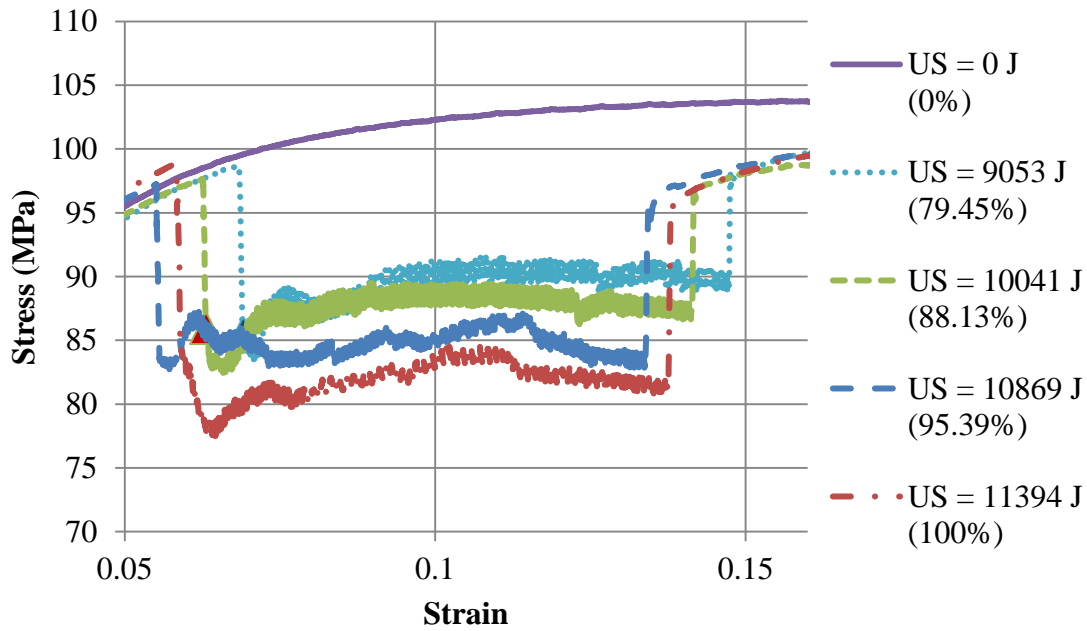
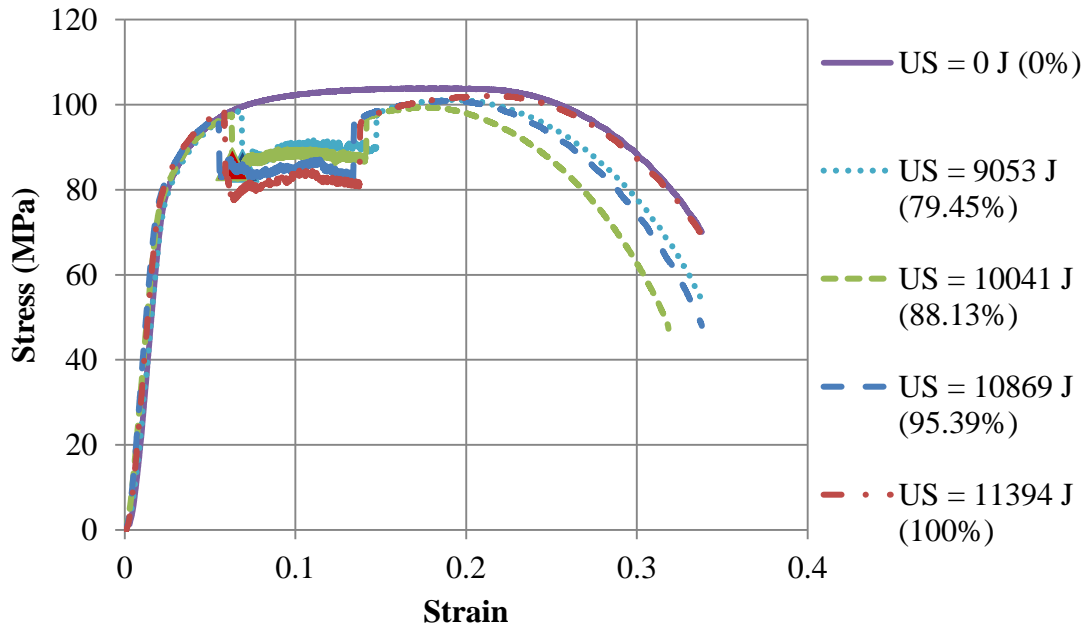


Figure 3.12 The effect of ultrasound on stress-strain curves of Aluminum 1100-O: overview (top), details of softening (bottom)

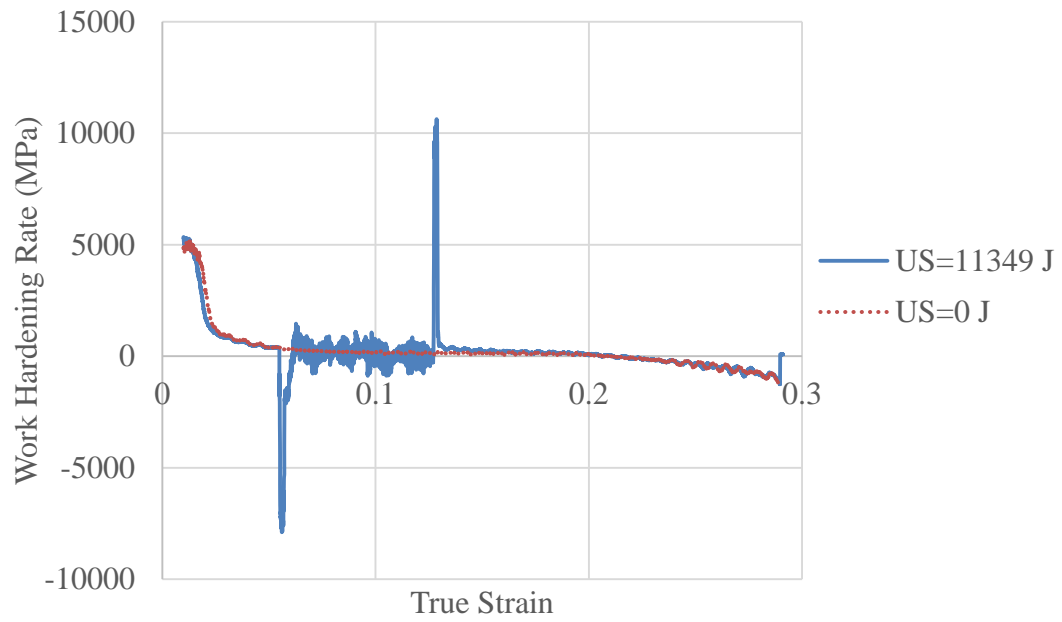


Figure 3.13 The work hardening rate as a function of true strain for Aluminum 1100-O with and without ultrasound.

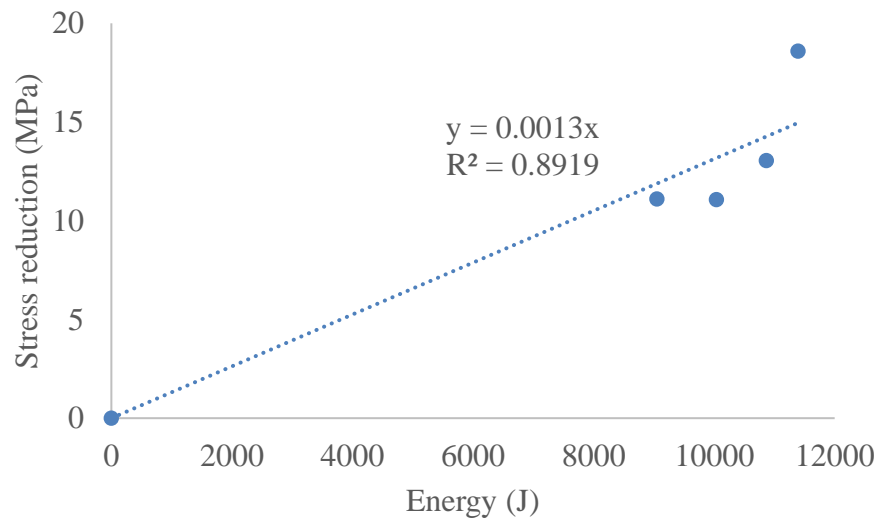
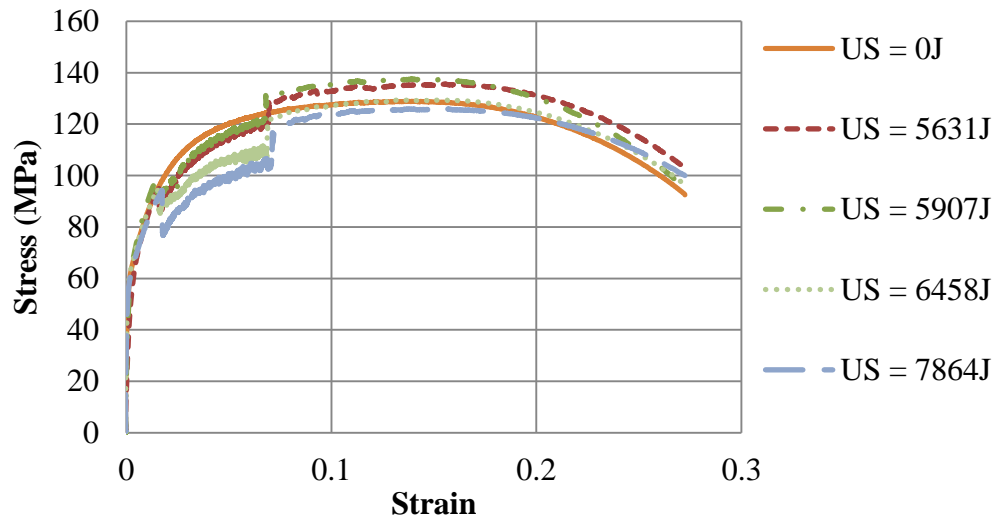


Figure 3.14 The stress reduction versus ultrasonic energy input relation of Aluminum 1100-O

3.3.1.2 Aluminum 6061-O

The same experimental procedure was repeated for aluminum 6061-O. Due to the relatively low hardness and strength of the material, the time interval of the applied ultrasound is extended from 10s to 20s. A total of 14 tests are carried out successfully and 6 of them are selected to present their stress strain curves at 5 different levels of energy input: 0 J, 5631 J, 5907 J, 6458 J, 7864 J (**Figure 3.15**). When the ultrasound is stopped, the stress-strain curves show residual hardening effects at low energy levels (US = 5631 J, 5907 J) and residual softening at high levels (US = 6458J, 7864 J). The stress reduction is linearly related to the ultrasonic energy as indicated by **Figure 3.16**. **Figure 3.17** shows the work hardening rate curve of Aluminum 6061-O with and without ultrasound. The two curves show overlapping throughout the course except at the time when ultrasound is started and stopped. The initial value of the work hardening rate of Aluminum 6061-O (4e4 MPa) is much higher than that of Aluminum 1100-O (5000 MPa) which indicates a higher dislocation density in Aluminum 6061-O when yielding starts. The radical changes in stress due to ultrasound (indicated by the magnitude of the spikes) are less significant in Aluminum 6061-O than in Aluminum 1100-O. It makes sense because Aluminum 6061-O has a higher dislocation density which requires more energy to achieve a similar stress reduction. Moreover, the existence of precipitates and their interactions with dislocations could also add to the dissipation of ultrasonic energy. **Figure 3.18** shows the effect of different ultrasonic irradiation time intervals on the softening and residual behaviors of materials. Specifically, the ultrasound is applied for 10 s, 20 s, and 30 s at three separate tests. The ultrasonic power for the 10 s and 20 s irradiation tests are held at a similar level (348W and 359

W) whereas for 30s irradiation test the power is higher (528W). The 10 s and 20 s irradiation tests show similar stress reductions during softening and similar residual effects after the ultrasound is stopped. The 30 s irradiation test shows slightly higher stress reduction during softening and slightly higher residual hardening than the 10 s and 20 s irradiation tests. These observations indicate that the softening and residual effects are not accumulated effects and therefore do not depend on the time interval of the ultrasonic irradiation.



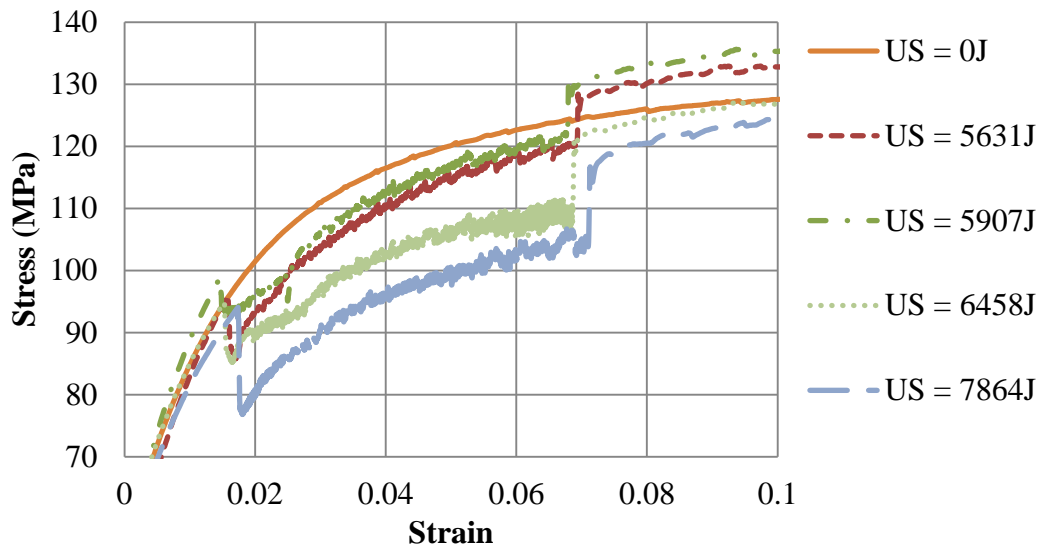


Figure 3.15 The effect of ultrasound on stress-strain curves of Aluminum 6061-O: overview (top), details of softening (bottom)

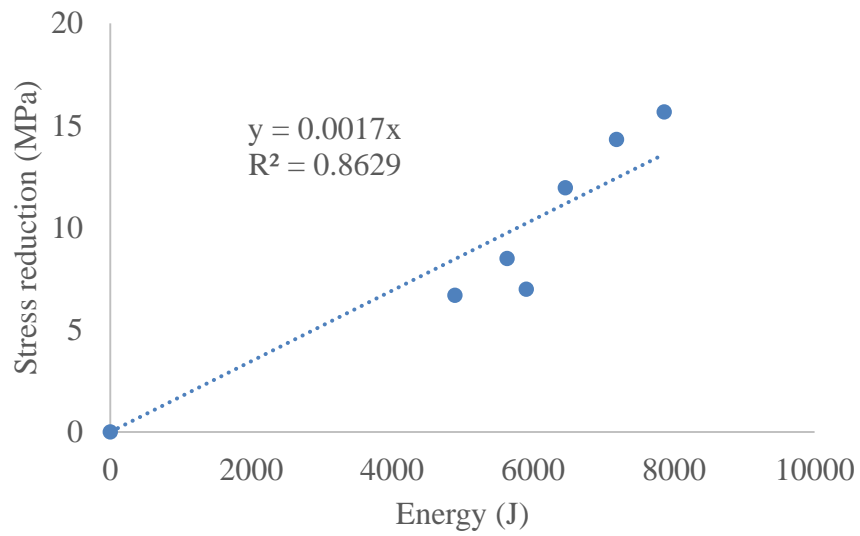


Figure 3.16 The stress reduction versus ultrasonic energy input relation of Aluminum 6061-O

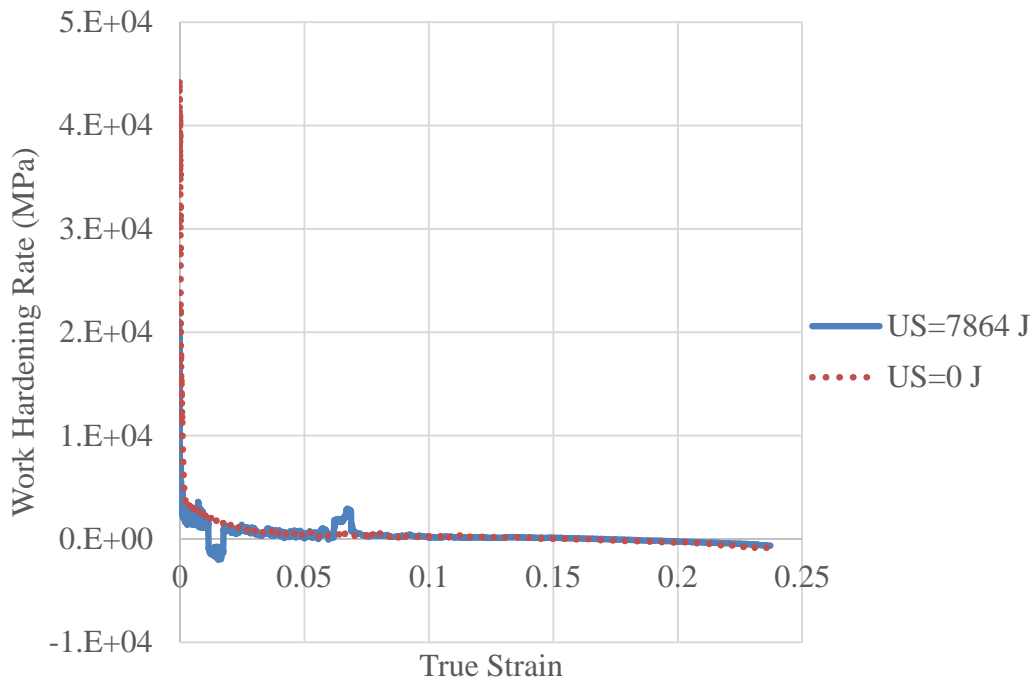


Figure 3.17 The work hardening rate as a function of true strain for Aluminum 6061-O with and without ultrasound.

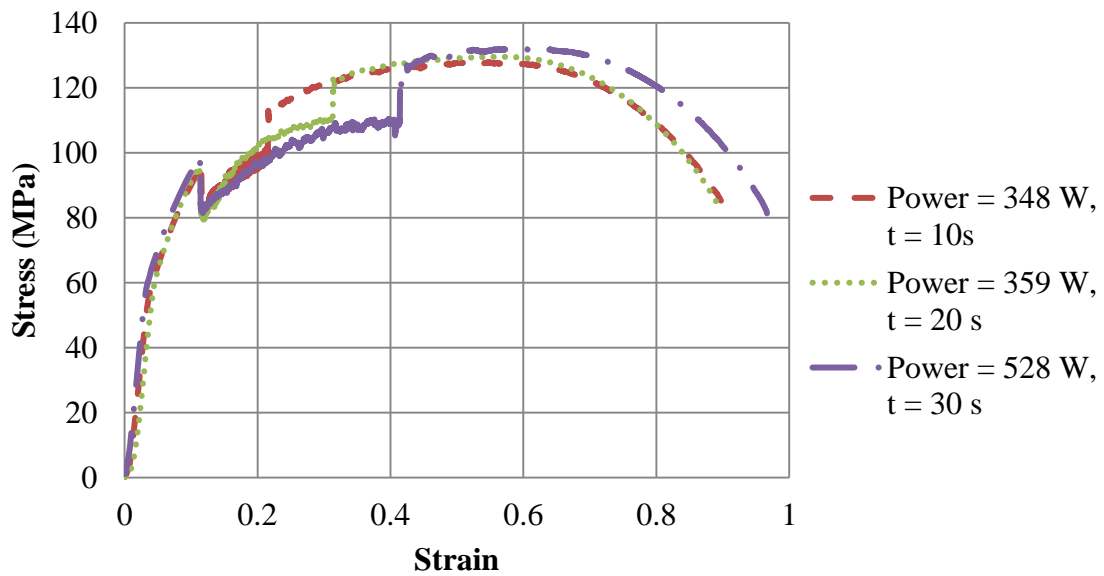


Figure 3.18 The effect of different irradiation time intervals on the softening and residual behavior of material of Aluminum 6061-O

3.3.1.3 Aluminum 6061-T6

A set of preliminary tests were initially carried out applying the ultrasound separately at strains with in (a) the *elastic* and (b) the *plastic* tensile deformation regions. The yield stress that separates the elastic and plastic regions was determined based on 0.2% offset in plastic strain. The stress strain curves with and without an ultrasound vibration were recorded and compared. These preliminary tests are designed to show qualitatively the acoustic softening behavior in the elastic and plastic deformation regions. Triplicate tests were performed with the stress-strain characteristics of one of three tests being shown in **Figure 3.18** and **Figure 3.19**.

When the ultrasonic vibration was applied within the elastic deformation region, the static stress immediately decreases. The starting point of ultrasonic vibration is shown in **Figure 3.18** (bottom). The stress reduction gradually increases until it stabilizes at around 59.45 MPa. Then the stress strain curve runs parallel to the reference curve at the lower stress level. When the ultrasound is stopped (shown as the end of ultrasound in **Figure 3.18**), the static stress gradually increases. However, the stress strain relation after stopping the ultrasonic vibrations does not overlap with the reference curve, but runs parallel at a stress level approximately 14.86 MPa lower than the reference curve until fracture occurs, indicating a *residual softening* effect.

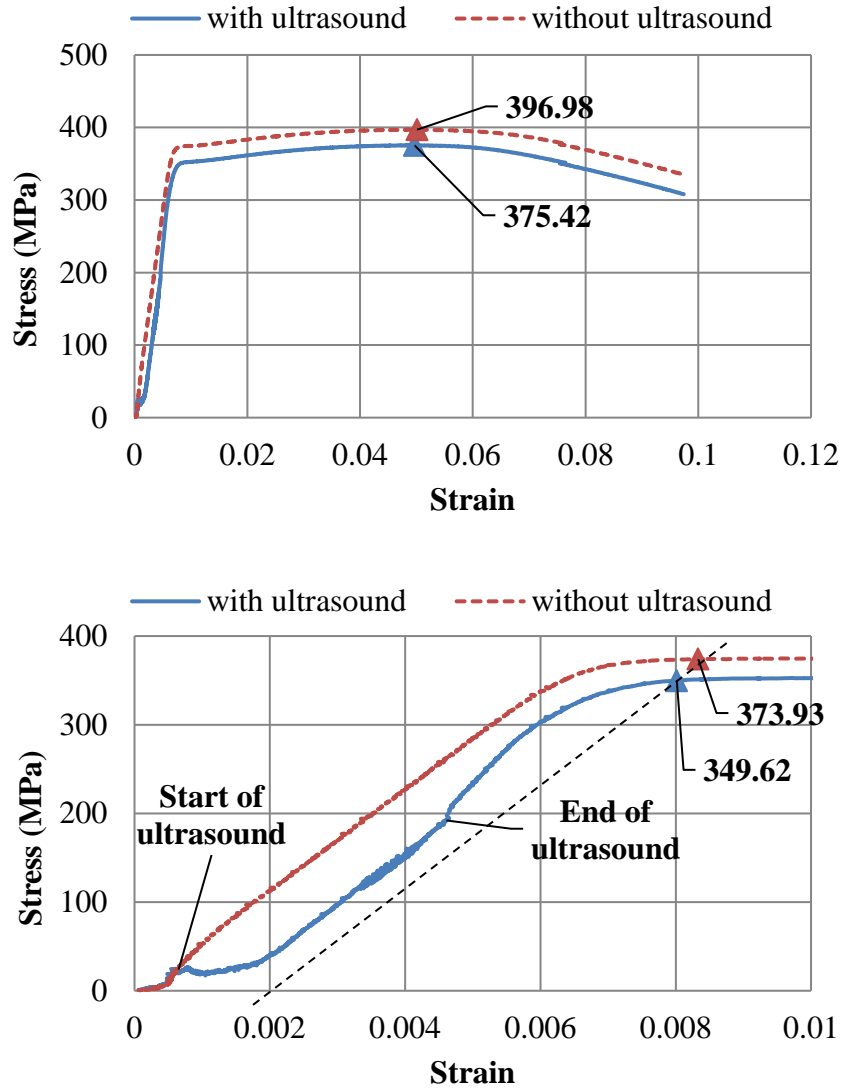


Figure 3.19 Stress strain relations with ultrasonic vibration in elastic deformation region for Aluminum 6061-T6: overview (top) and enlarged view (bottom)

When ultrasound vibration was applied within the plastic deformation region (**Figure 3.19**), similar behavior of stress strain relations is observed. The static stress is reduced by approximately 29.04 MPa in the plastic region. After the termination of ultrasonic vibration, a residual softening of approximately 15.64 MPa in stress reduction is observed.

The detailed comparisons of acoustic softening and residual softening induced by ultrasound in elastic and plastic regions are listed in **Table 3.3**. The data are based on 3 repeated tests, which are shown in **Table 3.4**. The yield stresses are determined based on 0.2% offset of plastic strain as indicated by the black dash line in **Figure 3.18**.

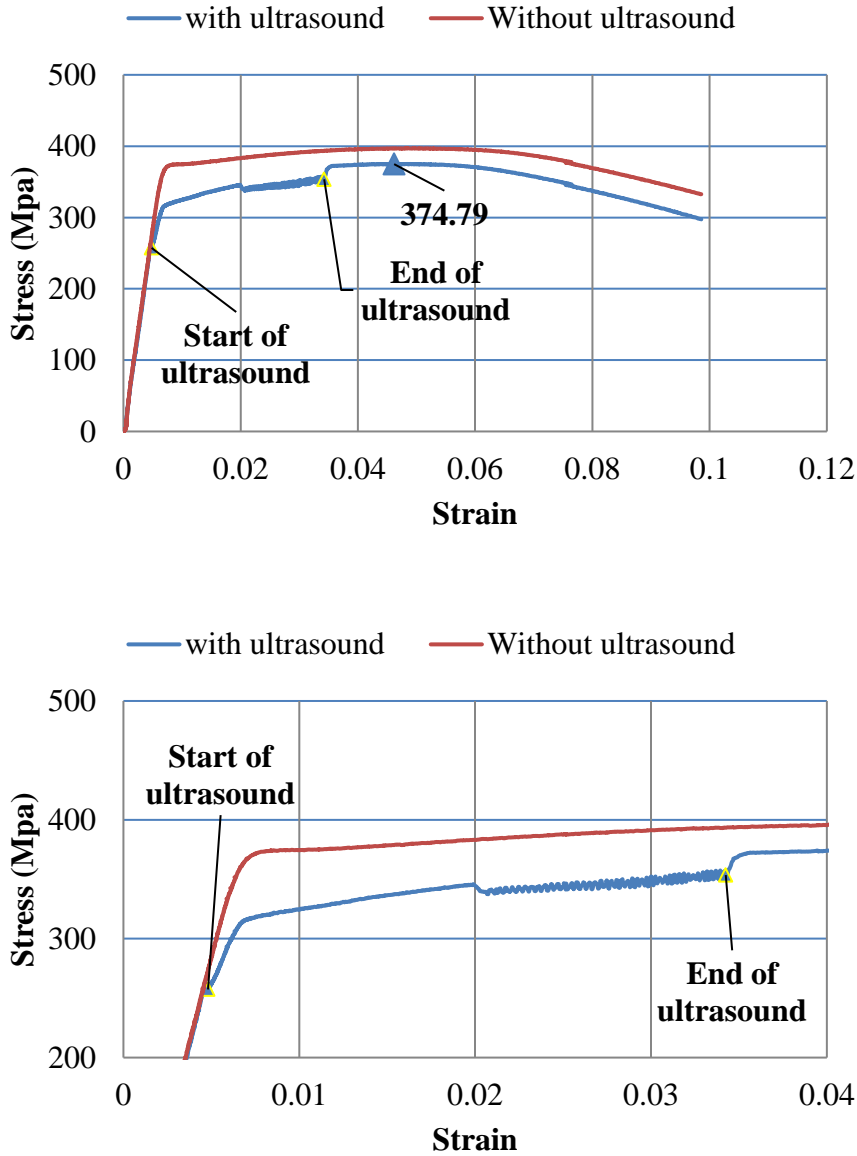


Figure 3.20 Stress strain curve with ultrasonic vibration in plastic deformation region for Aluminum 6061-T6: overview (top) and enlarged view (bottom).

Table 3.3 Comparison of effects of ultrasound applied in elastic and plastic deformation regions

	Acoustic Softening (MPa)	Residual Softening (MPa)	YS (0.2 %) (MPa)	UTS (MPa)
Without Ultrasound	0.00	0.00	372.46	395.12
Ultrasound in Elastic Region	59.45	14.86	348.38	376.58
Ultrasound Close to Plastic Region	29.04	15.64	320.39	375.10

Table 3.4 The repeated tests of effects of ultrasound applied in elastic and plastic deformation regions

Tests	Acoustic Softening (MPa)		Residual Softening (MPa)		Quasi-static Load (MPa)	
	Elastic	Plastic	Elastic	Plastic	YS (0.2%)	UTS
1	50.85	29.62	11.40	11.44	372.43	394.26
2	74.24	45.11	22.68	23.10	373.93	396.98
3	53.29	12.40	10.49	12.39	371.02	394.12
Aver.	59.45	29.04	14.86	15.64	372.46	395.12

Based on the preliminary tests, the following observations can be drawn: 1) the application of ultrasound on a specimen during tensile testing has the effect of reducing the static tensile stress in the stress strain relation, i.e., displays the effect of acoustic softening. 2) The ultrasound reduces the necessary static stress but does not change the slope of the stress strain relation, i.e., the Young's modulus of material in the elastic deformation region

remains the same. 3) The ultrasonic vibration has a *residual softening* effect on the material, i.e., the required static stress causing material to fail is lower after the application of ultrasound.

Following the preliminary tests, more tests were carried out by varying the amplitude of the ultrasound while keeping the other operation parameters unchanged. 26 runs that are completed with success, 6 tests are selected to present their stress strain curves at different amplitudes which lead to different levels of ultrasonic (US) energy input: 0 J, 915J, 2684 J, 3718 J, 5506 J and 6040 J (**Figure 3.20**). By setting the maximum ultrasonic energy input as the 100% energy level, the energy inputs are converted into percentages for clarity. As the ultrasonic energy level increases, the stress reduction increases accordingly and the material becomes “softer”. In the four lowest energy levels, the softening curves show a combined effect of acoustic softening, i.e. stress reduction, and strain hardening. In the other two high energy levels however, the strain hardening diminishes and the curves become straight lines, which are similar to curves reported by Blaha and Langenecker when ultrasonic intensity is large (Langenecker 1963). During the experiment, a thermal camera is used to record the temperature gradient at the acoustic softening spot. Two thermocouples are glued to the surface of the spot to identify the temperature increase. The room temperature is 70 °F (21 °C) and the highest temperature during ultrasonic irradiation is recorded by the thermal couples to be 120 °F (49 °C). No significant temperature increases is recorded by the thermal camera. As a result, the thermal softening effect in the experiments is considered insignificant.

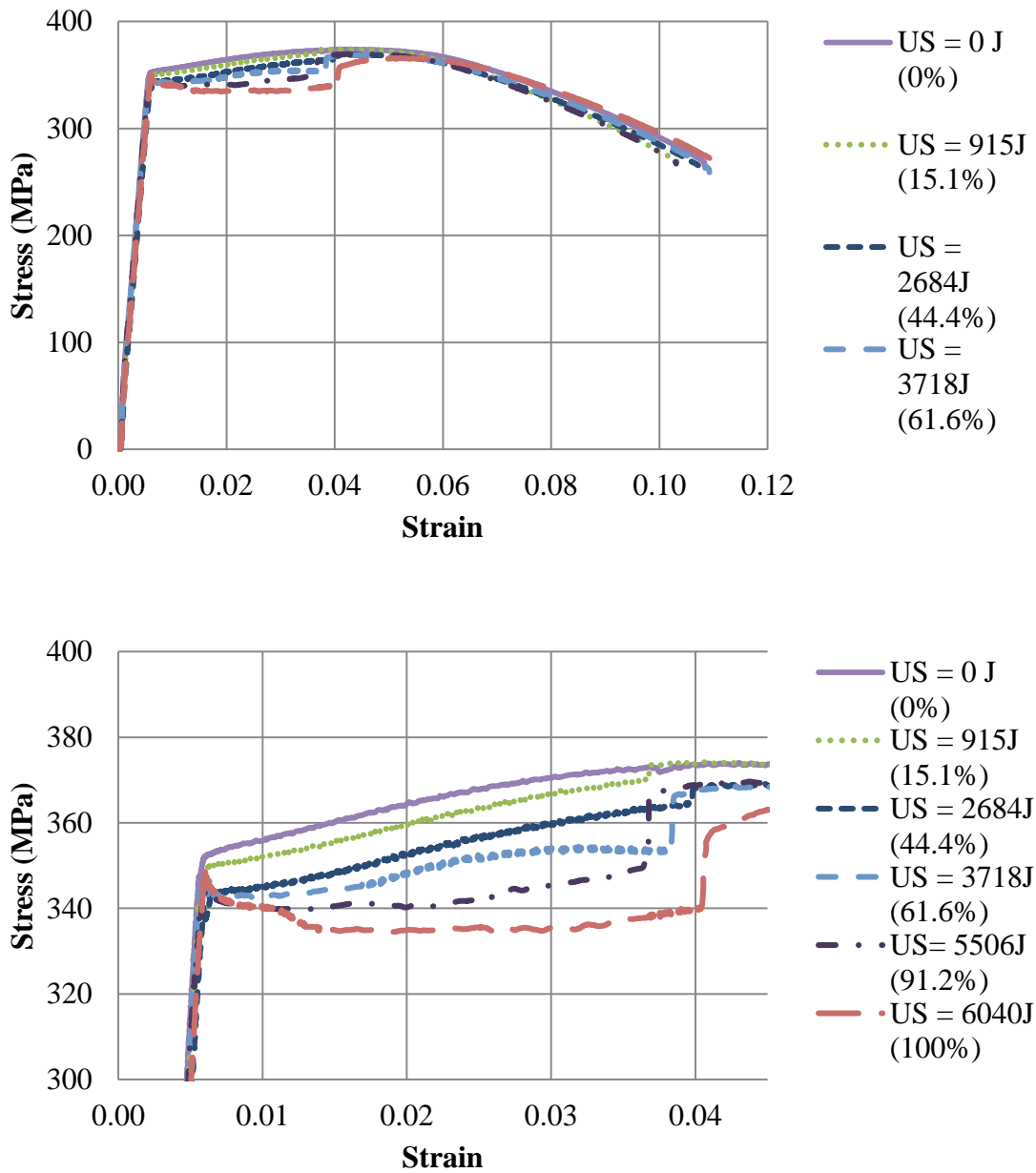


Figure 3.21 The engineering stress-strain relations at different levels of ultrasound (US) (top). The zoom-in of the stress-strain relations to show the details of the softening phenomena (bottom).

Figure 3.21 shows the work hardening rate with true stress-strain curve for Aluminum 6061-T6. As the true plastic strain reaches 0.5, the value of working hardening rate

becomes negative indicating the initiation of necking and the onset of plastic instability. It can be seen from the enlarged view that the application of ultrasound slightly shift the onset point of plastic instability.

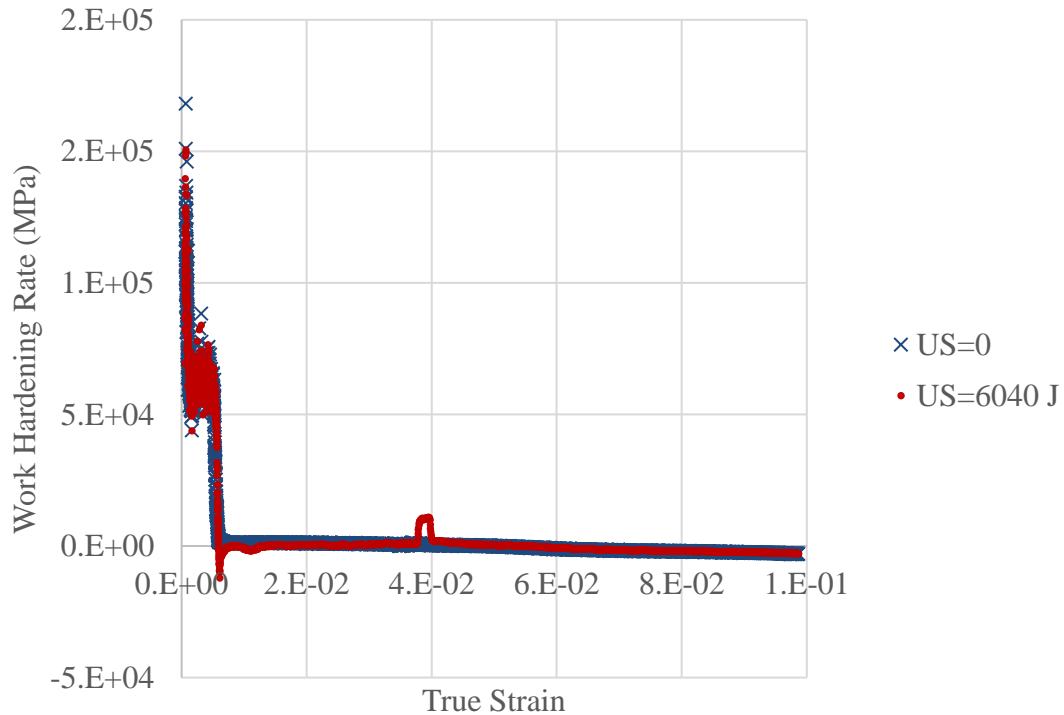


Figure 3.22 The work hardening rate as a function of true strain for Aluminum 6061-T6

In order to better understand the relation between stress reduction and energy input, the engineering stress-strain relations are converted into true stress-strain relations for calculating the stress reduction. The stress reduction is approximated by averaging the reduction at two sampled points ($\epsilon_{tr}=0.02$, $\epsilon_{tr}=0.03$) that are taken from the softening process. The calculation is summarized and shown in **Table 3.5**. It is then plotted against the energy input and a strong linear correlation is shown (**Figure 3.23**).

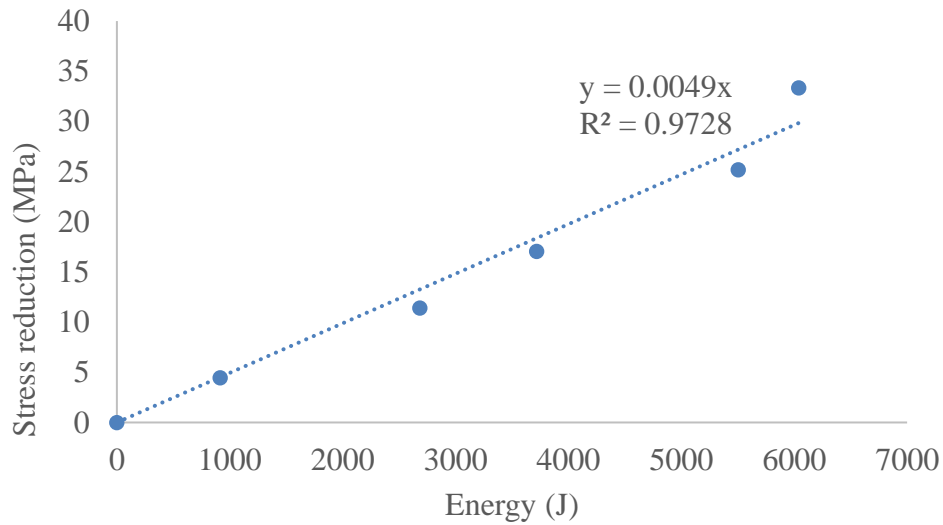


Figure 3.23 The stress reduction as a function of ultrasonic energy input for Aluminum 6061-T6.

Table 3.5 The summary of the calculated stress reduction

Energy level (E_u) (J)	Stress at $\epsilon_{tr} = 0.02$ (MPa)	Stress at $\epsilon_{tr} = 0.03$ (MPa)	Average stress ($\bar{\sigma}$) (MPa)	Averaged stress reduction ($\overline{\Delta\sigma}$) (MPa)	Stress reduction Ratio (η)
0	372.10	381.88	376.99	0	1.00
916	366.95	378.11	372.53	4.45	0.99
2684	359.65	371.52	365.59	11.40	0.97
3718	355.82	364.05	359.94	17.05	0.96
5560	347.34	356.31	351.83	25.16	0.94
6040	341.75	345.55	343.65	33.34	0.92

In summary, the major observations from the effect of ultrasound on Aluminum 6061-T6 include:

1. The ultrasound has the effect of reducing static tensile stress on the stress strain relation.
2. A residual softening effect is observed after the ultrasound is turned off.

3. The stress reduction is observed to be linearly proportional to the ultrasonic energy input.
4. The Young's modulus does not change in the elastic deformation region.

3.3.1.4 Copper 11000-O

For copper 11000-O, a total of 12 tests are successfully carried out and 4 different energy levels are presented in **Figure 3.24**. Residual softening is observed after ultrasound is stopped. A strong linear relation is found between stress reduction and energy input (**Figure 3.25**). The stress reduction and energy input for copper are significantly higher than the other materials (**Figure 3.26**). This is due to the fact that copper has a much higher work hardening rate which leads to higher reduction of stress and higher consumption of ultrasonic energy than the aluminum.

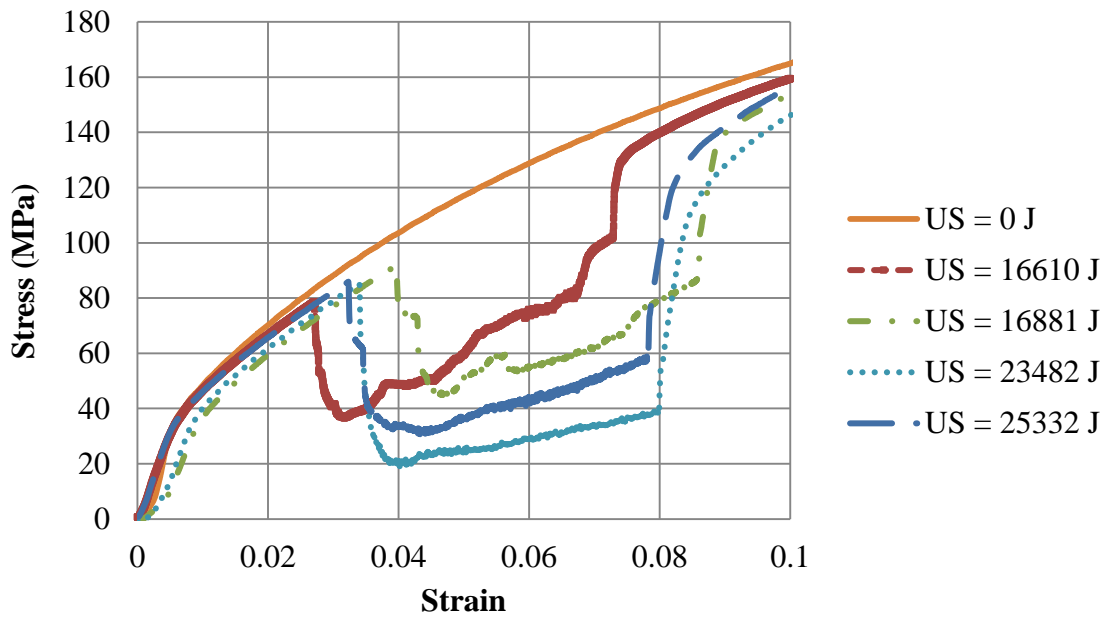
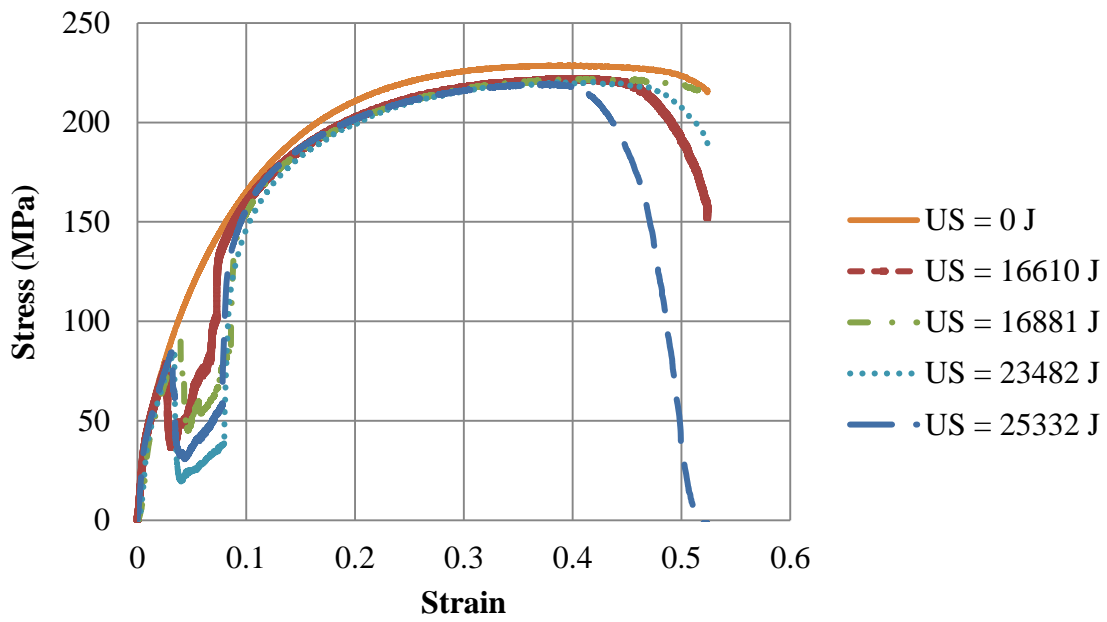


Figure 3.24 The effect of ultrasound on stress-strain curves of Copper 11000-O: overview (top), details of softening (bottom)

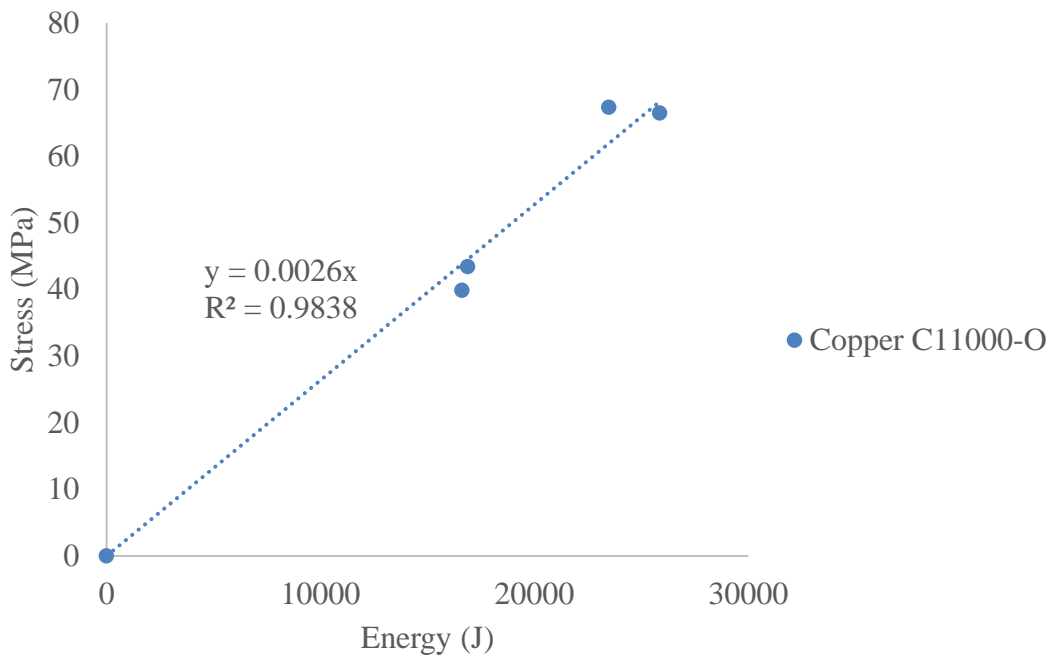


Figure 3.25 The stress reduction versus ultrasonic energy input relation

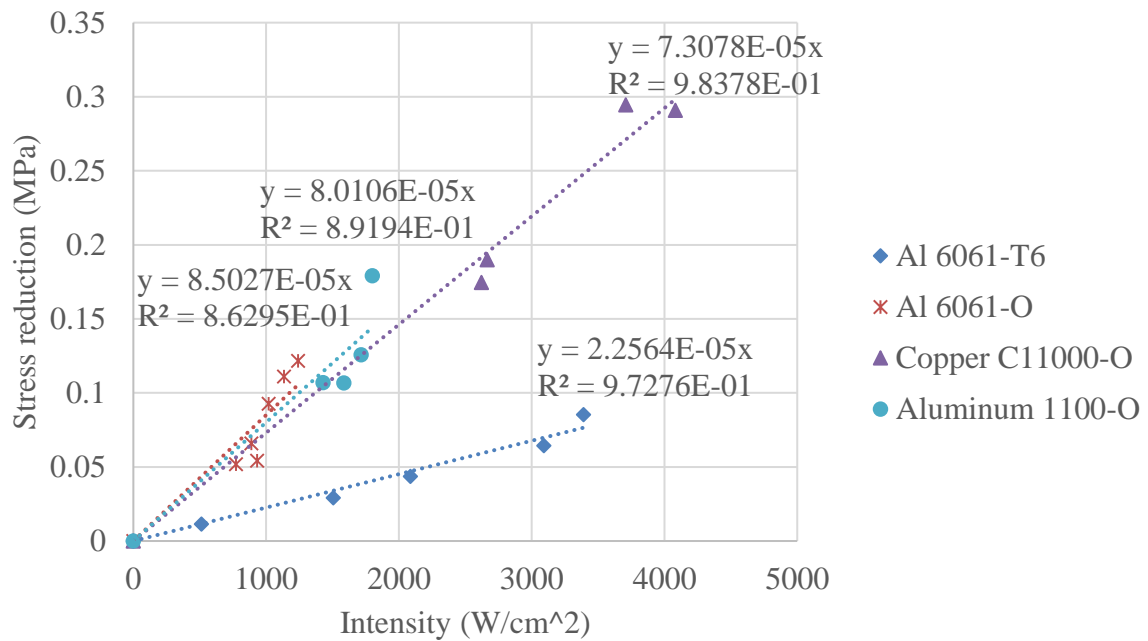


Figure 3.26 The stress-intensity curves of all materials under study

3.3.2 Comparison of Acoustic Softening Among Different Materials

The observations indicate a reduction of flow stresses when the ultrasound is applied in aluminum and copper studied. The reduction is shown to have a strong linear relation to the applied ultrasonic energy. In this section, this relation is compared among different aluminum. Due to the divergences in specimen diameters and ultrasonic irradiation time while testing different materials, the energy (unit: J) is converted to intensity (unit: W/cm^2) so that the effects of irradiation time and specimen dimension are removed. The stress-intensity relations are used for comparison. The differences in stress-intensity relations are discussed based on the qualitative differences in microstructures of the materials.

Before starting the discussion, some features of microstructures in four aluminums are compared in **Table 3.6**.

Table 3.6 The comparison of microstructure of four different aluminum

	Single crystal	1100-O	6061-O	6061-T6
Grain boundary	No	Yes	Yes	Yes
Dislocation Density (m/m^{-3})	10^4	10^5	10^7	10^8
Precipitates	None	None	Incoherent $\beta'(Mg_2Si)$	Coherent $\beta'(Mg_2Si)$

3.3.2.1 Aluminum single crystals and Aluminum 1100-O

Figure 3.27 shows the stress-intensity curves of aluminum single crystals and aluminum 1100-O. The data of single crystals are obtained from the work of Blaha and Langenecker (Langenecker 1963). The aluminum single crystal has 99.993% purity whereas aluminum 1100 is commercially pure with 99% purity. The aluminum single crystal comprises of a single grain with one crystallographic orientation whereas the aluminum 1100 comprises of randomly oriented grains whose orientations vary from crystal to crystal.

Figure 3.27 shows that the single crystal yields much higher stress reduction than the 1100-O does when subjected to ultrasound of same intensity. The difference in stress reduction may be associated with the differences in structures. For aluminum single crystal, the magnitude of stress reduction depends on how the ultrasonic wave is oriented with respect to its slip plane. The reduction is most significant when the direction of the ultrasonic waves is aligned with the slip plane, and least significant when the propagation direction is orthogonal to the slip plane. Specifically, when the single crystal is subjected to a tensile load, its dislocations travel along the slip plane whose direction depends on the crystallographic orientation of the crystal. The tensile stress increases when the traveling dislocations are impeded by obstacles (impurity atoms or other dislocations). If the ultrasound is aligned with the slip plane, the ultrasonic waves facilitate the travel of dislocations by helping them overcome the obstacles, thus causing reduction in tensile stress. In Langenecker's work, the angle between the slip plane and the propagation direction is re-

ported to be $26^\circ \sim 28^\circ$, which indicates that the ultrasound direction has a significant influence on the tensile stress (Blaha and Langenecker 1959a). For polycrystalline aluminum, however, the crystals are more randomly oriented and no favorable orientation can be found for stress reduction. When the dislocation on a favorable slip plane is activated and travels in a grain, it will be constrained by its less-favorably oriented neighbors. As a result, the stress reduction in aluminum 1100 is significantly lower than in aluminum single crystals. In addition to microscopic structures, the energy loss while delivering ultrasonic energy into the specimen could also affect the stress reduction. This loss, however, is difficult to quantify due to the differences in experimental setups.

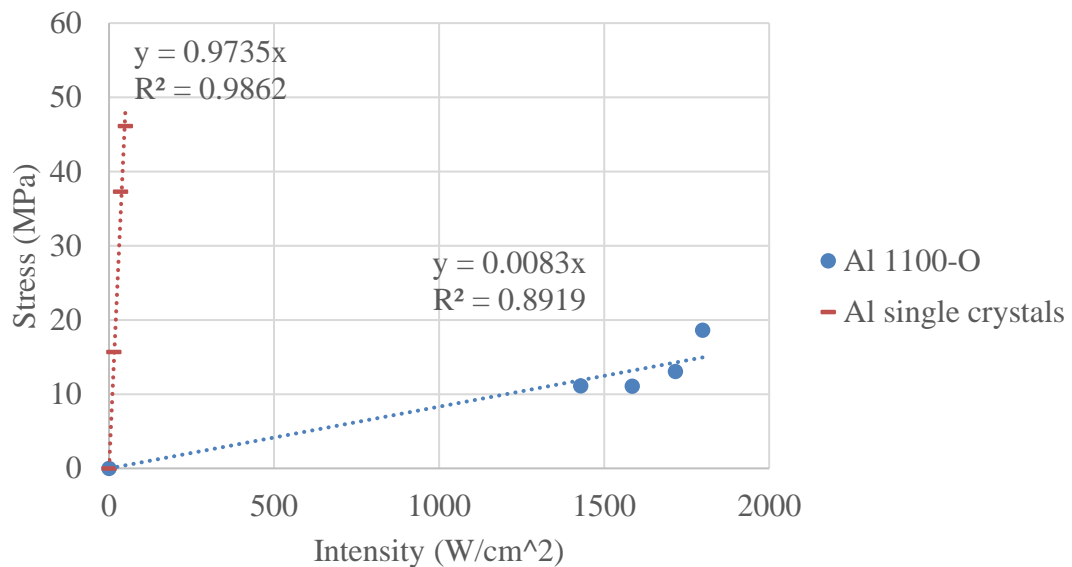


Figure 3.27 Comparison of stress-intensity curves between aluminum single crystals and aluminum 1100-O

3.3.2.2 Comparison between 6061-O and 6061-T6

It is shown in **Figure 3.28** that the stress reduction of aluminum 6061-O is slightly higher than that of aluminum 6061-T6. Since the aluminum 6061-O is obtained by annealing aluminum 6061-T6 to -O state, the chemical compositions of the two materials are the same. The difference in stress reduction is postulated to be caused by the precipitate growth during annealing process. Specifically, the Aluminum 6061-T6 is strengthened by small size ($\sim 100 \text{ \AA}$) precipitates of coherent $\beta'(Mg_2Si)$ which pin dislocations and impede their moving. In the annealing process, the precipitates grow in size and decrease in number. The process is thermodynamically spontaneous due to the fact that large size particles are more energetically stable than small ones. The coherent $\beta'(Mg_2Si)$ become incoherent due to the size increase. The resulted large size precipitates ($\sim 1000 \text{ \AA}$) are less effective in impeding the moving of dislocations. The number of precipitate-dislocation interactions is also reduced due to the reduction in the number of precipitates. Moreover, the precipitates diffuse from inside the grain towards the grain boundaries, leading to less impediments to dislocations. As a result, the acoustic softening is more significant in aluminum 6061-O than in aluminum 6061-T6.

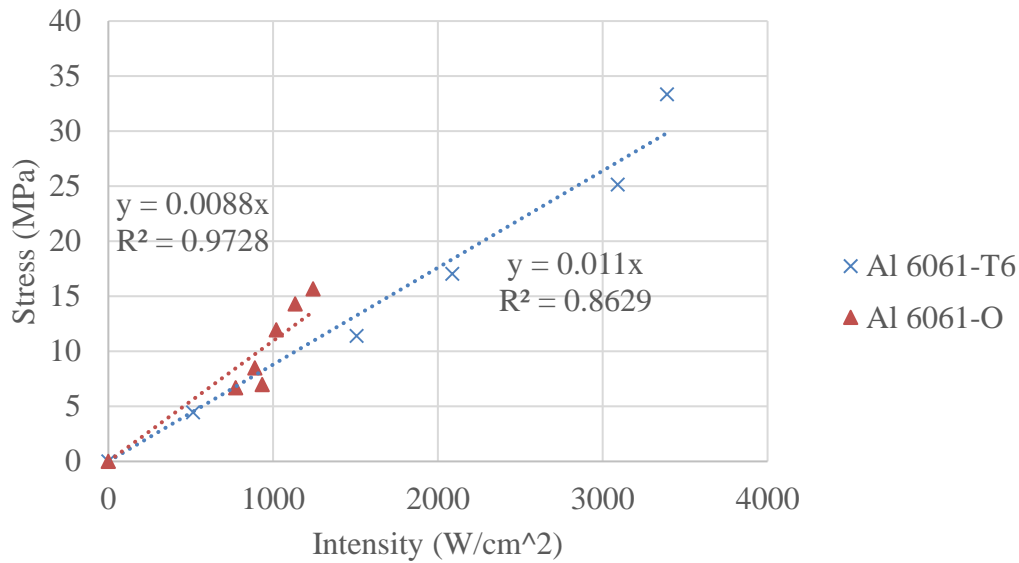


Figure 3.28 Comparison of stress-intensity curves between Aluminum 6061-T6 and Aluminum 6061-O

3.3.2.3 Comparison between 1100-O and 6061-O

The stress-intensity curves of aluminum 6061-O is compared to that of aluminum 1100-O in **Figure 3.29**. Both materials have polycrystalline structures and are in annealed state. The 1100-O is commercially pure with 99% purity and 1 % tramp elements (iron and silicon) whereas the 6061-O has 95% purity and alloy elements (Magnesium, Silicon, Chromium, etc.). Due to the fact that the aluminum 6061-O is obtained by annealing aluminum 6061-T6, there exist precipitates incoherent β' (Mg_2Si). The size of the precipitates are larger than those in aluminum 6061-T6 and the distribution of the precipitates are close to grain boundaries. In contrast, the aluminum 1100-O has no precipitates but only small amount of inclusions. Both materials has certain amount of dislocations. The grain size of

aluminum 6061-O is smaller than aluminum 1100-O. Based on the comparison, the aluminum 1100-O is expected to yield greater stress reduction than aluminum 6061-O due to its lack of precipitates strengthening and larger grain size. However, this is assumption deviates from our experimental observation which shows higher stress reduction in aluminum 6061-O than in aluminum 1100-O. The cause of such divergence is unclear at this point. Further investigation into the microstructure of the materials is required to understand the underlying mechanisms. This could be a part of the future work.

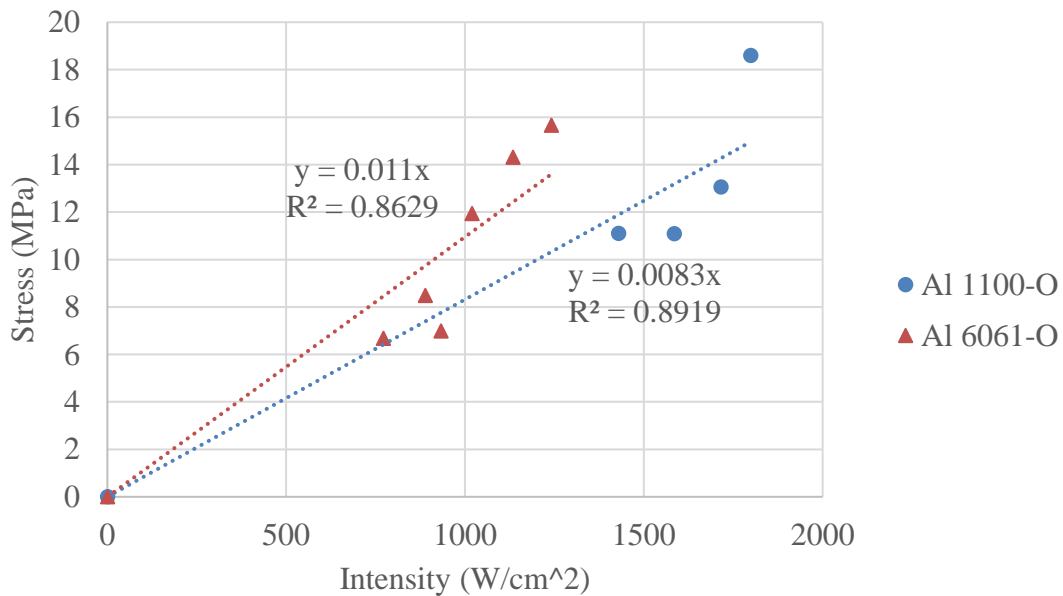


Figure 3.29 Comparison of stress-intensity curves between Aluminum 1100-O and Aluminum 6061-O

3.4 Analytical Model of Acoustic Softening

Based on the experimental observations, the linear correlation between stress reduction and ultrasonic intensity input is characterized using an analytical model;

$$\frac{\bar{\sigma}}{\bar{\sigma}_0} = 1 - dI_u \quad (3.1)$$

Where $\bar{\sigma}$ is the flow stress under ultrasonic irradiation, $\bar{\sigma}_0$ is the reference flow stress without ultrasonic irradiation, I_u is the ultrasound intensity which can be derived from the experiment, and d is a constant that fits the model to experimental data. At room temperature, the values of d for the four different materials are shown in **Table 3.8**. In the UAM process, while the sonotrode amplitude is known, a direct measure of ultrasonic energy is not applicable. Therefore a relation is introduced to estimate the oscillation magnitude of the ultrasonic field based on the ultrasound intensity. The relation is derived based on the definition of sound intensity and is written as (Frederick 1965):

$$I_u = \rho \bar{A}^2 \omega^2 c \quad (3.2)$$

Where \bar{A} is the equivalent oscillation amplitude of the ultrasound field. ρ is the density of the medium, c is the speed of sound in the medium, and ω is the angular frequency of the ultrasound, defined as $\omega = 2\pi f$. f is the frequency of ultrasound and is fixed at 20 kHz. Since the bonding interface is very close to the sonotrode surface (roughly 0.1 mm), it is assumed that in UAM the oscillation amplitude of the ultrasonic field is the same as the amplitude of the sonotrode. Consequently, the ultrasound intensity can be characterized using vibration amplitude. This characterization relies on the assumption that the amplitude of the ultrasound at the bonding interface equals the vibration amplitude of the sonotrode. In reality, however, intermittent slip takes place between the sonotrode and the top foil as well as between the top foil and the built feature, which leads to an overestimation of the

energy input at the bonding interface. On the other hand, the acoustic softening effect of the ultrasonic energy is underestimated in our experimental investigation due to the fact that a portion of the delivered ultrasonic energy is dissipated in the supporting frame rather than the in the specimen.

Table 3.7 The value of model constant d for different materials

	Aluminum 6061-T6	Aluminum 6061-O	Aluminum 1100-O	Copper 11000-O
Value of d (cm^2/W)	2.2564E-05	8.5027E-05	8.0106E-05	7.3078E-05

The following chapter shows how the acoustic softening model is accounted in a plasticity framework. Besides acoustic softening, other influential factors of plastic deformation are also taken into consideration.

Chapter 4

4 A Plasticity Model for UAM

As is shown in the literature review (section 2.2.2), the plastic deformation is affected by a number of factors: ultrasonic energy, plastic strain rate, temperature, friction, and dynamics. Among these factors, ultrasonic energy, plastic strain rate, and temperature have a direct influence on material plasticity. The ultrasonic energy and temperature cause acoustic and thermal softening whereas the high strain rate causes strain rate hardening in materials. The existing plasticity models such as the power law model (GS Kelly and Advani 2013), cyclic plasticity model (A. Siddiq and Ghassemieh 2008a), crystal plasticity model (Amir Siddiq and Sayed 2012), or the dislocation-based crystal plasticity model (Pal and Stucker 2012) are either phenomenological models that are too simple to account for all the effects or physically based models that are too complicated to be sufficiently supported and validated by experimental data. As a result, an appropriate plasticity model needs to be selected or tailored such that it is capable to account for all the unique effects of UAM, and at the same time, be simple enough to be validated by the existing experimental data. As a result, the Johnson-Cook model is selected to serve this purpose. The Johnson-Cook model is effective in modeling large deformations, high strain rates, and

high temperatures (G. Johnson and Cook 1983). The model is phenomenological, which indicates that it is difficult to interpret the physics behind the plasticity behavior. For the same reason, however, it has a relatively simple mathematical form and does not require excessive data from microscopic studies to be able to represent the macroscopic plasticity. The Johnson-Cook model is a particular type of von Mises plasticity model with an explicit form of hardening law and rate dependence. The original Johnson-Cook model is based on the equation (G. Johnson and Cook 1983):

$$\sigma = (A + B\bar{\epsilon}^n)(1 + C \ln \frac{\dot{\epsilon}}{\dot{\epsilon}_0})(1 - T^{*m}) \quad (4.1)$$

Where $\bar{\epsilon}$ is the equivalent plastic strain, $\dot{\epsilon}$ is the equivalent plastic strain rate, $\dot{\epsilon}_0$ is a reference equivalent plastic strain rate defined as: $\dot{\epsilon}_0 = 1 \text{ s}^{-1}$. A is the yield strength measured at room temperature as $\bar{\epsilon} = 0 \text{ s}^{-1}$ and $\dot{\epsilon} = \dot{\epsilon}_0$. B is the strain-hardening constant; n the strain-hardening exponent, C the strain-rate hardening constant, m the thermal-softening exponent, and T^* is a nondimensionalized temperature defined as: $T^* = \frac{T - T_{room}}{T_{melt} - T_{room}}$, where T_{room} is the room temperature and T_{melt} is the melting temperature of the material. The different terms on the right hand side of equation (4.1) are associated to different effects. The first bracketed term is associated to strain hardening, the second term to strain rate hardening, and the third term to softening at elevated temperature. At room temperature ($T = 20 \text{ }^\circ\text{C}$), zero strain ($\bar{\epsilon}^n = 0 \text{ s}^{-1}$), and reference strain rate ($\dot{\epsilon} = \dot{\epsilon}_0$), the JC model is reduced to:

$$\sigma = A + B\bar{\epsilon}^n \quad (4.2)$$

Based on quasi-static tests, a set of material parameters for aluminum 6061 under -T6 and -O conditions are identified and shown in **Table 4.1**. The comparison between model prediction and experimental data are shown in **Figure 4.1**.

Table 4.1 JC model constants for Aluminum 6061 –T6 and -O

Aluminum 6061	<i>A</i> /MPa	<i>B</i> /MPa	<i>n</i>
-T6	311.22	240.11	0.28
-O	55.00	165.35	0.40

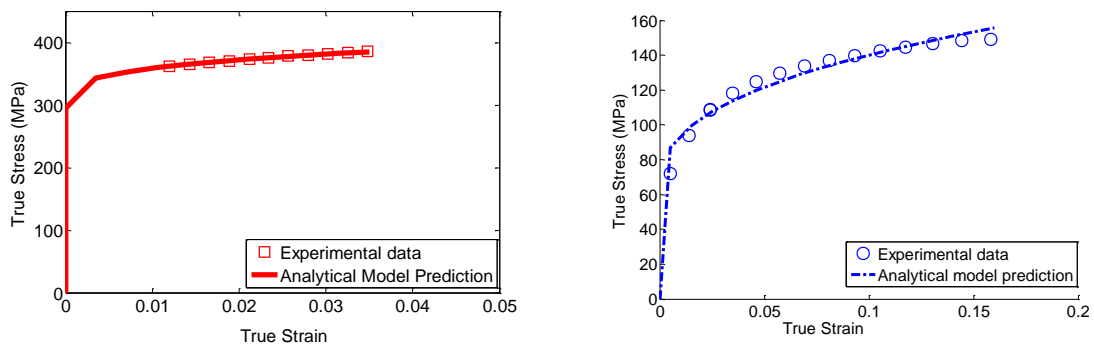


Figure 4.1 The comparison of experimental data and model prediction for Aluminum 6061 -T6 (left) and –O (right).

The Johnson-Cook model, despite its modeling advantages and mathematical simplicity, fails to predict the stress with accuracy when high strain rate (beyond 10^3 s^{-1}) and ultrasound-induced softening are involved (Lesuer, Kay, and LeBlanc 2001; Sakino 2006). Therefore, the original JC model is modified to tackle these issues and the modifications are detailed in the following two sections.

4.1 Strain Rate Hardening

The existence of high strain rate ($10^3 \text{ s}^{-1} \sim 10^5 \text{ s}^{-1}$) deformation in UAM has been demonstrated by several researchers (Gunduz et al. 2005; Sriraman et al. 2011; Sriraman, Babu, and Short 2010; Yang, Janaki Ram, and Stucker 2009). In this study, the strain rate is estimated based on two assumptions: 1) there is no slip between the sonotrode and the top surface of the top foil, i.e. the top surface and the sonotrode move together, and 2) the bottom surface of the top foil is fully welded to the built feature and undergoes no displacement. These two assumptions define an extreme deformation case for the top foil and would not be satisfied simultaneously most of the time. However, with these assumptions, an upper limit of the strain rate can be estimated in order to define the range within which the strain rate varies. The sonotrode amplitude A is between 5 to 40 μm while the thickness of the top foil t is 150 μm . The sonotrode frequency is $f = 20 \text{ kHz}$. As a result, the maximum shear strain γ_{max} and maximum strain rate $\dot{\gamma}_{max}$ in the top foil can be estimated as:

$$\gamma_{max} = \frac{A}{t} \quad (4.3)$$

$$\dot{\gamma}_{max} = \omega\gamma_{max} = 2\pi f\gamma_{max} \quad (4.4)$$

An similar estimation is used in the work by Sriraman et al. (Sriraman et al. 2011): The maximum shear strain rate is estimated to be between 4.2×10^3 and $3.4 \times 10^4 \text{ s}^{-1}$. While the strain rate hardening at low strain rate is well captured by the standard JC model, it starts to increase dramatically at high strain rate, which is beyond the modeling scope of the standard JC model. It has been shown in multiple experimental investigations that metals with face-centered-cubic (f.c.c.) structures demonstrate a dramatic increase of the dependence of dynamic flow stress on the instantaneous strain rate as it exceeds a certain

threshold (typically around 10^2 s^{-1}) (Lesuer, Kay, and LeBlanc 2001; Sakino 2006; Yadav and Chichili 1995). This change of strain rate sensitivity is due to the change of deformation mechanism. At low strain rate, the deformation is governed by the cutting or by-passing of obstacles (such as other dislocations, point defects, or precipitates, etc.) by the dislocations. As the strain rate exceeds the threshold, the deformation starts to be controlled by phonon drag forces and the flow stress necessary to deform the material increases abruptly.

Based on the change of mechanism, Lesuer et al. proposed two strain rate hardening models which yield satisfactory predictions at low and high strain rates (Lesuer, Kay, and LeBlanc 2001). However, at intermediate strain rate ($10^3 \text{ s}^{-1} \sim 10^4 \text{ s}^{-1}$) between low and high strain rates, the model predicts an abrupt change in stress which deviates from the real case. In the real deformation, the transition of mechanism will not take place in all forest dislocations simultaneously and therefore the sharp turn prediction is physically unrealistic (Lesuer, Kay, and LeBlanc 2001). This intermediate strain rate overlaps well with the UAM strain rate. However, no feasible model has been found in the literature that captures the strain rate hardening at the intermediate strain rate. As a result, a strain rate hardening model is developed based on the experimental data presented by Yadav and Chichili (Yadav and Chichili 1995) (**Figure 4.2**).

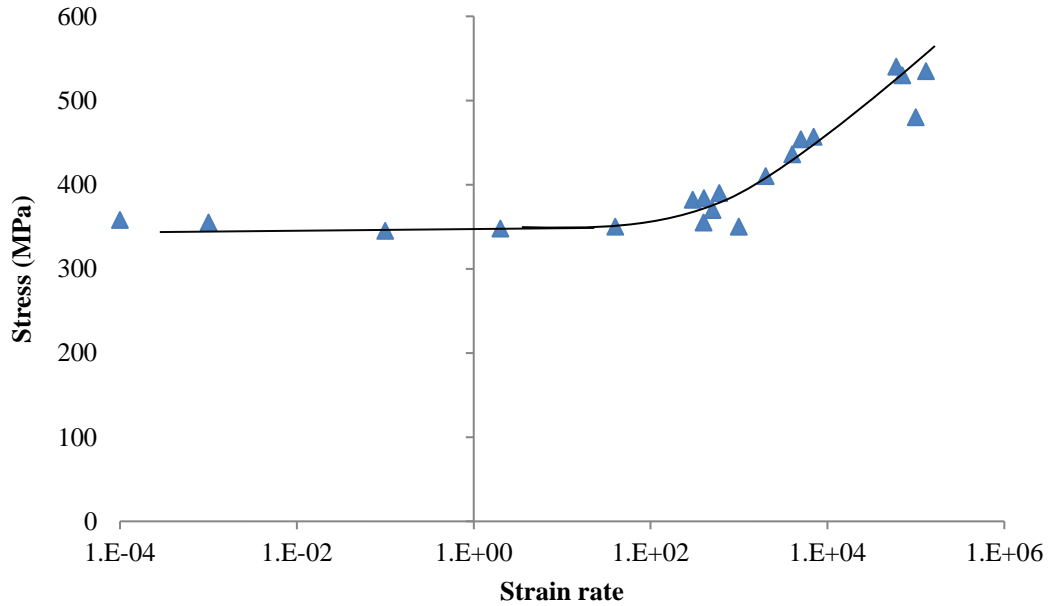


Figure 4.2 The strain rate sensitivity diagram reproduced from Yadav and Chichili (Yadav and Chichili 1995)

Yadav and Chichili collected rate sensitivity data for aluminum 6061-T6 from multiple studies (Yadav and Chichili 1995). Their data are adopted for model development since most of the data fall in the intermediate strain rate ($10^3 \text{ s}^{-1} \sim 10^4 \text{ s}^{-1}$) range. **Figure 4.2** shows that the flow stress is not sensitive to strain rate when it falls below 40 s^{-1} . Beyond the threshold of 40 s^{-1} , the stress starts to increase at an increasing rate. Notice that the rate sensitivity diagram is plotted with the strain rate being evaluated in logarithmic scale. If evaluated in regular scale, the stress-strain relation follows a power law function. Since the developed model applies only to intermediate strain rate which is not a large span of strain rate, a power law model can be introduced as:

$$\frac{\bar{\sigma}}{\sigma_0} = C + D \left(\frac{\dot{\epsilon}}{\dot{\epsilon}_{th}} \right)^p \quad (4.5)$$

Where $\bar{\sigma}_0$ is the reference yield stress evaluated at the reference strain rate $\dot{\bar{\epsilon}}_0$ and at room temperature. The reference strain rate is set to the rate sensitivity threshold $\dot{\bar{\epsilon}}_{th} = 40 \text{ s}^{-1}$. The same model is also applied to Aluminum 6061-O and the constants are identified based on the experiemntal data of Sakino and Ogawa (Ogawa 2002; Sakino 2006). The rate sensitivity threshold is set to $\dot{\bar{\epsilon}}_{th} = 100 \text{ s}^{-1}$. When the strain rate $\dot{\bar{\epsilon}}$ is less than or equal to $\dot{\bar{\epsilon}}_{th}$, its value is set equal to $\dot{\bar{\epsilon}}_{th}$ in equation (4.6), leading to a strain rate hardening factor of unity; when the strain rate is greater than $\dot{\bar{\epsilon}}_{th}$, its actual value is used in equation 4.12 for calculating the hardening factor. The relation is written as:

$$\frac{\bar{\sigma}}{\bar{\sigma}_0} = \begin{cases} C + D(1)^p, & \text{if } \dot{\bar{\epsilon}} \leq \dot{\bar{\epsilon}}_{th} \\ C + D\left(\frac{\dot{\bar{\epsilon}}}{\dot{\bar{\epsilon}}_{th}}\right)^p, & \text{if } \dot{\bar{\epsilon}} > \dot{\bar{\epsilon}}_{th} \end{cases} \quad (4.6)$$

C , D , and p are constants whose values are determined by fitting the model to the experimental data. From equation (4.6) it can seen that C , D determine the intial strain rate hardening whereas D , p determine the hardening rate. The values of C , D , and p for Aluminum 6061-O and 6061-T6 are shown in **Table 4.2**. The predictions from the proposed model are compared with the experimental data for validation (**Figure 4.3**).

Table 4.2 JC model parameter values for aluminum 6061-T6 and -O

Aluminum 6061	C	D	p
-T6	0.46	0.49	0.10
-O	0.77	0.39	0.22

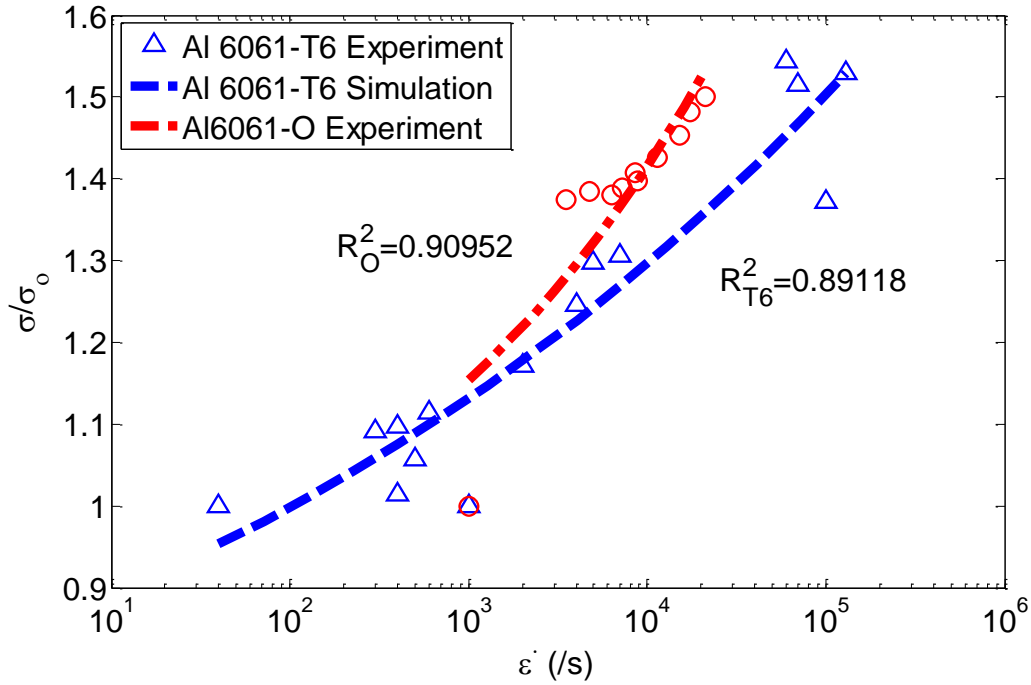


Figure 4.3 The strain rate sensitivity comparison between model prediction and experimental data for aluminum 6061-T6 and aluminum (Ogawa 2002; Sakino 2006; Yadav and Chichili 1995).

Once the strain rate model is established, it is introduced into the Johnson-Cook model to replace the original strain rate hardening term. According to Yadav et al., the shapes of the stress-strain curves are identical at high strain rates, indicating that the strain rate hardening term is not coupled to the strain hardening term (Yadav and Chichili 1995). As a result, the modified Johnson-Cook model (thus far) is written as:

$$\sigma = (A + B\bar{\epsilon}^n) \left\{ C + D \left(\frac{\dot{\epsilon}}{\dot{\epsilon}_{th}} \right)^p \right\} (1 - T^*m) \quad (4.7)$$

The modified model is evaluated at various strain rates which range between the reference strain rate and $100,000 \text{ s}^{-1}$ for both Aluminum 6061-T6 and Aluminum 6061-O (**Figure 4.4**).

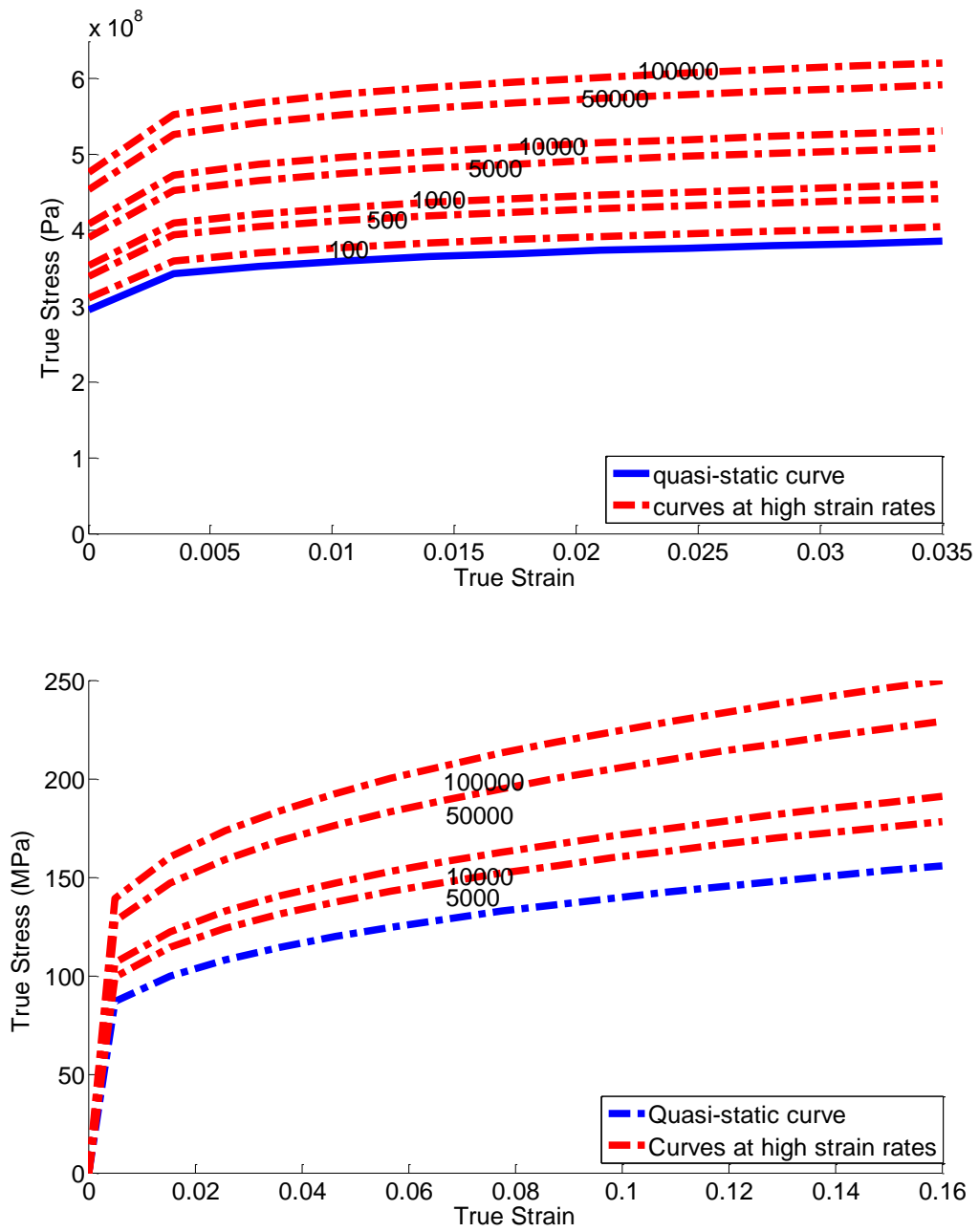


Figure 4.4 The effect of strain rate hardening in Aluminum 6061-T6 (top) and -O (bottom)

4.2 Acoustic Softening

The development of an analytical model for the acoustic softening effect has been presented in the previous chapter (Section 3.4) and is not repeated here. The analytical model is introduced into the Johnson-Cook model and the modified model is written as follows:

$$\sigma = (1 - dI_u)(A + B\bar{\varepsilon}^n)\left\{C + D\left(\frac{\dot{\varepsilon}}{\dot{\varepsilon}_{th}}\right)^p\right\}(1 - T^{*m}) \quad (4.8)$$

The values of constant d in acoustic softening term for Aluminum 6061-T6 and -O are shown in **Table 4.3**. The term associates stress reduction to energy intensity based on our study of acoustic softening. In the UAM process, however, a direct measure of ultrasonic intensity is not possible but the sonotrode amplitude is known. Therefore a relation is introduced to estimate the oscillation magnitude of the ultrasonic field based on the ultrasound intensity. The equation is already presented in the previous chapter and is repeated here:

$$I_u = \rho \bar{A}^2 \omega^2 c \quad (4.9)$$

This equation is obtained as follows. Based on the definition of sound intensity:

$$I = p \cdot v \quad (4.10)$$

where p is the acoustic pressure, and v is the particle velocity of the ultrasonic wave. The acoustic pressure traveling through a solid can be calculated using the equation (Lindsay 1960):

$$p = \rho \omega A c \quad (4.11)$$

where ρ is density, A is particle amplitude, ω is circular frequency, and c is the ultrasound wave speed in the solid medium. Assuming the displacement of the particle to be $x = A\cos(\omega t)$, the particle velocity can be derived as:

$$v = \frac{dx}{dt} = -\omega A \sin(\omega t) \quad (4.12)$$

The magnitude of the particle velocity is $v = \omega A$. As a result, the ultrasound intensity is written:

$$I_u = \rho \omega^2 A^2 c \quad (4.13)$$

Based on equation (4.19), the ultrasound intensity is characterized using equivalent amplitudes so that a relation between stress reduction and amplitude can be established. The acoustic softening effect is evaluated at different amplitudes by assuming a reference strain rate and room temperature. The stress-strain curves are shown in **Figure 4.5**.

Table 4.3 The acoustic softening constants for aluminum 6061-T6 and -O

Aluminum 6061	d (cm²/W)
-T6	2.2564E-05
-O	8.5027E-05

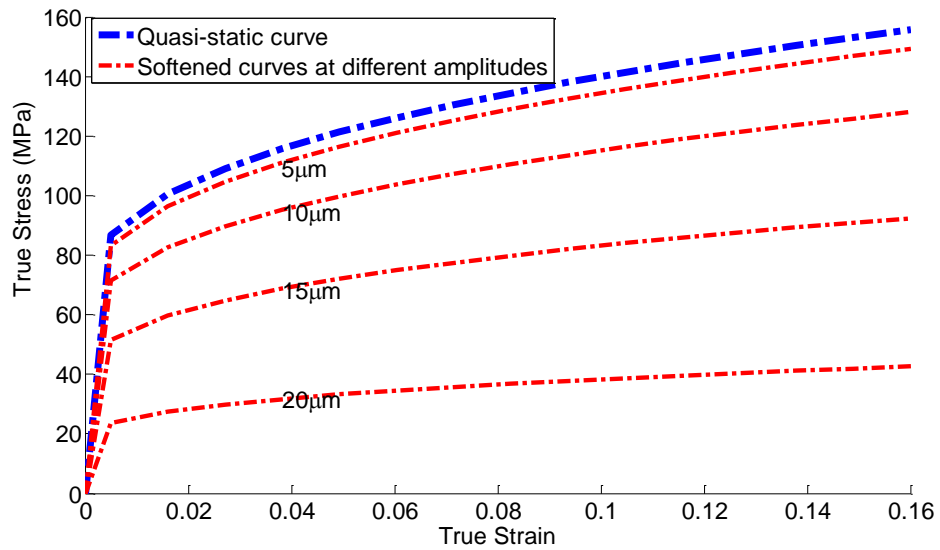
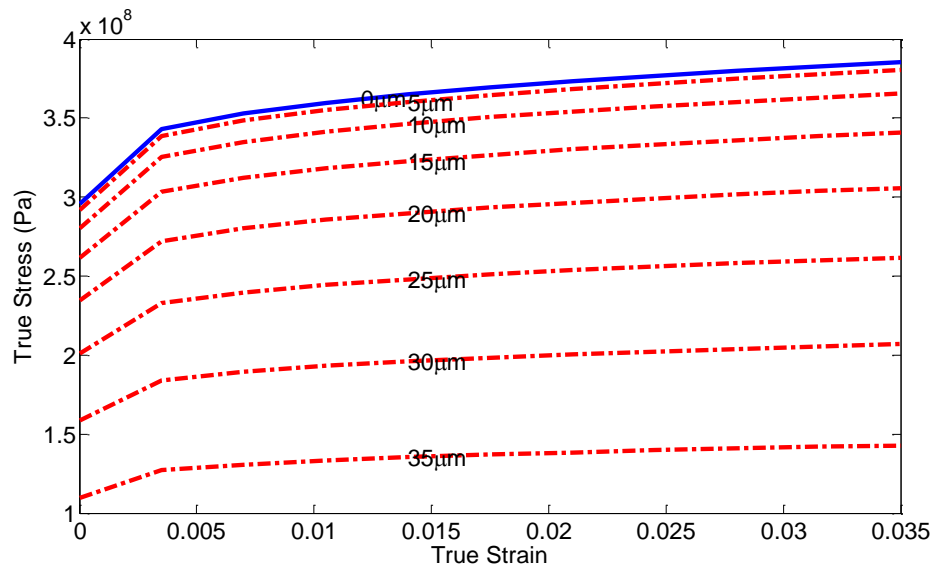


Figure 4.5 The acoustic softening for Aluminum 6061-T6 (top) and -O (bottom).

4.3 Thermal Softening

The effect of temperature on aluminum 6061-T6 and -O is discussed in this section. It has been shown that the mechanical strength of metals that undergo an aging process

exhibit strong dependencies on temperature (Epler 2004). For aluminum 6061-T6, the typical T6 hardening treatment process involves the solution treatment at around 810 K which is followed by quenching and artificial aging. The solution heat treatment enables the solid solution to be supersaturated homogeneously. The quenching process then takes the supersaturated solid solution to a two-phase region of the phase diagram. In the aging step, the magnesium silicide (Mg_2Si) phase is precipitated and evenly distributed inside the grains. The precipitated particles strengthen the alloy by pinning the dislocations and impeding their motion. When the temperature increases, however, the precipitates start to diffuse towards the grain boundaries, thus decreasing the strength of aluminum 6061-T6 significantly.

In contrast, aluminum 6061-O does not show so significant temperature dependence as the aluminum 6061-T6. The aluminum 6061-O is annealed from aluminum 6061-T6 and therefore it also has precipitates Mg_2Si . However, during annealing, these Mg_2Si particles increase in sizes and decrease in density, leading to a reduction in the number of dislocation-precipitate interactions and therefore a reduction in strengthening. As a result, the yield stress of the aluminum 6061-O is much lower than that of aluminum 6061-T6. When aluminum 6061-O is heated, the size and density of the precipitates barely change and therefore no significant change in strength is shown. **Figure 4.6** shows how the Aluminum-O and -T6 depend on temperature. In the UAM process, the substrate that fixes the built feature is heated to 300°F (around 150 °C). However, the local temperature at the bonding interface could be higher due to heat dissipation from interfacial friction and severe plastic deformation.

In the modified Johnson-Cook model, the temperature dependencies for aluminum 6061-O and -T6 behave differently. The temperature dependence for Aluminum 6061-T6 is shown throughout the tested temperature range whereas for -O, it can be seen when the temperature exceeds 200 °C. Specifically, when the temperature is below 200 °C, the nondimensionalized temperature T^* is set to zero by letting $T = T_{room}$ and the thermal softening term to be unity; when temperature is above 200 °C, the thermal softening is introduced using the term:

$$\frac{\bar{\sigma}}{\bar{\sigma}_0} = 1 - T^{*m} \quad (4.14)$$

At this point, the reference temperature is no longer the room temperature but the temperature threshold beyond which thermal softening starts to take effect. As a result, the temperature threshold $T = 205$ °C is set as the new “room temperature” for calculating the softening term. The values in the thermal softening exponent are identified based on fitting the model to experimental data. The values of the exponent are summarized in **Table 4.4** together with the associated room (reference) temperature and melt temperature of the material. **Figure 4.7** shows the comparison between the prediction from the softening term and the experimental data. The term in the original Johnson-Cook model is shown to be effective in capturing the stress reduction and therefore is kept without any modification.

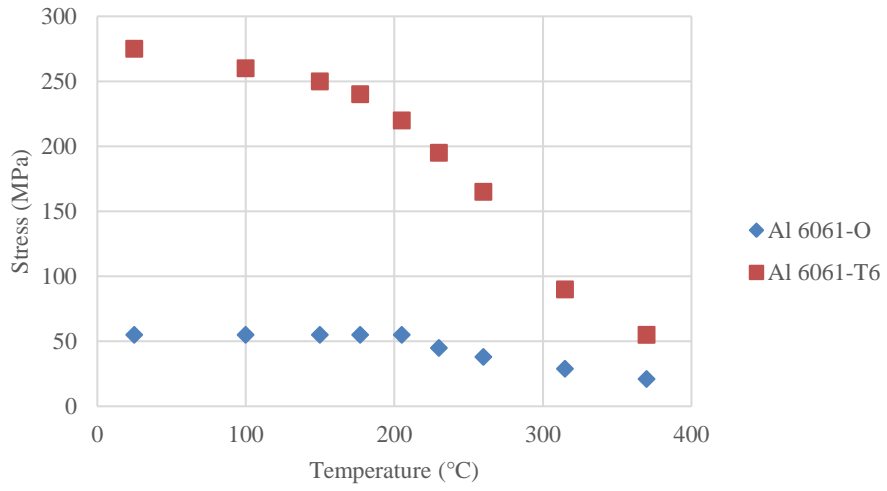
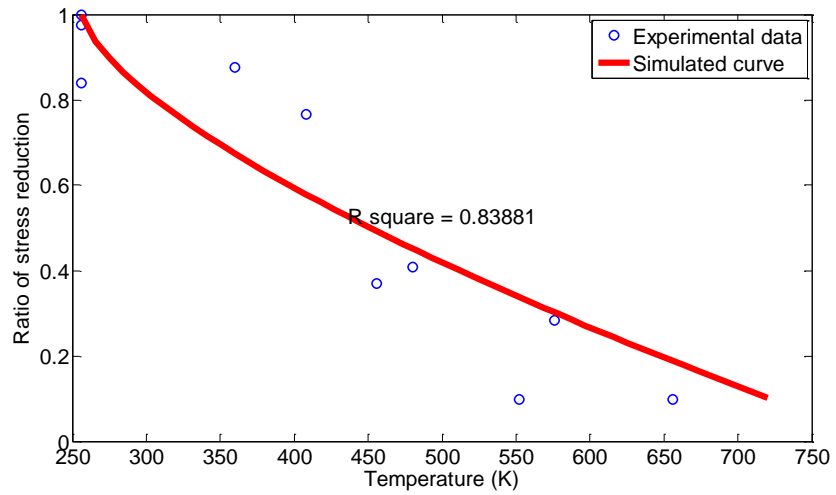


Figure 4.6 The temperature dependencies of Aluminum 6061-O and T6 (Kaufman 1999).



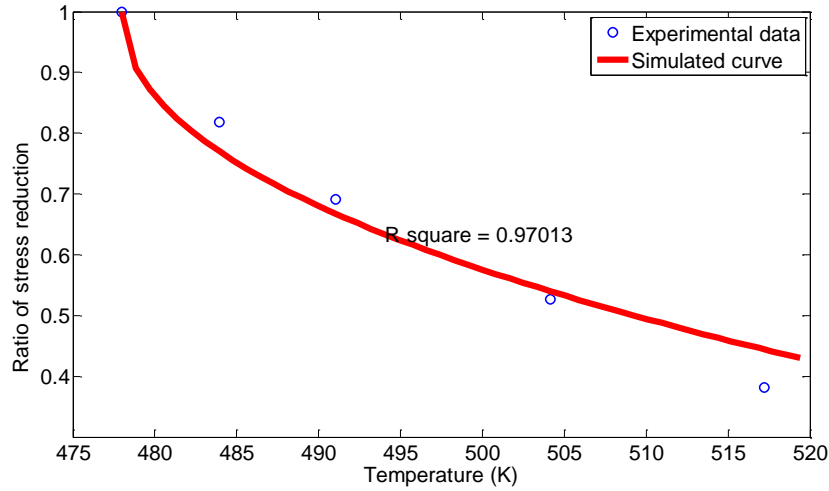


Figure 4.7 The comparison between model prediction and experimental data for thermal softening in Aluminum 6061 -T6 (top) and -O (bottom)

Table 4.4 The values of thermal exponent for Aluminum 6061-T6 and -O.

Aluminum 6061	m	Reference Temperature (°C)	Melting temperature (°C)
-T6	0.4668	25	889
-O	0.6779	205	616

4.4 Summary

To summarize, a plasticity model is proposed by modifying the Johnson-Cook model in order to capture the unique effects of ultrasound. The final form of the modified Johnson model is presented as follows:

$$\sigma = (1 - dI_u)(A + B\bar{\epsilon}^n)\left\{C + D\left(\frac{\dot{\bar{\epsilon}}}{\dot{\bar{\epsilon}}_{th}}\right)^p\right\}(1 - T^{*m}) \quad (4.21)$$

In equation (4.21), the constants A , B , and n are determined to characterize the strain hardening effect based on the quasi-static tensile tests carried out for Aluminum 6061-T6 and

-O. The constants C , D , p are determined for a power law model that captures the hardening at intermediate strain rate ($10^3 \text{ s}^{-1} \sim 10^4 \text{ s}^{-1}$) based on the experimental data in the literature. The acoustic softening is studied by carrying out experiments on the two materials. A linear relation is found between stress reduction and ultrasound intensity and constant d is identified for the relation. The thermal softening effect in Aluminum 6061-T6 and -O are studied and the values of constant d are determined accordingly. The new constants associated to the modified Johnson-Cook model are shown in **Table 4.5**. The changes made in the modified Johnson-Cook model are summarized in **Table 4.6**.

Table 4.5 Constants for the modified Johnson-Cook model

Al	$A(\text{MPa})$	$B(\text{MPa})$	n	C	D	p	$d(\text{cm}^2/\text{W})$	m
-T6	311.22	240.11	0.28	0.46	0.49	0.10	2.2564E-05	0.47
-O	55.00	165.35	0.40	0.77	0.39	0.22	8.5027E-05	0.68

Table 4.6 Comparison between the original and the modified Johnson-Cook models.

	Classical JC model	Modified JC model
Strain hardening	Characterized based on quasi-static test	Characterized based on quasi-static test
Strain rate hardening	Inaccurate prediction beyond strain rate of 10^3 /s	Accurate prediction up to strain rate 10^5 /s
Thermal softening	Characterized based on tests at elevated temperatures	Characterized based on tests at elevated temperature
Acoustic softening	Not available	Characterized based on acoustic softening studies

The new plasticity model was developed in this chapter and the thermal and friction models will be presented in the next chapter. The thermal softening in the plasticity model depends on the temperature obtained from the thermal model whereas the strain and strain rate depend on the interfacial friction force which is determined by the friction model.

Chapter 5

5 A Thermal and a Friction Model for UAM

In this chapter, a thermal and a friction model are established to account for the heat transfer and mechanical interaction between the sonotrode, top foil, and built feature. The thermal model is presented first and is followed by the friction model.

5.1 Thermal Model in UAM

The energy equation is governed by:

$$\rho c \frac{\partial T}{\partial t} = \dot{q} + \nabla \cdot (\mathbf{k} \cdot \nabla T) \quad (5.1)$$

where ρ is density, c is specific heat, T is temperature, \mathbf{k} is the conductivity tensor, and ∇ is the nabla operator: $\nabla = (\frac{\partial}{\partial x}, \frac{\partial}{\partial y}, \frac{\partial}{\partial z})$. \dot{q} is the heat rate per unit volume due to dissipation of plastic deformation. The work done by plastic deformation is written:

$$\dot{w}_{pl} = \boldsymbol{\sigma} : \dot{\boldsymbol{\epsilon}}^{pl} \quad (5.2)$$

where \dot{w}_{pl} is the rate of plastic work per unit volume done by plastic deformation, $\boldsymbol{\sigma}$ is the stress tensor, $\dot{\boldsymbol{\epsilon}}^{pl}$ is the plastic strain rate tensor. It has been shown that not all of the plastic work is converted to heat as metals undergo dynamic plastic deformation (Hodowany et al. 2000). Most of the plastic work is dissipated into heat while the rest is stored in defect

structures such as dislocations, grain boundaries, and stacking faults that are generated due to plastic deformation. For aluminum, the fraction of plastic work which is converted into heat is shown to vary between 0.2 and 1.0 depending on the magnitude of the plastic strain (Hodowany et al. 2000). As the plastic strain exceeds 0.4, however, the heat fraction is stabilized around 0.95. Due to the large deformation (a plastic strain up to 0.47) in UAM bonding, a constant heat fraction of 0.95 is assumed. As a result, the rate of heat flow per unit volume due to plastic deformation is written:

$$\dot{q}_{pl} = \eta_p \dot{W}_{pl} = \eta_p \boldsymbol{\sigma} : \dot{\boldsymbol{\epsilon}}^{pl} \quad (5.3)$$

where η_p is the heat fraction of plastic work: $\eta_p = 0.95$. The volumetric heat flux \dot{q} is assumed to be equal to \dot{q}_{pl} in equation 5.1 and:

$$\rho c \frac{\partial T}{\partial t} = \eta_p \boldsymbol{\sigma} : \dot{\boldsymbol{\epsilon}}^{pl} + \nabla \cdot (\mathbf{k} \cdot \nabla T) \quad (5.4)$$

The boundary conditions associated to the governing equation include a prescribed temperature and a heat flux. The temperature of the top foil and the sonotrode is assumed to be 20 °C which is the room temperature. The built feature is prescribed to an initial temperature that could vary between 20 °C and 150 °C depending on the set of operating parameters. The heat flux at the interface between the top foil and the built feature takes into account interfacial friction. Assuming that the frictional work is dissipated completely into heat, the heat flux can be written as:

$$\dot{q}_f = \boldsymbol{\tau} : \dot{\boldsymbol{s}} \quad (5.5)$$

where \dot{q}_f is the frictional heat rate per unit area, $\boldsymbol{\tau}$ is the friction stress tensor, $\dot{\boldsymbol{s}}$ is the rate of differential motion tensor. The heat conduction from the frictional heat flux is assumed to be equally partitioned between the top foil and the built feature since the two surfaces

are of the same material. The convective boundary condition is not considered since its contribution is small when the welding time under study lasts only a fraction of a second.

Due to the existence of voids at the bond interface of each layer, the built feature demonstrates a thermal conductivity with a transverse isotropy along the direction normal to the bond interface. The voids are filled with air and therefore their thermal conductivity is much lower than that of the bulk material. Foster established a laminated finite element model in which bulk material and bond interface layers alternate (Daniel R Foster 2014). The thermal conductivity of the bond interface layers is predicted using four different analytical models by Misnar, Maxwell, Russel, and Bruggemann assuming a 37% (a typical averaged weld density produced from Solidica Formation Machine) bonded area and the lowest prediction is adopted here (Daniel R Foster 2014). As a result, the effective thermal conductivity in the direction normal to the laminated layers is estimated to be $112 \text{ W}/(\text{m}\cdot\text{K})$ in comparison to $155 \text{ W}/(\text{m}\cdot\text{K})$ for the conductivity of bulk aluminum.

The thermal contact conductance at the sonotrode-top foil and the top foil-built feature interfaces depend on the surface topography, contact pressure, and conductivities of the materials in contact. In the UAM, the top foil undergoes severe plastic deformation on its top and bottom surfaces and forms close contact with the sonotrode and the built feature, leading to high thermal contact conductance. Jedrasiak et al. used a thermal conductance of $10^6 \text{ W}/(\text{mK})$ for both interfaces (Jedrasiak et al. 2014). Jenq et al. proposed an analytical model for predicting the thermal contact conductance of metals under plastic contact based on the plastic contact theory by (Abbott and Firestone 1995; K. L. Johnson 1985)

and the thermal contact conductance model developed by (Cooper, Mikic, and Yovanovich 1969):

$$h_c = \frac{2k_s n b_c}{(1 - \sqrt{A_t/A_n})^{1.5}} \quad (5.6)$$

where k_s is the harmonic mean conductivity defined as $\frac{1}{k_s} = \frac{1}{k_1} + \frac{1}{k_2}$, n is the density of asperities, b_c is the mean radius of spherical asperity, A_n is the nominal contact area, and A_t is the real contact area (Jenq and Sheu 1994). In plastic contact, A_t is written (Abbott and Firestone 1995):

$$A_t = 2\pi R_m \omega \quad (5.7)$$

where R_m is the mean radius of curvature of the asperity and ω is the interference of the asperities defined as the difference between the height of asperities and the separation distance of the contact surfaces. For Aluminum 6061, assuming an initial surface roughness of 2.22 μm , under contact pressure of around 100 MPa and plastic contact condition, the thermal contact conductance is calculated to be $10^5 \text{ W}/(\text{K} \cdot \text{m}^2)$. The constants used for determining the thermal model are summarized in **Table 5.1**.

Table 5.1 Constants for thermal model

Thermal Conductivity (W/K · m)	155 (horizontal), 112 (normal)
Thermal Contact Conductance (W/K · m²)	10 ⁵
Specific heat (J/kg · K)	896
Thermal expansion (/ K)	23.4×10 ⁻⁶
Heat fraction of plastic work (-)	0.95

5.2 Friction Model in UAM

Based on the literature review (section 2.2.4), the most influential factors for the friction coefficient between top foil and built feature are temperature and normal load. As the temperature increases, the change in the stresses that drives plastic deformation of surface asperities causes the friction coefficient to first increase and then decrease. This change of friction coefficient is captured by the experimental studies of Zhang et al. (Cunbo Zhang, Zhu, and Li 2006). The kinetic friction coefficient between two aluminum foils (Al 3003-H18, 100 μm thick) subjected to a normal load of 10kg at various slip rate and temperatures was measured. The friction tests are carried out on a Gleeble™ 1500D system, the temperature varying between 25 °C and 250 °C and the slip rate between 0.8 mm/s – 800 mm/s. The results showing the effect of temperature are shown in **Figure 5.1**. The slip rate is reported to have little influence on the friction coefficient in the range tested.

The normal load affects the friction coefficient by means of affecting the effective contact area between asperities. It has been shown by Williamson and Greenwood that in a Hertzian contact, as the normal load increases, the effective contact area increases at an order higher than the order of unity (Greenwood, J. A., & Williamson 1966). Since the overall friction force increases linearly with the normal load, the friction coefficient is reversely related to the normal load. This effect is shown in the work of Naidu and Raman who studied the variation of friction coefficient under different loads for aluminum 6061-T6 (Naidu and Raman 2005). They found that the variation of the friction coefficient with respect to the normal load can be modeled using a power law model as is shown in **Figure 5.28**.

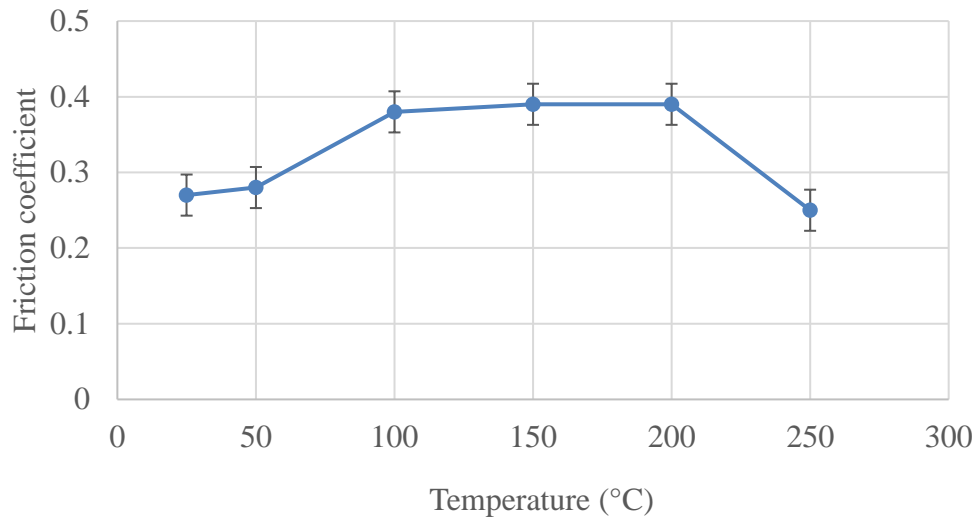


Figure 5.1 The variation of friction coefficient as a function of temperature reproduced from (C Zhang and Li 2008).

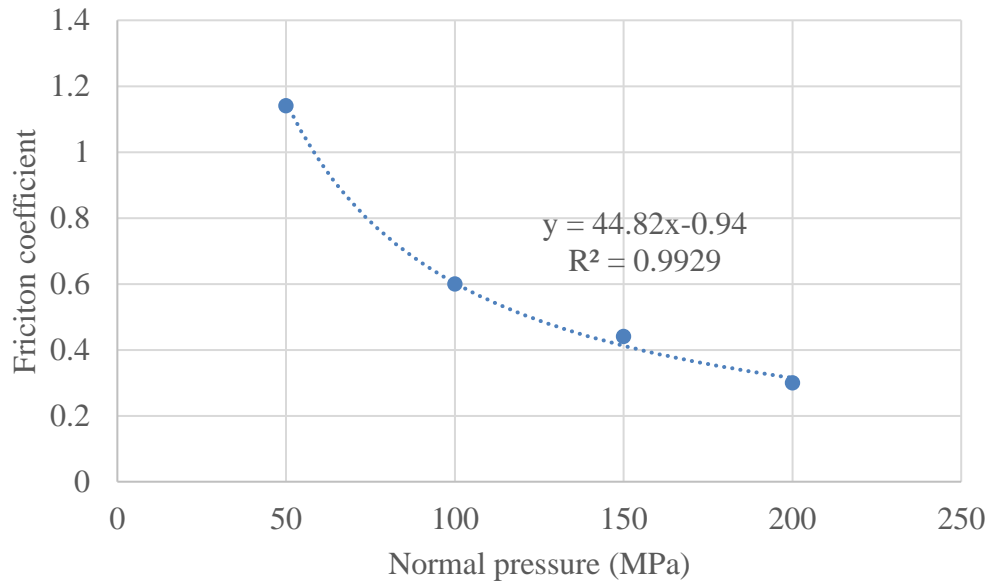


Figure 5.2 The variation of friction coefficient with respect to the normal pressure reproduced from (Naidu and Raman 2005).

A friction model is established to account for both effects. Considering the two factors as independent, the friction coefficient is modeled:

$$\mu = \mu_0(T_0, P_0)\xi(T, T_0)\eta(P, P_0) \quad (5.8)$$

where μ_0 is the friction coefficient at a reference temperature T_0 and a reference normal pressure P_0 . $\xi(T)$ is the contribution from the temperature, and $\eta(P)$ is the contribution from the normal pressure. Both $\xi(T)$ and $\eta(P)$ are calibrated with respect to the reference temperature T_0 and the reference normal load P_0 . Since both tests are carried out at room temperature, the room temperature is set as the reference temperature: $T_0 = 20^\circ\text{C}$. Due to the lack of information regarding the normal pressure in Zhang's work, the reference pressure is determined by mapping the friction-temperature data to the friction-pressure data for determining the reference pressure. Specifically, at the reference temperature $T_0 = 20^\circ\text{C}$, the friction coefficient indicated by the temperature-friction plot is 0.27. Since the pressure-friction relation is a monotonic function, the pressure at which the friction coefficient is equal to 0.27 is 230 MPa (Figures 5.1 and 5.2). As a result, the reference pressure is set to: $P_0 = 230\text{ MPa}$.

The temperature effect is modeled using linear interpolation:

$$\xi(T) = \sum_j (\prod_{i \neq j} \frac{\hat{T} - \hat{T}_i}{\hat{T}_j - \hat{T}_i}) \hat{\mu}_j, i = 1, 2, \dots, 6 \quad (5.9)$$

where $\hat{T} = \frac{T}{T_0}$, $\hat{\mu} = \frac{\mu}{\mu_0}$, (T_k, μ_k) ($k = i, j$) are the experimental data sets shown in **Figure**

5.1. The pressure effect is modeled using a power law function:

$$\eta(P) = a\left(\frac{P}{P_0}\right)^b \quad (5.10)$$

where a, b are constants identified by fitting the power law model to the normalized experimental data sets. Finally, the friction model is written:

$$\mu = \mu_0 a \left(\frac{P}{P_0}\right)^b \sum_j \left(\prod_{i \neq j} \frac{\hat{T} - \hat{T}_i}{\hat{T}_j - \hat{T}_i} \right) \hat{\mu}_j, i = 1, 2, \dots, 6$$

The constants introduced in the model are shown in **Table 5.2**.

Table 5.2 Model constants for friction model

μ_0	$T_0(^{\circ}\text{C})$	$P_0(\text{MPa})$	a	b
0.3	25	200	1.05	-0.94

This section presents the thermal and friction models that are developed based on the UAM process and the specific material used. These models will be assembled in Chapter 7 to for establishing a comprehensive UAM model.

Chapter 6

6 The Assembly of Submodels for the UAM Model

6.1 Integration of Sub-models

In this section, sub-models are integrated and solved using the finite element method. The sub-models include the plasticity, thermal, friction, and dynamic models. The chapter starts with the integration of the plasticity model to solve for the constitutive relation (section 6.1.1). The constitutive relation is then used to solve the dynamic equation. Since the dynamic model is coupled with the thermal model, they have to be solved simultaneously. The integration schemes are shown in section 6.1.2. The friction model is integrated to the thermo-mechanical model as a boundary condition. The frictional force serves as a boundary condition for the dynamic model and the frictional heat serves as a boundary condition for the thermal model (section 6.1.3). Finally, the coupling of all the submodels are summarized in section 6.1.4.

6.1.1 Plasticity Model Integration

6.1.1.1 Fundamentals of Plasticity

The integration of the Johnson-Cook plasticity model requires introducing the yield criterion and making assumptions about the flow rule, the hardening rule, and the rate-independency of the plasticity model. These rules and assumptions are explained in this section. Specifically, the plastic deformation represents the *irreversible* relative displacement of atoms along certain planes when subjected to external load. The stress limit necessary to trigger such irreversible displacement is defined by the yield criterion below which the deformation is elastic and beyond which the deformation becomes plastic. The relation can be written as.

$$f < 0: \text{Elastic deformation}$$

$$f = 0: \text{Plastic deformation}$$

where f is the yield criterion and $f = 0$ defines the yield surface in the stress space. Different yield criteria have been proposed, among them the von Mises and the Tresca criteria are the two most commonly used criteria to predict the yielding of metals. **Figure 6.1** shows the yield surfaces defined by von Mises and Tresca in 2-D stress space. The stress state is represented by a point which moves within (elastic state) or on the yield surface (plastic state). In this work, the von Mises yield criterion is used.

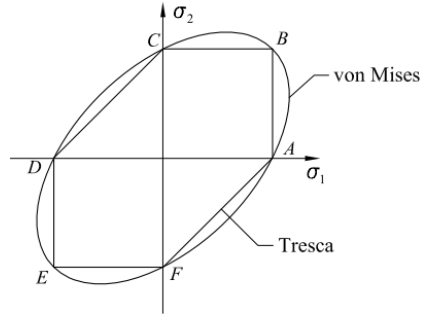


Figure 6.1 The yield surfaces defined by the von Mises and the Tresca yield criteria in 2-D stress space

Due to the interactions between dislocations and other particles, the yield surface evolves as the plastic flow continues, resulting in either increase or decrease of the stress. For aluminum alloys, the yield surface expands in size and the yield stress increases as the plastic flow continues. This increase is defined by a hardening rule. The von Mises yield criterion and the hardening rule are written as follows:

$$f(\boldsymbol{\sigma}, \boldsymbol{\varepsilon}_p) = J(\boldsymbol{\sigma}) - r(\boldsymbol{\varepsilon}_p) - \sigma_y = 0 \quad (6.1)$$

where f is the yield function, σ_y the initial yield stress, and r the hardening rule. Based on the von Mises yield criterion, J is the von Mises stress which is written as:

$$J(\boldsymbol{\sigma}) = \sqrt{\frac{3}{2} \boldsymbol{\sigma}' : \boldsymbol{\sigma}'} \quad (6.2)$$

where $\boldsymbol{\sigma}'$ is the *deviatoric part* of the Cauchy stress tensor defined as: $\boldsymbol{\sigma}' : \boldsymbol{\sigma}' = \boldsymbol{\sigma} - \frac{1}{3} \text{tr}(\boldsymbol{\sigma}) \mathbf{I}$. The hardening is assumed to be isotropic, i.e., the yield surface only expands in size but does not change in its shape or shift its origin (**Figure 6.2**). The assumption is valid for polycrystalline materials due to their random crystallographic orientations.

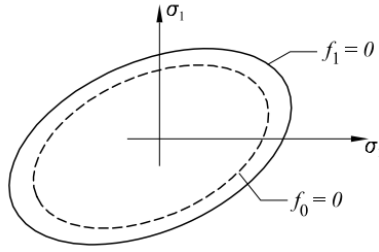


Figure 6.2 The expansion of yield surface due to isotropic hardening.

The flow rule defines the magnitude and the direction of the plastic strain rate $\dot{\boldsymbol{\varepsilon}}_p$. By considering the associated flow rule which states that the potential function is identical to the yield function, and the normality condition which is a consequence of Drucker's maximum dissipation principle, the flow rule can be written as:

$$\dot{\boldsymbol{\varepsilon}}_p = \dot{\lambda} \frac{\partial f(\boldsymbol{\sigma})}{\partial \boldsymbol{\sigma}} = \dot{\lambda} \mathbf{n} \quad (6.3)$$

where $\dot{\lambda}$ is a plastic multiplier that represents the magnitude of $\dot{\boldsymbol{\varepsilon}}_p$; $\mathbf{n} = \frac{\partial f(\boldsymbol{\sigma})}{\partial \boldsymbol{\sigma}}$ defines the unit normal vector of $\dot{\boldsymbol{\varepsilon}}_p$ which is *always* normal to the yield surface (normality condition). The multiplier $\dot{\lambda}$ can be determined by introducing the consistency condition which states that under the rate-independent framework, the stress must always stay on the yield surface during plastic loading, i.e. $f = \dot{f} = 0$. The relation can be further written as follows:

$$f(\boldsymbol{\sigma}, \boldsymbol{\varepsilon}_p) = \dot{f}(\boldsymbol{\sigma}, \boldsymbol{\varepsilon}_p) = \frac{\partial f(\boldsymbol{\sigma})}{\partial \boldsymbol{\sigma}} : \dot{\boldsymbol{\sigma}} - \frac{\partial f}{\partial \boldsymbol{\varepsilon}_p} \dot{\boldsymbol{\varepsilon}}_p = 0 \quad (6.4)$$

With these plasticity rules and assumptions introduced, the integration of the plasticity model is explained in the next section.

6.1.1.2 Integration of the Plasticity Model

The plasticity model is integrated at each point in the constitutive matrix \mathbf{D}^{ep} which defines the elasto-plastic constitutive relation between the stress $\boldsymbol{\sigma}$ and the total strain $\boldsymbol{\varepsilon}$:

$$\boldsymbol{\sigma} = \mathbf{D}^{ep} : \boldsymbol{\varepsilon} \quad (6.5)$$

Since \mathbf{D}^{ep} is nonlinear, it has to be solved iteratively. First partition the total strain into elastic and plastic contributions:

$$\boldsymbol{\varepsilon} = \boldsymbol{\varepsilon}_e + \boldsymbol{\varepsilon}_p \quad (6.6)$$

Based on Hooke's law for linear elasticity, the stress-strain relation can be written as:

$$\boldsymbol{\sigma} = \mathbf{D} : (\boldsymbol{\varepsilon} - \boldsymbol{\varepsilon}_p) \quad (6.7)$$

where \mathbf{D} is the linear *elastic* stiffness matrix. Introducing the von Mises yield criterion, the associated flow rule, and the normality condition, the plastic strain rate is written as:

$$\dot{\boldsymbol{\varepsilon}}_p = \dot{\lambda} \frac{\partial f(\boldsymbol{\sigma})}{\partial \boldsymbol{\sigma}} \quad (6.8)$$

rewriting equation (6.7) in rate form and inserting equation (6.3) yields:

$$\dot{\boldsymbol{\sigma}} = \mathbf{D} : \left(\dot{\boldsymbol{\varepsilon}} - \dot{\lambda} \frac{\partial f(\boldsymbol{\sigma})}{\partial \boldsymbol{\sigma}} \right) \quad (6.9)$$

In order to determine the magnitude of $\dot{\lambda}$, the consistency condition is introduced:

$$\frac{\partial f(\boldsymbol{\sigma})}{\partial \boldsymbol{\sigma}} : \dot{\boldsymbol{\sigma}} - \frac{\partial r}{\partial \boldsymbol{\varepsilon}_p} \dot{\boldsymbol{\varepsilon}}_p = 0 \quad (6.10)$$

Inserting equation (6.9) into (6.10) and letting $H = \frac{\partial r}{\partial \boldsymbol{\varepsilon}_p}$, $\mathbf{n} = \frac{\partial f(\boldsymbol{\sigma})}{\partial \boldsymbol{\sigma}}$, the plastic multiplier $\dot{\lambda}$ can be derived in explicit form:

$$\dot{\lambda} = \frac{\mathbf{n} : \mathbf{D} : \dot{\boldsymbol{\varepsilon}}}{\mathbf{n} : \mathbf{D} : \mathbf{n} + H} \quad (6.11)$$

Inserting equation (6.11) back into equation (6.9) yields:

$$\dot{\boldsymbol{\sigma}} = \left(\mathbf{D} - \frac{\mathbf{D}:\mathbf{n}\otimes\mathbf{n}:\mathbf{D}}{\mathbf{n}:\mathbf{D}:\mathbf{n}+H} \right) : \dot{\boldsymbol{\varepsilon}} \quad (6.12)$$

Comparing equation (6.12) with equation (6.5), the constitutive matrix \mathbf{D}^{ep} is written as:

$$\mathbf{D}^{ep} = \mathbf{D} - \frac{\mathbf{D}:\mathbf{n}\otimes\mathbf{n}:\mathbf{D}}{\mathbf{n}:\mathbf{D}:\mathbf{n}+H} \quad (6.13)$$

Once $\dot{\boldsymbol{\sigma}}$ at time t is obtained (equation (6.12)), the stress, strain, and isotropic hardening factor at time $t + \Delta t$ can be updated accordingly (the time increment is denoted by the subscript):

$$\boldsymbol{\sigma}_{t+1} = \boldsymbol{\sigma}_t + \dot{\boldsymbol{\sigma}}_t \quad (6.14)$$

$$\boldsymbol{\varepsilon}_{t+\Delta t}^p = \boldsymbol{\varepsilon}_t^p + \dot{\lambda}_t \mathbf{n} \quad (6.15)$$

Going back the constitutive matrix \mathbf{D}^{ep} and updating the isotropic hardening factor r in the yield function f , since $dr = Hd\lambda$:

$$r_{t+\Delta t} = r_t + Hd\lambda_t \quad (6.16)$$

The process is implemented in the commercial finite element software ABAQUS as a user-defined material subroutine (VUMAT). The subroutine is coded in Fortran 95 and the script can be found in Appendix A.

Once the constitutive relation is integrated and the constitutive matrix $[\mathbf{D}]^{ep}$ obtained, $[\mathbf{D}]^{ep}$ can be used to calculate the stiffness matrix $[\mathbf{K}]$ in the dynamic equation. Specifically, the discretized governing equation of dynamics is written as:

$$[\mathbf{M}] \left\{ \frac{\partial^2 \mathbf{u}}{\partial t^2} \right\} + [\mathbf{C}] \left\{ \frac{\partial \mathbf{u}}{\partial t} \right\} + [\mathbf{K}] \{\mathbf{u}\} = \{\mathbf{F}\} \quad (6.17)$$

where $\{\mathbf{u}\}$ is the nodal displacement vector, $\left\{ \frac{\partial \mathbf{u}}{\partial t} \right\}$ the nodal velocity vector, and $\left\{ \frac{\partial^2 \mathbf{u}}{\partial t^2} \right\}$ the nodal acceleration vector. $[\mathbf{M}]$ is the global mass matrix, $[\mathbf{C}]$ the global damping matrix,

$[\mathbf{K}]$ the global stiffness matrix, and $\{\mathbf{F}\}$ the external load vector. At each time increment of the mechanical (dynamic) analysis, a *quasi-static* equilibrium is achieved:

$$[\mathbf{K}]\{\mathbf{u}\} = \{\mathbf{F}\} \quad (6.18)$$

The stiffness matrix $[\mathbf{K}]$ can be written in terms of the deformation matrix $[\mathbf{B}]$ and the constitutive matrix $[\mathbf{D}^{ep}]$:

$$[\mathbf{K}] = [\mathbf{B}]^T [\mathbf{D}^{ep}] [\mathbf{B}] \quad (6.19)$$

Since the constitutive matrix $[\mathbf{D}^{ep}]$ is nonlinear, $[\mathbf{K}]$ must be solved iteratively. Writing equation (6.18) in incremental form and using a tangent stiffness matrix $[\mathbf{K}_T]$ to approximate the nonlinear stiffness matrix $[\mathbf{K}]$:

$$[\mathbf{K}_T]\{\Delta\mathbf{u}\} = \{\Delta\mathbf{F}\} \quad (6.20)$$

Since $\{\Delta\mathbf{F}\}$ is known, $\{\Delta\mathbf{u}\}$ can be readily obtained using the above equation. Then $\{\Delta\boldsymbol{\varepsilon}\}$ can be calculated from $\{\Delta\mathbf{u}\}$ using the deformation matrix $[\mathbf{B}]$:

$$\{\Delta\boldsymbol{\varepsilon}\} = [\mathbf{B}]\{\Delta\mathbf{u}\} \quad (6.21)$$

Inserting equations (6.19) and (6.21) back to the incremental form of equation (6.18) yields:

$$[\mathbf{B}]^T [\mathbf{D}^{ep}]\{\Delta\boldsymbol{\varepsilon}\} = \{\Delta\mathbf{F}\} \quad (6.22)$$

Since $[\mathbf{D}^{ep}]$ is obtained, the stress increment is obtained using the following equation:

$$\{\Delta\boldsymbol{\sigma}\} = [\mathbf{D}^{ep}]\{\Delta\boldsymbol{\varepsilon}\} \quad (6.23)$$

Inserting equation (6.23) into equation (6.22), rewriting the equation into differential form, and integrating over the material domain yields:

$$[\mathbf{B}]^T \{\boldsymbol{\sigma}\} = \{\mathbf{F}\} \quad (6.24)$$

Let $\{\mathbf{q}\} = [\mathbf{B}]^T \{\boldsymbol{\sigma}\}$ and defining the force residual $\{\mathbf{r}\}$ as:

$$\{\mathbf{r}\} = \{\mathbf{q}\} - \{\mathbf{F}\} \quad (6.25)$$

Equation (6.25) is used as a convergence criterion and is checked at each iteration. The above process can be summarized into four steps:

1. Apply the load increment ΔF and calculate for Δu and $\Delta \varepsilon$ using the tangent stiffness matrix (equations (6.18)-(6.21))
2. Solve for D^{ep} by integrating the constitutive relation and updating $\Delta \sigma$ (equations (6.22) and (6.23))
3. Compute the residual r (equation (6.25))
4. If $\|r\| > \text{tolerance}$, let $\Delta F = -r$ and return to step 1.

6.1.2 Thermo-mechanical Model Integration

The dynamic model is fully coupled with the thermal model presented in section (5.1) since the thermal and mechanical solutions strongly affect each other. The equations are written as:

$$\rho c \frac{\partial T}{\partial t} = \dot{q} + \nabla \cdot (\mathbf{k} \cdot \nabla T) \quad (6.26)$$

$$\rho \frac{\partial^2 \mathbf{u}}{\partial t^2} = \mathbf{f} + \nabla \cdot \boldsymbol{\sigma} \quad (6.27)$$

where ρ is the density, c the specific heat, T the temperature, \mathbf{k} the conductivity vector, and ∇ the nabla operator: $\nabla = (\frac{\partial}{\partial x}, \frac{\partial}{\partial y}, \frac{\partial}{\partial z})$. \dot{q} is the heat rate per unit volume due to heat dissipation, \mathbf{u} the displacement vector, \mathbf{f} the body force tensor, and $\boldsymbol{\sigma}$ the stress tensor. In the thermo-mechanical model, the equations are fully coupled as the material properties in stress analysis depend on local temperature and the heat generation in thermal analysis

depends on the work due to frictional and plastic stresses. In order to achieve the coupling, the mechanical and thermal models have to be solved simultaneously. The explicit integration schemes are selected for their advantages in solving highly nonlinear, high speed dynamics and contact involved problems. Specifically, the heat transfer equation is integrated using the explicit forward-difference time integration scheme written as (Abaqus 2015):

$$T_{i+1} = T_i + \Delta t_{i+1} \dot{T}_i \quad (6.28)$$

Where the subscript is the time increment number, T the temperature, Δt the time increment. \dot{T}_i is calculated at the end of the increment i and is written as:

$$\dot{T}_i = \mathbf{C}^{-1}(\mathbf{Q}_i - \mathbf{F}_i) \quad (6.29)$$

where \mathbf{C}^{-1} is the inverse lumped capacitance matrix, \mathbf{Q}_i and \mathbf{F}_i are the applied heat source vector and the internal thermal flux vector at the end of increment i . The dynamic equation is integrated using the explicit central-difference integration scheme (Abaqus 2015):

$$\dot{\mathbf{u}}_{i+1/2} = \dot{\mathbf{u}}_{i-1/2} + \frac{\Delta t_{i+1} + \Delta t_i}{2} \ddot{\mathbf{u}}_i \quad (6.30)$$

$$\mathbf{u}_{i+1/2} = \mathbf{u}_i + \Delta t_{i+1} \dot{\mathbf{u}}_{i+1/2} \quad (6.31)$$

where \mathbf{u} is the displacement vector, $\dot{\mathbf{u}}$ is velocity vector, and $\ddot{\mathbf{u}}_i$ is acceleration vector. The acceleration vector is defined as:

$$\ddot{\mathbf{u}}_i = \mathbf{M}^{-1}(\mathbf{P}_i - \mathbf{I}_i) \quad (6.32)$$

where \mathbf{M}^{-1} is the inverse mass matrix. \mathbf{P}_i and \mathbf{I}_i are the applied load vector and the internal force vector.

The explicit integration schemes are conditionally stable and therefore stability criteria need to be imposed. For the mechanical model, the criterion is based on the mechanical wave propagation: within the time increment, the distance that the ultrasound wave

propagates should not exceed the minimum dimension of any finite element. The criterion on Δt_{me} is written as (Abaqus 2015):

$$\Delta t_{me} \approx \frac{L_{min}}{c_d} \quad (6.33)$$

where L_{min} is the dimension of the minimum element, c_d is the longitudinal wave speed defined as:

$$c_d = \sqrt{\frac{E}{\rho}} \quad (6.34)$$

where E is the Young's modulus. For the integration of the thermal model, the criterion is defined such that within the time increment, the distance that thermal wave propagates should not exceed the minimum dimension of any element. The criterion on Δt_{th} is written as (Abaqus 2015):

$$\Delta t_{th} = \frac{l_{min}^2}{2\alpha} \quad (6.35)$$

where l_{min} is the dimension of the minimum element and α the thermal diffusivity. Based on the finite element model setup and on the thermal and mechanical properties defined in sub models, the maximum time increment for the mechanical model is 2e-8 seconds and for the thermal model is 1e-3 seconds. The maximum time increment for integrating the thermo-mechanical model is constrained by the smaller increment of the two and therefore is 2e-8 seconds.

6.1.3 Friction Model Integration

The critical friction stress τ_{crit} necessary to initiate friction is determined based on Coulomb's friction law: the product of friction coefficient and normal pressure. The friction coefficient is determined at each time increment based on the friction model which characterizes the two influential factors: normal pressure and temperature. The values of these factors are obtained from the stress and thermal analyses by solving the thermo-mechanical model. The shear stress τ obtained from stress analysis is compared to the critical friction stress τ_{crit} such that the surfaces in contact stick as $\tau < \tau_{crit}$, and slip as $\tau \geq \tau_{crit}$. The friction stress also governs the heat dissipation from friction work which serves a heat flux boundary condition for the thermal model.

6.1.4 Summary

In summary, five sub-models including thermal, dynamic, plasticity, and friction models are integrated and solved using the finite element method. The five sub-models are coupled with each other and a schematic of the couplings is shown in **Figure 6.1**. Each dashed box contains an individual equation that supports the sub models. Each solid line indicates a coupling between the *solution* from the equation in a dashed box and a specific parameter in another equation. The arrow indicates the cause-effect relationship between the parameters. For instance, the heat dissipation from both friction and plastic deformation contribute to the heat flux \dot{q} in the thermal model whereas the temperature solution from the thermal model contributes to the thermal softening in the plasticity model. From the energy point of view, the lines and arrows also indicate the energy flow within the thermodynamic system.

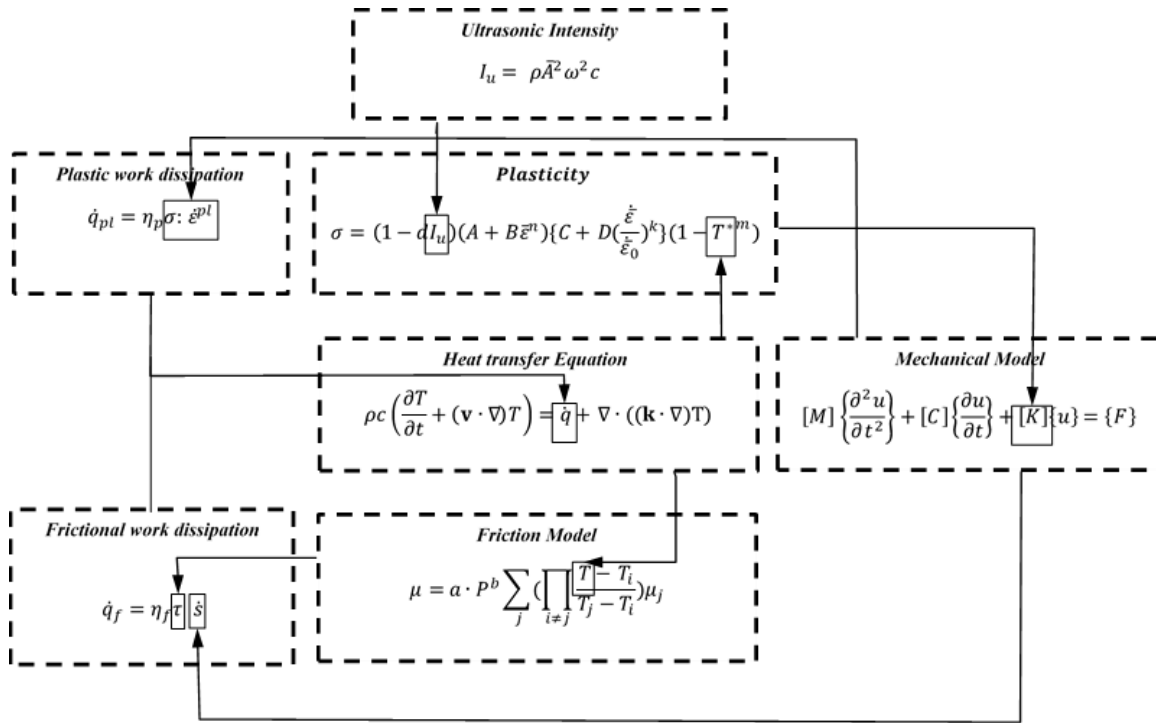


Figure 6.3 The couplings between sub-models

6.2 The Setup of UAM Model in ABAQUS

The setup of a 3-D thermo-mechanical model in ABAQUS is described. The model introduces a sonotrode, a top foil, and a built feature (**Figure 6.2** (left)). The titanium sonotrode is modeled as a rigid shell whereas the aluminum top foil and the built features are modeled as deformable solids. The laminated built feature is simplified to a parallelepiped with homogenous material properties. The sonotrode has a radius of 76.2 mm (3 in.). The nominal width of the foil, the sonotrode, and the built feature are 23.876 mm (0.94 in.). The thickness of the foil is 0.13 mm (0.0051 in.). The length of the built feature is set to 63.5 mm (2.5 in.).

At the contact interface between the top foil and the built feature, the layers consisting of surface asperities are observed to undergo severe plastic deformation on both surfaces in contact. The layer is characterized by the refinement and “flow” like morphology of the sub-grains and is typically 10 – 60 μm in thickness from the weld interface (K. Johnson et al. 2011). As a result, two plastic deformation layers are introduced and attached to the mating surfaces of the top foil and the built feature respectively (**Figure 6.2** (right)). The elastic properties in the plastic deformation layers are lower than those in the bulk material due to the existence of surface asperities. When subjected to compression force, the asperities crush and the layer yields larger deformation than the bulk material underneath. The effective elastic modulus is determined by assuming a Hertzian contact between two rough surfaces (K. L. Johnson 1985):

$$\frac{1}{E^*} = \frac{1-\nu_1^2}{E_1} + \frac{1-\nu_2^2}{E_2} \quad (6.36)$$

where E_1 , E_2 , ν_1 , ν_2 are the elastic modulus and Poisson’s ratio of the two materials in contact. For the contact between aluminum 6061-T6 foils, $\nu_1 = \nu_2 = 0.33$, the effective modulus is roughly half of the elastic modulus: $E^* = 0.56E$. Both plastic layers are 20 μm thick according to observation made by Johnson et al. and the overall thickness of the top foil is 150 μm (K. E. Johnson 2008).

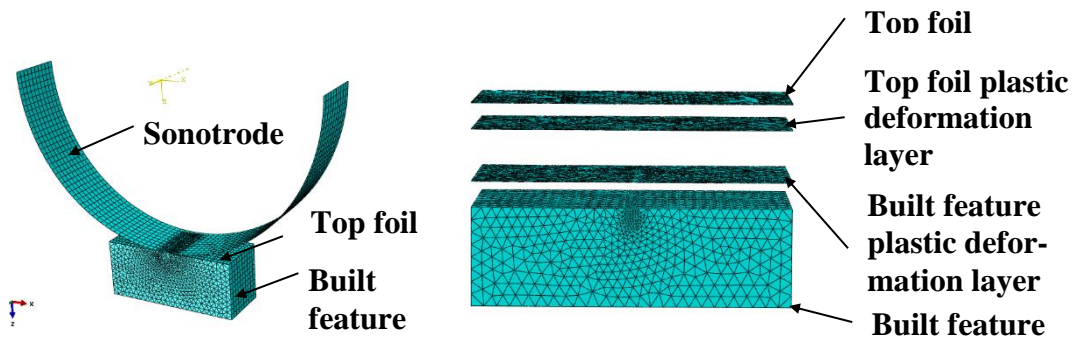


Figure 6.4 UAM model overview (left), and the plastic deformation layers between the top foil and built feature (right, the sonotrode is removed for clarity)

Both mechanical and thermal boundary conditions are imposed in the model. The sonotrode is subjected to a compression load in the normal direction and a sinusoidal displacement at 20 kHz along the width of the foil in horizontal direction. Clamping is imposed at the bottom of the built feature. Along the rolling direction of the sonotrode, the part of the top foil behind the rolling path is already “bonded” and thus is fully constrained to the built feature whereas the part ahead of the rolling path is clamped at the end to minimize the dynamics effects from the top foil. The thermal boundary conditions include pre-heating the top foil and built feature while maintaining the sonotrode at room temperature (25 °C).

Mechanical and thermal contact interactions are defined between the sonotrode and the top foil as well as between the top foil and the built feature. In the normal direction on both contact interfaces, a surface-to-surface “hard” contact is defined which minimizes the penetration of the slave surface (with soft material) into the master surface (with hard material or rigid body) at the contact locations using a penalty method and impedes the transfer

of tensile stress across the contact interface (Abaqus 2015). At the sonotrode-top foil interface, a “rough” surface contact is defined which imposes no slip along the horizontal direction. The assumption of the top being “grabbed” by the sonotrode without slipping is an ideal assumption for simplifying the problem, and is probably very realistic since the sonotrode surface has a tailored rough surface to ensure such “grabbing”. The influence of a potential slipping could be covered in future work.

In order to capture the plastic deformation underneath the sonotrode with sufficient accuracy and at the same time reduce computational cost, a contact patch is generated with refined mesh for the top foil, built feature, and plastic deformation layers in between (**Figure 6.2** (right)). The 4-node linear tetrahedral element (C3D4) is selected for meshing due to its robustness over hexagonal shape and being able to adapt to relatively complex geometries. The linear elements are preferred over quadrature due to their robustness under contact conditions which leads to less convergence issues. The mesh size is determined based on the criterion of being able to capture the Hertzian contact stress distribution (J. M. Gibert et al. 2009).

The ABAQUS Explicit solver is used to interface with the user defined subroutine VUMAT for solving the model. The simulation is run on a high-performance computing (HPC) cluster with 80 processors for roughly 24 hours (Intel Xeon processors, 2.33 GHz). The simulation time is set to 0.5 ms which covers 10 vibration cycles of the sonotrode. Since the rolling speed (0.03 m/s) is much lower than the vibration speed (0.4-4 m/s), the sonotrode is assumed to be dwelling and only oscillation is considered in the simulation.

Table 3.1 shows the range of variation of each operating parameter used for simulating the UAM process. The results will be shown in section 6.4.

Table 6.1 The operating parameters used for UAM simulation

Amplitude	Frequency	Compression load	Temperature	H/W
10-35 μm	20 kHz	1600-6000 N	25-150 $^{\circ}\text{C}$	0.2-2.0

6.3 Bond Quality Evaluation using Asperity Layer Model

6.3.1 Introduction

In this section, an asperity layer model is proposed to associate the UAM model prediction to the bond quality. Specifically, the established UAM model is capable of predicting deformation stress and strain, displacement, temperature, contact stress, and contact area at the bonding interface. However these predictions cannot be directly quantified and associated to bond quality. From the literature review in section 2.5, it is shown that most of the existing bond quality evaluations are experiment-based and are destructive to the bonds. The only exception is the linear weld density which is defined as the ratio of the bonded area over the total area. As a result, attempts are made to develop a model that relates the deformation of asperities to the linear weld density. These attempts are also supported by experimental studies presented in section 2.5.7 which conclude that the deformation of the asperity layer serves as a good indicator of bond quality.

Finite element models of asperities have been introduced for studying sliding contacts between rough surfaces. Pei et al. (2005) for instance, studied the contact between a

rigid smooth surface and a deformable rough surface by generating a 3-D finite element model of a self-affine fractal surface. J_2 plasticity is introduced for modeling the plastic deformation of asperities. The authors found that the contact area varies linearly with the normal load while the contact pressure barely changes. They further point out that the plastic deformation of asperities serves as an equalizer that reduces the sensitivity of area to surface roughness and leads to more uniform contact distribution. Deshpande et al. also studied the indentation and frictional sliding between a single rigid asperity and a deformable film using finite element models (Deshpande et al. 2007). The asperities are idealized as 2-D uniform sinusoidal and wedge shapes whose geometries are defined in terms of wave length to amplitude ratios ($\frac{w}{A}$). Cases are studied in the ratios of 10 and 20. They point out that the continuum plasticity is valid only when the asperity size is relatively large. This threshold is reported to be in the order of tens of micrometers (Song et al. 2015). When the asperity size is comparable to the dislocation source spacing, however, dislocation-based plasticity has to be introduced. Sun et al. simulate the ploughing of 2-D sinusoidal asperities using dislocation-based plasticity and find that the plastic contact pressure depends only on the wave length but not the amplitude of the sinusoidal shape (Song et al. 2015). At the same $\frac{w}{A}$, larger asperities are easier to deform due to the fact that more dislocations are available for nucleation. The ratios $\frac{w}{A}$ used for modeling the sinusoidal asperities are 20 and 50. In summary, it is shown that the asperities can be approximated by uniform sinusoidal shapes for studying their deformation under contact and sliding friction. As a

result, a 3-D finite element model of a sinusoidal asperity layer is established for characterizing the asperity deformation. The effective contact area ratio due to the deformation is then calculated and related to the linear weld density with the same definition.

6.3.2 Model Setup

A 3-D finite element model of sinusoidal asperities is established. The modeling process is similar to the one proposed by Padró (Padró 2015). Specifically, surfaces bounded by sinusoidal curves are generated by importing a set of control point coordinates in SolidWorks. The surfaces are then extruded to a solid body, tiled to a patterned asperity layer, and imported into ABAQUS for finite element analysis (**Figure 6.3** (left)). The sonotrode-textured foil is reported to have a surface roughness of $R_a = 10 \mu m$ (Friel et al. 2010; Kulakov and Rack 2010) where R_a is arithmetic average roughness defined as:

$$R_a = \frac{1}{N} \sum_{i=1}^N |y_i| \quad (6.37)$$

y_i is the vertical distance from the i th point on the surface profile to the mean line, and N is the number of points measured along the surface profile. However, roughness is not sufficient to precisely model the microgeometry of the asperity and little information other than R_a has been found in the literature. As a result, the 3-D sinusoidal asperity model is established such that the amplitude is fixed to $10 \mu m$ while the wave length to amplitude ratio ($\frac{w}{A}$) can take different values: $\frac{w}{A} = 8, 20$ (**Figure 6.3** (right)). The two ratios are selected based on their extensive use in the literature. Since the asperity size is on the order of tens of microns which is large comparing to dislocation spacing, the continuum plasticity

is valid to implement. The material properties (Aluminum 6061-O) assigned to the model are summarized in **Table 6.2**.

Table 6.2 The material properties assigned to the asperity model

Young's modulus	Poisson's ratio	Yield strength	Ultimate tensile strength
69 GPa	0.33	130 MPa	150 MPa

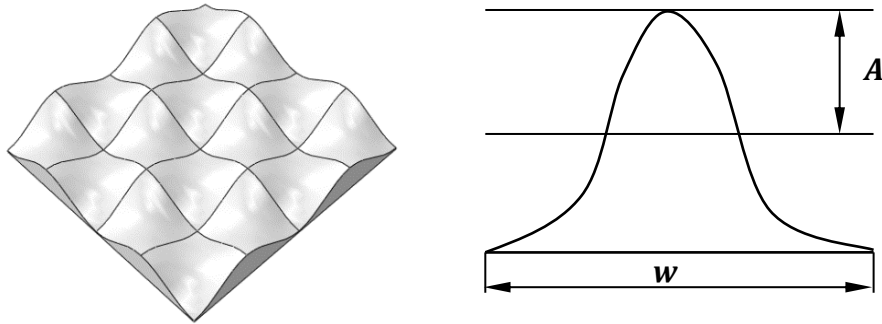


Figure 6.5 the amplitude and wavelength of 2-D sinusoidal shape (left) and the 3-D sinusoidal shape (right)

6.3.3 Preliminary Test

A compression test is carried out to determine the appropriate wavelength to amplitude ratios for UAM process. The test setup includes a top foil which is modeled as a rigid plane and an asperity layer which is modeled as deformable solid part. The amplitude A of the sinusoidal asperity is fixed to $10\ \mu\text{m}$ whereas the wave length to amplitude ratio $\frac{w}{A}$ is varied at two different levels: 8 and 20 (**Figure 6.4**). Uniform normal pressure of 30 MPa which is equivalent to a load of 1600 N is applied to the top foil for simulating the compression from the sonotrode. The bottom surface of the asperity layer is fixed while the

four vertical sides are free of constraints. The interaction between the top foil and asperity layer is modeled with ABAQUS surface-to-surface hard contact formulation. A constant friction coefficient of 0.4 is assigned to the mating surfaces based on the work of Zhang et al.(Cunbo Zhang and Li 2006). The 3-D model is meshed using C3D4 mesh.

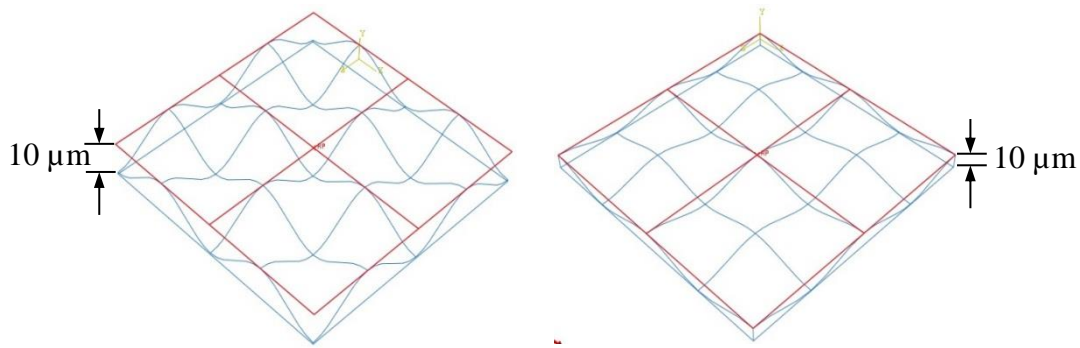


Figure 6.6 3-D top foil and sinusoidal asperity layer with $w/A=8$ (left) and $w/A=20$ (right).

Figure 6.5 shows the deformation of the asperity layer at $\frac{w}{A}$ equals 8 and 20, the top foil is removed for clarity of view. An ultimate tensile stress of 350 MPa is reached within the asperities in both cases (red contour), which indicates that the plastic deformation in these regions is sufficient for generating plastic flow and forming bonds. It can be seen that for small-spacing asperities ($\frac{w}{A} = 8$) the maximum stresses are distributed at the bottom rims of the asperities whereas for large-spacing asperities ($\frac{w}{A} = 20$) the maximum stresses are distributed at the peaks of asperities. The difference is speculated to be caused by the collapse of small-spacing asperities due to their slender geometries. In UAM, however, this is not the case since asperities only collapse under both compression and sufficient ultrasonic

vibration. As a result, the small-spacing asperities may not be realistic to capture the deformation of asperities.

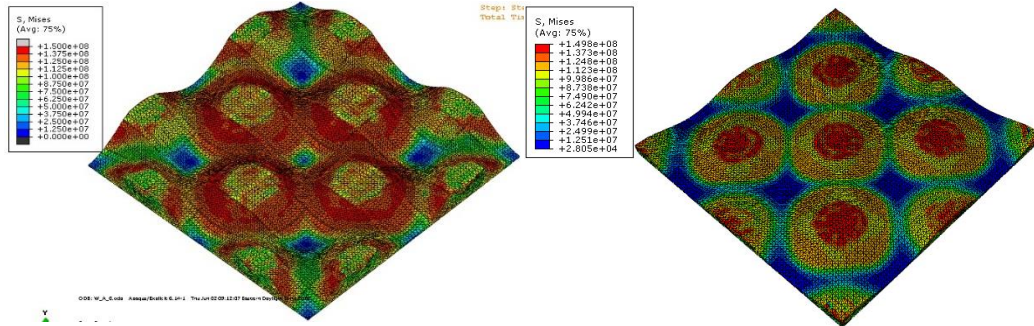


Figure 6.7 Steady state stress and strain response of asperity layer subjected to 30 MPa pressure: $w/A=8$ (left) and $w/A=20$ (right)

The deformation of the asperity layer is measured in terms of the top foil displacement in the normal direction and the effective contact area at the contact interface. The top foil displacement is $4.33 \mu\text{m}$ for small spacing asperities and $2.99 \mu\text{m}$ for large spacing asperities. The effective contact area is normalized by the total area of the top foil due to the difference in overall dimensions of the two models. For small spacing asperities, the normalized effective contact area is 10.60% and for large spacing asperities, the value is 6.86%. These results further validate our speculation that the small spacing asperities collapse under normal compression and lead to greater displacement of the foil and higher normalized effective contact area. As a result, large spacing asperities ($\frac{w}{A} = 20$) is selected for the UAM process.

6.4 Results

In this section, results generated from the UAM model are presented and discussed. In section 6.4.1, the UAM model is validated by predicting the foil deformation in bonding Aluminum 1100-O. The model predictions are then compared with experimental measurements. In section 6.4.2, the UAM model is run at two different height-to-width ratios to understand the effect of the built feature aspect ratio on stresses close to the bond interface. In section 6.4.3, the different energy dissipations within the UAM bonding are evaluated using the UAM model. In section 6.4.4, the asperity layer model is implemented in the UAM model to associate the material deformation at the bond interface to the linear weld density of the bonds. The predictions are then compared to experimental studies in the literature.

6.4.1 Validation of UAM Model

In this section, the model is first validated by comparing its predictions with experimental studies. Kelly et al. studied the variation of post-weld foil deformation under different combinations of process parameters (pressure, amplitude, and weld speed) (GS Kelly and Advani 2013). The change in width and thickness of the foil under different process parameters are examined using an image processing software Image J. The foil with 13 mm width and 0.52 mm thickness is selected and its deformation in width is compared with the obtained deformation for validating the UAM model. The model parameters for the modified Johnson-Cook are shown in **Table 6.3**. Specifically, the model parameters for strain hardening and acoustic softening are determined based on our experimental studies.

The strain rate hardening and thermal softening models are calibrated based on data from the literature (Kaufman 1999).

Table 6.3 Model constants of the modified JC model for Aluminum 1100-O

Al	A (MPa)	B (MPa)	n	C	D	p	d (cm²/W)	m
1100	83.09	76.37	0.38	0.46	0.49	0.10	8.01E-05	0.51

6 combinations of process parameters are selected from Kelly's work. The peak-peak vibration amplitude is set to 3 levels: 10 μm , 18 μm , and 36 μm whereas the compression is set to 2 levels: 78.9 MPa and 45.2 MPa. The preheat temperature is held at 135 $^{\circ}\text{C}$ and the weld speed is fixed at 40 mm/s. In the UAM model, the dwell time is chose as a parameter in replace of the weld speed. Specifically, the dwell time Δt is estimated using the ratio of contact length (w) over weld speed (v) (**Figure 6.6**): $\Delta t = \frac{w}{v}$. Since the minimum contact length is constrained by the size of the element, it is assumed that the contact length is equal to the length of the element along the rolling direction of sonotrode. As a result, the dwell time is estimated to be $\Delta t = 0.000285$ second and is equivalent to 57 cycles. Due to the high computational cost of the UAM model, the simulation is usually limited to 10 cycles. In order to predict the deformation after 57 cycles based on the simulation of 10 cycles, an assumption is made that the deformation of the foil is constantly increasing during the dwell time. It is a bold but reasonable assumption since the bonding process is sensitive to weld speed, meaning that plastic deformation takes place throughout the dwell time. Further, it is observed from the simulation that the width of the top foil is constantly

increasing. The deformation of the width can also be observed from the strain history of the element at the edge of the top foil (**Figure 6.7**). As a result, the deformation in width is evaluated using the relation:

$$\frac{\Delta W}{W_o} = \frac{\delta \Delta t}{W_o \Delta t_s} \quad (6.38)$$

where ΔW is the overall deformation in width of the top foil, W_o is the initial width of the foil, δ is the overall deformation in width predicted by the UAM model, Δt is the dwell time and Δt_s is the simulation time of the UAM model. Based on the relation shown in equation 6.38, the predictions of foil width deformation are given in **Table 6.4** and are compared to the experimental data from Kelly et al. in **Figure 6.8**. A good agreement between the UAM model predictions and the experimental measurements can be seen. However, the foil deformation predicted by the model is constantly higher than the measurements from the experiment. This overestimation is most likely due to the no slip assumption between the sonotrode and the top foil. This assumption leads to excessive deformation of the top foil driven by the motion of sonotrode. In reality, however, slip exists at the sonotrode-top foil interface and reduces the actual deformation of the top foil.

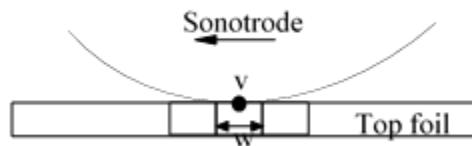


Figure 6.8 The contact length between top foil and sonotrode

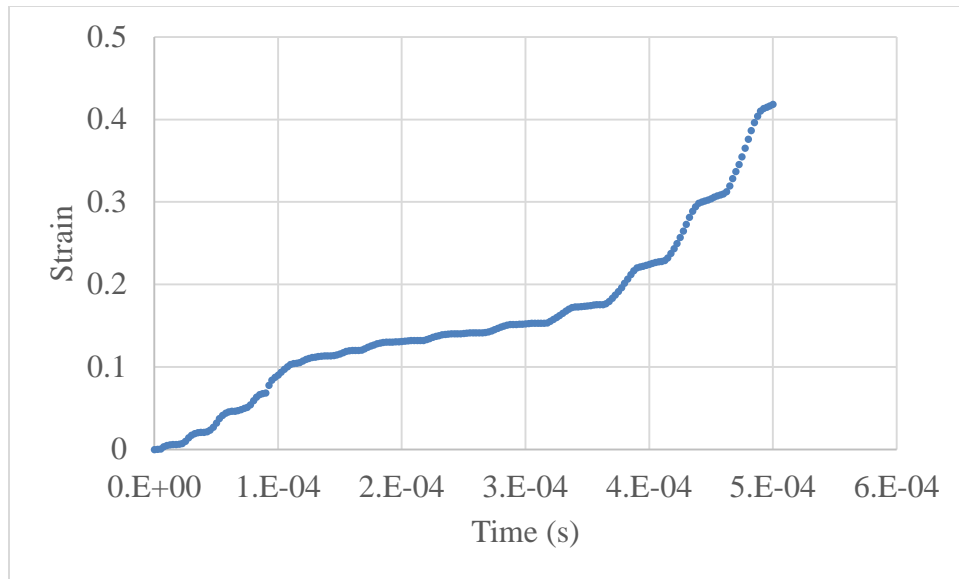


Figure 6.9 The strain history of an element on the edge of the top foil

Table 6.4 The predictions of width deformation by UAM model

Amplitude \ Pressure	10 μm	18 μm	36 μm
45.2 MPa	2.39%	7.26%	14.28%
78.9 MPa	4.20%	7.15%	24.4%

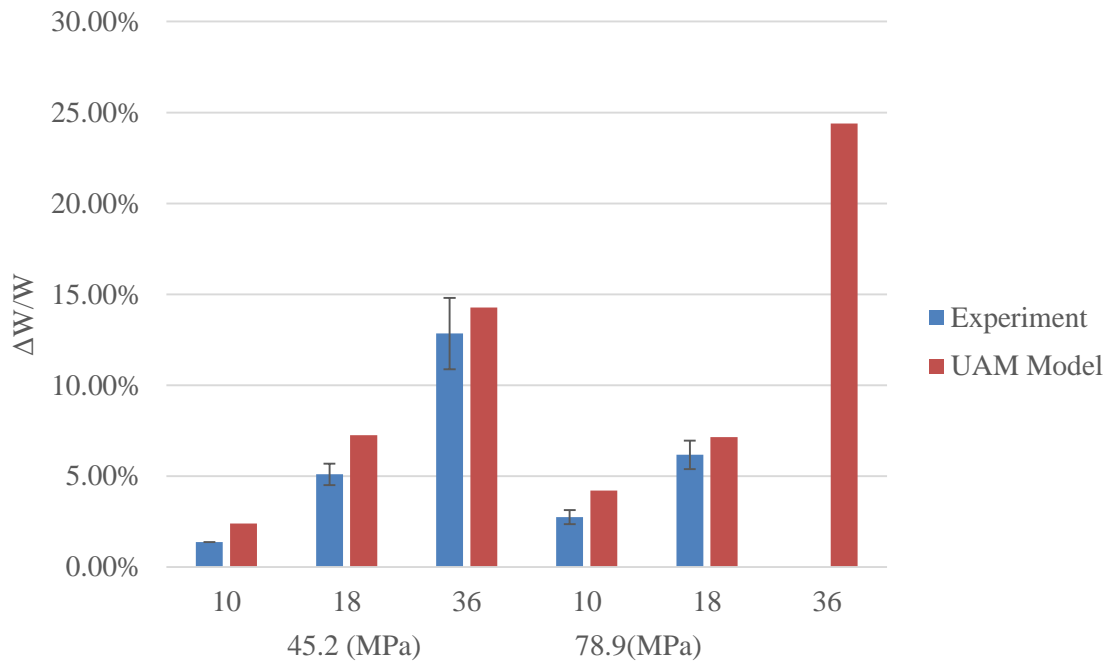


Figure 6.10 he comparison of width deformation between model prediction and experimental data. Experimental data is reproduced from work of Kelly et al. (GS Kelly and Advani 2013).

6.4.2 The Effect of Height-to-width Ratio on Stresses

The UAM model is setup to run at various height-to-width ratios and the stress variations are examined. The material in use is Aluminum 6061-T6. Some parameters are fixed: the amplitude to 10 μm ; the compression to 1600 N; the preheat temperature to 150°C; the simulation time to 0.0007 second (14 cycles). The different stress histories are compared at the critical height (height-to-width ratio equals to 1.0) and at a height away from the critical value (height-to-width ratio equals to 0.2). Notice that in this study the strain rate is set to a constant instead of being calculated based on local strain at each time increment. The value of the constant is estimated using equation (4.4). The reason for using a constant strain rate is that it allows the effect of dynamics to be more visible on the stress

history. If the strain rate varies with time and location, it introduces additional variations to the stress history thus making the dynamic effect less visible.

The dynamic responses of the built feature at various height-to-width ratios are first examined before showing the stress histories (**Figure 6.11**). The dashed line represents the amplitude of the sonotrode and the solid lines represent the oscillation responses from the built feature. It can be observed that both the amplitude and the phase of the dynamic response varies with the height-to-width ratio. The amplitude is modulated due to the difference between the forcing frequency of the sonotrode and the natural frequency of the built feature. Such responses can be explained by considering a simple case in which the built feature is a single-degree-of-freedom (SDOF) oscillator. Neglecting damping and assuming the forcing function to be:

$$F(t) = F_0 \cos \Omega t \quad (6.39)$$

also assuming zero initial conditions, the response of the built feature can be written as:

$$u(t) = \left[\frac{2F_0}{m(\Omega^2 - \omega_n^2)} \sin\left(\frac{\Omega - \omega_n}{2}t\right) \right] \sin\left(\frac{\Omega + \omega_n}{2}t\right) \quad (6.40)$$

where F_0 is the force amplitude, Ω is the circular frequency of the forcing function, ω_n is the natural circular frequency of the built feature. The response oscillates at a high frequency $\left(\frac{\Omega + \omega_n}{2}\right)$ while its amplitude $\left(\frac{2F_0}{m(\Omega^2 - \omega_n^2)}\right)$ oscillates at a low frequency $\left(\frac{\Omega - \omega_n}{2}\right)$. As the height-to-width ratio increases from 0.2 to 1.0, the natural frequency of the built feature decreases and approaches 20 kHz ($\omega_n \rightarrow \Omega$). As a result, the oscillation frequency and phase of the oscillator approaches those of the force. At a height-to-width ratio of 1.0, the amplitude is shown to reach a maximum as the built feature oscillates in phase with the sonotrode (**Figure 6.11**).

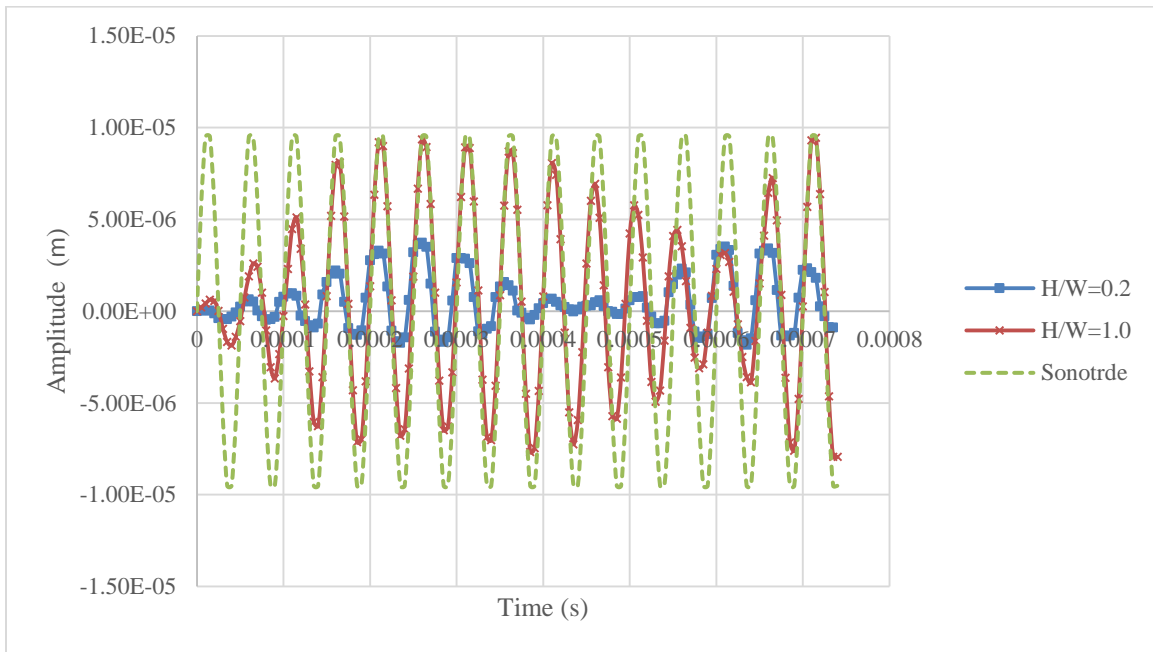


Figure 6.11 The dynamic responses of the built feature at different height-to-width ratios

The dynamics of the built feature has a significant influence on the stresses which is shown as follows. The stresses measures are taken from both the center and the edge of four different layers of the UAM model: top foil, top foil plastic layer, built feature plastic layer, and built feature (**Figure 6.12**). The plastic layers represent the surface asperities of the top foil and the built feature. The stresses considered in this discussion are all taken from the center and the “edge defect” (bond degradation at the edge of the foil) will be discussed separately.

Figure 6.13 shows the stresses in the bulk material of the top foil and its plastic layer as the height-to-width ratio equals 0.2. The yield stress is 225 MPa as indicated by the red centered line. Several observations can be made. First, the top foil undergoes plastic

deformation in both bulk material and plastic layer. Stresses from both bulk material and the plastic layer are above the yield stress in most of the weld cycles. The stress in plastic layer is higher than that in bulk material, indicating more plastic deformation takes place at the bond interface. The maximum stress in the plastic layer is 303.26 MPa and in the bulk material is 265.32 MPa. Second, large amplitude oscillations that resemble “spikes” are observed in both layers. Each spike represents a change in the stress as the sonotrode moves from one extreme position to the other. Therefore each weld cycle yields two spikes. The amplitude of the spike is associated to the amplitude of the differential motion between the top foil and the built feature. Due to the beat phenomenon in the built feature, the amplitude of the differential motion varies periodically which leads to the variation of the spike amplitude. The spike amplitude at the maximum stress in the bulk material layer is 89.96 MPa and in the plastic layer is 77.94 MPa. Furthermore, the spikes are superimposed with the dynamic stresses caused by beating. Since both the dynamic stress and the spike amplitude are driven by beating, they reach the maximum at the same time, thus leading to the maximum in the superimposed stress. The dynamic stress is 175.36 MPa at the maximum stress in the bulk material layer and 225.32 MPa in the plastic layer.

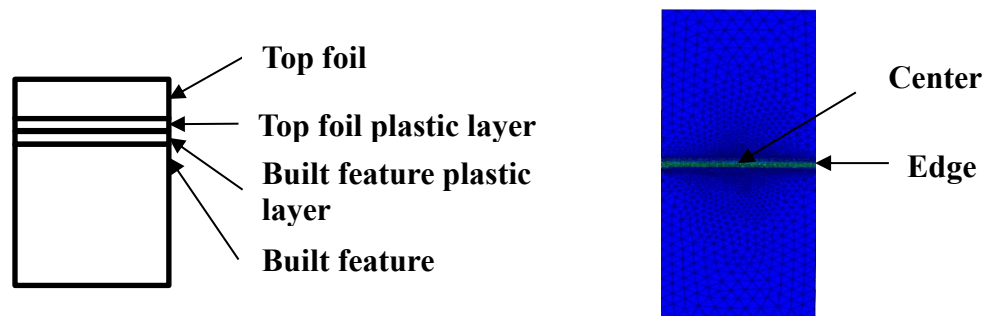


Figure 6.12 The locations of the measuring points on the built feature: side view (left) and top view (right).

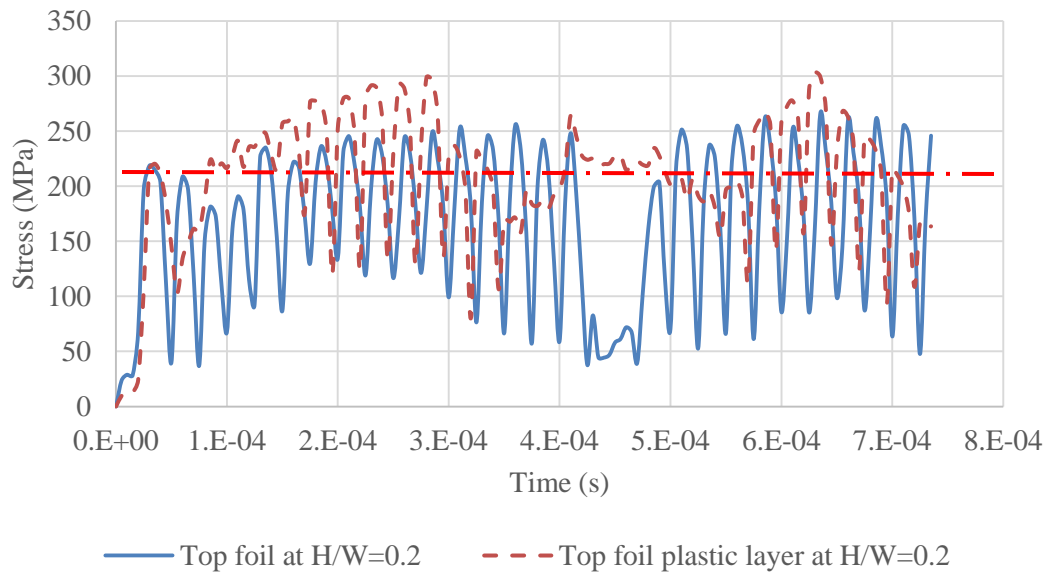


Figure 6.13 The stress history in the top foil and its plastic layer at H/W=0.2

Figure 6.14 shows the stresses in the built feature and its plastic layer at an aspect ratio of 0.2. The stresses in the plastic layer are higher than in the built feature. The stress in the plastic layer becomes plastic as the dynamic stress approaches its maximum whereas the stress in the bulk material remains elastic in the entire course. Both stresses show strong amplitude-modulation and stress superposition between friction and dynamic stresses. The maximum stresses in the plastic layer and the bulk material of built feature are 259.24 MPa 199.53 MPa respectively. A contribution to the stress comes from the oscillation stress whose amplitude is 65.16 MPa in the plastic layer and 25.49 MPa in the built feature. The remainder is due to the dynamic stresses whose amplitude is 194.08 MPa in the plastic layer and 174.04 MPa in the built feature.

In summary, the stresses in top foil bulk material, top foil plastic layer, built feature plastic layer, and built feature bulk material are examined at the height-to-width ratio of 0.2. Stresses in the plastic layers of both the top foil and the built feature exceed the yield stress and are higher in their bulk material counterparts, which indicates more plastic deformation at the bond interface. The stresses result from the superposition of the high frequency oscillating stresses due to sonotrode vibration and the low frequency dynamic stresses due to the beat phenomenon in built feature vibration. The oscillation amplitude is higher in the top foil than in the built feature, which indicates that the stresses in top foil are more influenced by the vibrating sonotrode. In contrast, the amplitude modulation of the stress due to the beat phenomenon is more significant in the built feature than in the top foil, which indicates that the stresses in built feature are more influenced by the vibration of the built feature. To conclude, the stresses close to the bond interface are significantly affected by the dynamics of both the sonotrode and the built feature. The maximum stresses and the dynamic and friction stresses that contribute to the stress are summarized in **Table 6.5**.

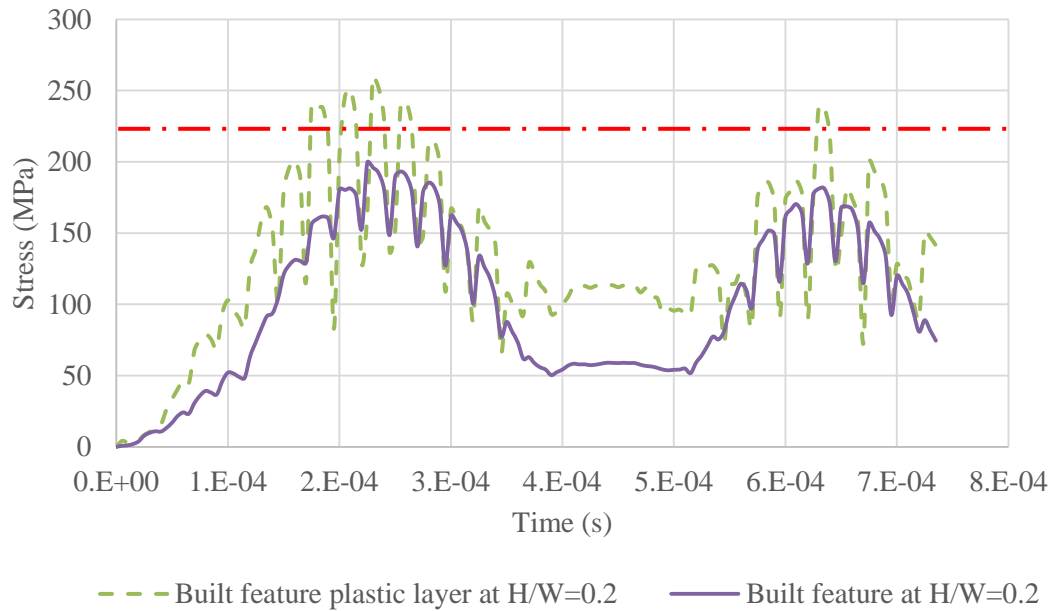


Figure 6.14 The stress histories in the built feature and its plastic layer at H/W=0.2

At height-to-width ratio equals 1.0, the stresses in top foil and its plastic layer are shown in **Figure 6.15**, and the stresses in the built feature and its plastic layer are shown in **Figure 6.16**. In **Figure 6.15**, both stresses exceed the yield stress as the dynamic stress approaches its maximum, but the oscillation amplitudes are much smaller than the ones obtained for a height-to-width ratio of 0.2. Moreover, the stresses in the plastic layer are smaller than the stresses in the bulk material, indicating sticking at the interface and a lack of plastic deformation in the bond layer. In the built feature, the stresses in the plastic layer are higher than those in the bulk material of the built feature (**Figure 6.16**). However, neither the plastic layer nor the built feature undergo plastic deformation, which indicates insufficient plastic deformation at the bond interface. The maximum stresses as well as the

oscillation and dynamic stresses that contribute to the maximum stress are shown in **Table 6.5**.

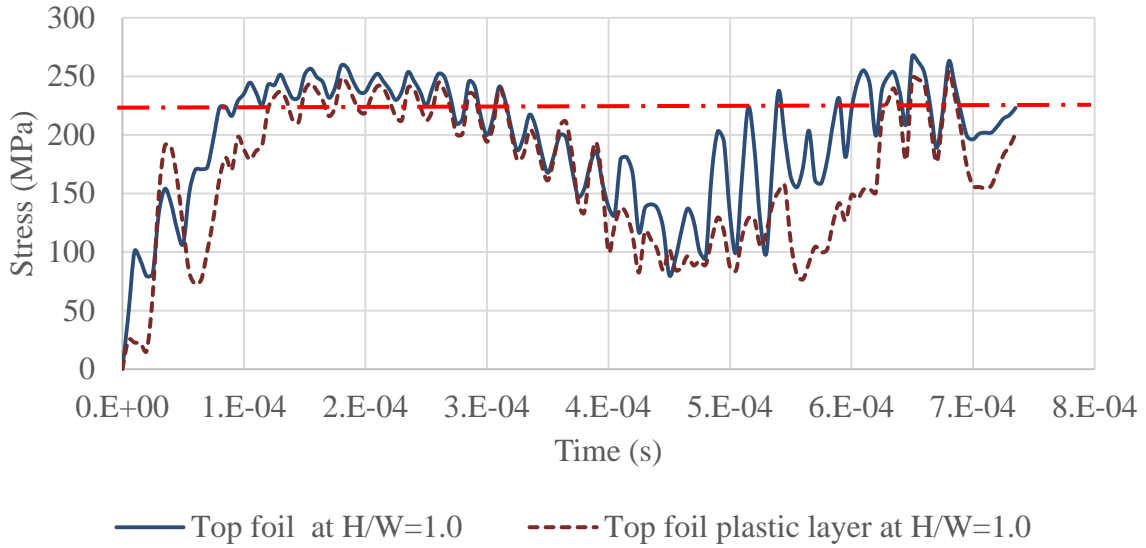


Figure 6.15 The stress histories in the top foil and its plastic layer at H/W=1.0

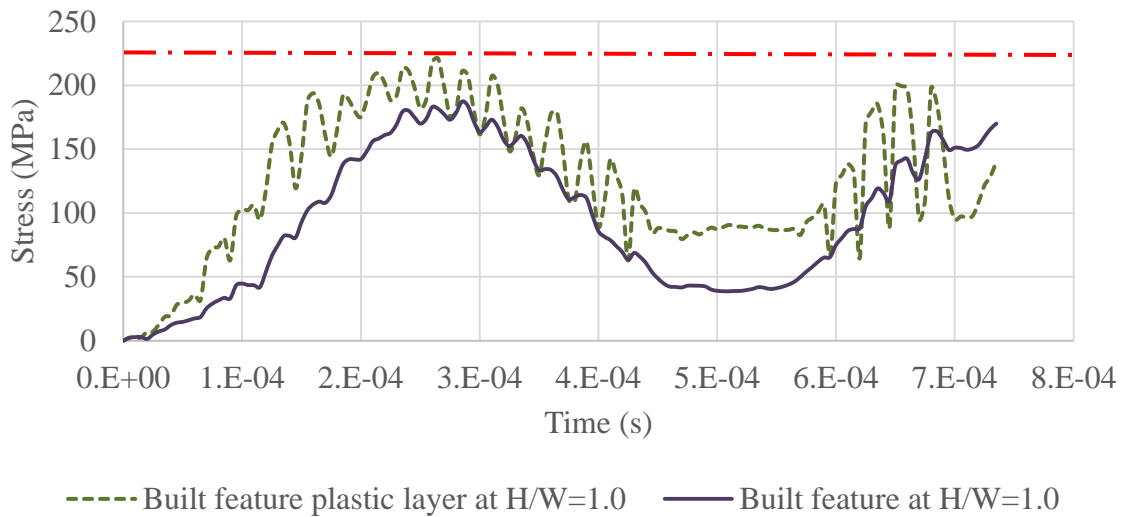


Figure 6.16 The stress histories in the built feature and its plastic layer at H/W=1.0

Table 6.5 Comparison of maximum stresses, friction stresses, and dynamic stresses at H/W=0.2 and H/W=1.0

	H/W=0.2			H/W=1.0		
	Max. stress (MPa)	Contribution from dynamic stresses (MPa)	Contribution from friction stresses (MPa)	Max. stress (MPa)	Contribution from dynamic stresses (MPa)	Contribution from friction stresses (MPa)
Top foil	265.32	175.36	89.96	267.19	228.04	39.15
Top foil plastic layer	303.26	225.32	77.94	253.78	215.29	20.49
Built feature plastic layer	259.24	194.08	65.16	220.97	198.46	22.51
Built feature	199.53	174.04	25.49	187.25	180.14	7.11

Figure 6.17 shows the comparison of maximum, friction, and dynamic stresses at height-to-width ratio of 0.2 and 1.0. The sum of friction stresses and dynamic stresses yields the maximum stresses. In the case of the 0.2 aspect ratio, the maximum stresses in the plastic layers are well above the yield stress whereas in the case of 1.0, only the maximum stresses in top foil plastic layer exceeds the yield stress. Moreover, the maximum stresses show significant differences between the plastic layers of the top foil and the built feature. These differences in the maximum stress are largely contributed by the differences in the friction-induced stresses and little differences are seen in the dynamic stresses. As a result, it can be concluded that at the critical height-to-width ratio, the bond

degradation is caused by the insufficient plastic deformation at the bond interface due to the significant reduction in friction stresses.

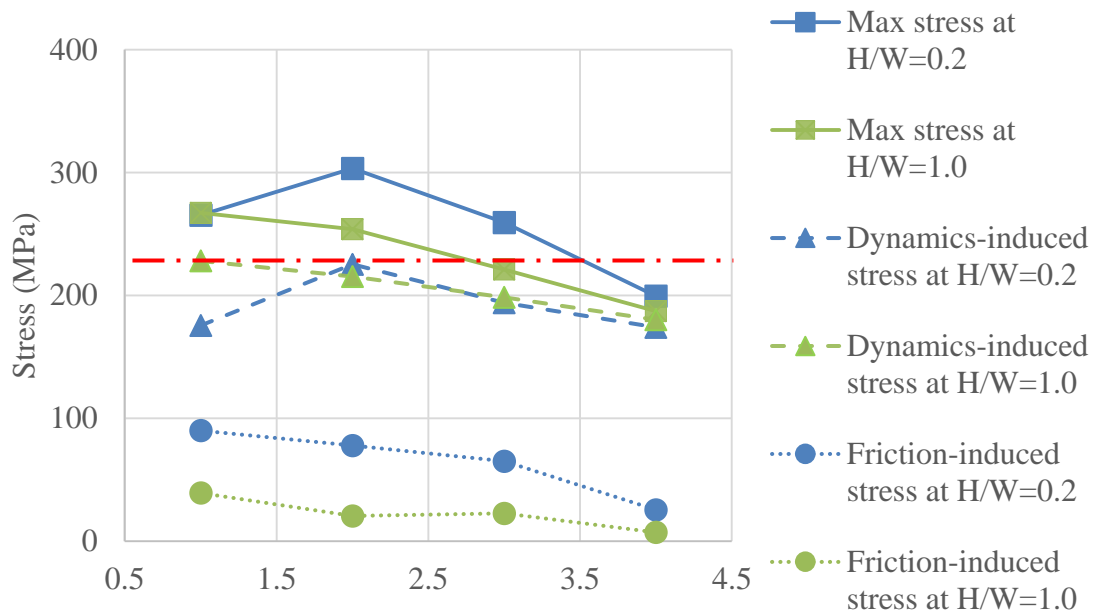


Figure 6.17 The comparison of the maximum, friction, and dynamic stresses at H/W=0.2 and H/W=1.0

In summary, the dynamic and stress histories at different height-to-width ratios are examined and compared. The dynamics of the built feature changes as the height-to-width ratio varies. A beat phenomenon is observed at the critical height-to-width ratio of 1.0. The stresses are shown to be a superposition between the friction stresses and the dynamic stresses. Specifically, the friction stresses depend on the magnitude of the differential motion between the top foil and the built feature. The dynamic stresses depend on the dynamics of the built feature. An insufficient plastic deformation is observed close to the bond

interface at the critical aspect ratio and is assumed to be the cause of the bond degradation. The lack of plastic deformation is shown to be due to the lack of frictional stresses which is further associated to the beat phenomenon observed at the critical aspect ratio.

6.4.3 Energy Flow in UAM

From the energy point of view, the UAM is a process that joins metal foils using ultrasonic energy. While the energy flows are difficult to measure experimentally, they can be quantified in the numerical model. In this section, the different energy flows within the UAM model are examined and discussed.

Here we confine our study to the overall energy exchange within the entire model and therefore the control volume is set to the entire UAM system. Since there exists no exchange of matter between the UAM system and its surroundings, the system is considered as a closed system. For the closed system, the conservation of energy for the system can be written (the first law of thermodynamics):

$$\frac{dE}{dt} = \dot{Q} - \dot{W} \quad (6.41)$$

where \dot{Q} is the rate of total heat transferred to the system, \dot{W} is the rate of total work done by the system, $\frac{dE}{dt}$ is the rate of change of energy of the system which can be further decomposed:

$$E = E_I + E_{KE} + E_P \quad (6.42)$$

where E_I is the internal energy, E_{KE} is the kinetic energy, and E_P is the potential energy.

The energy balance equation is reformulated in ABAQUS as (Abaqus 2015):

$$E_{TOT} = E_I + E_{KE} + E_{FD} + E_{VD} - E_W = constant \quad (6.43)$$

where E_{TOT} is the total energy of the system. E_I is the internal energy defined as the sum of elastic, plastic, and “artificial” strain energies. Artificial strain energy refers to the energy used for resisting hourglass mode (zero energy mode due to the reduced-integration of the elements) in a finite element model. E_{KE} is the kinetic energy. E_{FD} and E_{VD} are energy due to friction and viscous dissipation respectively. E_W is the work of the external forces and the prescribed boundary conditions which include the compressional force in normal direction and the force that drives the vibration of the sonotrode. The total energy should be close to zero or remain at a constant level based on the energy balance. These quantities are examined and discussed as follows.

Figure 6.16 shows the evolution of the external work and the different energies with respect to time. The material used for the UAM model is Aluminum 1100-O. The operating parameter settings are shown in **Table 6.6**. The simulation is run for 10 cycles or equivalently 0.0005 seconds and the energies are calculated based on the time interval. From the plot, it can be observed that a majority of the external work is converted to the kinetic energy of the system (1.44e-3 J). It is found that the kinetic energy is almost entirely associated to the vibration of the sonotrode and the kinetic energy due to vibration of the built feature can be neglected. Since this energy study is focused on the energy flow in bonding process, the kinematic energy will not be considered. The second highest energy in the system is the internal energy (1.09e-4 J) which includes elastic, plastic, and artificial strain energy. Specifically, the artificial strain energy remains zero throughout the simulation time which indicates that the model is free of hourglass effect. The elastic strain energy

is 2.52×10^{-5} J whereas the plastic dissipation is 8.35×10^{-5} J. This indicates that the majority of energy dissipation within the UAM system is due to plastic deformation. Further, the energy dissipation due to plastic deformation and friction are compared in **Figure 6.19**. The contribution from plastic deformation (8.35×10^{-5} J) is shown to be far greater than from friction (2.45×10^{-6} J). Similar conclusions are made by Sriraman et al. and Gao et al (Gao and Doumanidis 2002; Sriraman et al. 2011; Sriraman, Babu, and Short 2010). Sriraman et al find that the temperature increase at the bond interface is associated to the yield strength of the material and therefore conclude that the dissipation due to plastic deformation is the major contributor of interfacial heat generation. Opposite conclusions are made by Siddiq et al.(A. Siddiq and Ghassemieh 2008a; Amir Siddiq and Sayed 2012) who claimed that heat dissipation at the bond interface is largely contributed by friction. However, no detailed justification is provided. The remaining energies such as viscous dissipation and creep dissipation are close to zero and their contribution are negligible.

Table 6.6 The operating parameters used for studying energy flow

Amplitude	Compression	Simulation time	Preheat temperature
9 μm	6000 N	0.0005 s (10 cycles)	135 $^{\circ}\text{C}$

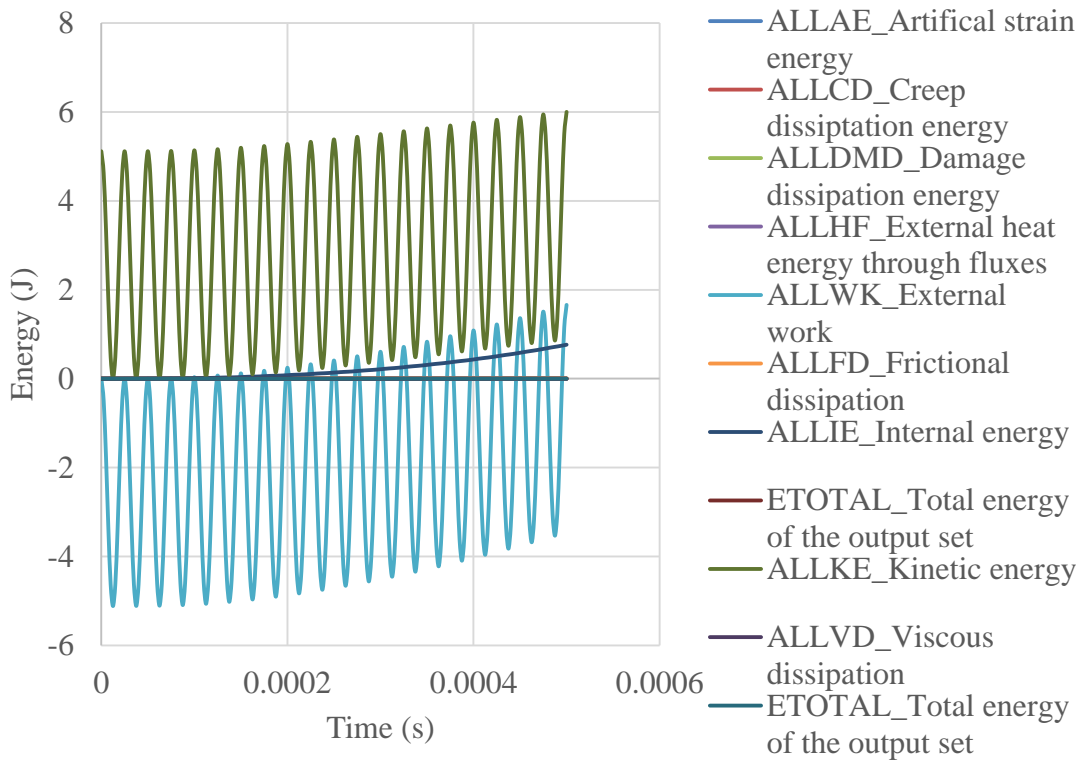


Figure 6.18 An overview of the work and energies involved in the UAM process

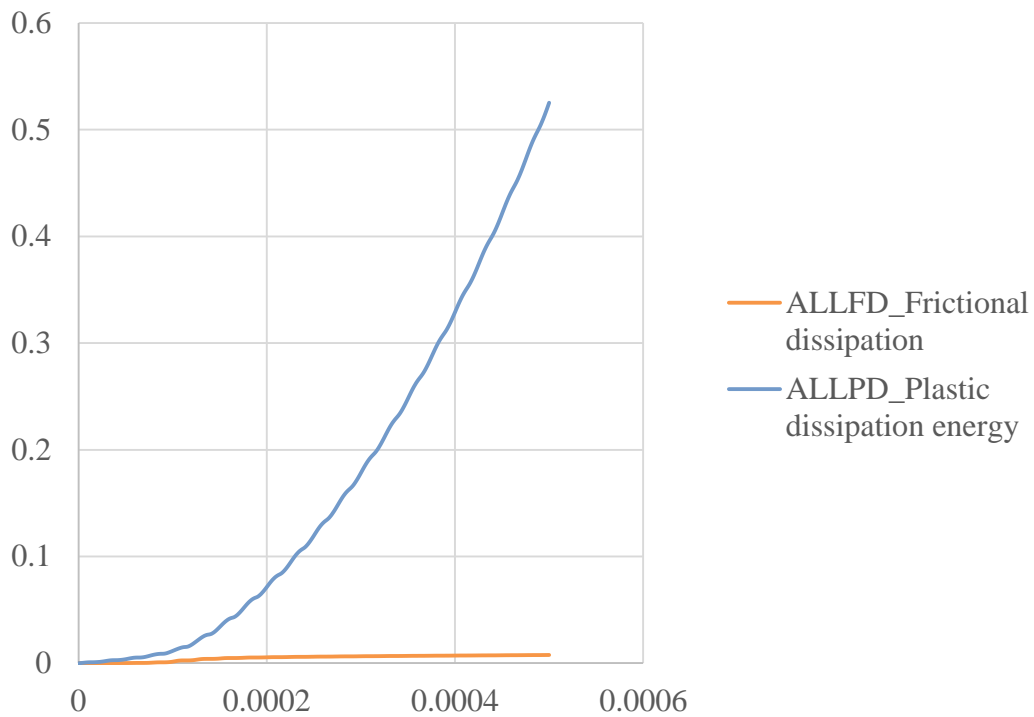


Figure 6.19 The comparison of energy dissipation due to friction and plastic deformation

It should be noted that the ultrasonic and thermal energy that contribute to the acoustic and thermal softening are not accounted for in the above energy balance equation of the UAM model since they are introduced by artificially modifying the constitutive equation of the material. These energies, however, can be estimated by taking the difference between the integrated areas underneath stress strain curves from the UAM simulations with and without ultrasonic and thermal irradiation (**Figure 6.20.**). For instance, when the simulation is run without ultrasonic irradiation, the area underneath the stress-strain curve represents the total increase of strain energy due to work from the external load. When

the simulation is run under ultrasonic irradiation, the lowering in tensile stress leads to reduction of the work due to external load. The amount of reduction is equal to the ultrasonic energy consumed to achieve the softening. The relation can be written as:

$$W_{non-soft} = W_{soft} + E_u \quad (6.44)$$

where $W_{non-soft}$ is the work done by external load without ultrasound, W_{soft} is the work done by external load with ultrasonic irradiation, E_u is the ultrasonic energy contributing to acoustic softening. In the specific case under study, the ultrasound is estimated to cause a stress reduction of 56%. Similar analyses can be applied for estimating the thermal energy consumption. With the preheat temperature used in the study, the thermal softening effect is estimated to reduce the stress by 31%. As a result, the total energy consumed for acoustic softening in 10 weld cycles is estimated to be 5.40e-4 J and for thermal softening is 2.99e-4 J. The amount of different energies that participate in the UAM bonding process can be defined in **Table 6.7** and the proportions are visualized in **Figure 6.19**.

Table 6.7 The summary of different energies within the UAM system for 10 weld cycles

Elastic Strain Energy	Plastic Dissipation	Friction Dissipation	Acoustic Softening	Thermal Softening	Others
2.52e-5 J	8.35e-5 J	2.45e-6 J	5.40e-4 J	2.99e-4 J	1.53e-08 J

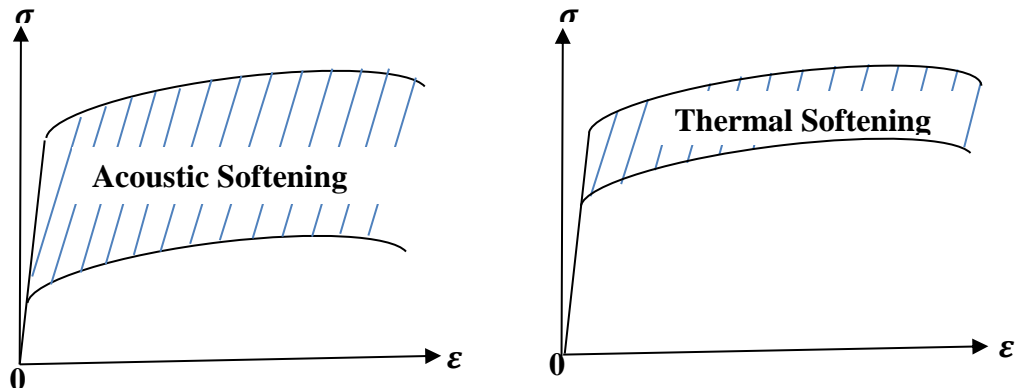


Figure 6.20 The schematics of energy consumption estimation based on a stress strain curve for acoustic softening (left) and thermal softening (right).

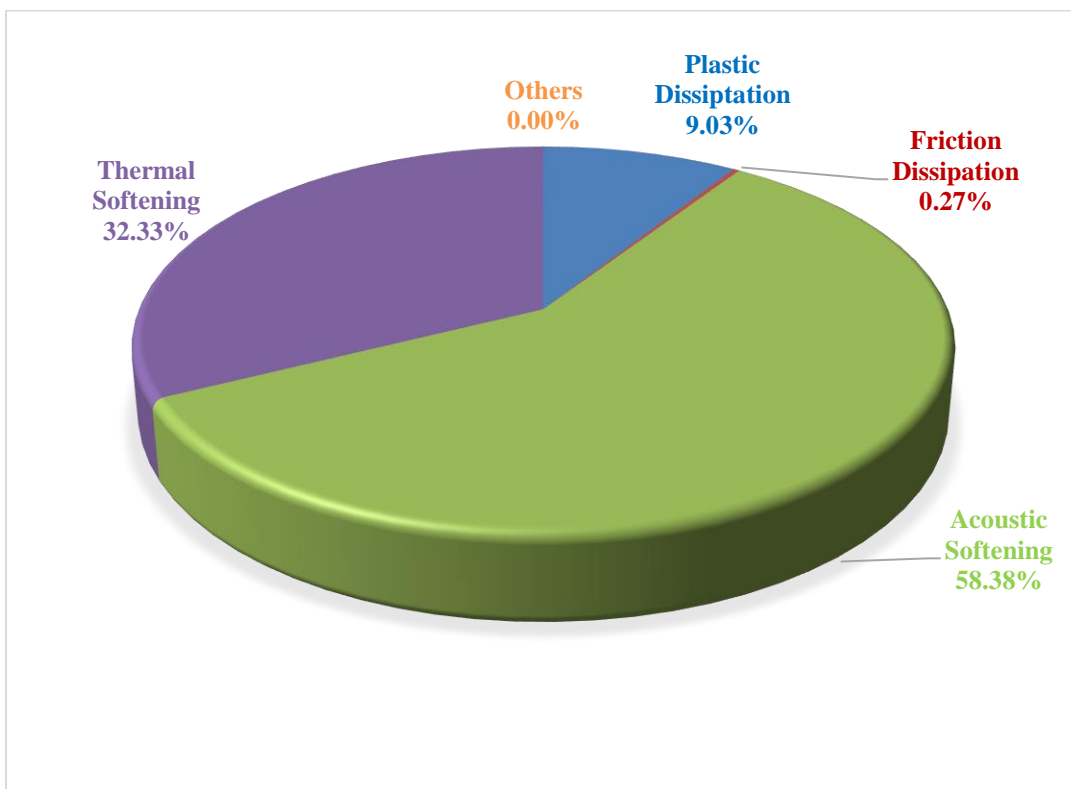


Figure 6.21 The proportion of different energies in UAM

6.4.4 Associating the UAM Predictions to Bond Quality

In this section, the asperity layer model developed in section 6.3 is introduced into the UAM model in order to associate the predictions of plastic deformation to the bond quality. The percentage of area in contact in the bond region is calculated and directly associated to the linear weld density. Then the model is run with different operating parameter combinations and the resulting linear weld densities are compared.

The asperity layer is built into the bond region on the top surface of the built feature and the plastic layers that represent asperities are removed accordingly. The entire bond region is covered by asperities whose amplitude-to-wave-length ratio is equal to 20. The selection of this ratio is discussed in section 6.3. As the welding starts, the sinusoidal asperities deform as they come into contact with the bottom surface of the top foil. The real contact area is calculated as the sum of areas of the element facets that are subjected to contact forces, whereas the nominal contact area is defined as the overall area of the region where contact takes place. The ratio of real contact area and the overall contact area is equivalent to the linear weld density in UAM which is defined by Kong et al as the percentage of real contact area A_r to the apparent weld region A_p (Kong, Soar, and Dickens 2005):

$$\alpha = \frac{A_r}{A_p} \times 100\% \quad (6.45)$$

The material selected for testing the UAM model is Aluminum 6061-T6. The combinations of the operating parameters are selected based on the experimental work by Wolcott et al.(Wolcott, Hehr, and Dapino 2014). They carried out a series of UAM bonding tests using a very high power ultrasonic additive manufacturing (VHP-UAM) machine

whose amplitude can reach as high as 46.8 μm and normal load can reach 15 kN. Due to the significant increase of power, some materials that previously were not able to be welded are tested in the study. These materials include the Aluminum 6061-T6 which is bonded using amplitude between 28 μm and 33 μm , normal load between 4000 N and 6000 N, and weld speed between 84.6 mm/s and 106.8 mm/s. The bond quality are then evaluated using push-pin test to identify the optimum operating parameters.

Based on the process parameters used in the literature, the model is run at two different compression loads: 4000 N and 6000 N, and three different amplitudes: 10 μm , 20 μm and 35 μm . The preheat temperature is set to 150 °C. The simulation time is 0.0005 s (10 cycles). The predicted linear weld densities for different cases are presented in **Figure 6.20**. It is shown that the predicted linear weld density varies between 22.3% and 36.9% and depends on both the amplitude and the normal load. The linear weld density is improved by increasing either the amplitude or the normal load. The dependence of the linear weld density on the amplitude is close to linear. The prediction is reasonable since higher amplitude leads to more significant acoustic softening and higher shearing strain to initiate plastic deformation, and higher normal load leads to higher compression and shearing force that also facilitate the deformation. As a result, the highest linear weld density (36.9 %) is found under the highest amplitude (35 μm) and the higher normal load (6000 N). The push-pin test, however, shows that the strongest bond depends only on the amplitude (Wolcott, Hehr, and Dapino 2014). When the normal load is higher than 4000N, the bond quality becomes constant as the normal load increases. This divergence in the prediction is due to the different bond criteria used for bond quality evaluation. The linear weld density and

the maximum load for breaking the specimen are not necessarily correlated. A bond that yields high linear weld density could give low load at breaking due to excessive strain hardening and cyclic stressing which improve interface contact but weaken the bond (Kong, Soar, and Dickens 2003). Similarly a bond that yields high load at breaking could give low linear weld density due to the inhomogeneous distribution of high strength bonds.

The results is further compared to the linear weld density reported by Kong et al. (Kong, Soar, and Dickens 2003) who carry out a series of bond tests on Aluminum 6061-O. The linear weld density is shown to vary between 16 % - 45 % which is similar to the range of our prediction: 22.31% - 36.90%. The variation of the linear weld density with respect to the amplitude and the normal compression is shown in **Figure 6.21**. Similar to our finding, strong dependence is observed on both operating parameters and the dependence on the amplitude is close to linear. Also, the increase of normal load by 75% (in Kong's work) and by 50% (in our work) both lead to the increase of 5%-10% in the linear weld density. However, the amplitude used in Kong's work (8.4 μm – 14.3 μm) is lower than the amplitude used in our work (10 μm - 35 μm). This divergence could be caused by multiple factors. First, the temper of the materials used in two tests are different. Kong at al. use the O temper whereas T6 temper is used in our test. The yield strength of Aluminum 6061-O is around 65 MPa whereas for Aluminum 6061-T6 the yield strength is 300 MPa. The difference in the strength of the materials requires different ultrasound intensity for achieving satisfactory bonds. Second, the asperity model is a phenomenological model and does not reflect the physical behavior of the asperities. As a result, the model has to be calibrated by the experimental data of linear weld density before quantitative predictions

are carried out. Parameters such as the nominal bond area as well as the spacing of the asperities may require adjustment depending on the material or the surface topography of the foils used in the experiments.

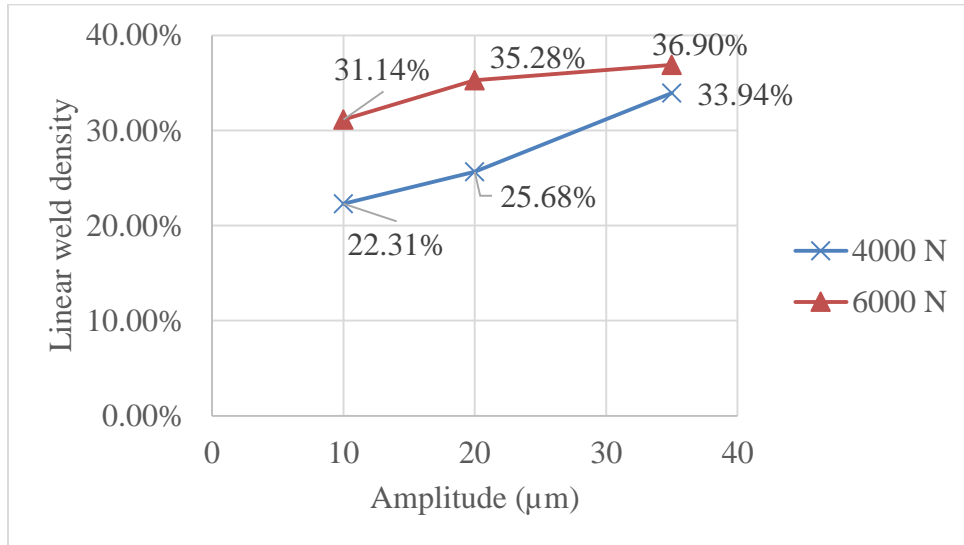


Figure 6.22 The bond quality of Aluminum 6061-T6 at different amplitude and compression combinations.

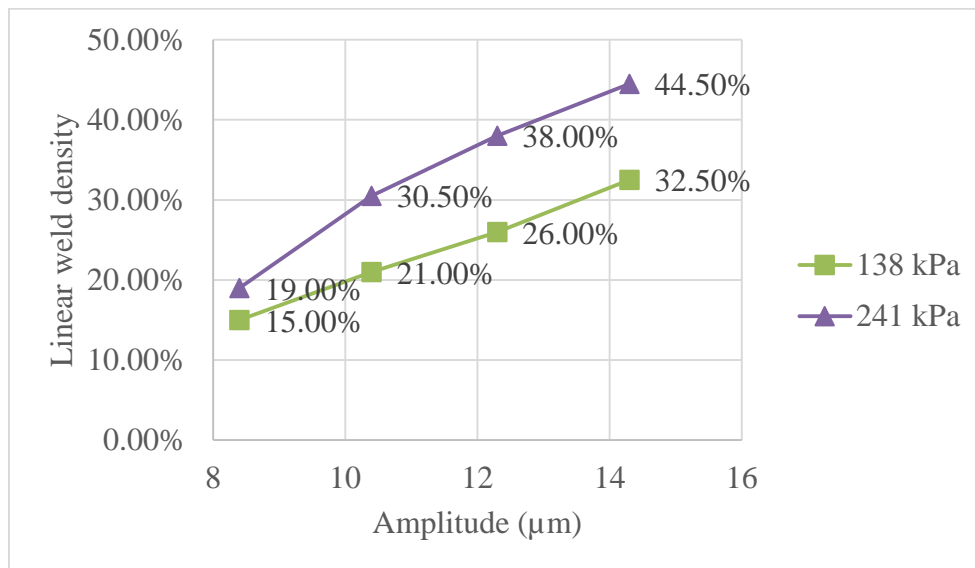


Figure 6.23 The bond quality of Aluminum 6061-O at different amplitude and compression combinations

By using the linear weld density as the bond quality criterion, the height-to-width ratio problem can now be reconsidered to identify the threshold for bond/debond. The material assigned to the model is Aluminum 6061-T6 and the material properties are the same as in the last test. Two sets of weld parameters are used: one optimum set which yields high quality bonds and one less satisfactory set which yields low quality bonds. Both sets are obtained from the work by Wolcott et al. who carried out a design of experiments study to optimize weld parameters for Aluminum 6061-T6 (Wolcott, Hehr, and Dapino 2014). The bond quality are evaluated using push-pin tests. The two sets of weld parameters are shown in **Table 6.8**. The model is run at different height-to-width ratios: 0.2, 0.6, 0.8, 1.0, 1.2, 1.4, 1.8 and 2.0 and the results are shown in **Figure 6.22**.

For tests using the optimum weld parameter setting, the predicted linear weld density varies between 38% and 46% as the height-to-width ratios varies between 0.2 and 2.0. The minimum value of the linear weld density is reached at the height-to-width ratios of 1.2 which yields the minimum density of 38.67%. This value is relatively high compared to the experimental measurement. According to Foster, the lower limit of the typical linear weld density obtained from the Solidica Formation machine is around 37 % for Aluminum 3003-H18 (D. R. Foster, Dapino, and Babu 2013). The linear weld density, however, could vary depending on the material and the operating parameters in use. In general, the weldability of Aluminum 6061-T6 is not as good as Aluminum 3003-H18 and therefore requires higher power for bonding. However, the operating parameters (a compressive load of 6000 N and an amplitude of 35 μm) used for welding 6061-T6 in our test are much higher than

the maximum capabilities of the Solidica Formation machine (a compressive load of 2200 N and an amplitude of 26 μm). As a result, it is possible that by using significantly higher weld parameters, the minimum linear weld density could be improved. Experimental studies are needed to validate this point. The variation of the linear weld density indicates a drop as the height-to-width ratio increases from 0.8 to 1.0 and the value remains below 40% up to a ratio of 1.4. Kong et al. uses a threshold of $45\% \pm 5\%$ for identifying the “good bond” for Aluminum 6061-O and therefore 40% is adopted as the threshold that separates bond/debond. Therefore, the debond due to resonance of the built feature takes place as the height-to-width ratio varies between 1.0 and 1.4 for the specific material and operating parameters tested.

For tests using less satisfactory weld parameter setting, a reduction of 12.7% is observed in the linear weld density comparing to tests using optimum weld parameter setting. The data also shows a smaller range (27.9% - 32.5%) as the height-to-width ratio varies from 0.2 to 2.0. The linear weld density is well below the bonding threshold of 40%. By introducing the asperity layer to the UAM model, the macroscopic dynamics of the built feature is successfully related to the linear weld density at the bond interface.

Table 6.8 The weld parameter sets for studying the H/W ratio problem for Aluminum 6061-T6

Weld set	Compression load (N)	Amplitude (μm)	Preheat temperature ($^{\circ}\text{C}$)	Simulation time (s) (# of cycles)
Optimum	6000	35	150	0.001 (20)
Less satisfactory	4000	25	150	0.001 (20)

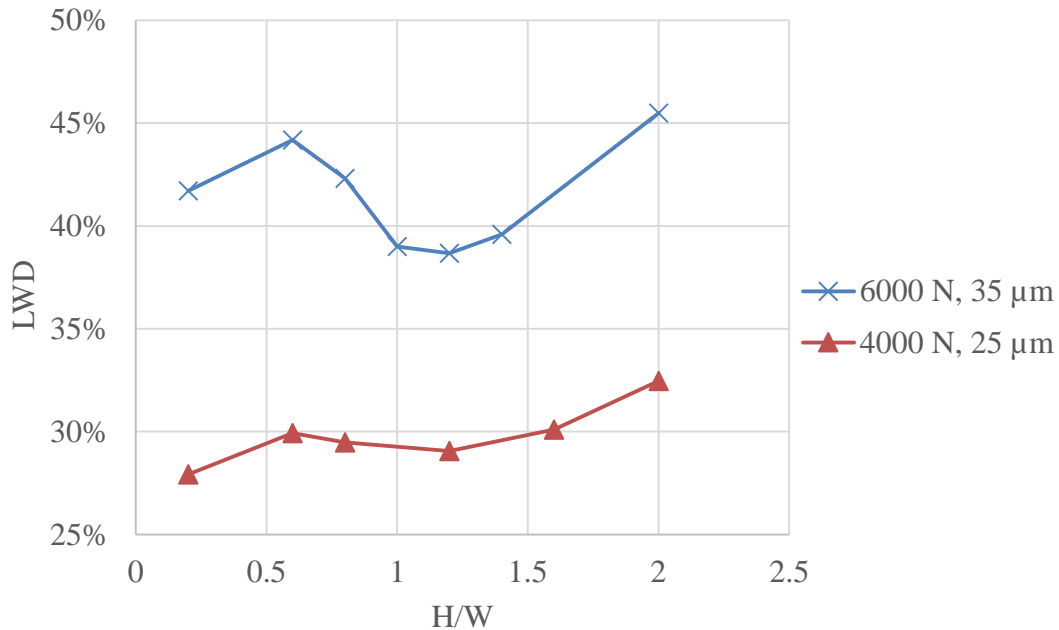


Figure 6.24 The linear weld density (LWD) for bonding Aluminum 6061-T6 at different height-to-width (H/W) ratios.

6.5 Summary

This chapter presents the integrated UAM model and shows the implementation of the model to predict the deformation of foils, to understand the stress state of the materials close to the bond interface, to understand the energy flow in the UAM system, and to evaluate the effects of different weld parameters on the linear weld density of the bond. The UAM model is a new tool to understand the UAM bonding process by examining the dynamics of its components, and associating the dynamics to the stress and strain of the material close to the bond interface. The model also provides insights into the energy flow within the system. By associating the plastic deformation predictions at the bonding interface to the linear weld density of the bond, UAM model shows its capability in predicting

the optimum process parameters for process optimizations. In the next chapter, the research questions are answered based on the completed work. The different contributions of this work and the potential future research that could further expand the implementation of the model are also highlighted.

Chapter 7

7 Concluding Remarks

In this chapter, the research questions presented in Chapter 2 are answered. These research questions are:

1. How can the acoustic softening effect be taken into account in the modeling of the UAM process?

1.1 How can one design an experiment to quantify the acoustic softening effect?

1.2 How to analytically model acoustic softening?

2. Which analytical models should be integrated to better characterize the UAM process?

2.1 How to establish a plasticity model that incorporates acoustic and thermal softening?

2.2 How to account for all the factors associated with heat transfer and friction in UAM?

2.3 How to account for the variation of dynamic conditions in a UAM model?

2.4 How can the UAM model be validated?

3. What are the criteria used for evaluating bond quality and how can they be used to evaluate the performance of the UAM model?

4. How can one evaluate the performance of the proposed UAM model in terms of optimization of process parameters?

5. How can one quantify the energy flow in the UAM process?

7.1 Research Question 1

The acoustic softening should be accounted for in a plasticity framework which characterizes the plastic behavior of the material. However, due to the lack of experimental data for modeling, experimental studies are carried out in the first place. To answer the two sub questions:

- An experimental setup similar to the one used by Blaha and Langenecker is established and acoustic softening is quantified in terms of stress reduction on the stress-strain curves.
- Based on the experimental observations, a relationship is established between the stress reduction and the ultrasound intensity. The analytical model is proposed to characterize this relationship.

7.2 Research Question 2

The models that should be accounted for in the UAM model include the plasticity, thermal, friction, and dynamic models. These models are explained by answering the sub questions:

- A new plasticity model was developed. It takes into account acoustic and thermal softening, and hardening due to high strain rate.
- A thermal model is introduced and is closely coupled with the dynamic model making the UAM model a thermo-mechanical model.
- Friction is accounted by establishing a friction model that characterizes the friction coefficient. Contributions from all the influential factors are identified from the literature and accounted for in the model. The friction model is closely coupled with the thermal model.
- The dynamics of the UAM system is accounted for in a dynamic model which is solved using finite element method. Due to the expensive computational cost of the high frequency vibration, a lumped parameter model consisting of mass-spring networks is proposed as an alternative to reduce the computational cost. The implementation of the model could be a part of the future work.
- Each of the sub-model can be validated by comparing its prediction with experimental data from our own experiments or from experiments in the literature. For instance, the plasticity model that incorporates acoustic softening is validated by comparing the predicted stress-strain curves with the

acoustic softened curves from our experiments. The integrated UAM model is validated by comparing its predictions on the material deformation with experimental studies reported in the literature.

7.3 Research Question 3

There are various criteria for evaluating the bond quality and the one selected for this study is the linear weld density. An asperity model is developed by idealizing and simplifying the shape and size of the asperities. The model is then implemented in the UAM model and the effective contact area between the top foil and the deformed asperities is calculated. The effective contact area is then used for calculating the linear weld density. The performance of the model can be evaluated by comparing the predicted linear weld density with those reported from experimental studies in the literature.

7.4 Research Question 4

By using the same materials and operating parameter setups, the UAM model can be used for process optimization and the predicted optimum process window can be compared to the ones achieved through design of experiments (DOE) (i.e., setting up a series of experiments in which operating parameters are varied to search for the set of parameter that yields the optimum bond quality). Further, the predicted bond quality can also be assessed if the DOE results is evaluated using linear weld density.

7.5 Research Question 5

The overall energy flows in the UAM system can be quantified simply by calculating the different works and energies using the UAM model. A more detailed energy quantification at a specific location or at a specific moment would require additional processing but is doable with the UAM model.

7.6 Contributions

A list of contributions from this work to the understanding of the UAM bonding process is listed as follows:

- The first experimental investigation on the acoustic softening of several materials that are extensively used in UAM process: Aluminum 6061-T6, Aluminum 6061-O, and Copper 11000-O.
- The work proposed a plasticity framework by modifying the Johnson-Cook plasticity model and accounted for the strain rate hardening, acoustic and thermal softening in the UAM process.
- The work presented an asperity model to associate the material deformation to UAM bond quality. By using the model, the thermo-mechanical model is able to predict bond quality for the first time.
- The work developed a lumped parameter consisting mass-spring network for characterizing the dynamics of the built feature.

- The thermo-mechanical UAM model explicitly elucidated how the macroscopic dynamics of the UAM system affect the internal stresses and the deformation of the material close to bond interface
- The thermo-mechanical UAM model showed the energy conversion within the UAM system
- The thermo-mechanical model showed its potential in UAM process optimization.

7.7 Future Work

- To account for the cyclic effects in the plasticity model. The model framework may have to be changed.
- The softening effect could be better characterized using a physically-based model if changes in the microstructure (ex. the density of the dislocations, the rotation of grain orientations, the change in size and location of the precipitates in Aluminum 6061-T6 alloys, etc) of the softened materials are studied.
- Improve and integrate the lumped parameter dynamic model into the UAM model.
- Validate the bond quality predictions by carrying out experimental studies using different weld parameter combinations.

Appendices

Appendix A The User Defined Material Subroutine (VUMAT)

```
C
C Coding for Isotropic Hardening Plasticity VUMAT-Modified Johnson-Cook Model
C
SUBROUTINE VUMAT(
C Read only -
1 NBLOCK, NDIR, NSHR, NSTATEV, NFIELDV, NPROPS, LANNEAL,
2 STEPTIME, TOTALTIME, DT, CMNAME, COORDMP, CHARLENGTH,
3 PROPS, DENSITY, STRAININC, RELSPININC,
4 TEMPOLD, STRETCHOLD, DEFGRADOLD, FIELDOLD,
5 STRESSOLD, STATEOLD, ENERINTERNOLD, ENERINELASOLD,
6 TEMPNEW, STRETCHNEW, DEFGRADNEW, FIELDNEW,
C Write only -
7 STRESSNEW, STATENEW, ENERINTERNNEW, ENERINELASNEW)
C
INCLUDE 'VABA_PARAM.INC'
C
DIMENSION PROPS(NPROPS), DENSITY(NBLOCK), COORDMP(NBLOCK),
1 CHARLENGTH(NBLOCK), STRAININC(NBLOCK, NDIR+NSHR),
2 RELSPININC(NBLOCK, NSHR), TEMPOLD(NBLOCK),
3 STRETCHOLD(NBLOCK, NDIR+NSHR), DEFGRADOLD(NBLOCK, NDIR+NSHR+NSHR),
4 FIELDOLD(NBLOCK, NFIELDV), STRESSOLD(NBLOCK, NDIR+NSHR),
5 STATEOLD(NBLOCK, NSTATEV), ENERINTERNOLD(NBLOCK),
6 ENERINELASOLD(NBLOCK), TEMPNEW(NBLOCK),
7 STRETCHNEW(NBLOCK, NDIR+NSHR), DEFGRADNEW(NBLOCK, NDIR+NSHR+NSHR),
8 FIELDNEW(NBLOCK, NFIELDV), STRESSNEW(NBLOCK, NDIR+NSHR),
9 STATENEW(NBLOCK, NSTATEV), ENERINTERNNEW(NBLOCK),
1 ENERINELASNEW(NBLOCK)

CHARACTER*80 CMNAME

C LOCAL ARRAYS
C -----
C EELAS - ELASTIC STRAINS
C EPLAS - PLASTIC STRAINS
C FLOW - DIRECTION OF PLASTIC FLOW
C -----
C
```

```

C
PARAMETER(ZERO=0.D0, ONE=1.D0, TWO=2.D0, THREE=3.D0, SIX=6.D0,
1 ENUMAX=.4999D0, TOLER=1.0D-6, HALF=0.5D0, THIRD =
2 1.D0/3.D0, OP5=1.5D0, FORTY=40.D0, OP5R = 0.6667D0,
3 TWENTY=20.D0, THOUSAND_K=7.2685D2)

C -----
C VUMAT FOR ISOTROPIC ELASTICITY AND ISOTROPIC MISES PLASTICITY
C CANNOT BE USED FOR PLANE STRESS
C
C -----
C          VUMAT FOR JOHNSON - COOK MODEL
C -----
C      PROPS(1) - YANG'S MODULUS
C      PROPS(2) - POISSON'S RATIO
C      PROPS(3) - INELSTIC HEAT FRACTION
C      PARAMETER OF JOHNSON - COOK MODEL:
C      PROPS(4) - A
C      PROPS(5) - B
C      PROPS(6) - n
C      PROPS(7) - C
C      PROPS(8) - D
C      PROPS(9) - b
C      PROPS(10) - m
C      PARAMETERS OF ACOUSTIC SOFTENING:
C      PROPS(11) - d (SOFTENING COEFF)
C      PROPS(12) - I (ULTRASOUND ENERGY/INTENSITY)
C -----
C          STATE VARIABLES FOR TRACKING INTERNAL PARAMETERS
C -----
C      STATENEW(K, 1) = PLASTIC STRAIN
C      STATENEW(K, 2) = PLASTIC STRAIN RATE
C      STATENEW(K, 3) = YIELD STRENGTH
C      STATENEW(K, 4) = YIELD FLAG
C      STATENEW(K, 5) = THERMAL SOFTENING FACTOR
C      STATENEW(K, 6) = ESTIMATE PLASTIC STRAIN USING MISES STRAIN
C      STATENEW(K, 7) = ESTIMATE STRAIN RATE USING MISES STRAIN RATE
C      STATENEW(K, 8) = DIFFERENCE BETWEEN MISES STRESS AND YIELD STRESS
C      STATENEW(K, 9) = PLASTIC WORK
C      STATENEW(K, 10) = FACTOR
C -----
C ELASTIC PROPERTIES
C
      EMOD=PROPS(1)
      ENU=MIN(PROPS(2), ENUMAX)
      EBULK3=EMOD/(ONE-TWO*ENU)
      EG2=EMOD/(ONE+ENU)
      EG=EG2/TWO
      EG3=THREE*EG
      ELAM=(EBULK3-EG2)/THREE
      NVALUE=NPROPS/2-1
C TEMPERATURE INFO
      TEMP_ROOM=TWENTY          !ROOM TEMP IN CELCIUS
      TEMP_MELT=THOUSAND_K     !MELT TEMP IN CELCIUS

```

```

C
C CALCULATE PREDICTOR STRESS AND ELASTIC STRAIN
C
  IF ( STEPTIME .EQ. ZERO ) THEN
  DO K = 1, NBLOCK
  TRACE = STRAININC(K,1) + STRAININC(K,2) + STRAININC(K,3)
  STRESSNEW(K,1) = STRESSOLD(K,1)
  *      + EG2 * STRAININC(K,1) + ELAM * TRACE
  STRESSNEW(K,2) = STRESSOLD(K,2)
  *      + EG2 * STRAININC(K,2) + ELAM * TRACE
  STRESSNEW(K,3) = STRESSOLD(K,3)
  *      + EG2 * STRAININC(K,3) + ELAM * TRACE
  STRESSNEW(K,4)=STRESSOLD(K,4) + EG2 * STRAININC(K,4)
  IF ( NSHR .GT. 1 ) THEN      !!FOR 3D CASES
  STRESSNEW(K,5)=STRESSOLD(K,5) + EG2 * STRAININC(K,5)
  STRESSNEW(K,6)=STRESSOLD(K,6) + EG2 * STRAININC(K,6)
  END IF
  END DO
  ELSE

C
  DO K = 1, NBLOCK

C
  PEEQOLD=STATEOLD(K,1)
  CALL VUHARD(YIELDOLD, HARD, PEEQOLD, PROPS(4))
  TRACE = STRAININC(K,1) + STRAININC(K,2) + STRAININC(K,3)

C
  S11 = STRESSOLD(K,1) + EG2 * STRAININC(K,1) + ELAM * TRACE
  S22 = STRESSOLD(K,2) + EG2 * STRAININC(K,2) + ELAM * TRACE
  S33 = STRESSOLD(K,3) + EG2 * STRAININC(K,3) + ELAM * TRACE
  S12 = STRESSOLD(K,4) + EG2 * STRAININC(K,4)
  IF ( NSHR .GT. 1 ) THEN
  S13=STRESSOLD(K,5) + EG2 * STRAININC(K,5)
  S23=STRESSOLD(K,6) + EG2 * STRAININC(K,6)
  END IF

C
  SMEAN=THIRD*(S11 + S22 + S33)

C
  S11 = S11 - SMEAN
  S22 = S22 - SMEAN
  S33 = S33 - SMEAN
  IF ( NSHR .EQ. 1 ) THEN
  SMISES = SQRT(OP5*(S11*S11+S22*S22+S33*S33+TWO*S12*S12))
C
  TRY USE THE MISES STRAIN FOR STRAIN RATE ESTIMATION
  STRAINMISES = SQRT(OP5R*(STRAININC(K,1)*STRAININC(K,1)+
1 STRAININC(K,2)*STRAININC(K,2)+STRAININC(K,3)*STRAININC(K,3)+
2 TWO*STRAININC(K,4)*STRAININC(K,4)))
  ELSE
1 SMISES = SQRT(OP5*(S11*S11+S22*S22+S33*S33+TWO*S12*S12
1 +TWO*S13*S13+TWO*S23*S23))
C
  TRY USE THE MISES STRAIN FOR STRAIN RATE ESTIMATION
  STRAINMISES = SQRT(OP5R*(STRAININC(K,1)*STRAININC(K,1)+
1 STRAININC(K,2)*STRAININC(K,2)+STRAININC(K,3)*STRAININC(K,3)
2 +TWO*STRAININC(K,4)*STRAININC(K,4)
3 +TWO*STRAININC(K,5)*STRAININC(K,5)

```

```

4 +TWO*STRAININC(K,6)*STRAININC(K,6))
  END IF
  STRAINRATE = STRAINMISES/DT
C   READ PARAMETERS OF JOHNSON-COOK MODEL
C
  A= PROPS(4)
  B= PROPS(5)
  EN = PROPS(6)
  C = PROPS(7)
  D = PROPS(8)
  EB = PROPS(9)
  EM= PROPS(10)
C   READ PARAMETERS OF ACOUSTIC SOFTENING MODEL
  DCOEFF = PROPS(11)
  E = PROPS(12)
C
C CALCULATE ACOUSTIC SOFTENING FACTOR
  ACOUSTIC_SOFT=ONE-DCOEFF*E
C CALCULATE THERMAL SOFTENING FACTOR
  IF (TEMPOLD(K) .LT. TEMP_ROOM) THEN
    TEMP_DIMENSIONLESS = ZERO
  ELSE
    TEMP_DIMENSIONLESS = (TEMPOLD(K)-TEMP_ROOM)/(TEMP_MELT-TEMP_ROOM)
  END IF
  THERMAL_SOFT = ONE-TEMP_DIMENSIONLESS**EM
C CALCULATE STRAIN RATE HARDENING FACTOR, STATEOLD(*,2) STORES STRAIN RATES
C
  IF ( STATEOLD(K,2) .LT. FORTY) THEN
    IF (STRAINRATE .LT. FORTY) THEN
      TVP1 = C+D
      HARD1 = HARD
    ELSE
      TVP = D*(STRAINRATE/FORTY)**EB ! AN ESTIMATION OF STRAIN RATE!
      TVP1 = C+TVP
      HARD1 = HARD*TVP1+YIELDOLD*D*(ONE/FORTY)**EB*EB*
1(STRAINRATE)**(EB-ONE)
    END IF
  ELSE
    TVP = D*(STATEOLD(K, 2)/FORTY)**EB
    TVP1 = C+TVP
    !THE DERIVATIVE CHANGES FOR STRAIN RATE MODEL, 40 /s IS THE REFERENCE
    !HARD1 IS THE DERIVATIVE OF STRAIN, NOT STRAIN RATE!!!
    CONST = (ONE/FORTY)**EB
    !CONST = (ONE/DT)*(ONE/FORTY)**EB
    HARD1 = HARD*TVP1+YIELDOLD*D*CONST*EB*(STATEOLD(K, 2))**(EB-ONE)
  END IF
C CONSIDER BOTH SOFTENING AND HARDENING FACTORS FOR "HARD" AND "YIELDOLD"
  HARD2 = HARD1*THERMAL_SOFT*ACOUSTIC_SOFT
  YIELDOLD = YIELDOLD*TVP1*THERMAL_SOFT*ACOUSTIC_SOFT
  SIGDIF = SMISES - YIELDOLD
  FACYL D = ZERO
  IF (SIGDIF .GT. ZERO) FACYL D = ONE !ELSE DEQPL = 0
  DEQPL = FACYL D*SIGDIF/(EG3 + HARD2) !UPDATE DEQPL EXPLICITLY
C UPDATE STATE VARIABLES, STATE(*,1) STORES STRAIN, STATE(*, 2) STORES

```



```

C STRAIN RATE, STATE(*, 3) STORES ACTIVE YIELD FLAG
  STATENEW(K, 1) = STATEOLD(K, 1)+DEQPL
  STATENEW(K, 2) = DEQPL/DT
  STATENEW(K, 3) = YIELDOLD !TRACK THE CHANGE OF YIELD SURFACE
  STATENEW(K, 4) = FACYLD
  STATENEW(K, 5) = THERMAL_SOFT
  STATENEW(K, 6) = STRAINMISES !ESTIMATE STRAIN USING MISES STRAIN
  STATENEW(K, 7) = STRAINRATE !ESTIMATE STRAIN RATE USING MISESE
  STATENEW(K, 8) = SIGDIF

C
C UPDATE STRSSES
  YIELDNEW = YIELDOLD + HARD2*DEQPL
  FACTOR = YIELDNEW/(YIELDNEW + EG3*DEQPL)!FACTOR IS FLOW DIRECTION
  STRESSNEW(K, 1) = S11*FACTOR + SMEAN
  STRESSNEW(K, 2) = S22*FACTOR + SMEAN
  STRESSNEW(K, 3) = S33*FACTOR + SMEAN
  STRESSNEW(K, 4) = S12*FACTOR
  IF (NSHR .GT. 1) THEN
    STRESSNEW(K, 5) = S13*FACTOR
    STRESSNEW(K, 6) = S23*FACTOR
  END IF

C
C UPDATE THE SPECIFIC INTERNAL ENERGY -
C
  IF ( NSHR .EQ. 1 ) THEN
    STRESSPOWER = HALF * (
      * ( STRESSOLD(K,1) + STRESSNEW(K,1) ) * STRAININC(K,1) +
      * ( STRESSOLD(K,2) + STRESSNEW(K,2) ) * STRAININC(K,2) +
      * ( STRESSOLD(K,3) + STRESSNEW(K,3) ) * STRAININC(K,3) ) +
      * ( STRESSOLD(K,4) + STRESSNEW(K,4) ) * STRAININC(K,4)
    )
  ELSE
    STRESSPOWER = HALF * (
      * ( STRESSOLD(K,1) + STRESSNEW(K,1) ) * STRAININC(K,1) +
      * ( STRESSOLD(K,2) + STRESSNEW(K,2) ) * STRAININC(K,2) +
      * ( STRESSOLD(K,3) + STRESSNEW(K,3) ) * STRAININC(K,3) ) +
      * ( STRESSOLD(K,4) + STRESSNEW(K,4) ) * STRAININC(K,4) +
      * ( STRESSOLD(K,5) + STRESSNEW(K,5) ) * STRAININC(K,5) +
      * ( STRESSOLD(K,6) + STRESSNEW(K,6) ) * STRAININC(K,6)
    )
  END IF
  ENERINTERNNEW(K) = ENERINTERNOLD(K) + STRESSPOWER / DENSITY(K)

C
C UPDATE THE DISSIPATED INELASTIC SPECIFIC ENERGY -
C
  PLASTICWORKINC = HALF * (YIELDOLD+YIELDNEW) * DEQPL
  ENERINELASNEW(K) = ENERINELASOLD(K) + PLASTICWORKINC / DENSITY(K)
C TRACK THE DISSIPATED INELASTIC ENERGY
  STATENEW(K, 9) = ENERINELASNEW(K)
  STATENEW(K, 10) = FACTOR
  END DO
  END IF

C
  RETURN
  END

```

```

C
C
C
SUBROUTINE VUHARD(SYIELD,HARD,EQPLAS, TABLE)
C
INCLUDE 'VABA_PARAM.INC'
CHARACTER*80 CMNAME
C
DIMENSION HARD(3)
C
DIMENSION TABLE(3)
C
PARAMETER(ZERO=0.D0, ONE=1.D0)

C
C
C GET PARAMETERS, SET HARDENING TO ZERO
C
A= TABLE(1)
B= TABLE(2)
EN= TABLE(3)
HARD= ZERO

C
C
C CALCULATE CURRENT YIELD STRESS AND HARDENING RATE
C
IF (EQPLAS.EQ.0.0) THEN
    SYIELD= A
ELSE
    HARD= EN*B*EQPLAS**(EN-ONE)
    SYIELD= A+B* EQPLAS**EN
END IF
RETURN
END

C
C
C
CC UMATHT IS FOR DEFINING THERMAL MATERIAL MODELS IN ABAQUS/EXPLICIT
CC
SUBROUTINE UMATHT(U,DUDT,DUDG,FLUX,DFDT,DFDG,
1 STATEV,TEMP,DTEMP,DTEMDX,TIME,DTIME,PREDEF,DPRED,
2 CMNAME,NTGRD,NSTATV,PROPS,NPROPS,COORDS,PNEWDT,
3 NOEL,NPT,LAYER,KSPT,KSTEP,KINC)
C
INCLUDE 'VABA_PARAM.INC'
C
CHARACTER*80 CMNAME
DIMENSION DUDG(NTGRD),FLUX(NTGRD),DFDT(NTGRD),
1 DFDG(NTGRD,NTGRD),STATEV(NSTATV),DTEMDX(NTGRD),
2 TIME(2),PREDEF(1),DPRED(1),PROPS(NPROPS),COORDS(3)
FOUT=111
OPEN(UNIT=111,FILE='C:\TEMP\THERMAL.OUT',STATUS='UNKNOWN')
C
COND = PROPS(1)
SPECHT = PROPS(2)
C
INPUT SPECIFIC HEAT
DUDT = SPECHT

```

```
DU = DUDT*DTEMP
U = U+DU
C
C INPUT FLUX = -[K]*{DTEMPX}
DO I = 1, NTGRD
    FLUX(I) = -COND*DTEMPX(I)
END DO
C
C INPUT ISOTROPIC CONDUCTIVITY
C
DO I = 1, NTGRD
    DFDG(I, I) = -COND
END DO
C
RETURN
END
```

The focus of this chapter is the dynamics modeling of the built feature. The motivation of this work stems from the high computational cost for predicting transient dynamics of the built feature using the finite element method. The high frequency characteristics of the problem and the conditional stability of the numerical integration scheme require extremely small step increments and a large number of iterations which lead to high computational cost. In order to reduce the computational cost, a lumped parameter model consisting of mass-spring networks is developed to replace the finite element model. The mass-spring network model has been extensively used in computer graphics for modeling isotropic and anisotropic behavior of materials under static load but has not been used for studying their dynamic responses. Preliminary tests of the model have shown its capability of predicting modal frequencies and mode shapes of parallelepiped solids. Based on the predicted mode shapes, a transient dynamic response can be obtained using mode-superposition. The predictions of modal parameters from the mass-spring model are compared with those from a finite element model in order to evaluate their accuracy, the computational cost, and the convergence. The limitations of the model are also pointed out for future work.

Introduction

In the investigation of the height-to-width bond failure issue, Gibert et al. pointed out that at the critical height-to-width ratio, due to resonance, the large amplitude transversal vibration of the built feature counteracts with the vibration of the sonotrode (J. M. Gibert, Austin, and Fadel 2010). In order to better understand the role of resonance in the reduction of the differential motion, a dynamic model able to capture natural frequencies and mode shapes of the built feature at critical height-to-width ratio is needed.

Different dynamic models have been proposed to characterize the motion of the built feature in order to study the height-to-width ratio problem. The most extensively adopted models are finite element models. Zhang et al. (Zhang et al., 2006) developed a 2-D finite element model and applied transient dynamic analysis using the commercial software package ANSYS. However, the 2-D model provides only an approximation of the primary modal frequency and mode shape of the 3-D case. As the mode number increases, the prediction from the 2-D case diverges from the 3-D case. This is due to the weakening of the assumption of plane strain about the cross section as the mode shapes become complicated at higher order (Cosby et al., 2013). Gibert et al. (Gibert et al., 2009) established a 3-D finite element model for the built feature and performed a preliminary dynamic transient analysis using the commercial software ABAQUS/Explicit. Due to the high frequency characteristics, the analysis is computationally expensive and the simulations are run for only 2 milliseconds (40 cycles) (McCullough, Arbor, and Austin n.d.). As a result, the time limit may impede the foil from undergoing plastic deformation sufficiently, and a simpler and less computationally demanding dynamic model is required.

A mass-spring system is intuitive and simple in representing a continuum with mass particles that are linked by massless linear springs. The system was first introduced into the dynamical theory of Crystal Lattices (Born and Ann, 1914; Born, 1954), and later a mass-spring network was used in computer graphics to model the isotropic and anisotropic behaviors of materials (Nealen et al., 2006). The displacement of the particle i of mass m_i is defined by \mathbf{x}_i . The motion of each particle is governed by Newton's second law: $f_i = m_i \ddot{\mathbf{x}}_i$. The force f_i is the sum of external forces (friction, gravity, etc.) and internal forces exerted by the springs, and $\ddot{\mathbf{x}}_i$ is the acceleration of the particle i . Gravity is small compared with the internal forces and is therefore ignored. Under the assumption that the continuum undergoes elastic deformation, the internal forces between particle i and j , $f_{in,ij}$, are calculated based on Hooke's law: $f_{in,ij} = \sum k_{ij}(\mathbf{x}_i - \mathbf{x}_j)$, where k_{ij} is the stiffness of the spring that connects particles i and j , and depends on the configurations of the springs and the directional dependence of material's mechanical properties (isotropic or anisotropic). The spring stiffness can be determined either by finding optimal parameters that match the measured deformation data or from analytical expressions. The data-driven approach can be found in work by San-Vicente et al. (San-Vicente, 2012), and Louchet et al. (Louchet et al., 1995). The analytical approach can be found in work by Baudet et al. (Baudet et al, 2009), and Ladd et al. (Ladd et al., 1997). The data-driven approach may experience convergence issues, i.e., convergence towards zero, or negative spring stiffness (Lloyd et al., 2007). The analytical approach provides a more realistic spring stiffness based on the elasticity and dynamical theory of the discrete model. However, its application

is limited by the over simplified structure of the model. The detailed explanation is presented in sections 7.1.2 and 7.1.3. In this work, the analytical approach is used to determine spring stiffness. The prediction from the mass-spring model depends on the mesh resolution and the spring configuration. With a defined configuration, finer mesh leads to more accurate prediction but if the mesh is too fine the computational cost may goes up and undermines the use of such model. As a result, the established mass-spring system should be evaluated in terms of effectiveness and computational efficiency.

2-D Mass-spring Models

First we establish a 2-D model with UAM assumptions about UAM similar to those used by Zhang et al. in their 2-D model (Zhang et al, 2010). The 2-D plane is normal to the bonding interface and along the direction of the ultrasonic vibration. Plane strain conditions are adopted. In establishing the mass-spring model, we determine first the shape and spring configuration of the unit cell which is the minimum rectangular cell that is repeated in space for forming the mass-spring network. The possible shapes of the unit cell include rectangular, triangular, and hexagonal shapes. Since the built feature is a parallelepiped and its cross section is rectangular, rectangular unit cells were selected. Then a rectangular unit cell with the simplest spring configuration consisting of four edge springs is evaluated based on tensile and shearing tests. It is obvious that the edge springs of the square cell are capable of capturing the tensile deformation but fail the shearing tests. Since the rectangular cell is not constrained by torsional springs at the vertices, the structure can deform freely in the shearing tests without deforming any of the edge springs (**Figure B.1** (left)). As a

result, two diagonal springs are introduced to account for the shearing effects (**Figure B.1** (right)). The two diagonal springs have equal stiffness coefficients. The spring constants for both the edge and the diagonal springs are derived based on tensile and shearing tests of actual physical models presented by Baudet et al. (Baudet et al, 2009). Based on the energy method, the relations between the internal forces and deformations are established and elastic parameters (Young's modulus and Poisson's ratio) can be introduced. As only diagonal springs are stressed in small shear deformation, the spring constants of edge springs k_i and diagonal springs k_d are easily obtained:

$$k_i = \frac{E(j^2(3\nu+2)-i^2)}{4x_0y_0(1+\nu)}, \quad (i,j) \in \{x_0, y_0\} \text{ with } i \neq j \quad (\text{B.1})$$

$$k_d = \frac{E(x_0^2+y_0^2)}{4x_0y_0(1+\nu)} \quad (\text{B.2})$$

where x_0 and y_0 represent the width and height of the unit cell. In this study, square unit cells are implemented for their simplicity and effectiveness: $x_0 = y_0$. E is the Young's modulus, and ν is the Poisson's ratio. Kot et al. (Kot et al., 2014) provided a comprehensive demonstration of the limitation of the model showing that for any particle models with central forces (the spring forces depend only on the distance between masses), Poisson's ratios in 2-D and 3-D can always be written in terms of the Lamé constants λ and μ :

$$\nu_{2D} = \frac{\lambda}{\lambda+2\mu} \quad (\text{B.3})$$

$$\nu_{3D} = \frac{\lambda}{2(\lambda+\mu)} \quad (\text{B.4})$$

For an isotropic solid, $\lambda = \mu$ holds for the central force models (Rice, 1993), and equation (B.3) and (B.4) become:

$$\nu_{2D} = 1/3 \quad (\text{B.5})$$

$$\nu_{3D} = 1/4 \quad (\text{B.6})$$

Therefore the mass-spring system provides exact prediction only for materials with Poisson's ratio $\nu_{2D} = 1/3$ in a 2-D case and $\nu_{3D} = 1/4$ in a 3-D case. However, by introducing some corrective forces, any Poisson's ratio can be considered (Baudet et al., 2009). Aluminum alloys have a Poisson's ratio of 1/3 and thus can be modeled using a 2-D mass spring model. For the 3-D case, additional modifications are required to adapt the model for the assigned material.

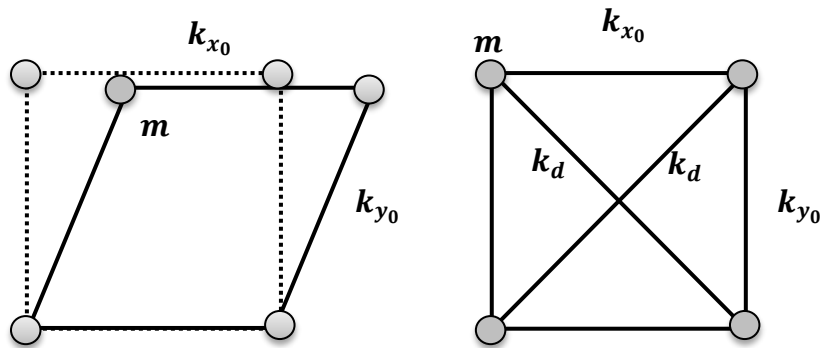


Figure 7.1 The unit cell without diagonal springs which fails in shear test (left), the unit cell with diagonal springs (right).

Once the spring constants are determined, the governing equations of the system can be obtained using an energy method. The steps are shown as follows:

1. Write the Lagrangian of the mass spring system as the difference between the kinetic energy and the potential energy of the springs,
2. Derive the equations of motion by applying the principle of least action.

For the potential energy of the springs, consider an arbitrary displacement Δ_i of the discrete mass m_i (Figure B.2). Assuming small deformations for the springs, the

change in length of the spring is approximated using a Taylor expansion. In the edge springs:

$$\begin{aligned} \Delta_i &= \sqrt{(i_0 + \Delta i)^2 + \Delta j^2} - i_0 \\ &\approx \Delta i + \frac{\Delta j^2}{2i_0} + O(\Delta i^2, \Delta j^2), (i, j) \in \{x, y\} \text{ with } i \neq j \end{aligned} \quad (\text{B.7})$$

Since $\Delta i, \Delta j \ll i_0$, then $\frac{\Delta j^2}{2i_0} \approx 0$ and:

$$\Delta_i = \sqrt{(i_0 + \Delta i)^2 + j_0^2} - i_0 \approx \Delta i + O(\Delta i^2, \Delta j^2), (i, j) \in \{x, y\} \text{ with } i \neq j \quad (\text{B.8})$$

In the diagonal springs:

$$\Delta_d = \sqrt{(x_0 + \Delta x)^2 + (y_0 + \Delta y)^2} - \sqrt{x_0^2 + y_0^2} \approx \frac{x_0 \Delta x + y_0 \Delta y}{\sqrt{x_0^2 + y_0^2}} + O(\Delta x^2, \Delta y^2) \quad (\text{B.9})$$

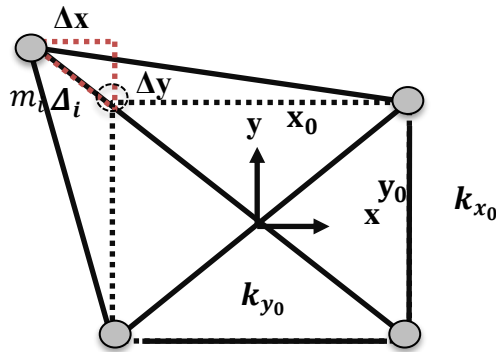


Figure 7.2 Arbitrary displacement of a discrete mass in a square unit cell

3-D Mass-spring Models

The 3-D model is a generalization of the 2-D model. The square unit cell is extended to a cubic cell with which three possible spring configurations are investigated. Fig. B.4 shows the three elementary configurations of the springs. By combining (a) (b), (a) (c), and

(a) (b) (c), three possible spring configurations are obtained. The configuration (a) (b) is a direct extension of the 2-D case in three dimensional space. Each mass is connected to 18 neighbors. Configuration (a) (c) replaces the face diagonal springs in (a) (b) with body diagonal springs, which reduces the number of connected neighbors of each mass to 14. Configuration (a) (b) (c) is the most complicated spring configuration with each mass connected to 26 neighbors. Trade-off must be made between the effectiveness of the system and the complexity of the spring configuration. Baudet et al. present the analytical expression of the edge spring stiffness (k_x) and the diagonal spring stiffness (k_d) for configuration (a) (c) based on tensile and shearing tests (Baudet et al., 2009):

$$k_x = \frac{Ex_0(4\nu+1)}{8(1+\nu)} \quad (\text{B.10})$$

$$k_d = \frac{3Ex_0}{8(1+\nu)} \quad (\text{B.11})$$

where x_0 is the edge length of the cubic cell, E is the Young's modulus, and ν is the Poisson's ratio. However, modal analysis on a single cubic cell indicates that this configuration is unstable in vibration. Similar observation is also reported by Ladd and Kinney (Ladd and Kinney, 1997) showing that the configuration is unstable to local torsional mode. Consequently the configuration (a) (b) is examined.

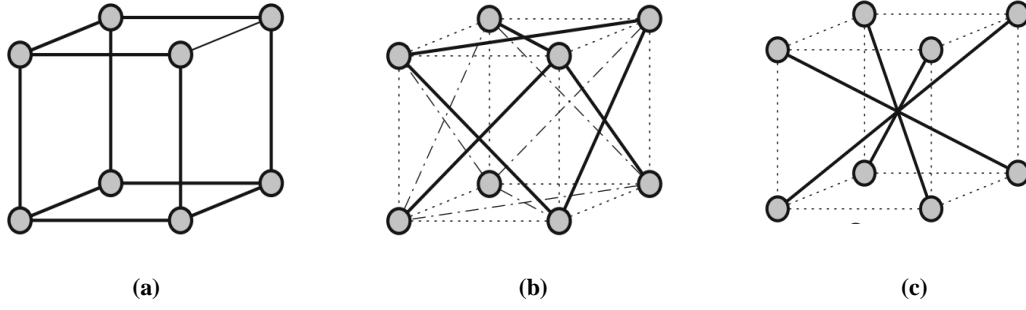


Figure 7.3 Elementary spring configurations for 3-D cubic unit cell

By assuming that the elastic material is isotropic and that all the springs have the same stiffness for the configuration (a) (b), the equation of motion can be written (Ladd et al., 1997):

$$\rho \frac{\partial^2 \mathbf{u}}{\partial t^2} = \frac{k}{x_0} (2\nabla(\nabla \cdot \mathbf{u}) + \nabla^2 \mathbf{u}) \quad (\text{B.12})$$

Where x_0 is the edge length of the cubic cell, k is the stiffness of the springs, \mathbf{u} is the displacement vector of the discrete mass. Based on linear elasticity theory, the equation of motion can be written in terms of the Lamé constants (Landau and Lifshitz, 1986):

$$\rho \frac{\partial^2 \mathbf{u}}{\partial t^2} = \lambda \nabla(\nabla \cdot \mathbf{u}) + \mu (\nabla^2 \mathbf{u} + \nabla(\nabla \cdot \mathbf{u})) \quad (\text{B.13})$$

By comparing equations (B.12) and (B.13), $\lambda = \mu = \frac{k}{x_0}$. Furthermore, the Young's modulus and Poisson's ratio can be expressed in terms of the Lamé constants:

$$E = \frac{\mu(3\lambda+2\mu)}{\lambda+\mu} = \frac{5k}{2x_0} \quad (\text{B.14})$$

$$\nu = \frac{\lambda}{2(\lambda+\mu)} = 0.25 \quad (\text{B.15})$$

The spring stiffness for configuration (a) (b) is thus determined by $k = \frac{2Ex_0}{5}$. The Poisson's ratio is fixed: $\nu = 0.25$. The spring deformations are approximated using Taylor expansion with the small deformation assumption:

$$\Delta_i = \sqrt{(i_0 + \Delta i)^2 + \Delta j^2 + \Delta k^2} - i_0 \approx \frac{i_0 \Delta i + \Delta j + \Delta k}{i_0} + O(\Delta i^2, \Delta j^2, \Delta k^2), \quad i, j, k \in (x, y, z) \quad (\text{B.16})$$

Since $\Delta i, \Delta j, \Delta k \ll i_0$,

$$\Delta_i = \sqrt{(i_0 + \Delta i)^2 + \Delta j^2 + \Delta k^2} - i_0 \approx \Delta i + O(\Delta i^2, \Delta j^2, \Delta k^2) \quad (\text{B.17})$$

$$\begin{aligned} \Delta_d &= \sqrt{(x_0 + \Delta x)^2 + (y_0 + \Delta y)^2 + (z_0 + \Delta z)^2} - \sqrt{x_0^2 + y_0^2 + z_0^2} \\ &\approx \frac{x_0 \Delta x + y_0 \Delta y + z_0 \Delta z}{\sqrt{x_0^2 + y_0^2 + z_0^2}} + O(\Delta x^2, \Delta y^2, \Delta z^2) \end{aligned} \quad (\text{B.18})$$

As is mentioned in the prior section that the 3-D mass-spring system gives an exact prediction only when the Poisson's ratio $\nu_{3D} = 1/4$. Since the material under study has a Poisson's ratio of $1/3$, additional care must be taken. According to Baudet et al. (Baudet et al., 2009), corrective forces can be introduced in addition to springs to account for additional Poisson's effects and thus expand the validity of the mass-spring model as the Poisson's ratio ranges between 0.1 to 0.5. The corrective forces can be introduced in transient dynamics analysis but not in modal analysis in which no forces are considered. The implementation of corrective forces will be a part of the future work.

Model Validation

The 2-D and 3-D mass-spring models are validated by comparing their predictions with those from the 2-D and 3-D finite element models. A modal analysis is carried out. In the modal analysis, the two models are compared in terms of computational time, mesh resolution, and convergence speed to solutions. Since the lumped parameter model is limited to modeling of materials with Poisson's ratio of 0.33 in 2-D and 0.25 in 3-D. The effect

of Poisson’s ratio on transient analysis is examined by running the finite element model at different Poisson’s ratios.

Modal Analysis

The built feature is known to undergo resonance at the critical height-to-width ratio, the proposed model needs to accurately characterize the modal parameters (modal frequencies and mode shapes) of the built feature. Moreover, as an alternative to modeling using the finite element method, the mass-spring model should be more computationally favorable. Therefore, a modal analysis is carried out on the built feature using the proposed 2-D and 3-D mass-spring systems.

The typical shape of the built feature is a parallelepiped. In the 2-D case, the nominal width of the foil is 0.9375 in. (23.8 mm) and the height of the built feature such that the height-to-width ratio equals one. UAM accepts a broad range of metals such as aluminum alloys, copper, zinc, nickel, and titanium. Aluminum is selected for its most extensive application in UAM. Since all aluminum alloys share similar density and elastic properties, the type of the aluminum is not specified. The properties are listed in **Table B.1**. Although the built feature is laminated and the material is not isotropic, the influence of anisotropy is small and thus can be neglected. As a result, it is assumed that the material in the built feature is homogeneous and isotropic.

Table B. 1 The material properties of aluminum alloys

Density (kg/m^3)	Young’s Modulus (GPa)	Poisson’s ratio
--------------------------------------	------------------------------	------------------------

In the modal analysis, the equations of motion in the mass-spring system are derived and assembled to form the system:

$$[M]\ddot{\mathbf{x}} + [K]\mathbf{x} = \mathbf{0} \quad (\text{B.19})$$

Where the mass matrix $[M]$ is diagonal and the stiffness matrix $[K]$ is symmetric and positive definite. Notice that the global mass and stiffness matrices are constructed such that the element matrices are superimposed, meaning that the mass/spring stiffness increases if multiple cells overlap at that position. Then the bottom of the parallelepiped is considered as fixed, leading to the suppressing of rows and columns in $[M]$ and $[K]$ matrices that correspond to nodes at the bottom. By inserting a general solution $\mathbf{x} = \mathbf{X}e^{-\omega t}$ to the system, the eigenvalue problem is formulated as:

$$([K] - \omega^2[M])\mathbf{X}e^{-\omega t} = \mathbf{0} \quad (\text{B.20})$$

yielding,

$$[K] - \omega^2[M] = 0 \quad (\text{B.21})$$

The eigenvalue problem can be readily solved using MATLAB.

2-D Case

The predictions from the modal analysis using mass-spring models are compared with those predicted by finite element models using the commercial software ABAQUS 6-14. **Figure B.4** shows the predictions for the first five modal frequencies from a mass-spring model consisting of 20x20 unit cells and a finite element model consisting of 60x60

elements in 2-D case. The predictions show good agreement. Further comparisons of mode shapes are shown in **Table B.2**. A relatively coarse mesh (10x10) is used for plotting the mass-spring model when being compared with the mesh of the finite element model (60x60) simply for the clarity of the plot showing the mode shapes. In the mass-spring model, the blue lines represent the undeformed shape and the red ones represent the deformed mode shapes. The mode shapes predicted by the mass-spring model match well with those from the finite element model although the mesh of the mass-spring model is less fine.

A convergence study is then performed on the predicted modal frequencies by varying the mesh resolutions for both models (**Table B.3**). The mass-spring model shows very stable predictions as the mesh resolution increases from 5x5 to 60x60, meaning that the model does not require a highly refined mesh to obtain reliable predictions (**Figure B.5**, (top)). The finite element model, however, demonstrates a significant change in predictions as the mesh resolution increases in all but the primary mode (**Figure B.5**, (bottom)). The predictions converge as the mesh resolution reaches 40x40. Moreover, the predictions from a 20x20 mass-spring model are compared with those from a 60x60 finite element model and the relative error between the two remains within 0.3% (**Figure B.6**). Finally, the two models are compared in terms CPU time required for solving the problem. The computer in use has an Intel 2.30 GHz double-core processor. The CPU time consumed for solving the 20x20 mass-spring model is 6.9 seconds whereas the time for solving the 60x60 finite element model is 1.6 seconds. It can be concluded that the mass-spring model re-

quires less number of elements than the finite element model does to obtain a similar prediction. However, the computing time of the 2-D mass-spring model is longer than that of the finite element model possibly because the code developed in this work is not as structurally concise and computationally efficient as the code used in the commercial software.

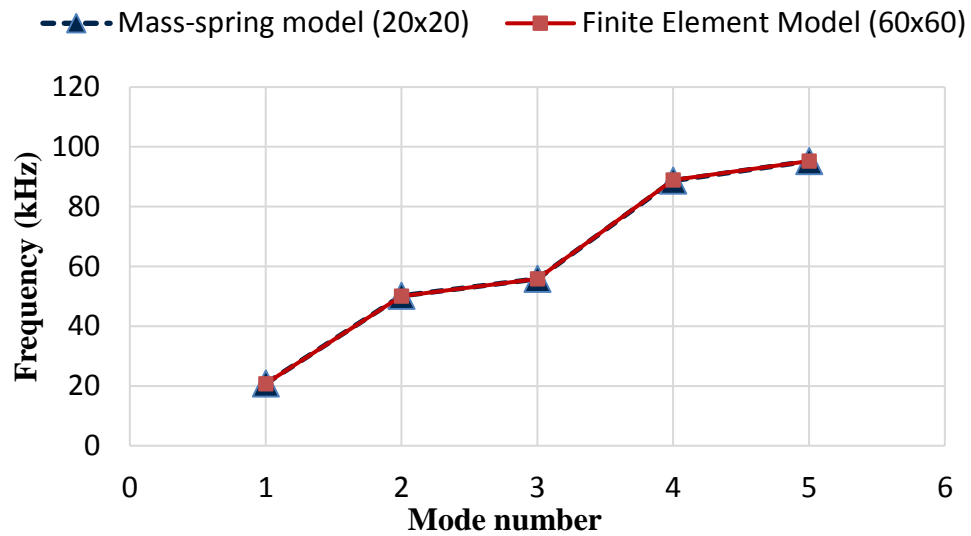
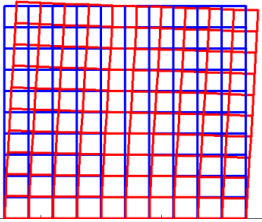
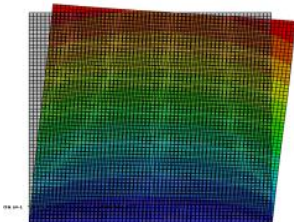


Figure B.4 Modal frequency predictions from 20x20 and 60x60 finite element model in 2-D

Table B. 2 Comparison of the mode shapes for the first five modes in 2-D case

Mode #	2-D mass-spring model (10x10)	2-D finite element model (60x60)
1		

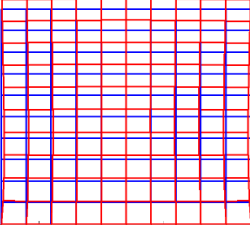
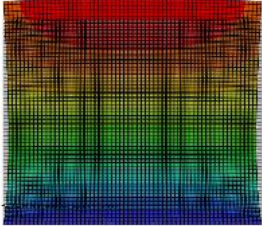
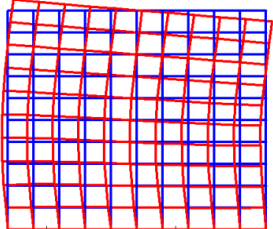
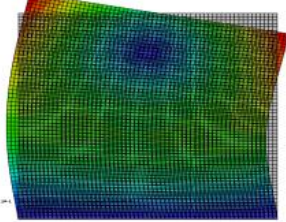
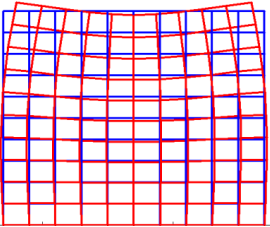
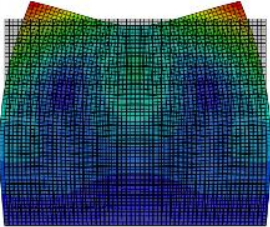
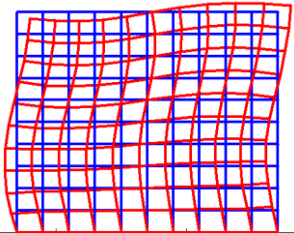
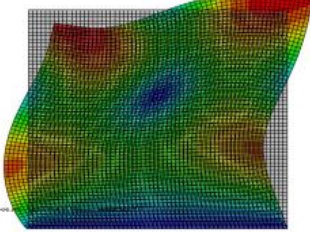
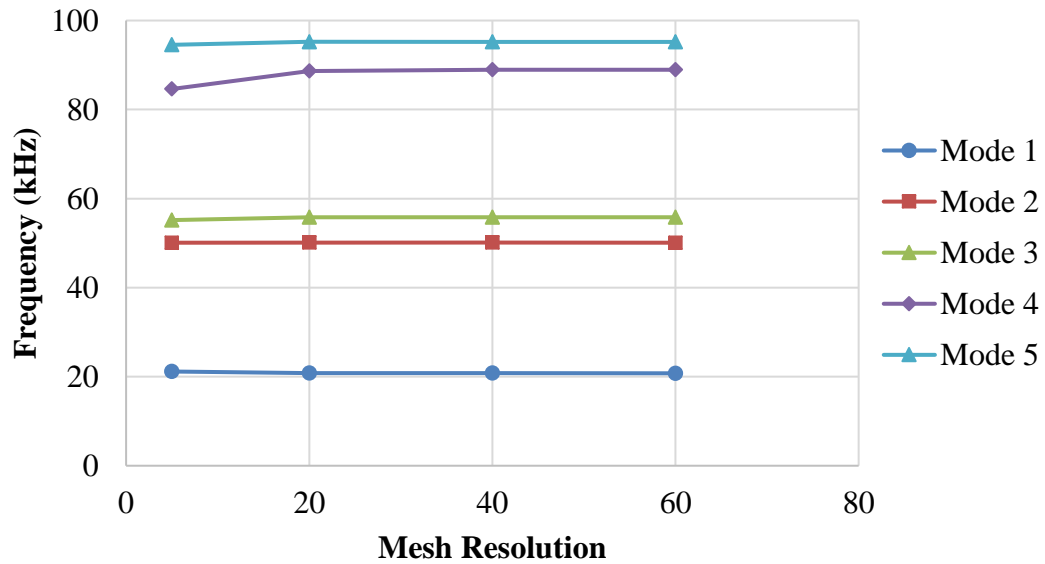
2		
3		
4		
5		

Table B. 3 Modal frequency predictions with different mesh resolutions in 2-D

Mode #	Mass-spring model (frequency: kHz)				Finite element model (frequency: kHz)			
	5x5	20x20	40x40	60x60	5x5	20x20	40x40	60x60
1	21.16	20.80	20.77	20.76	21.49	22.13	22.15	20.76
2	50.09	50.11	50.10	50.09	24.21	46.94	53.44	50.08
3	55.17	55.80	55.81	55.81	52.72	53.43	59.55	55.82
4	84.62	88.69	88.91	88.94	54.44	59.42	85.79	88.90
5	94.54	95.23	95.19	95.18	56.36	67.60	94.75	95.24



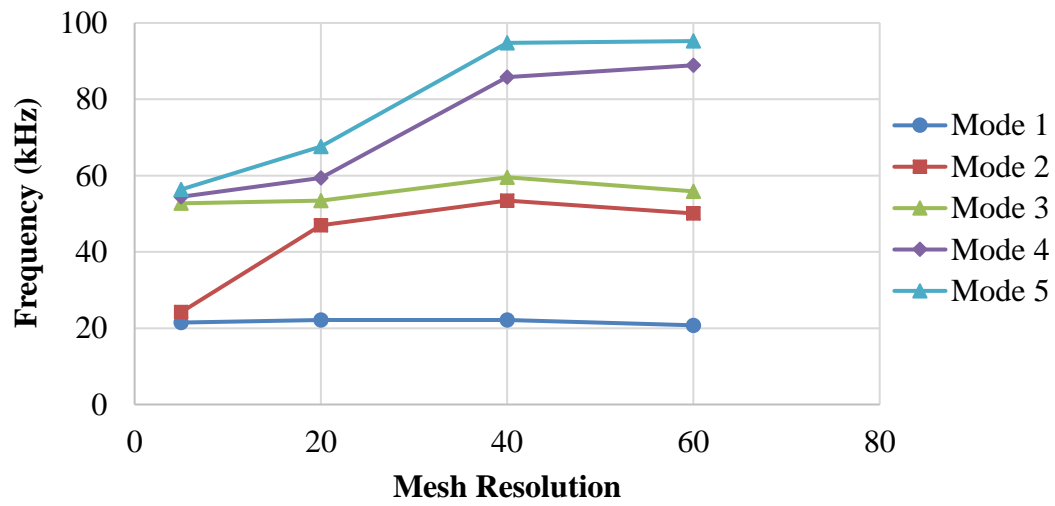


Figure B. 5 Convergence of the mass-spring model (top) and the finite element model (bottom) in 2-D

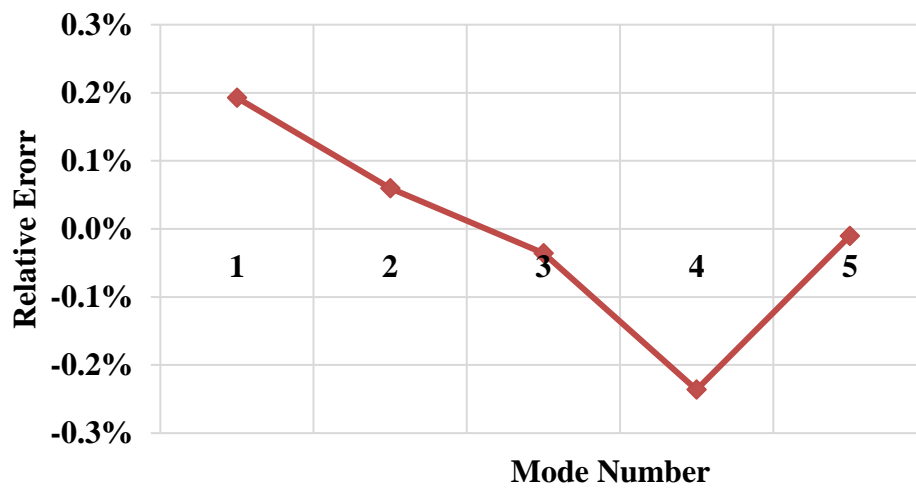


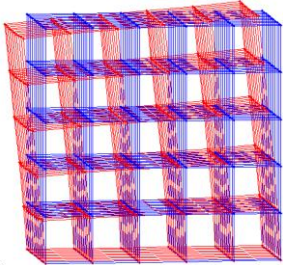
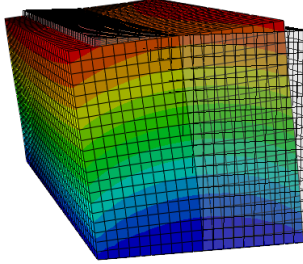
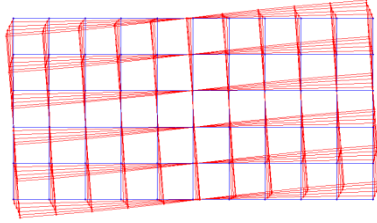
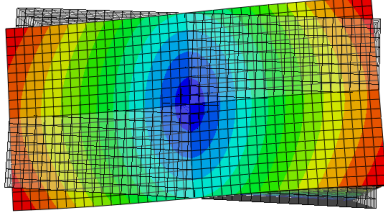
Figure B. 6 Relative difference (comparing to 60x60 finite element model) of frequency prediction of 20x20 mass-spring model

3-D Case

For the 3-D case, the geometry of the built feature is set to 0.9375 in. (23.8 mm) in height and width, and 1.875 in. (47.6 mm) in length. The length of the built feature is selected arbitrarily since the height-to-width ratio problem is not sensitive to length (Robinson et al., 2006). The material selected is the same as in the 2-D case. **Table B.4** presents a qualitative comparison of the first five mode shapes predicted by the two models. Again, the mass-spring model has a lower mesh resolution (5x5x10) than the finite element model (20x20x40), but this does not undermine its ability to predict the mode shapes. Most of the mode shapes are presented in top view or side view for clarity. **Figure B.7** compares the convergence of the two models in 3-D. Similar to the observations in the 2-D case, the predictions from the mass-spring model show little changes as mesh resolution increases from 3x3x6 to 12x12x24 whereas the predictions in the finite element model undergo radical changes. Specifically, at a mesh resolution of 5x5x10, the finite element model presents multiple “hourglass” mode shapes indicating insufficient mesh refinement and results in five modal frequencies being extremely close to each other. At a mesh resolution of 20x20x40, the predictions from the finite element model start to converge and small changes are found as the mesh is further refined. Notice that the finest mesh for the mass-spring model in the evaluation is only 12x12x24, whereas for the finite element model, it is 30x30x60. **Figure B.8** shows a comparison of the modal frequency prediction from a 3x3x6 mass-spring model and a 30x30x60 finite element model. The relative error between the prediction from the two models lies within 5% (**Figure B.9**). In terms of computational cost, the CPU time for computing the 3x3x6 mass-spring model is only 1.01 seconds,

whereas the time for the 30x30x60 finite element model is 6.2 seconds. This is probably due to the fact that the mesh resolution rather than the conciseness of the code starts to constrain the computing time as the model changes from 2-D to 3-D. Consequently, the 3-D mass-spring model requires a much lower mesh resolution and thus less computation time than the 3-D finite element model does to obtain a reliable prediction.

Table B.4 Comparison of the mode shapes for the first five modes in 3-D case

Mode #	3-D mass-spring model (5x5x10)	3-D finite element model (20x20x40)
1	 <p>A 3D wireframe model of a rectangular prism with a 5x5x10 grid of nodes. The nodes are colored in a gradient from blue to red, representing the displacement of the mass-spring model for the first mode.</p>	 <p>A 3D finite element mesh of a rectangular prism with a 20x20x40 grid of elements. The mesh is colored in a gradient from blue to red, representing the displacement of the finite element model for the first mode.</p>
2	 <p>A 3D wireframe model of a rectangular prism with a 5x5x10 grid of nodes. The nodes are colored in a gradient from blue to red, representing the displacement of the mass-spring model for the second mode.</p>	 <p>A 3D finite element mesh of a rectangular prism with a 20x20x40 grid of elements. The mesh is colored in a gradient from blue to red, representing the displacement of the finite element model for the second mode.</p>

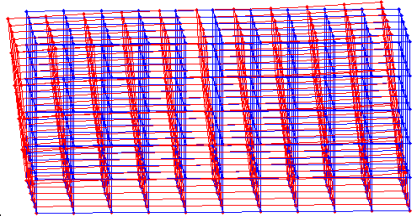
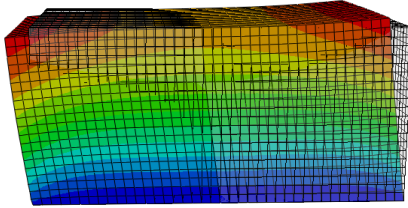
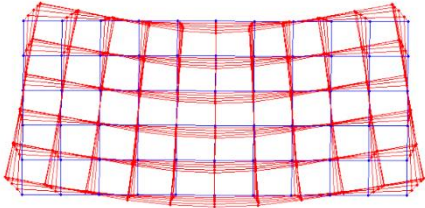
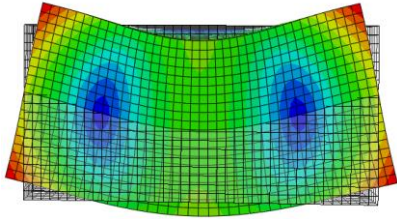
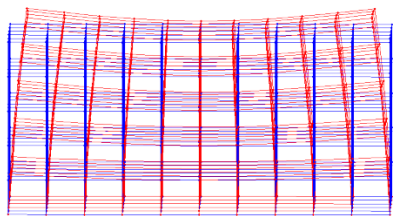
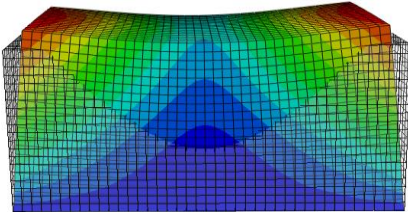
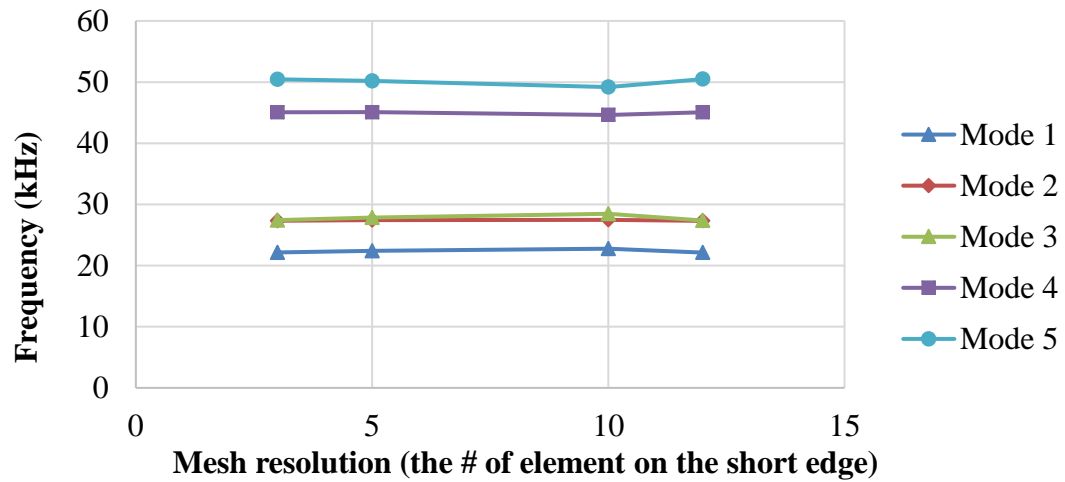
3		
4		
5		

Table B.5 Modal frequency predictions with different mesh resolutions in 3-D

Mode #	Mass-spring Model (Frequency: kHz)				Finite Element Model (Frequency: kHz)			
	3x3x6	5x5x10	10x10x20	12x12x24	5x5x10	10x10x20	20x20x40	30x30x60
1	22.8	22.4	22.2	22.1	20.3	22.6	22.7	22.7
2	27.5	27.4	27.3	27.3	20.4	27.9	28.0	28.1
3	28.5	27.9	27.4	27.4	20.5	28.1	28.1	28.1
4	44.6	45.1	45.1	45.1	20.7	41.3	46.0	46.1
5	49.2	50.2	50.5	50.5	20.7	41.3	51.8	51.8



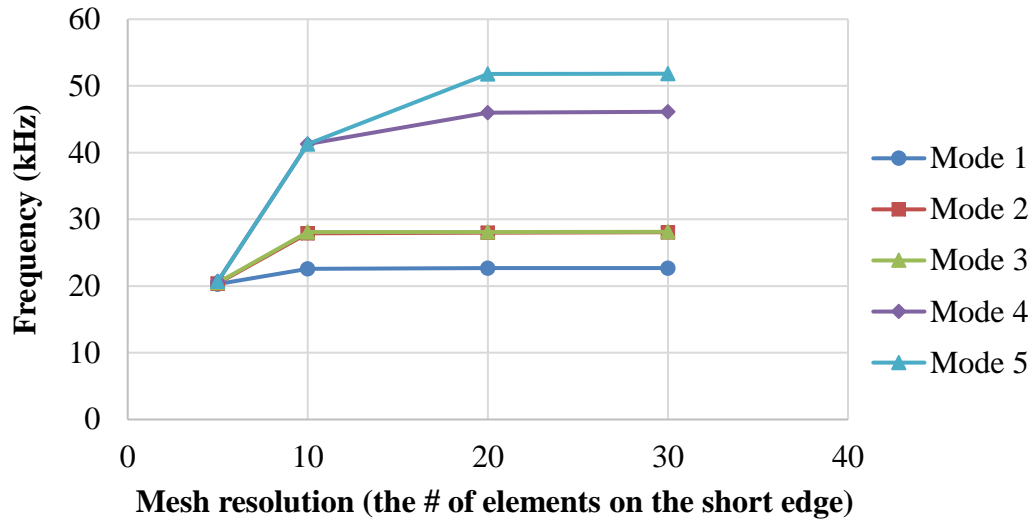


Figure B.7 Convergence of the mass-spring model (top) and the finite element model (bottom).

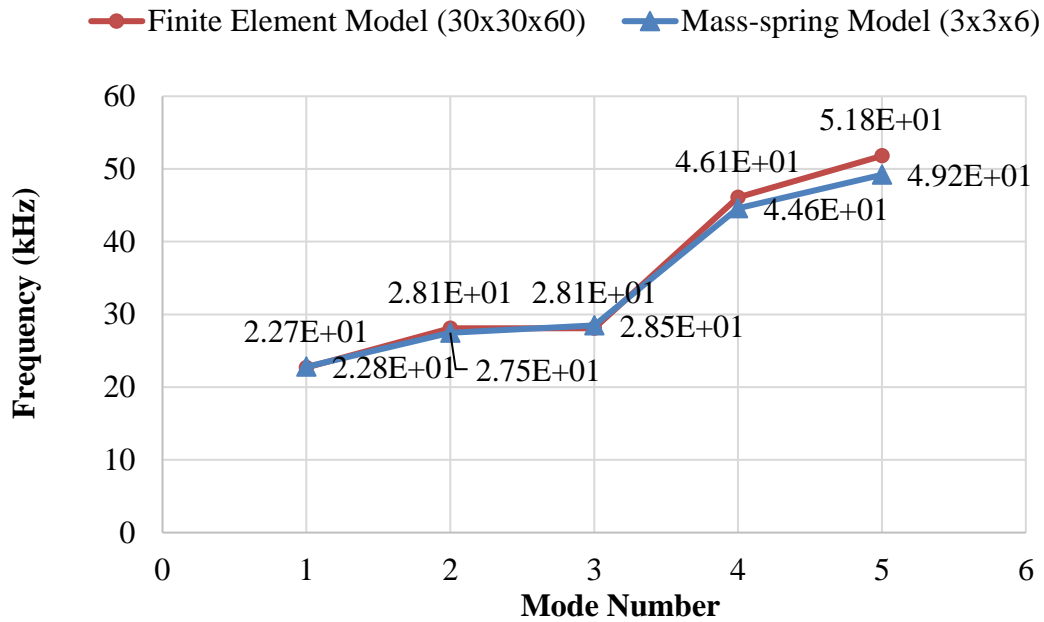


Figure B.8 Modal frequency predictions from 3x3x6 mass-spring model and 30x30x60 finite element model in 3-D

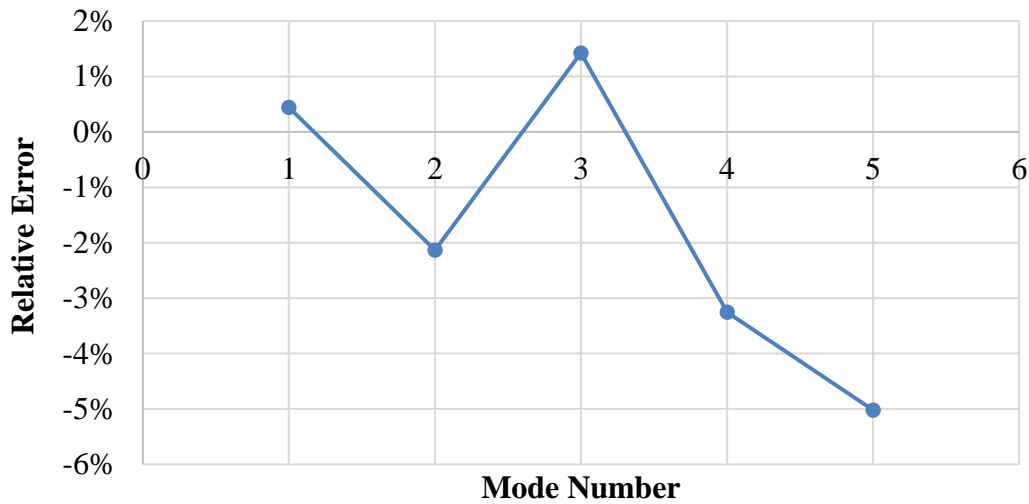


Figure B.9 Relative difference of frequency prediction of 20x20 mass-spring model

The effects of Poisson’s Ratio

The effect of Poisson’s ratios is examined by running the finite element model of the built feature under forced vibration of 20 kHz. The dimension and material properties of the model remain the same as the finite element model used in section 6.4.1. The boundary condition is imposed such that the top surface of the built feature is subjected to a traction force along the sonotrode vibration direction while the bottom surface remains clamped. The traction force is the interfacial friction which is calculated from a compression force of 1600N and a constant friction coefficient of 0.4 based on the Coulomb’s law: $F_f = \mu P = 640N$. The traction force assumed sinusoidal in time and its frequency is fixed to 20 kHz. The transient responses are measured at both center and edge along the width of the foil underneath the sonotrode and are shown in **Figure B.10**. No significant difference is observed between the responses with different Poisson’s ratios, meaning that in 3-

D case the materials with Poisson's ratio of 0.33 can be approximated using a mass-spring model with Poisson's ratio of 0.25. More tests are needed for future work to identify an interval of Poisson's ratio within which the dynamic responses can be approximated using mass-spring model.

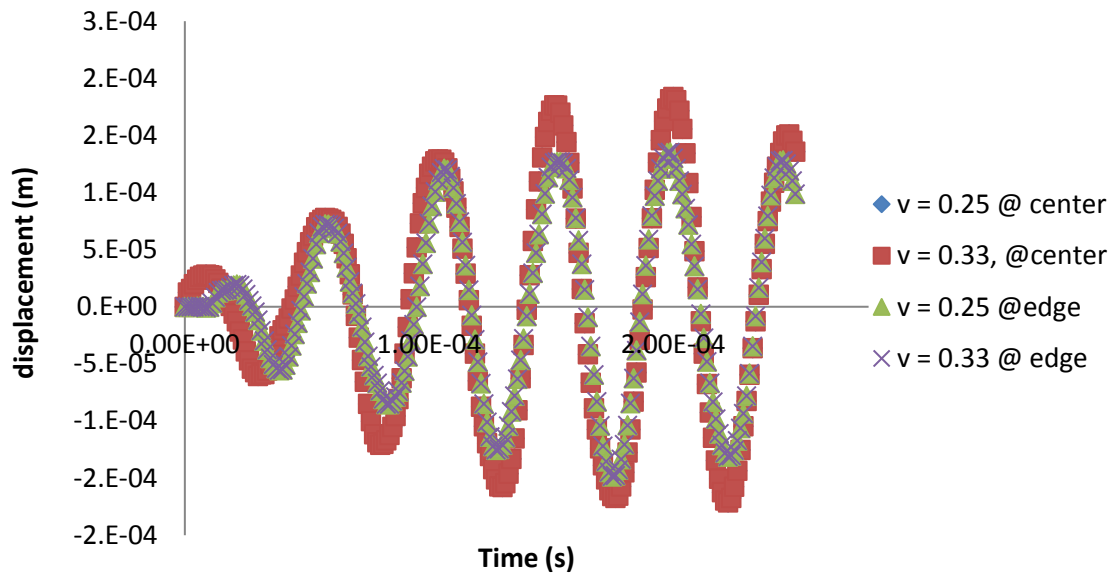


Figure B.10 The effect of Poisson's ratio on the transient response of the built feature.

Summary

In this section, a lumped parameter model consisting of mass-spring networks is established in both 2-D and 3-D to characterize the dynamics of the built feature with less computational cost. The model shows some promising results in terms of predicting natural frequencies and mode shapes of the built feature with coarse mesh in both 2-D and 3-D cases and with less computational time in 3-D case. The next step is to calculate the transient dynamic response of the built feature under forced vibration using mode superposition

method. Then the responses can be imported into finite element software for defining the dynamics of the built feature. In this way the computational time of the integrated UAM model is expected to reduce significantly.

Bibliography

- Abaqus. 2015. *User Manual ver. "6.14."* Providence: Hibbit Karlsson and Sorensen.
- Abbott, E. J., and F. A. Firestone. 1995. "Specifying Surface Quality: A Method Based on Accurate Measurement and Comparison." *SPIE MILESTONE SERIES MS 107*: pp.63-63.
- Baker, G. S., and S. H. Carpenter. 1965. "Simultaneous Deformation and Internal Friction Measurements." *Review of Scientific Instruments* 36(1): 29–31.
- Biddell, D. C., and D. H. Sansome. 1974. "The Development of Oscillatory Metal-Drawing Equipment—An Engineer's View." *Ultrasonics* 12(5): 195–205.
- Blaha, F., and B. Langenecker. 1955. "Dehnung von Zink- Kristallen Unter Ultraschalleinwirkung." *Die Natur-wissenschaften*: 556.
- Blaha, F, and B. Langenecker. 1959a. "Plastizitätsuntersuchungen von Metallkristallen in Ultraschallfeld." *Acta Metallurgica* 7(2): 93–100.
- Blaha, F, and B. Langenecker. 1959b. "Ultrasonic Investigation of the Plasticity of Metal Crystals."
- Broggiato, G. B., F. Campana, and L. Cortese. 2008. "The Chaboche Nonlinear Kinematic Hardening Model: Calibration Methodology and Validation." *Meccanica* 43(2): 115–24.
- Cheng, X. D., and X. C. Li. 2007. "Investigation of Heat Generation in Ultrasonic Metal Welding Using Micro Sensor Arrays." *Journal of Micromechanics and Microengineering* 17: 273–82.
- Cooper, M. G., B. B. Mikic, and M. M. Yovanovich. 1969. "Thermal Contact Conductance." *International Journal of Heat and Mass Transfer* 12(3): 279–300.

- Culp, D. R., and H. T. Gencsoy. 1973. "Metal Deformation with Ultrasound." In *1973 Ultrasonics Symposium*, IEEE., 195–98.
- Czichos, H. 1972. "The Mechanism of the Metallic Adhesion Bond." *Journal of Physics D: Applied Physics* 5(10): 1890.
- Daud, Y., M. Lucas, and Z. Huang. 2006. "Superimposed Ultrasonic Oscillations in Compression Tests of Aluminium." *Ultrasonics* 44: e511–15.
- Deshpande, V. S., D. S. Balint, A. Needleman, and E. Van Der Giessen. 2007. "Size Effects in Single Asperity Frictional Contacts." *Modelling and Simulation in Materials Science and Engineering* 15(1): S97–108.
- Dutta, R. K. et al. 2013. "The Effect of Tensile Deformation by in Situ Ultrasonic Treatment on the Microstructure of Low-Carbon Steel." *Acta Materialia* 61(5): 1592–1602.
- Eaves, A. E., A. W. Smith, W. J. Waterhouse, and D. H. Sansome. 1975. "Review of the Application of Ultrasonic Vibrations to Deforming Metals." *Ultrasonics* 13(4): 162–70.
- Epler, M. 2004. "Structures by Precipitation from Solid Solution." In *ASM Handbook, Volume 9: Metallography and Microstructures*, ed. Vander Voort. Materials Park, OH, 134–39.
- Espinosa, H. D., A. J. Patanella, and M. Fischer. 2000. "Dynamic Friction Measurements at Sliding Velocities Representative of High-Speed Machining Processes." *Transactions of the AMSE* 122(October).
- Fabrisonic. 2016. "Fabrisonic Inc." <http://fabrisonic.com/>.
- Foster, D. R., M. J. Dapino, and S. S. Babu. 2013. "Elastic Constants of Ultrasonic Additive

- Manufactured Al 3003-H18.” *Ultrasonics* 53(1): 211–18.
- Foster, D. R. 2014. “Mechanical and Thermal Characterization of Ultrasonic Additive Manufacturing.” Ohio State University.
- Frederick, J. R. 1965. *Ultrasonic Engineering*.
- Friel, R. J., K. E. Johnson, P. M. Dickens, and R. A. Harris. 2010. “The Effect of Interface Topography for Ultrasonic Consolidation of Aluminium.” *Materials Science and Engineering A* 527(16–17): 4474–83.
- Frost, H. J., and M. F. Ashby. 1982. *Deformation Mechanism Maps: The Plasticity and Creep of Metals and Ceramics*. Pergamon press. BOOK.
- Gao, Y., and C. Dourmanidis. 2002. “Mechanical Analysis of Ultrasonic Bonding for Rapid Prototyping.” *Journal of Manufacturing Science and Engineering* 124(2): 426.
- Gibert, J. M., 2009. “Dynamics of Ultrasonic Consolidation.”
- Gibert, J. M. et al. 2009. “Stick-slip Dynamics in Ultrasonic Consolidation.” : 1–11.
- Gibert, J. M., E. M. Austin, and G. M. Fadel. 2010. “Effect of Height to Width Ratio on the Dynamics of Ultrasonic Consolidation.” *Rapid Prototyping Journal* 16(4): 284–94.
- Gibert, J. M., G. M. Fadel, and M. F. Daqaq. 2013. “On the Stick-Slip Dynamics in Ultrasonic Additive Manufacturing.” *Journal of Sound and Vibration* 332(19): 4680–95.
- Gilman, T. et al. 2015. “Using Nonlinear Kinematic Hardening Material Models For Elastic-Plastic Ratcheting Analysis.” *ASME 2015 Pressure Vessels and Piping Conference* 137(June): 1–10.
- Greenwood, J. A., & Williamson, J. B. P. 1966. “Contact of Nominally Flat Surfaces.” *Proceedings of the Royal Society of London A: Mathematical, Physical and Engineering*

Sciences. 295(1442): 300–319.

Gunduz, I. E. et al. 2005. “Enhanced Diffusion and Phase Transformations during Ultrasonic Welding of Zinc and Aluminum.” *Scripta Materialia* 52(9): 939–43.

Hill, R., and J. R. Rice. 1972. “Constitutive Analysis of Elastic-Plastic Crystals at Arbitrary Strain.” *Journal of the Mechanics and Physics of Solids* 20(6): 401–13.

Hodowany, J, G Ravichandran, A. J. Rosakis, and P. Rosakis. 2000. “Partition of Plastic Work into Heat and Stored Energy in Metals.” *Experimental Mechanics* 40(2): 113–23.

Hopperstad, O. S., M. Langseth, and S. Remseth. 1995. “Cyclic Stress-strain Behaviour of Alloy AA6060 T4 , Part II : Biaxial Experiments and Modelling.” *International Journal of Plasticity* 11(6): 741–62.

Huang, H. et al. 2009. “Influence of Superimposed Ultrasound on Deformability of Cu.” *Journal of Applied Physics* 106(11): 113514–16.

Hung, J. C., Y. C. Tsai, and C. H. Hung. 2007. “Frictional Effect of Ultrasonic-Vibration on Upsetting.” *Ultrasonics* 46(3): 277–84.

Jedrasiak, P. et al. 2014. “Modeling of the Thermal Field in Dissimilar Alloy Ultrasonic Welding.” *Journal of Materials Engineering and Performance* 24(2): 799–807.

Jenq, S. T., and S. L. Sheu. 1994. “An Experimental and Numerical Analysis for High Strain Rate Compressional Behavior of 6061-O Aluminum Alloy.” *Computers & Structures* 52(1): 27–34.

Johnson, G. R, and W. H. Cook. 1983. “A Constitutive Model and Data for Metals Subjected to Large Strains, High Strain Rates and High Temperatures.” *Proceedings of the 7th International Symposium on Ballistics* (21): 541-547)

- Johnson, K., H. C. Edmonds, R. L. Higginson, and R. A. Harris. 2011. "New Discoveries in Ultrasonic Consolidation Nano-Structures Using Emerging Analysis Techniques." *Proceedings of the Institution of Mechanical Engineers, Part L: Journal of Materials Design and Applications* 225(4): 277–87.
- Johnson, K. L. 1985. "Contact Mechanics." *Journal of the American Chemical Society* 37(22): 1–17.
- Johnson, K E. 2008. "Interlaminar Subgrain Refinement in Ultrasonic Consolidation."
- Joshi, K. C. 1971. "The Formation of Ultrasonic Bonds between Metals." *Welding Journal*.
- Kaufman, J. G. 1999. *Properties of Aluminum Alloys: Tensile, Creep, and Fatigue Data at High and Low Temperatures*. ASM international. BOOK.
- Kelly, G. 2012. "A Thermo-Mechanical Finite Element Analysis of Acoustic Softening during Ultrasonic Consolidation of Aluminum Foils."
- Kelly, G. S., S. G. Advani, and J. W. Gillespie. 2012. "Thermo-mechanical Modeling of Acoustic Softening During Ultrasonic Consolidation of Thin Aluminum Foils." : 4048.
- Kelly, G. S., and S. G. Advani. 2013. "A Model to Characterize Acoustic Softening during Ultrasonic Consolidation." *Journal of Materials Processing Technology* 213: 1835–45.
- Kenik, E., and R. Jahn. 2003. "Microstructure of Ultrasonic Welded Aluminum by Orientation Imaging Microscopy." *Microscopy and Microanalysis* 9(S02): 720–21.
- Kirchner, H. O. K., W. K. Kromp, F. B. Prinz, and P. Trimmel. 1985. "Plastic Deformation under Simultaneous Cyclic and Unidirectional Loading at Low and Ultrasonic Frequencies." *Materials Science and Engineering* 68(2): 197–206.
- Kocks, U. F. 1987. "Constitutive Behavior Based on Crystal Plasticity." In *Unified*

Constitutive Equations for Creep and Plasticity, Springer. CHAP, 1–88.

Koellhoffer, S., J. W. Gillespie, S. G. Advani, and Travis a. Bogetti. 2011. “Role of Friction on the Thermal Development in Ultrasonically Consolidated Aluminum Foils and Composites.” *Journal of Materials Processing Technology* 211(11): 1864–77.

Kong, C. Y., R. C. Soar, and P. M. Dickens. 2005. “A Model for Weld Strength in Ultrasonically Consolidated Components.” *Proceedings of the Institution of Mechanical Engineers, Part C: Journal of Mechanical Engineering Science* 219(1): 83–91.

Kong, C. Y., R. C. Soar, and P. M. Dickens. 2003. “Characterisation of Aluminium Alloy 6061 for the Ultrasonic Consolidation Process.” *Materials Science and Engineering: A* 363(1–2): 99–106.

Kong, C. Y., R.C. Soar, and P. M. Dickens. 2004. “Optimum Process Parameters for Ultrasonic Consolidation of 3003 Aluminium.” *Journal of Materials Processing Technology* 146(2): 181–87.

Kragelski, I. V. 1965. *Friction and Wear*. Butterworths.

Krausz, A. S, and K. Krausz. 1996. *Unified Constitutive Laws of Plastic Deformation*. Elsevier. BOOK.

Kulakov, M., and H. J. Rack, 2010. “Surface Damage during Ultrasonic Consolidation of 3003-H18 Aluminum.” *Rapid Prototyping Journal* 16(1): 12–19.

Langenecker, B. 1963. “Effect of Sonic and Ultrasonic Radiation on Safety Factors of Rockets and Missiles.” *AIAA Journal* 1(1): 80–83.

Langenecker, B. 1966. “Effects of Ultrasound on Deformation Characteristics of Metals.” *Sonics and Ultrasonics, IEEE Transactions on* (1).

- Leagon, J.M. 2007. *Characterization of The Interlaminar Shear Strength of Ultrasonically Consolidated Components*
- Lee, S. 2013. “Process and Quality Characterization for Ultrasonic Welding of Lithium-Ion Batteries.”
- Lesuer, D R, G J Kay, and M M LeBlanc. 2001. “Modeling Large-Strain, High-Rate Deformation in Metals.” *Third Biennial Tri-Laboratory Engineering Conference Modeling and Simulation: 3–5.*
- Li, D., and R. Soar. 2009. “Influence of Sonotrode Texture on the Performance of an Ultrasonic Consolidation Machine and the Interfacial Bond Strength.” *Journal of Materials Processing Technology* 209(4): 1627–34.
- Lindsay, R. B. 1960. *Mechanical Radiation*. McGraw-Hill.
- Lum, I et al. 2009. “Effects of Superimposed Ultrasound on Deformation of Gold.” *Journal of Applied Physics* 105(2): 24905.
- Manes, A., L. Peroni, M. Scapin, and M. Giglio. 2011. “Analysis of Strain Rate Behavior of an Al 6061 T6 Alloy.” *Procedia Engineering* 10: 3477–82.
- Mao, Q., J. M. Gibert, and G. M. Fadel,. 2014. “Investigating the Ultrasound-Induced Acoustic Softening in Aluminum 6061.” In *Proceedings of the ASME 2014 International Design Engineering Technical Conferences & Computers and Information in Engineering Conference (IDETC/CIE 2014)*, Buffalo, NY.
- Mayer, M., and J. Schwize. 2003. “Thermosonic Ball Bonding Model Based on Ultrasonic Friction Power.” : 3–8.
- Mccullough, D. T, Ann Arbor, and Eric M Austin. “Stick-slip Dynamics in Ultrasonic

Consolidation for Nominal Width Features: Theory and Experiment.” : 1–39.

“McMaster Carr.” 2015. <http://www.mcmaster.com/>.

Mignogna, R. B., and R. E. Green J. 1979. “Multiparameter System for Investigation of the Effects of High-Power Ultrasound on Metals.” *Review of Scientific Instruments* 50(10): 1274–77.

Moore, D. F. 2013. *Principles and Applications of Tribology: Pergamon International Library of Science, Technology, Engineering and Social Studies: International Series in Materials Science and Technology*. Elsevier.

Naidu, N. K. R., and S. G. S. Raman. 2005. “Effect of Shot Blasting on Plain Fatigue and Fretting Fatigue Behaviour of Al-Mg-Si Alloy AA6061.” *International Journal of Fatigue* 27: 323–31.

Nevill, G. E., and F. R. Brotzen. 1957. “The Effect of Vibrations on the Static Yield Strength of a Low-Carbon Steel.” *Proceeding-American Society for Testing Material* 57: 751–58.

Ogawa, K. 2002. “Impact Tensile Strength of 6061-O Aluminum Alloy.” *Journal of Japan Institute of Light Metals* 52(3): 131–35.

Padró, P. M. 2015. “Finite Element Simulation of Elastic Contact between Rubber Rough Surface and Steel.”

Pal, D., and B. E. Stucker. 2012. “Modelling of Ultrasonic Consolidation Using a Dislocation Density Based Finite Element Framework: In This Paper a Dislocation Density Based Constitutive Model Is Developed and Implemented into a Crystal Plasticity Quasi-Static Finite Element.” *Virtual and Physical Prototyping* 7(1): 65–79.

- Pei, L., S. Hyun, J. F. Molinari, and Mark O. Robbins. 2005. "Finite Element Modeling of Elasto-Plastic Contact between Rough Surfaces." *Journal of the Mechanics and Physics of Solids* 53(11): 2385–2409.
- Pohlman, R., and E. Lehfeltdt. 1966. "Influence of Ultrasonic Vibration on Metallic Friction." *Ultrasonics* 4(4): 178–85.
- Ram, G. D. J., C. Robinson, Y. Yang, and B.E. Stucker. 2007. "Use of Ultrasonic Consolidation for Fabrication of Multi-Material Structures." *Rapid Prototyping Journal* 13(4): 226–35.
- Ram, G. D. J., Y. Yang, et al. 2007. "Interface Microstructures and Bond Formation in Ultrasonic Consolidation." : 266–83.
- Robinson, C. J., C. Zhang, and G. D. Janaki Ram. 2006. "Maximum Height to Width Ratio of Freestanding Structures Built Using Ultrasonic Consolidation." *Proceedings of 17th ...*: 502–16.
- Rusinko, A. 2011. "Analytical Description of Ultrasonic Hardening and Softening." *Ultrasonics* 51(6): 709–14.
- Rusynko, A. K. 2001. "Mathematical Description of Ultrasonic Softening of Metals within the Framework of the Synthetic Theory of Plasticity." *Materials Science* 37(4): 671–76.
- Sakino, K. 2006. "Strain Rate Dependence of Dynamic Flow Stress Considering Viscous Drag for 6061 Aluminium Alloy at High Strain Rates." *J. Phys. IV France* 134: 183–89.
- Schick, D. E. et al. 2010. "Microstructural Characterization of Bonding Interfaces in Aluminum 3003 Blocks Fabricated by Ultrasonic Additive Manufacturing." *Welding Journal* 89: 105–15.

- Schick, D. et al. 2011. "Transient Thermal Response in Ultrasonic Additive Manufacturing of Aluminum 3003." *Rapid Prototyping Journal* 17(5): 369–79.
- Siddiq, A., and E. Ghassemieh. 2008a. "Thermomechanical Analyses of Ultrasonic Welding Process Using Thermal and Acoustic Softening Effects." *Mechanics of Materials* 40(12): 982–1000.
- Siddiq, A., and T. E. Sayed. 2011. "Acoustic Softening in Metals during Ultrasonic Assisted Deformation via CP-FEM." *Materials Letters* 65(2): 356–59.
- Siddiq, A., and T. E. Sayed. 2012. "A Thermomechanical Crystal Plasticity Constitutive Model for Ultrasonic Consolidation." *Computational Materials Science* 51(1): 241–51.
- Siddiq, A., and T. E. Sayed. 2012. "Ultrasonic-Assisted Manufacturing Processes: Variational Model and Numerical Simulations." *Ultrasonics* 52(4): 521–29.
- Siddiq, Amir, and Siegfried Schmauder. 2006. "Crystal Plasticity Parameter Identification Procedure for Single Crystalline Material During Deformation." 7(1): 1–15.
- Siu, K. W., and A. H. W. Ngan. 2013. "Oscillation-Induced Softening in Copper and Molybdenum from Nano-to Micro-Length Scales." *Materials Science and Engineering: A*.
- Siu, K W, A. H. W. Ngan, and I. P. Jones. 2011. "New Insight on acoustoplasticity—Ultrasonic Irradiation Enhances Subgrain Formation during Deformation." *International Journal of Plasticity* 27(5): 788–800.
- Song, H., R. J. Dikken, L. Nicola, and E. van der Giessen. 2015. "Plastic Ploughing of a Sinusoidal Asperity on a Rough Surface." *Journal of Applied Mechanics* 82(7): 71006.
- Sriraman, M. R. et al. 2011. "Thermal Transients during Processing of Materials by Very High Power Ultrasonic Additive Manufacturing." *Journal of Materials Processing*

Technology 211: 1650–57.

Sriraman, M.R., S.S. Babu, and M. Short. 2010. “Bonding Characteristics during Very High Power Ultrasonic Additive Manufacturing of Copper.” *Scripta Materialia* 62(8): 560–63.

Swank, ML. 2010. “Support Materials Development and Integration for Ultrasonic Consolidation.”

Timoshenko, S.P. 1970. *Theory of Elasticity*. McGraw-Hill.

Truog, Adam G. 2012. “Bond Improvement of Al/Cu Joints Created by Very High Power Ultrasonic Additive Manufacturing.”

de Vries, E. 2004. “Mechanics and Mechanisms of Ultrasonic Metal Welding.”

White, D. R. 2003. “Ultrasonic Consolidation of Aluminum Tooling.” *Advanced materials & processes*.

Winsper, C. E, and D H Sansome. 1969. “Fundamentals of Ultrasonic Wire Drawing.” *J Inst Metals* 97(9): 274–80.

Winsper, C. E. and Sansome, D. H.. 1971. “Application of Ultrasonic Vibrations to the Plug Drawing of Tube.” *Metal Forming* 38(3): 71–75.

Wodara, J. 1986. “Joint Formation in the Ultrasonic Welding of Metallic Substances.” *ZIS Mitt.* 28(1): 102–8.

Wolcott, P J, A Hehr, and M J Dapino. 2014. “Optimized Welding Parameters for Al 6061 Ultrasonic Additive Manufactured Structures.” *Journal of Materials Research* 29(17): 2055–65.

Yadav, S, and D R Chichili. 1995. “The Mechanical Response of a 6061-T6 Al/A12O3

Metal Matrix Composite at High Rates of Deformation.” *Acta metall, mater.* 43(12): 4453–64.

Yang, Y., G.D. Janaki Ram, and B.E. Stucker. 2009. “Bond Formation and Fiber Embedment during Ultrasonic Consolidation.” *Journal of Materials Processing Technology* 209(10): 4915–24.

Yao, Z., G.Y. Kim, Z. Wang, et al. 2012. “Acoustic Softening and Residual Hardening in Aluminum: Modeling and Experiments.” *International Journal of Plasticity* 39: 75–87.

Yao, Z., G. Y. Kim, L. Faidley, et al. 2012. “Effects of Superimposed High-Frequency Vibration on Deformation of Aluminum in Micro/meso-Scale Upsetting.” *Journal of Materials Processing Technology* 212(3): 640–46.

Zhang, C., and L. Li. 2008. “A Friction-Based Finite Element Analysis of Ultrasonic Consolidation.” *The Welding Journal-New York-* 87(7): 187.

Zhang, C., A. Deceuster, and L. Li. 2009. “A Method for Bond Strength Evaluation for Laminated Structures with Application to Ultrasonic Consolidation.” *Journal of Materials Engineering and Performance* 18(8): 1124–32.

Zhang, C. and L. Li. 2007. “Effect of Friction on Ultrasonic Consolidation.” *ASME 2007 International*

Zhang, C., and L. Li. 2006. “A Study of Static and Dynamic Mechanical Behavior of the Substrate in Ultrasonic Consolidation.” *Solid Freeform Fabrication Symposium*: 546–57.

Zhang, C., Z. Zhu, and L. Li. 2006. “A Study of Friction Behavior in Ultrasonic Welding (Consolidation) of Aluminum.” *Proceedings of the AWS Conference: Session 7*: 151–56.

Zhu, Z, B P Wynne, E Ghassemieh, and a Siddiq. 2009. “Microstructural Analysis of

Ultrasonic Welded AA6061 by Electron Backscattered Diffraction.” *Rare Metal Materials And Engineering* 38: 147–51.